

Sediment Diagenesis and Characteristics of Grains and Pore Geometry in Sandstone Reservoir Rocks from a Well of the North German Basin

Dissertation
der Fakultät für Geowissenschaften
der Ludwig-Maximilians-Universität
München



vorgelegt von
Kim Phuong Lieu

München, 17.09.2013

Gutachter:

1. Prof. Dr. Wolfgang W. Schmahl

Ludwig Maximilians University of Munich,
Crystallography Section, Germany

2. Prof. Dr. Wladyslaw Altermann

University of Pretoria, Department of Geology, South Africa

Disputation: 15.01.2014

ACKNOWLEDGEMENTS

I would like to express my sincere gratitude to the Vietnamese Government, Vietnam Petroleum Institute for financial support of my doctoral study at the Ludwig-Maximilians University in Munich, Germany. The financial support by the German Federal Ministry of Education and Research (BMBF) for the NanoPorO (Nanostruktur und Benetzungseigenschaften von Sedimentkorn- und Porenraumoberflächen / eng.: Nanomorphology and Wetting Properties of Sediment Grain and Porespace Surfaces) project in which I have performed most of the present research is also acknowledged.

Furthermore, I would like to thank RWE Dea AG, the industrial partner in the NanoPorO project, for providing the samples and for the contribution of important petrophysical data.

Moreover, I am particularly grateful to my supervisors, Prof. Dr. Wladyslaw Altermann and Dr. Michaela Frei who not only gave me the freedom to follow my ideas, but also gave me guidance and support concerning academic issues and always encouraged me. I very much appreciate their expertise and their helpful suggestions and discussions, which were extremely valuable. Thanks also for the free and friendly environment that really motivated me in my every day studies. Thank you very much for your support.

Also I gratefully acknowledge Prof. Dr. Robert Stark for giving me his guidance in nanotechnology and the opportunity to work with advanced high-tech microscopic techniques in his research group.

I like to thank Prof. Dr. Wolfgang Schmahl for giving me the opportunity to conduct part of my investigations in his laboratories. My sincere thanks go to him for his administrative support at the Ludwig-Maximilians University in Munich.

Dr. Tanja Drobek, Dr. Michael Bauer, I like to thank for showing me the experimental approaches with the Confocal Laser Scanning Microscopy, Confocal Raman Microscopy and for supporting me with literature related to this study area. Mr. Joachim Strobel of RWE Dea AG has supported me with his expertise in petrophysics and his knowledge on the geology of the Oil and Gas fields of the North German Basin

Thanks also to my friends and colleagues Dr. Marek Janko, Dr. Christian Dietz, and Agnieszka Maria Voß from Physics of Surfaces (POS) group, TU Darmstadt, who shared

their expertise in Atomic Force Microscopy with me and motivated me and to all the colleagues in the group of Physics of Surfaces (POS) TU Darmstadt for the pleasant working atmosphere.

Further thanks to Dr. Philipp Komissinskiy from the Department of Materials and Geosciences at the Technische Universität Darmstadt, for access to the Scanning Electron Microscope facility and for his support in SEM related topics.

I am also grateful to Manuela Romero, María Concepción Baqué, Petra Gotta, Zoe Fintescu, and Hoa Pham Thi who encouraged and prompted me beyond my studies. Particularly, I like to thank Romero, Baqué and Gotta for their kind help in solving problems, for sharing their time with me and for cheering up my years in Germany.

I appreciate the help and recommendation of Dr. Bui Thi Luan, Prof. Vu Quang Binh and Prof. Ta Thi Kim Oanh from University of Science Ho Chi Minh City and HoChiMinh City Institute of Resources Geography, Viet Nam. Thank to Dr. Bui Thi Luan for her help and encouragement that prompted me to go ahead with my scientific career.

I would also like to acknowledge the Center for NanoScience (CeNS) and the Ludwig-Maximilians University in Munich, the Department of Earth and Environment Sciences, and the Center of Smart Interfaces and the Department of Materials and Geosciences of the Technische Universität Darmstadt, Germany for supporting the work in laboratories to carry out this investigation.

Finally, my deepest gratitude goes to my mother, my sisters and brothers and to all my friends in Vietnam for their support, their understanding and their interest in my live in Germany over the last years.

Thanks to all of you. Thank you very much!

ABSTRACT

The Rotliegend sandstone reservoir rocks from the Lower Saxony Basin in northern Germany have a high hydrocarbon accumulation capacity. The sandstones at a depth of roughly 2081 m to 5049 m in the investigated borehole, feature high porosity and permeability. They are sealed by overlying Zechstein deposits and directly overlap Carboniferous source rocks for gas accumulations. The diagenetic evolution of these sandstones caused severe deformation in pore space and grain morphology during deposition and burial. To facilitate a better extraction of the hydrocarbons from the sandstone reservoir rocks it is necessary to know the grain properties and interaction between the hydrocarbons and their surfaces. Hence the composition and structure of the grain surface have to be known. The major issue of this study is to determine on the pore geometry and the grain surface roughness, which were formed by the authigenic minerals during diagenesis and their influences on pore walls and connection paths. The parameters of the grain surface characteristics are the important input necessary to understand wetting properties and adhesive forces for the modeling of the hydrocarbons extraction techniques from sandstone reservoir rocks. Samples are analysed using non destructive, high resolution microscopy techniques such as Confocal Laser Scanning Microscopy (CLSM) and Atomic Force Microscopy (AFM) to determine their structure and surface roughness. Rock composition is revealed by optical microscopy and Raman spectroscopy. Crystal habits of authigenic minerals and cement textures are investigated by Scanning Electron Microscopy (SEM).

It is observed that the constituent of the sandstone is mainly quartz, feldspar, plagioclase and small amounts of volcanic, metamorphic and igneous rock fragments, deposited in fluvial or shallow water environments. The detrital grains experienced variations in grain morphology, the shape of the pore space formed between grains depend to diagenetic conditions. Most of the grain surfaces are coated with illite - chlorite, illite and chlorite authigenic minerals and some of them are covered with authigenic quartz or albite. Pore spaces are found to be largely filled by calcite and subordinate anhydrite. The authigenic minerals: quartz, albite, illite and chlorite also appear in pore – fillings. Authigenic minerals often overlap the grain surface leading to roughened pore walls, narrowed pore throats and deformed pore geometry.

The analysis of the grain morphology of three Rotliegend sandstone reservoirs which were taken from depth of about 2111 m – 5041 m depth reveals that authigenic and cement

minerals entirely covered the surface of grains at the depth of roughly 2111 m (RL I_2111). The surface of grains at approximately 4146 m depth (RL I_4146) is both overgrown with authigenic and cement minerals and slightly compacted while grains at roughly 5041 m depth (RL I_5041) are strongly compacted and overgrown with authigenic and cement minerals. The grain surfaces of sample at the 2111 m depth shows the highest roughness with the largest roughness parameter values. The grain surfaces with lower roughness and the lowest roughness are the surfaces of samples at the 4146 m and 5041 m depth respectively. Additionally, the irregularity of the grain surface expressed by the root mean square roughness (R_q) value is the largest for the grain surfaces of sample at the 2111 m depth and the smallest for those of sample at the 5041 m depth. Pore networks in sample at the 2111 m depth are completely filled by authigenic and cement minerals. Pore spaces in sample at the 4146 m depth are partly blocked by authigenic and cement minerals while pore spaces in sample at the 5041 m depth were less filled by authigenic and cements and are connected by pore paths. Therefore, the fluid flow through pore spaces in this sample is less affected compared to restricted fluid flows in sample at the 2111 m and 4146 m depth.

For the same three Rotliegend sandstone samples, the roughness of the authigenic minerals covering the grain surfaces was measured. It reveals that the roughness of illite - chlorite is the highest with the largest R_q value and that the roughness of chlorite is higher than that of illite. The grain surface of sample at the 2111 m depth is commonly coated with illite - chlorite and the surface of sample at the 4146 m and 5041 m depth is predominantly covered with illite. Therefore, the roughness of sample at the 2111 m depth is higher than of sample at the 4146 m depth and sample at the 5041 m depth. The other authigenic minerals: quartz, albite, halite, and calcite cover some of the grain surfaces so that their roughness values only represent a partial roughness value.

All results obtained in this work reveal the influence of the grain roughness on the pore shape, the permeability of the rocks and on the wetting and the adhesion properties of the grain surface. The results of this study will allow to calculate better models for hydrocarbon exploitation, to enhance oil recovery from sandstone reservoir rocks.

LIST OF FIGURES

Figure 2.1 Map of the study area and extent of the Lower Saxony Basin

Figure 3.2.1 Well RL I, sample 4146

Figure 3.2.2 Well RL I, sample 4797

Figure 3.2.3 Well RL I, sample 2111

Figure 3.2.4 Well RL I, sample 4839

Figure 3.2.5 Well RL I, sample 3139

Figure 3.2.6 Well RL I, sample 5041

Figure 3.2.7 Well RL I, sample 5049

Figure 3.2.8 Well RL I, sample 2111

Figure 3.2.9 Well RL I, sample 4146

Figure 3.2.10 Well RL I, sample 4839

Figure 3.2.11 Well RL I, sample 3319

Figure 3.2.12 Well RL I, sample 5041

Figure 3.2.13 Well RL I, sample 4212

Figure 3.2.14 Well RL I, sample 4839

Figure 3.2.15 Well RL I, sample 4838

Figure 3.2.16 Well RL I, sample 4896

Figure 3.2.17 Well RL I, sample 4904

Figure 3.2.18 Well RL I, sample 5049

Figure 3.2.19 Well RL I, sample 4146

Figure 3.2.20 Well RL I, sample 2081

Figure 3.3.1 SEM image showing filamentous authigenic illite

Figure 3.3.2 SEM image showing filamentous illite

Figure 3.3.3 SEM image showing the pore space between detrital grains

Figure 3.3.4 Authigenic illite with the ribbons

Figure 3.3.5 The authigenic clays in pore

Figure 3.3.6 The pore space is filled by mixed authigenic chlorite and illite

Figure 3.3.7 Mixed illite - smectite clays

Figure 3.3.8 SEM authigenic albite crystals

Figure 3.3.9 The jagged overgrowth of a thin authigenic clay layer

Figure 3.3.10 SEM image shows intergranular pore

Figure 3.3.11 SEM shows the individual chlorite

- Figure 3.3.12 SEM shows an authigenic clay flake
- Figure 3.3.13 Authigenic quartz in pores
- Figure 3.3.14 SEM shows quartz overgrowth and authigenic albite in pore
- Figure 3.3.15 The intergranular pores and pore throats
- Figure 3.2.16 SEM reveals authigenic cristobalite crystals
- Figure 3.3.17 Authigenic albite
- Figure 3.3.18 Cubic halite crystals cross clay coatings
- Figure 3.3.19 Authigenic siderite
- Figure 3.3.20 Calcite cement fills pores
- Figure 3.3.21 A detrital K – feldspar
- Figure 4.1 CLSM image of an albite authigenic mineral grown in the pore space of sample RL I_2111.
- Figure 4.2 CLSM image shows the structure of pore
- Figure 4.3 CLSM image of authigenic minerals in pores
- Figure 4.4 Grain surface and pore throat of sample RL I_4146
- Figure 4.5 CLSM image of the pore surface, SEM photographs of fibrous illites and EDX spectrum
- Figure 4.6 CLSM image of a pore throat.
- Figure 5.1 CLSM and AFM images, sample RL I_2111_Qu_1
- Figure 5.2 SEM images and EDX spectra, sample RL I_2111_Qu_1
- Figure 5.3 CLSM and AFM images, sample RL I_2111_Qu_2
- Figure 5.4 SEM images and EDX spectra, sample RL I_2111_Qu_2
- Figure 5.5 CLSM and AFM images, sample RL I_2111_A
- Figure 5.6 SEM images and EDX spectra, sample RL I_2111_A
- Figure 5.7 CLSM and AFM images, sample RL I_4146_Qu_1
- Figures 5.8 and 5.9 SEM images and EDX spectra, sample RL I_4146_Qu_1
- Figure 5.10 CLSM and AFM images, sample RL I_4146_E
- Figure 5.11 SEM images and EDX spectra, sample RL I_4146_E
- Figures 5.12 and 5.13 CLSM and AFM images, sample RL I_5041_Qu_1
- Figure 5.14 CLSM and AFM images, sample RL I_5041_Qu_1
- Figure 5.15 CLSM and AFM images, sample RL I_5041_Qu_4
- Figure 5.16 SEM images and EDX spectra, sample RL I_5041_Qu_4
- Figure 5.17 CLSM and AFM images, sample RL I_5041_D
- Figure 5.18 SEM images and EDX spectra, sample RL I_5041_D

Figure 5.19 Diagram of the root mean square roughness values of the minerals

Figure 6.1 A “pigeon – hole” model

LIST OF TABLES

- Table 2.1 Stratigraphy of reservoir rocks in the Lower Saxony Basin
- Table 3.1 Porosity and permeability of the selected samples
- Table 3.2 Diagenetic characteristic of the sandstones at the depth interval 2081 m – 5049 m
- Table 4.1 Definition of roughness parameters
- Table 4.2 Root mean square roughness R_q parameter calculated at 50x and 100x magnifications
- Table 4.3 Values of grain roughness parameters Rotliegend RL I well, at 10x magnification
- Table 5.1 Root mean square roughness (R_q) values of mineral coatings on grain surfaces sample RL I_2111
- Table 5.2 Root mean square roughness (R_q) values of cement surfaces, sample RL I_2111
- Table 5.3 Root mean square roughness (R_q) average values of grain surfaces, sample RL I_2111
- Table 5.4 Root mean square roughness (R_q) values of mineral coatings on grain surfaces sample RL I_4146
- Table 5.5 Root mean square roughness (R_q) values of cement surfaces, sample RL I_4146
- Table 5.6 Root mean square roughness (R_q) average values of grain surfaces, sample RL_4146
- Table 5.7 Root mean square roughness (R_q) values of mineral coatings on grain surfaces sample RL I_5041
- Table 5.8 Root mean square roughness (R_q) values of cement surfaces, sample RL I_5041
- Table 5.9 Root mean square roughness (R_q) average values of grain surfaces, sample RL I_5041
- Table 5.10 Root square mean roughness (R_q) values of the minerals
- Table 5.11 Porosity, permeability and roughness of the investigated samples

LIST OF ABBREVIATIONS

AFM	Atomic Force Microscopy
CLSM	Confocal Laser Scanning Microscopy
CO ₂	Carbon dioxide
EDX	Energy Dispersive X-ray system
R_a	Arithmetic average of the absolute values of the surface height deviations
R_q	Root mean square average of height deviations
SEM	Scanning Electron Microscopy

TABLE OF CONTENTS

1. INTRODUCTION	1
1.1 MOTIVATION	1
1.2 LITERATURE OVERVIEW OF PREVIOUS WORK	2
1.3 METHODOLOGY	3
1.3.1 Sampling	3
1.3.2 Research Methods	4
1.4 AIM OF THE THESIS	5
2. STUDY AREA	6
2.1 GEOGRAPHIC AND GEOLOGIC OVERVIEW	6
2.2 LOWER SAXONY BASIN TECTONIC AND STRATIGRAPHIC EVOLUTION	7
2.3 STRATIGRAPHY OF ROTLIEGEND RESERVOIR ROCKS IN THE LOWER SAXONY BASIN	9
2.3.1 Lower Rotliegend	10
2.3.2 Upper Rotliegend	11
2.4 DISTRIBUTION OF PETROLEUM IN THE LOWER SAXONY BASIN	12
3. PETROGRAPHY AND DIAGENESIS OF THE RESERVOIR SANDSTONE IN THE INVESTIGATED WELL OF THE NORTH GERMAN BASIN	14
3.1 METHODS	14
3.1.1 Optical microscopy	14
3.1.2 Scanning Electron Microscopy (SEM) and Energy Dispersive X-ray system (EDX)	15
3.2 PETROGRAPHY	15
3.2.1 Texture	16
3.2.2 Detrital mineral composition	22
3.2.3 Visible porosity	24
3.3 DIAGENESIS	29
3.3.1 Cement and authigenic minerals	31
3.3.2 Pore network	43
3.4 DISCUSSION	44

4. ANALYSIS OF PORE AND GRAIN GEOMETRY IN SANDSTONE RESERVOIR ROCKS FROM A WELL IN THE NORTH GERMAN BASIN	48
4.1 METHODS	49
4.1.1 Confocal Raman Microscopy	49
4.1.2 Confocal Laser Scanning Microscopy (CLSM)	50
4.2 ANALYTIC RESULTS	51
4.2.1 Grain roughness measurements	51
4.2.1.1 Sample RL I_2111	52
4.2.1.2 Sample RL I_4146	55
4.2.1.3 Sample RL I_5041	56
4.2.2 Pore space morphology	59
4.3 CONCLUSION	64
5. ROUGHNESS OF AUTHIGENIC MINERAL SURFACES OF SANDSTONE RESERVOIR ROCKS FROM A WELL IN THE NORTH GERMAN BASIN	67
5.1 METHODS	68
5.2 ANALYTIC RESULTS	69
5.2.1 Sample RL I_2111	69
5.2.2 Sample RL I_4146	84
5.2.3 Sample RL I_5041	96
5.3 CONCLUSION	109
6. DISCUSSION	113
6.1 THE DIAGENESIS	113
6.2 THE GRAIN MORPHOLOGY, GRAIN ROUGHNESS AND PORE GEOMETRY	114
7. CONCLUSION	116
REFERENCES	119
Appendix I: Macro samples, diagrams for estimation of grain sorting, categories of roundness for grains and grain size classification	126
Appendix II: Raman spectroscopy spectra and Confocal Laser Scanning Microscope image	129
Appendix III: Atomic Force Microscope, Scanning Electron Microscope images and Energy dispersive X-ray spectra	144

1. INTRODUCTION

1.1 MOTIVATION

Porous siliclastic sedimentary rocks are the most common reservoirs for oil and gas deposits worldwide. In northern Germany most commercial gas accumulation explored is deeply buried in the sandstone of the Rotliegend in Lower Saxony Basin. The sandstones in the Permian Rotliegend stratigraphy feature high porosity and permeability. In petroleum geology, pore space and grain geometry are important physical properties of reservoir rocks, particularly in sandstones, due to their influences on oil and gas reservoir quality. Therefore, a detailed study of grain morphology, grain surface roughness and pore geometry, and their impacts on wetting behaviour and adhesion properties of fluids to pore walls in sandstone reservoir rocks is an imperative issue in petroleum geology. The characteristics have influences on fluid flow movement through pores in rocks. During the last decades hydrocarbon was extracted from the sandstone reservoir rocks in the Permian Rotliegend in the Lower Saxony Basin. However, by exploitation with conventional methods considerable amount of the hydrocarbon have been lost, due to decreasing pressure, pore blocking, water invasion and the hydrocarbon adhering either to the pore spaces or to the grain surfaces, with extensive influence on the general reservoir quality assessment and oil production recovery.

In this work recent analytical developments applied in scientific fields such as in geosciences, are thus used to characterise the morphology of mineral grain surfaces and to investigate their pore geometry in sandstone rocks. Moreover, the fine surface structures and roughness of the authigenic minerals, which are formed during diagenesis, are studied. The grain surface roughness is one of the factors that significantly impact on wetting properties and permeability of sandstone reservoir rocks. The flow is restricted due to declining flow diameter caused by surface roughness. The most well known effects of micro and nano structures on wetting are super hydrophobicity known as “lotus effect”. The lotus effect is based on wetting of the rough surface. The liquids place on high peaks of the rough surface with small contact area and small adhesion forces. The wetting surface properties are not discussed in this thesis, which concentrates on the characterisation and interpretation of the mineral and grain surface parameters for oil and gas recovery.

The thesis is a part of the research project “NanoPorO – Nano-structure and Wetting Properties of Sedimentary Grains and Pore-Space Surfaces” financed by the German Federal

Ministry of Education and Research (BMBF) and the RWE-Dea AG. The study in this thesis discusses the characteristics of sedimentary grains of sandstone reservoir rocks. The grain features are altered due to diagenesis and show thus variations in grain morphology, surface roughness and pore geometry.

The findings of this thesis reveal the diagenetic history of sandstone reservoir rocks, grain morphology, grain surface roughness and a detailed insight into the geometry of pore spaces. The characteristics could be additional factors to petroleum exploitation techniques in order to enable the extraction of much higher amounts of hydrocarbons from reservoir rocks.

1.2 LITERATURE OVERVIEW OF PREVIOUS WORK

The North German Basin is part of the Central European Basin, which expands from England to Poland. In the last decades sandstone reservoir rocks in the North German Basin, particularly the Permian Rotliegend sandstone deposits were extensively investigated by the petroleum industry. Most commercial gas accumulations are found in the middle of the Rotliegend (George et al., 1993; George et al., 1997). These sandstones are highly porous and show a high permeability. However, diagenesis imposes problems for the reservoir quality of the Rotliegend sandstones. Detailed investigations have been carried out, which concentrated on the diagenetic effects on the reservoir quality of Permian Rotliegend sandstones. The diagenetic evolution of deeply buried sandstone reservoirs in Permian Rotliegend was studied by Gaupp, 1993. The influence of diagenetic alterations on the reservoir quality of Permian Rotliegend sandstones was described by Leveille et al., 1997 and the diagenesis of Early Permian Rotliegend deposits from northwest Germany was discussed by Platt, 1991. Hancock, 1978 suggested the possible impact of diagenesis for reservoir quality of Rotliegend sandstones in north western Germany. The consolidation of sediments results in pressure solution and precipitation of authigenic illite mineral. Ziegler, 1992 demonstrated that the fibrous illite in sandstones significantly reduced porosity. Also chlorite has a negative influence on the porosity and permeability of the Rotliegend reservoirs.

Various studies of the development and evolution of the Rotliegend sandstones in the Lower Saxony Basin were performed by Betz, 1987; Bachmann et al., 1997. These publications present the stratigraphic evolution and interpretation of subsidence and uplift periods that were affected by tectonic activity.

Many investigations concentrated on the depositional system and stratigraphy of the Rotliegend deposits and sedimentary facies, e.g. (Glennie, 1972; Falke, 1976; Gast, 1991; Kiersnowski et al., 1995; Gaupp et al., 2000). Petrographic studies were undertaken to characterise the depositional environment and diagenesis with regarding to porosity, permeability and reservoir quality (Glennie et al., 1978; Hancock, 1978; Almon, 1981; Rossel, 1982; Seemann, 1982; Goodchild et al., 1986; Pye et al., 1986; Gaupp, 1996; Leveille et al., 1997). Also controls on clay mineral distribution and chemistry in the Early Permian Rotliegend of Germany were investigated by Platt, 1993. This investigation shows formation of authigenic clay minerals at burial depth and of clay cement related to grain dissolution.

Petrographic and geochemical investigations of Rotliegend sandstones were carried out in order to compare Rotliegend sandstone diagenesis burial depth from the northern and southern margin of the North German Basin (Schöner, 2006).

In this study, the emphasis lays on the morphology of the mineral grain surfaces facing into the pore space and the pore geometry in the Rotliegend sandstone reservoir rocks.

Selected results of this study were submitted in several conference proceedings (Altermann et al., 2010; Drobek et al., 2010; Lieu et al., 2010; Drobek et al., 2011; Liêu et al., 2012).

1.3 METHODOLOGY

1.3.1 Sampling

To study petrography, diagenesis of sedimentary rocks, characteristics of sedimentary grains and pore space geometry in sandstone reservoir rocks, sandstone samples were collected from cores in the Lower Saxony Basin of northern Germany. Investigated sandstone samples, taken from core plugs which were provided by RWE Dea AG, were derived from sandstone reservoir rocks of the RL I well in the Rotliegend natural gas field. The area is located between Hannover and Bremen in the Lower Saxony Basin of northern Germany. Then, selected samples were analysed by thin section petrography, pore geometry, grain morphology and grain roughness. The analytic methods used were optical microscopy, Scanning Electron Microscopy (SEM), Energy Dispersive X-ray system (EDX) and Confocal Raman Microscopy, Confocal Laser Scanning Microscopy (CLSM) and Atomic Force Microscopy (AFM). Also software VK Analyser, Nano Scope Analysis and WITec Project were applied to analyse data.

Petrographic and diagenetic studies are available for a set of samples taken from the depth of roughly 2081 m to 5049 m. Three sample sets marked RL I_2111, RL I_4146 and RL I_5041 (see appendix I.1) were selected to investigate grain morphology, pore geometry, surface roughness. Selection of these samples was based on their mineralogy, porosity and sedimentary texture.

1.3.2 Research Methods

The different analytical steps of each method applied in this study are described in detail in the general introductions to the different chapters.

Petrographic analysis with optical microscope was used to determine grain shape, grain size and mineral composition of rock. Distributions of detrital grains, cement of rock and estimation of pore space between grains are revealed. The coatings surrounding grains by authigenic minerals or sharp crystal structure of authigenic quartz could be observed in thin section. Crystal habits of authigenic minerals and cement textures were determined by Scanning Electron Microscopy (SEM) and combined chemical element analysis by an energy dispersive X-ray system (EDX) (see chapter 3).

Subsequently, the samples marked RL I_2111, RL I_4146 and RL I_5041 were investigated for pore geometry, grain morphology and surface roughness analyses.

Confocal Raman Microscopy and Confocal Laser Scanning Microscopy (CLSM) were used for enhancing the composition of rocks, analysing pore space morphology and grain geometry. The determination of the rock components was done via the Raman spectrum at each imaged point on grain surface. The pore morphology was evaluated from 3-D and profiles (CLSM). The grain roughness was calculated and was expressed by the root mean square roughness (R_q) parameter, which is the vertical deviations measured from the mean plane, as discussed in chapter 4.

Through CLSM analysis, the features of the rough grain surface can be shown at micrometre size resolution. The surfaces of the authigenic mineral coatings could not be recognised at this scale. Thus for the same samples the roughness of the authigenic mineral surfaces and the pore space morphology were subsequently investigated at the nanometre size with Atomic Force Microscopy (AFM) and combined with SEM. The grain surface irregularity is expressed by the R_q parameter. Comparisons of the roughness of the dominant authigenic mineral coatings and of the grains are shown in chapter 5.

1.4 AIM OF THE THESIS

In this work, the mineral composition of rocks and the source of clastic grains, their textures and depositional setting are shown. The post depositional alterations and their influences on the grain morphology and pore geometry of sandstone reservoir rocks from the RL I well in Permian Rotliegend from the Lower Saxony Basin are studied. The authigenic mineral growth into the pore spaces and on the grain surfaces is investigated. The fine structure and the roughness of the authigenic minerals are determined. The characteristics of sandstone rocks, the diagenetic history, their pore geometry and grain surface features are revealed. The results show that properties of the grain surface are complicated due to varying authigenic minerals covering the grains. The grain surface changes from smooth to very rough and the pore geometry varies from flat to fractal surfaces of crystal facets.

The methods used and the results obtained in this thesis, contribute to a better understanding of the grain surface characteristics and storage behaviour and fluid flow movement through sandstones. The findings can be used to enhance the third phase of oil production, because the current combined total oil exploitation by primary and secondary methods allows only less than 40% of the recovery of the original oil (Donaldson et al., 1985). Therefore, the main achievement of this research is the high resolution characterisation of sandstone reservoir rocks and their hydrocarbon storage behaviour, which can be applied to enhance tertiary exploitation methods in oil and gas exploitation and to extract much more amount of the hydrocarbon from reservoir rocks.

In the following chapter 3 the interpretation of the characterisations of the petrography and diagenesis of sandstone reservoir rocks will be discussed. The pore geometry and grain morphology are treated in chapter 4. The fine structures and the roughness of the authigenic minerals are described in chapter 5. Discussion and conclusion are given in chapter 6 and chapter 7.

2. STUDY AREA

2.1 GEOGRAPHIC AND GEOLOGIC OVERVIEW

The study area (the location of the sampled boreholes) is located between Hannover and Bremen in the Lower Saxony Basin, north Germany (Figure 2.1). The Lower Saxony Basin (LSB) is a 300 km east - west and 65 km north - south stretching basin and is the most important oil provenance of Germany. The Lower Saxony Basin is built up by coals and carbonaceous shales (Upper Carboniferous), Lower Permian Rotliegend sandstones and overlying Upper Permian Zechstein evaporites. The Zechstein evaporites are overlain by Triassic shales and sandstones, Cretaceous chalks and Tertiary and Quaternary sediments (Scheck et al., 1999).

To the north, the Lower Saxony Basin is bordered by the Pompeckj Block platform, where thick Permian, Triassic and in parts Early Jurassic strata are unconformably overlain by Albian and younger strata.

The western extent of the Lower Saxony Basin is bordered by the Central Netherlands High.

To the south the Lower Saxony Basin is bordered by the Münsterland platform, where Upper Cretaceous chalks are unconformably overlain by Carboniferous strata (Rhenish Massif, Variscan basement and Rotliegendes), and by the terrains of Lower Saxony mountains. These mountains are formed by Triassic and in part Jurassic sediments, which were folded and faulted during the latest Cretaceous and Paleocene phases of basin inversion.

To the east the Lower Saxony Basin is limited by north - south trending Jurassic Gifhorn trough (Betz et al., 1987).

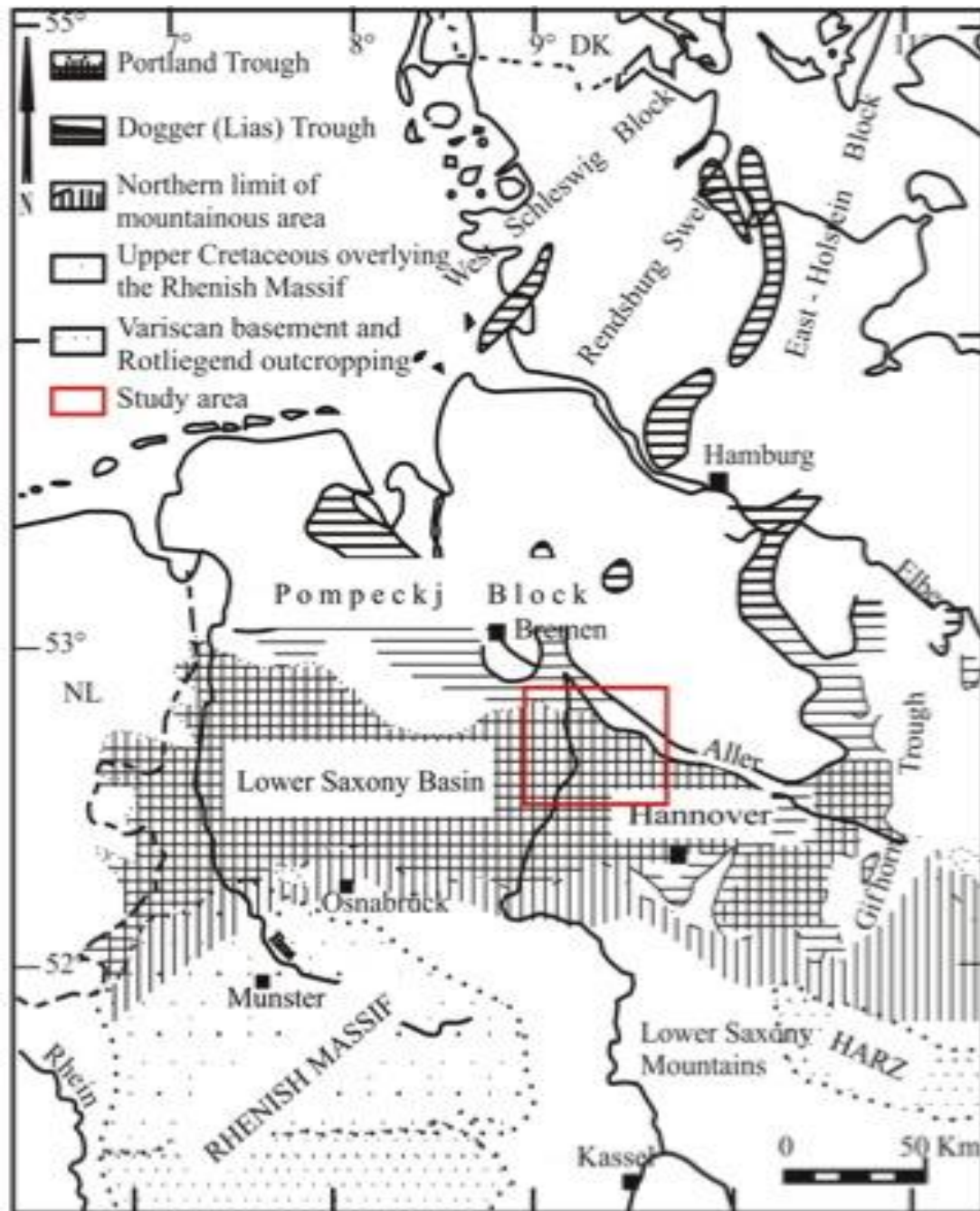


Figure 2.1 Map of the study area and extent of the Lower Saxony Basin (Betz et al., 1987)

2.2 LOWER SAXONY BASIN TECTONIC AND STRATIGRAPHIC EVOLUTION

The Lower Saxony Basin is part of the North German Basin. The Lower Saxony Basin was affected by the multiphase deformation processes. The basin was initiated by rifting and/ or thermal subsidence of lithosphere during the Permian (Plein, 1978; Ziegler, 1982; Van Wees et al., 2000). The rifting centre was situated in the north of the Lower Saxony Basin. Basement and basin fill of the Lower Saxony Basin are composed of Carboniferous, Permian, Mesozoic and Cenozoic sedimentary rocks (Purvis, 1989; Purvis, 1992). Carboniferous

sediments were accommodated in a period of regional subsidence in the Variscan foreland (Ziegler, 1990), which was caused by collision of the Variscan orogen with the margin of the Rheohercynian shelf.

The Lower Permian Rotliegend unconformably overlies the Upper Carboniferous sediments, as a result of the Hercynian orogeny and the effects of the Variscan orogenic belt (Seemann, 1982). Local volcanic activity followed post – orogenic movements as evidenced by the occurrence of volcanic rocks in the Lower Rotliegend strata (Table 2.1). The Rotliegend sandstones were deposited in a period of pronounced subsidence extending into the Middle Triassic (Scheck et al., 1997). These sandstones are important for gas accumulations in the Lower Saxony Basin (Drong et al., 1982; Ziegler, 1982). The Upper Rotliegend clastics and the Zechstein evaporites were deposited above the Lower Rotliegend sandstones (Plein, 1978; Sannemann et al., 1978). This is a result of flooding of the basin by the rapid Zechstein marine transgression (Glennie et al., 1983). In the Zechstein deposits halite and anhydrite occur which reflect evaporitic conditions. The Zechstein evaporites are the main seal for gas in the Rotliegend. The halite and anhydrite were observed in the studied sandstones at the around 2100 m depth. This could be an indication of the overlying Zechstein evaporites which deposited closed to the studied Rotliegend sandstones (see chapter 3).

In the Middle Triassic regionally extensional stress led to a reconfiguration of NNE – SSW trending trough (Gifhorn Trough) of the basin (Scheck et al., 1999). During Triassic times the Lower Saxony Basin received the sediments which are characterised fluvial to lacustrine and Playa-lake deposits by the Lower and Upper Triassic (Bunter and Keuper) and the Mid Triassic (Muschelkalk) (Aigner et al., 1992). Minor uplift events occurred during Keuper time (Upper Triassic) and were followed by deposition of terrestrial and fluvial intercalations. During the Jurassic the depositional setting of the Lower Saxony Basin shifted to open shallow marine. Sediments, consisting of shales, carbonate and sands were deposited in the basin (Gramann et al., 1997). During the Late Jurassic - Early Cretaceous, the basin formation was accompanied by plutonic activity (Betz et al., 1987; Brink et al., 1992). In the Late Cretaceous – Early Cenozoic, the onset of the Alpine Orogenesis caused tectonic inversion (Ziegler, 1990). The inversion started in the Coniacian (Paleocene) (Baldschuhn et al., 1991) and induced uplift and erosion in the central part of the Lower Saxony Basin (Ziegler, 1990; Baldschuhn et al., 1991). In the Eocene and Oligocene periods the basin was buried under a layer of deltaic and shallow marine sediments. From the Early Miocene to present times, the basin commenced uplift (Mälzer et al., 1983; Ziegler, 1992; Goes et al., 2000). In addition,

the drop in global sea level, from the Mid Cretaceous to the present caused the exhumation of the area.

2.3 STRATIGRAPHY OF ROTLIEGEND RESERVOIR ROCKS IN THE LOWER SAXONY BASIN

Sandstone reservoir rocks are mainly found in the Lower Permian Rotliegend stratigraphy of the Lower Saxony Basin, north Germany. The Rotliegend comprises siliciclastic sediments deposited in a subsiding intra-cratonic basin (Glennie, 1986). The investigated Rotliegend sandstone reservoir rocks were extracted from a well with the depth of roughly 2081 m – 5049 m, in the Lower Saxony Basin, north Germany. The Rotliegend sediments are underlain by Carboniferous source rocks and overlain and sealed by Upper Permian Zechstein evaporites. The Rotliegend strata of the North German Basin can be divided into several subgroups (Schröder et al., 1995). This subdivision of the Rotliegend stratigraphy is based on lithostratigraphy and commonly accepted as given in table 2.1.

Table 2.1 Stratigraphy of reservoir rocks in the Lower Saxony Basin (Plein, 1995; Schröder et al., 1995) and ages according to Menning, 1995.

Group	Subgroup	Formation	Member	Lithology	Age	Time stratigraphy	
Rotliegend	Upper Rotliegend	Elbe	Hannover	Heiderbeck	evaporite/shale/sandstone	258	Permian
				Munster	evaporite/shale/sandstone		
				Niendoft	evaporite/shale/sandstone		
				Dambeck	evaporite/shale/sandstone		
				Bahnsen	evaporite/shale/sandstone		
				Wustrow	evaporite/shale/sandstone/basalt		
				Ebsdorf	evaporite/shale/sandstone		
		Dethlingen	Einloh	evaporite/shale/sandstone	260		
			Strackholt	evaporite/shale/sandstone			
			Schmarbeck	evaporite/shale/sandstone			
			Wettenbostel	evaporite/shale/sandstone			
			Gralstorf	evaporite/shale/sandstone			
			Findorf	shale/sandstone			
Sande	evaporite/shale/sandstone						
Havel	Mirow	evaporite/shale/sandstone	262				
	Parchim	evaporite/shale/sandstone/ conglomerate/basalt	264				
Müritz		shale/sandstone/conglomerate	266				
Lower Rotliegend				rhyolite/andesite/sediments	296		

2.3.1 Lower Rotliegend

The Lower Rotliegend consists of volcanic rocks spreading in the German and Polish part of the basin. The volcanic suite comprises mainly rhyolites, andesites and minor basalts and brecciated volcanic agglomerates with tuffaceous layers. The strata can reach a thickness of roughly 2500 m (Scheck et al., 1999). Five volcanic eruptive stages are recognised in the German beginning in the Late Carboniferous (Stephanian) and extending up into the Permian (Benek et al., 1996; McCann, 1996): Based on the lithostratigraphic succession of the Lower Rotliegend, the extrusive activity can be divided into (1) the pre-ignimbrite stage (Late Carboniferous) (andesite), (2) the ignimbrite stage, Lower Rotliegend (Permian) (explosive), (3) the post-ignimbrite stage, (4) the late rhyolite stage and (5) Upper Rotliegend (Permian)

the late basalt stage. The upper part of the Lower Rotliegend was eroded and consequently accumulated by the Upper Rotliegend deposition (Bachmann et al., 1997).

2.3.2 Upper Rotliegend

The Müritz Subgroup in the Upper Rotliegend was deposited in local basins and comprises mainly grey, black and reddish-brown laminated siltstones, mudstones with intercalated fine grained sandstones (Plein, 1995).

The Havel Subgroup sediments comprise fluvial and eolian sandstones interbedded with muddier playa-lake deposits (Seemann, 1982; Purvis, 1992; Plein, 1995). This subgroup may be divided into the Parchim and Mirow Formations. The formations are characterised by two fining-upward cycles (Gebhardt et al., 1995). In the Parchim Formation the sedimentation was influenced by a rift system with N-S trending horst and graben structures (Gast, 1988). A wadi system, which developed in the graben structures, acted as transport routes for the fluvial sediments from the south and contained volcanic conglomerates and sediments from uplifted highlands (the Variscan Mountains). Eolian sandstones were largely transported from the northeastern to the southwestern areas. To the north and northeast eolian facies intercalated sandy – silty - muddy sediments were overlain by the conglomerates. Towards the basin centre sediments are deposited in playa lake environments, leading to the formation of salty swamps and the precipitation of halite (Schneider et al., 1993). The Mirow Formation overlaying the Parchim Formation contains dominantly sandstones and fine-grained cyclic playa sediments and is distributed across the basin. Towards the end of Mirow Formation times, eolian sediments spread westwards, while fluvial sediments were dominant in the eastern basin (Schneider et al., 1993).

The Elbe Subgroup can be divided into Dethlingen and Hannover Formation. The deposition of the Dethlingen Formation coincided with a period of thermal subsidence and expansion of the basin. The greatest extension of the Rotliegend was reached in the upper Hannover Formation (Plein, 1993; Plein, 1995). The sediment input significantly advanced into the basin. Predominantly alluvial fan, wadi and eolian deposits were deposited along the southern basin margin. The northern margin of the basin is dominated by mudstones and halite. Clastics input continued to accumulate in the east and southeast of the basin. In Hannover Formation times, the variations in water levels led to changes in both, the halite and clastic distribution in the basin. The development of thick clastic deposits occurred in the southern margin of the basin but only a small rim of clastics was formed in the northern margin

(Schneider et al., 1993). The central part of the basin is a cyclic succession of playa sediments associated with thick halite. Significant deposits of sabkha evaporation and associated muds occur to the west. By the end of Hannover Formation times, the playa lake extended far to the south. The sediments of the basin largely contained of playa muds, silts and associated anhydrite with rare thick sandy intervals (Schneider et al., 1993).

The Rotliegend sandstone reservoir rocks studied extracted from at the depth of roughly 2081 m – 5049 m are well rounded to rounded in grain shape and deposited in multiple phase of fluvial or shallow water environment with laminated structure (see chapter 3). These sandstones are properly found in fluvial facies in the Havel Subgroup.

2.4 DISTRIBUTION OF PETROLEUM IN THE LOWER SAXONY BASIN

The majority of hydrocarbon deposits in Rotliegend sandstone reservoir rocks in the Lower Saxony Basin of northern Germany are originated from underlying Carboniferous source rocks, which are coal deposits and carbonaceous shales (Cornford, 1998). The Carboniferous rocks are not exposed at the surface in most parts of the North German Basin, but buried deeply under Permian to Cenozoic sediments. Nowadays, there are a number of deep wells which have reached Carboniferous source rocks in north Germany and the southern North Sea. The Carboniferous sediments were deposited in the rapidly subsiding Variscan foreland (Ziegler, 1990). These sediments accommodated in nonmarine environment with a thickness of roughly 9000 m of Westphalian age (Carboniferous), called the Coal Measures (Collinson et al., 1993). In the bounds of the Carboniferous – Rotliegend, the Coal Measures have a thickness of roughly 1000 m to 3000 m (Leeder et al., 1990). The Coal Measures of Westphalian age (Carboniferous) are the principal source rocks for gas accumulations in the Northern German Basin (Cornford, 1998). Westphalian coals and carbonaceous shales are dominated by type III kerogen, which is rich in vitrinite derived from terrestrial plant tissues, and in charcoal (inertinite) (Cornford, 1998). In the south of the Variscan front in the deformed zone, Carboniferous rocks have been metamorphosed and kerogen has been overly matured with regards to maximum gas generation since the Late Carboniferous. In the north of the Variscan highlands in the underformed foreland basin, Carboniferous rocks without having been buried sufficiently are not matured enough for maximum gas generation. The gas generation derived from the Late Carboniferous source rocks expelled into the overlying the Rotliegend sandstone reservoir rocks with high porosity.

The studied Rotliegend sandstone reservoir rocks were cemented by silica cement that is related to meteoric water circulation in a fluvial environment (see chapter 3). According to the investigation by Glennie, 1986, the Rotliegend sandstones deposited in a fluvial setting have been related with deposition in a variety of arid, terrestrial environments, mainly ephemeral fluvial systems, various types of eolian deposits, desert – lake environments and adjacent sabkhas. The reservoir quality of the Rotliegend is strongly influenced by the depositional environments. Most commercial gas accumulations are found in eolian facies and some in fluvial facies in the Rotliegend sandstone reservoir rocks in Havel Subgroup (George et al., 1993; George et al., 1997). Those sandstones are clean, show high porosity and deposited away from the water table to show the best preservation of porosity and permeability. Diagenesis is a problem for reservoir quality in the Rotliegend, as compaction pressure solution and precipitation of illite and/or chlorite have a negative impact on the porosity and permeability of the Rotliegend reservoirs (see chapter 3).

The Zechstein salt represents the seal-rock for virtually all gas accumulations in Rotliegend reservoirs. The near perfect seal of the Zechstein is the main reason for the existence of the large gas fields of the Carboniferous sources (Gautier, 2003).

3. PETROGRAPHY AND DIAGENESIS OF THE RESERVOIR SANDSTONE IN THE INVESTIGATED WELL OF THE NORTH GERMAN BASIN

The investigation of the petrography and diagenesis of sandstones of the North German Basin reveals the sediment provenance, depositional environments and history of post – depositional alterations. Sedimentary rock petrography in general, concentrates on the detail description of the composition and the textural relationship of the rocks. Clastic grains are packed together in fine grained matrix and cement. The constituents of the sandstone samples permit identification of the source of rocks. All the investigated sandstones are quartz – rich, also containing feldspar, locally abundant metamorphic and volcanic rock fragments, indicating that the clastic grains derived from weathered igneous and/or volcanic rocks. The sandstones with well-rounded to rounded clastic grains indicate the textural maturity related to sediment recycling of the deposits in bed load transport. The sediments with laminations are recognisable as an accommodation in multiple phases of fluvial or shallow water marine or lacustrine reworking. Additionally, silica cement is quite abundant in the sandstone that is associated with meteoric water circulation in a subaerial fluvial setting. Furthermore, the changes of mineralogy of the rocks in the depositional environment are investigated. The precipitation of authigenic minerals and cements in pore spaces and surrounding grains during diagenesis is shown. Less stable minerals as feldspars and volcanic fragments are dissolved and replaced by authigenic minerals. The history of diagenesis and their effects on the porosity, permeability are illustrated. The growth of diagenetically formed clay minerals narrows pore spaces and roughens pore walls and pore throats leading to reducing storage capacity, changes in fluid/rock wetting properties and in fluid flows through pores in the sandstones. Also for the Rotliegend sandstone rocks such processes must be evaluated and can lead to a decrease of the permeability and reservoir quality.

3.1 METHODS

3.1.1 Optical microscopy

Thin sections were prepared from 19 sandstone samples from the Rotliegend RL I well, taken at the depth of around 2081 m to 5049 m, in Lower Permian Havel Subgroup (Chapter 2). Pores within the sandstones were stained blue by epoxy resin. Thin sections were either

polished or covered with glass after staining. All thin sections were studied with a Leica DM 2500M petrographic microscope under plane and cross polarised light. The investigation describes the characteristics of detrital, authigenic mineralogy, porosity, and texture. The samples showed some alternating lamination of coarser and finer grains and differing cement and pore space volume.

3.1.2 Scanning Electron Microscopy (SEM) and Energy Dispersive X-ray system (EDX)

The samples RL I_2111, RL I_4146 and RL I_5041 were separated into small grain groups and mounted on top of a conical sample holder. Crystal morphology of the authigenic minerals, type of authigenic minerals, their relationship to framework grains and pore network were examined with Scanning Electron Microscope (SEM) and element analysis was done by an Energy Dispersive X-ray system (EDX). This analysis reveals the texture and fabric of sandstones and aids to recognise the post depositional alteration. For this purpose the samples were coated with a gold layer in an SCD 050 sputter coater. The sputter coater was operated for 40 seconds at a current of 40 Volts. The resulting gold film was only about 10 nm thick, to improve the resolution. The Philips scanning electron microscope XL 30 FEG (SEM) system used was operated with beam voltages of 15 kV and with 25-30 kV for the Energy dispersive X-ray system (EDX). SEM images were taken digitally in secondary electron (SE) mode and as chemical element spectra.

3.2 PETROGRAPHY

Petrographic investigation is dealing with the source, occurrence, structure and history of rocks, especially sedimentary rocks. The classification or terminology of the sedimentary rocks was used in relevant fields as description of the composition, properties and classification of rocks by Folk, 1974, 1980; Pettijohn, 1975. The source of sedimentary rocks was investigated by Pettijohn et al., 1972. This study refers to textural maturity, mineralogical classification, sediment provenance, which can be diagnostic an environment of deposition.

The sandstone rocks studied from the well in the North German Basin from the depth of 2081 m to 5049 m, located between Hannover and Bremen, are fine to medium in grain size, moderately to well sorted and rounded to well rounded in grain shape. The most abundant component of the sandstone rocks is quartz with pale, milky, greyish brown colour, leached and weathered alkaline feldspar and plagioclase and rock fragments. Calcite dominated carbonate cement usually fills the pore spaces. The pore spaces are generated by arrangements

of detrital grains and ranging from 5% up to 20%. The pores are occluded due to the precipitation of the authigenic minerals as quartz, albite, anhydrite, clays and calcite during diagenesis.

3.2.1 Texture

The sediment distribution is not uniform, where sandstones are laminated by intercalation of very fine grained sediments (Appendix I.1_4146, Figure 3.2.1) and sometimes are interbedded by a thick layer of very fine sandstone, as seen at the depth of 2111 m and 4797 m (Appendix I.1_2111, Figure 3.2.2). These demonstrate that the sediments were deposited in a basin in which environmental conditions were unstable and flow velocity changed.

Most of the sandstones contain a little clay fraction. The sorting of grains is moderate to well. Diagrams are used to visually illustrate and estimate the sorting of sediments (Pettijohn, 1975), (see appendix I.2). However, in the laminated sandstones the sorting of the grains varies from laminae to laminae, but the sorting is not very high. The coarser sand grains always contain the finer grains embedded in between (Figure 3.2.1). The sand grains are rounded to very rounded (Figures 3.2.3 and 3.2.4), based on categories of roundness from low to high sphericity (Pettijohn, 1975), (see appendix I.3). However, rounding and sphericity of fine grains are less and less developed than in the medium and coarse grains (Figures 3.2.5, 3.2.6 and 3.2.7). The abundant grain size varies from 0.2 mm to 0.5 mm in diameter, although it is sometimes larger than 0.5 mm in diameter (Figure 3.2.4) or below 0.1 mm in diameter (arrows in figures 3.2.1 and 3.2.2), using the Udden – Wentworth scale: clay size is less than 0.039 mm; silt: 0.039 – 0.0625 mm; sand: 0.0625 – 2 mm etc (see appendix I.4).

The grain distribution is of high density. The grain to grain contacts are mainly parallel to the long axis of the grains (Figure 3.2.8), suggesting that the grains were compacted mechanically. At higher depth the grains are more compacted, so many of the contacts between grains have undergone solution leading to the penetration of one grain into another. Therefore, the grain contacts are concavo – convex (Figures 3.2.9 and 3.2.10), and where solution is more intense, the contacts between grains become sutured (Figures 3.2.10 and 3.2.11).

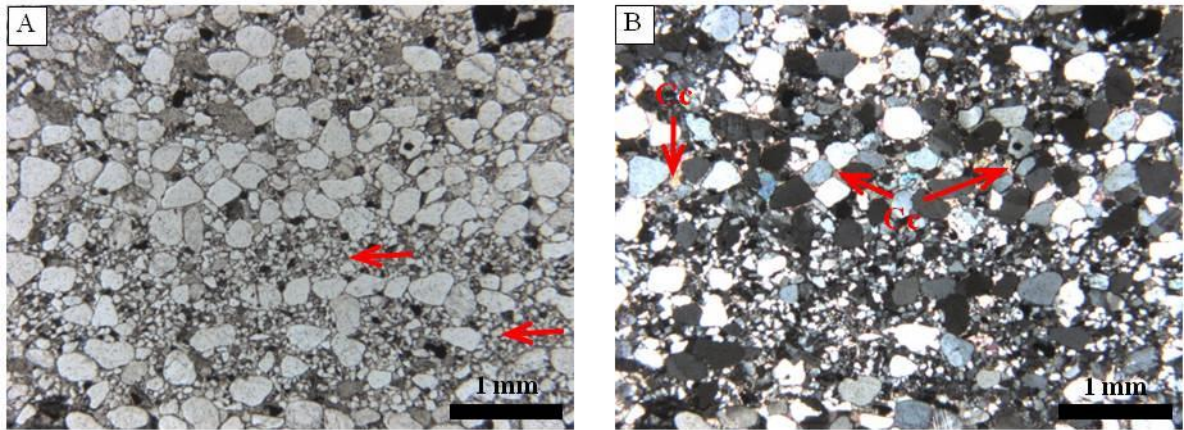


Figure 3.2.1 Well RL_I, sample 4146, photomicrograph, plane polarised light (image A), cross polarised light (image B).

The sandstone is laminated (arrows), with laminae being defined by changes in grain size. The sorting of grains changes from laminae to laminae, but in larger grain laminae, the coarser sand grains always contain the smaller grains between the large one. The coarse grains are ca. 0.3 mm in diameter and finer grains are less than 0.1 mm in diameter. Pore spaces have been filled by calcite (Cc).

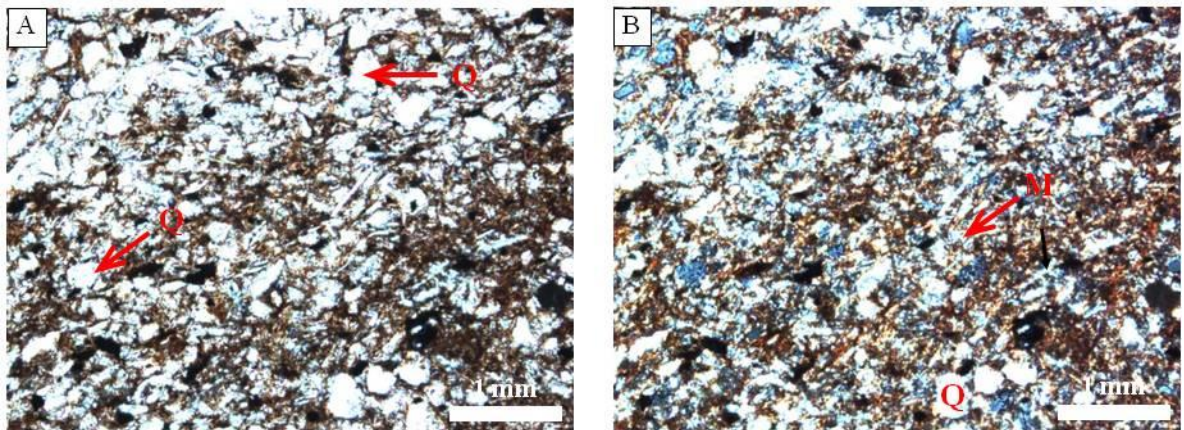


Figure 3.2.2 Well RL_I, sample 4797, photomicrograph, plane polarised light (image A), cross polarised light (image B).

The very fine sandstone contains mainly quartz grains (Q), that are less than 0.1 mm in diameter and thin mica flakes including biotite and muscovite. Muscovite (M) is more abundant with bright colours, seen under cross polarised light (image B). Clay matrix, brown in colour, is subordinated to the component of siltstone.

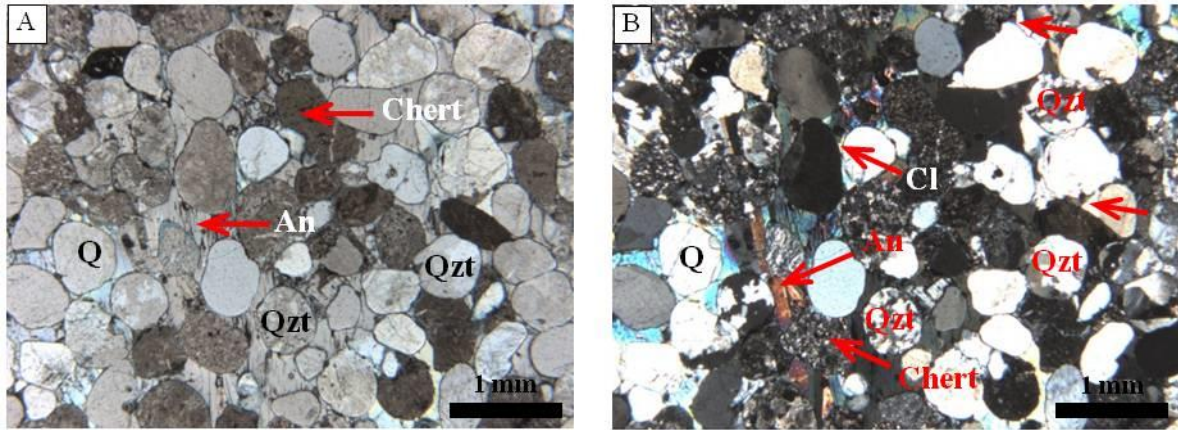


Figure 3.2.3 Well RL_I, sample 2111, photomicrograph, plane polarised light (image A), cross polarised light (image B).

The sandstone contains mainly monocrystalline quartz grains (Q), and polycrystalline quartz grains (Qzt) and subordinate feldspar grains and lithic fragments with common size at 0.5 mm in diameter such as chert fragments with fine-grained quartz, chalcedony rich. The detrital grains are well to very well rounded and spheroidal. The sorting of grains varies from well to very well. Clay coatings (Cl) cover the grain surfaces. Anhydrite cement (An) and minor patchy quartz cement (arrow) fill the pores.

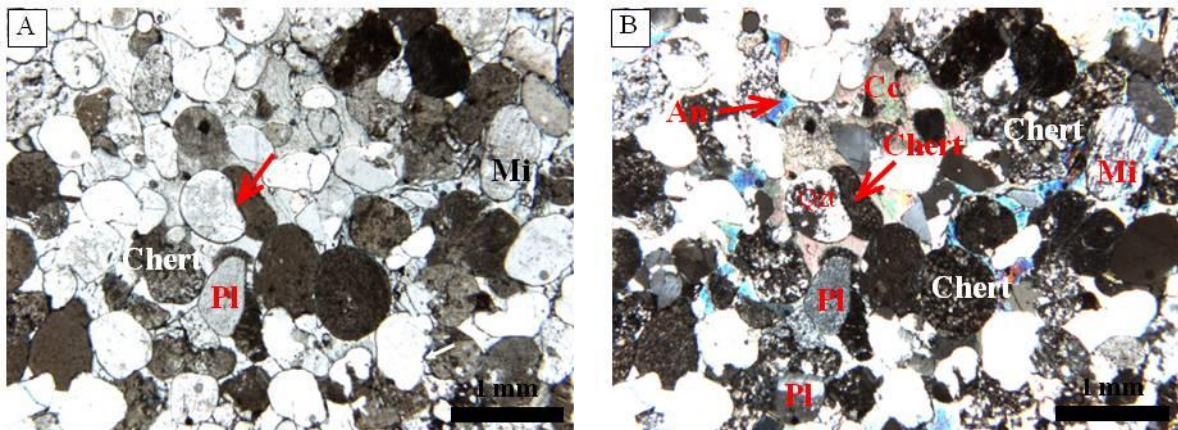


Figure 3.2.4 Well RL_I, sample 4839, photomicrograph, plane polarised light (image A), cross polarised light (image B).

This coarse sandstone contains abundant quartz (Q), feldspar, plagioclase grains (PI), microcline (Mi) and rock fragments such as chert and polycrystalline quartz (Qzt) with grain sizes larger than 0.5 mm in diameter. The grains are well rounded and spheroidal, and rarely elongated. The sorting of the grains is moderated to good. The grain contacts are concavo – convex and sutured (arrows). The sandstone is densely packed and compacted. Most of the pore spaces are filled by calcite cement (Cc) and anhydrite (An). No open pores can be seen.

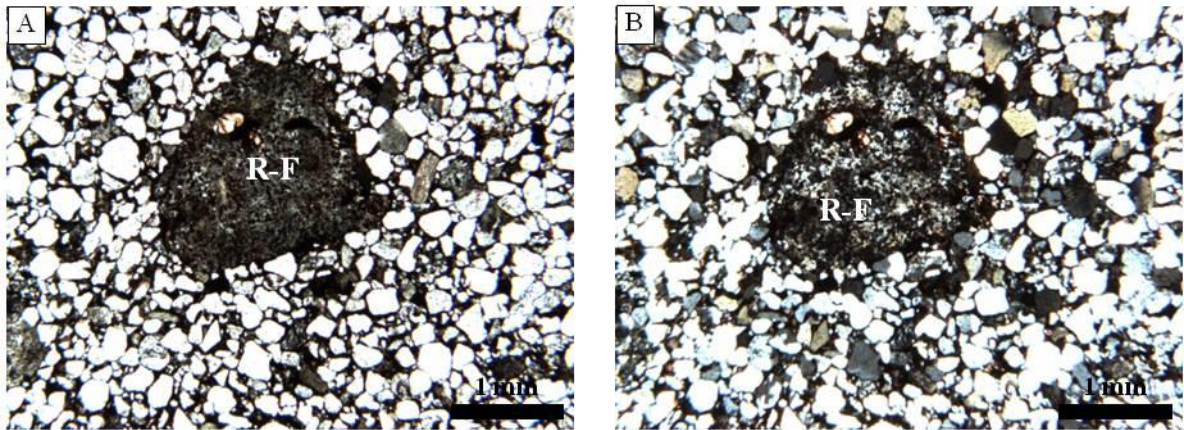


Figure 3.2.5 Well RL_I, sample 3139, photomicrograph, plane polarised light (image A), cross polarised light (image B).

The large rock fragment (R-F) in the middle of the photomicrographs is embedded in finer grains. Most of them are less than 0.25 mm in diameter. They are fine sand grains with subangular to subrounded grain shape and sometimes elongated. The sorting of grains is moderate to good.

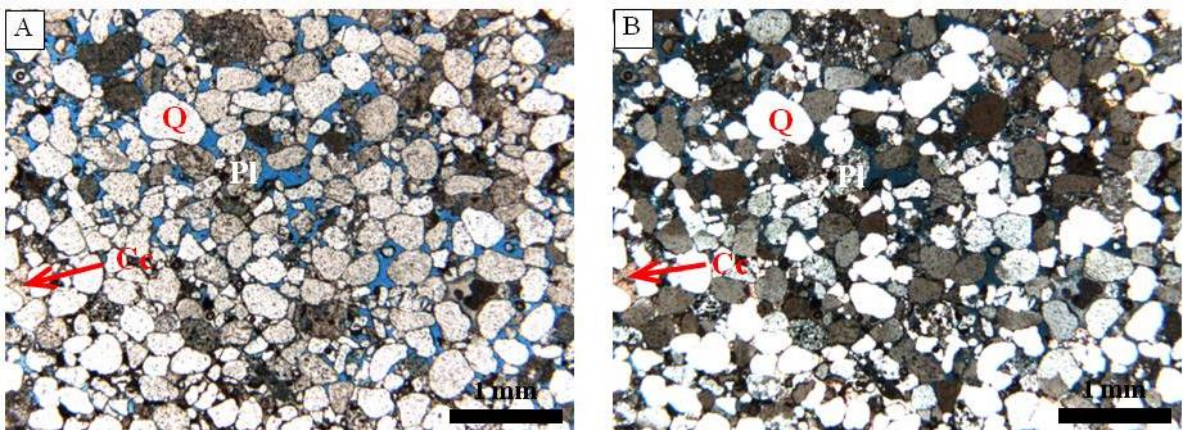


Figure 3.2.6 Well RL_I, sample 5041, photomicrograph, plane polarised light (image A), cross polarised light (image B).

The photomicrographs are showing porous sandstone. Calcite cement (Cc) fills pore spaces, open pores are stained blue. The grain contacts in the sandstone are tangential and long. The common grain size is 0.3 - 0.5 mm in diameter sometimes smaller grains are less than 0.2 mm in diameter. The abundant grain composition is quartz (Q), including monocrystalline and polycrystalline quartz, and minor amounts of feldspar and plagioclase grains (Pl). The detrital grains are subrounded to rounded and spheroidal. The sorting of the grains is moderate to good.

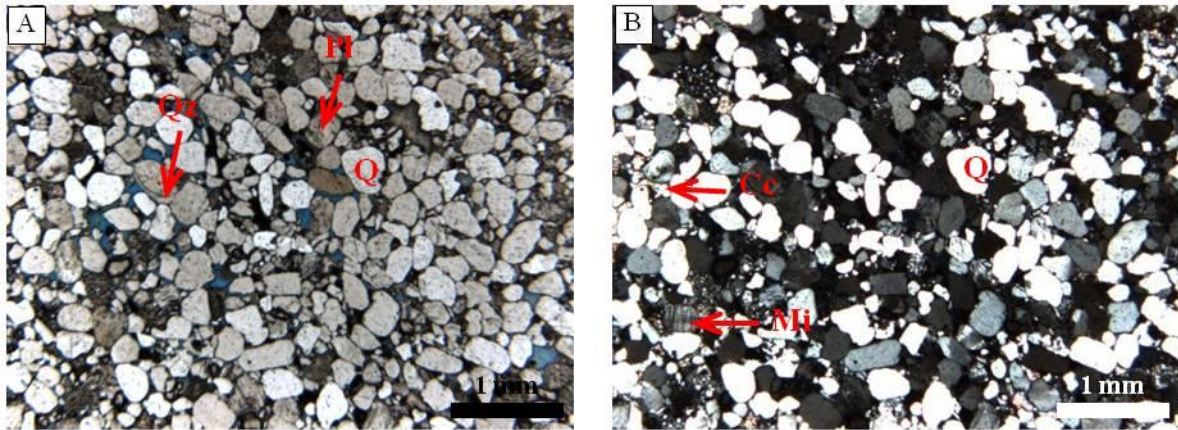


Figure 3.2.7 Well RL_I, sample 5049, photomicrograph, plane polarised light (image A), cross polarised light (image B).

This medium grain sandstone, with grain sizes varying from 0.2 – 0.4 mm in diameter, is cemented by pore-filling calcite (Cc), and quartz overgrowth (Qz) on detrital grains. Open pores are blue. The grains are subrounded to rounded and elongated, subspheroidal sometimes spheroidal. The sandstone contains predominantly quartz (Q), amounts of feldspar, microcline (Mi), plagioclase grains (Pl) and minor rock fragments.

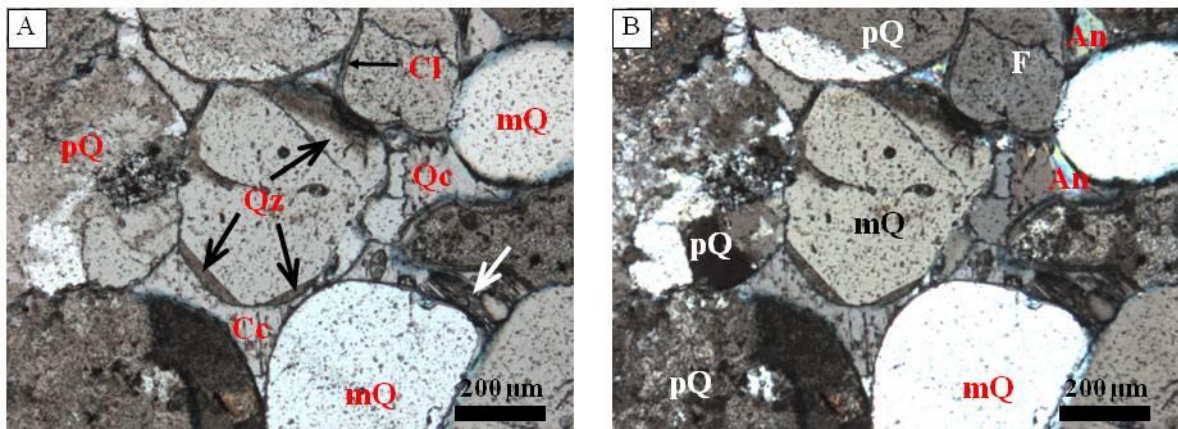


Figure 3.2.8 Well RL_I, sample 2111, photomicrograph, plane polarised light (image A), cross polarised light (image B).

Most of the detrital grains are coated with a thin dark rim of hematite cement. Clay mineral coatings (Cl) cover the feldspar surfaces. Syntaxial quartz overgrowths (Qz) are on the quartz surface. Pore spaces are filled by calcite (Cc), anhydrite (An) cement and sometimes patches of quartz cement (Qc). The sandstone contains monocrystalline quartz (mQ), polycrystalline quartz (pQ), rock fragments and feldspar grains (F). The contacts between the grains are long contacts. In the right picture A, the arrow points to dissolved feldspar, forming intragranular pores.

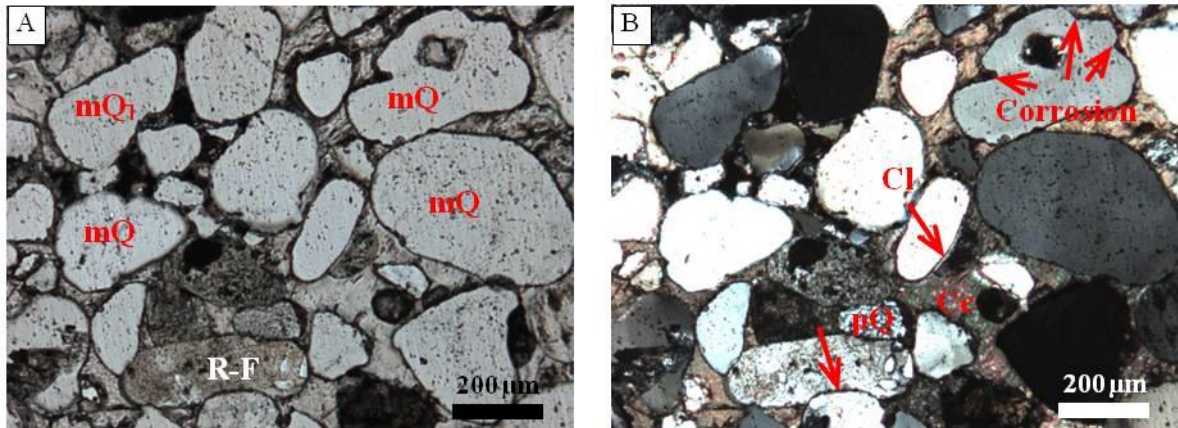


Figure 3.2.9 Well RL_I, sample 4146, photomicrograph, plane polarised light (image A), cross polarised light (image B).

The sandstone is well cemented by calcite (Cc) that fills the pores. Most of the grain surface is coated by a thin dark rim of iron oxide and sometimes clay grain coatings (Cl) cover the quartz surfaces. The contacts between grains are long and concavo - convex (arrow). The components of the sandstone are quartz grains (mQ, pQ), minor rock fragments (R-F) and feldspar grains. Some of the quartz grains are corroded.

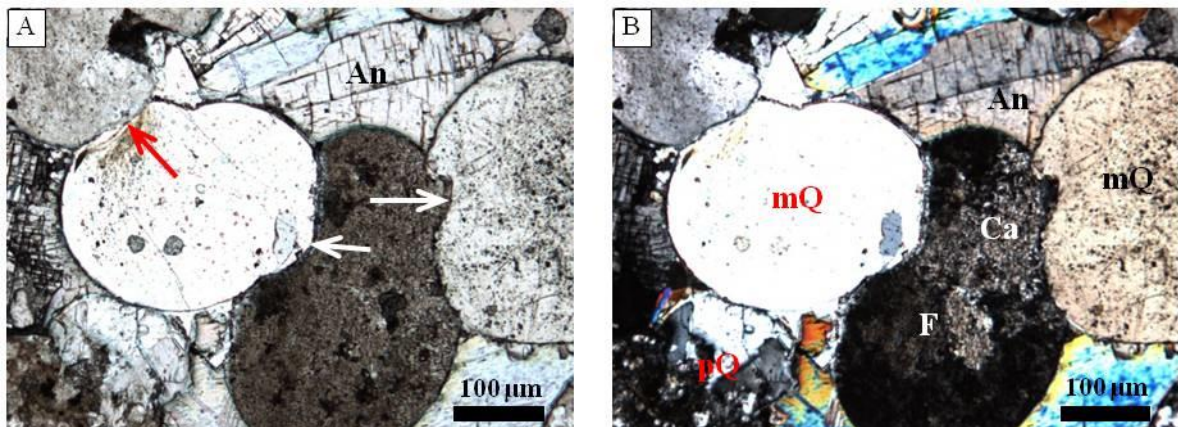


Figure 3.2.10 Well RL_I, sample 4839, photomicrograph, plane polarised light (image A), cross polarised light (image B).

The grains have undergone compaction leading to pressure dissolution. The contacts between grains are concavo - convex and sutured (arrows). The sandstone contains monocrystalline (mQ) and polycrystalline quartz grains (pQ), rock fragments of polycrystalline quartz, volcanic clasts and feldspar grains (F) which are partly replaced by calcite (Ca). The clastic grain shapes are very round. The sandstone is cemented by anhydrite (An) and calcite. Quartz cement seems to be absent.

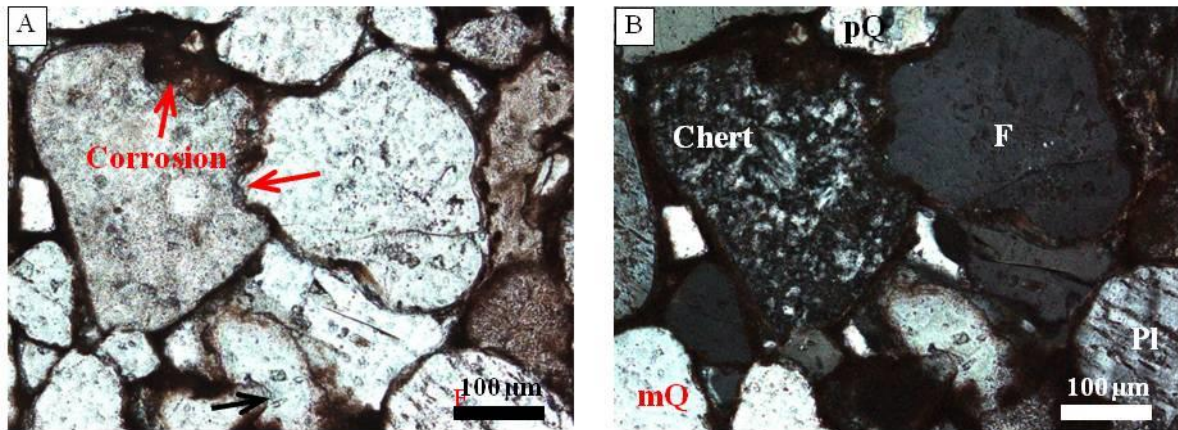


Figure 3.2.11 Well RL_I, sample 3319, photomicrograph, plane polarised light (image A), cross polarised light (image B).

The clastic grains are coated by a brown rim of hematite, seen under polar plane. The margins of some grains are corroded. Some grains show saturated and concavo - convex contacts, as pointed out by the arrows. The components of the sandstone are prevailed by quartz (mQ, pQ), feldspar (F), plagioclase (Pl) grains and chert fragments (Chert).

3.2.2 Detrital mineral composition

The sandstone samples are composed of the three main constituents, quartz, feldspar and lithic fragments. Each grain group and its constituents are discussed below.

Quartz

The quartz constituents are monocrystalline and polycrystalline quartz and about 50% - 60% in total sandstone volume. Monocrystalline quartz (mQ) is commonly rounded to very rounded with grain sizes varying from 0.1 mm to 0.5 mm in diameter. Some quartz grains are in undulose extinction, which individual quartz grain appears black sweeping extinction when the microscope stage is rotated under cross polarised light (A, B Figure 3.2.12). It is a result of strain and is found in quartz grains weathered from igneous and metamorphic rocks (Adams et al., 1988). Rarely the margins of some of the quartz grains are embayed (Figures 3.2.9 and 3.2.11). This is a result of corrosion of quartz from a volcanic origin in the investigated sandstones. The surfaces of some quartz grains are overlain by authigenic quartz in the form of overgrowth and syntaxial overgrowth (Figures 3.2.8, 3.2.13 and A, B Figure 3.2.14). The original quartz surfaces are seen by a dark rim in polarised light. If the overgrowth is well developed, the overall shape of the quartz grain has changed from well rounded to subeuhedral and euhedral, as a result of diagenesis.

Polycrystalline quartz (pQ) grains with prominent sizes of 0.1 mm to 1 mm in diameter are subrounded to very rounded. Most polycrystalline quartz grains are composed of several crystals. The contacts between the sub – grains are sutured and aligned (A, B Figure 3.2.15 and Figure 3.2.16). Probably, the quartz is originated from igneous and metamorphic rock fragments.

Feldspar

The feldspar grain group consists of sodium-calcium feldspars (plagioclase), alkaline feldspars and potassium feldspars (microcline, K-feldspar). Microcline and K-feldspar are more abundant. Feldspars are important framework grains of the sandstones, but much less abundant than quartz accounting only for 5% up to 15% volume. Most feldspar grains are elongated, sub-spheroidal and rounded. Feldspar grains are less stable compared to quartz and rock fragments consisting principally of quartz. Therefore, most of them are altered and replaced by authigenic minerals and dissolved along the contact boundaries due to increasing pressure in burial stage. The solutions are precipitated in pore spaces, forming authigenic albite (C, D Figure 3.2.14 and A, B Figure 3.2.15). Plagioclases (Pl) are recognised by multiple twinning, some of them are replaced by calcite (Figures 3.2.16 and 3.2.17), while microcline (Mi) and K-feldspar (F) are easily identified from the perthite and cross – hatched twinning (C, D Figure 3.2.15 and Figure 3.2.18). The feldspar grains which are drastically dissolved sometimes show only the remained feldspar rinds (C D Figure 3.2.12 and Figure 3.2.18). This solution leads to forming of micro pores within them. Some K-feldspar grains are also replaced by calcite (C, D Figure 3.2.15, Figures 3.2.10, 3.2.16 and 3.2.17), and only some feldspar specks are remained. Locally the K-feldspar grains are completely replaced by calcite, so that they are not easy to recognise by the typical feldspar features.

Lithic fragments

Rock fragments are important components of the sandstones. The rock fragment volume in the sandstones is about 15% - 25%. The lithic fragments are volcanic clasts, metamorphic, igneous and sedimentary rock fragments. The sedimentary lithic fragments with subangular and angular shape contain very fine grains and are less common (Figure 3.2.5). The clasts (Chert) are round (A, B Figure 3.2.14) and made up of very fine – grained quartz (micro quartz), but some clasts are embayed at the margins (Figure 3.2.11). This has occurred as a result of corrosion of the clasts during diagenesis. The fragments of quartzite and igneous

rocks in sandstones are rich in quartz. An alignment of quartz grains as in quartzite fragments is in conjunction with deformation as witnessed by elongate polycrystalline quartz (C, D Figure 3.2.14). The igneous lithic fragments consisting of principal quartz, feldspar and minor alkali minerals have previously undergone alteration due to auto hydrothermal reaction and feldspars have been subject to sericite alteration (Figure 3.2.19).

3.2.3 Visible porosity

The visible porosity of most sandstone samples is very heterogeneous widely changing from less than 5% up to 20% in volume. The porosity and permeability of the samples discussed herein were measured by the RWE petrological laboratory in Wietze (Table 3.1)

Table 3.1 Porosity and permeability of the selected samples

Sample	Porosity (%)	Permeability (mD)	Grain Density	Description
2111	4.4	0.25	2.670	Rotliegend 1
4146	8.7	4.04	2.656	Rotliegend 1
5041	15.0	53.45	2.645	Rotliegend 1

The porosity changes depend on the grain size, geometry and the degree of cementation. The pore geometry and grain morphology are discussed in chapter 4. The visible pores are more abundant in the primarily coarse grained sandstones, at the depth of 4910 m and below (Figure 3.2.12). Most pores are intergranular with subordinate proportions of intragranular porosity due to partial dissolution of feldspars and volcanic rock fragments. At the interval of 2081 m – 3369 m, the visible porosity is very poor, less than 5% in volume and grain size is less than 0.3 mm. Almost every pore space is filled by cements such as hematite, carbonate and anhydrite. Additionally, authigenic quartz and albite are drastically overgrown, occluding pores and on detrital grains (Figures 3.2.15 and 3.2.20). At the depth of 4146 m - 4908 m, the quantity of carbonate cements decreases, therefore pore spaces are of about 5% - 7% volume and grain size varies from 0.2 mm – 0.5 mm. In contrast, the visible porosity makes up to 20% volume at the depth interval of 4910 m – 5049 m, and the pores are connected by pore throats (C, D Figure 3.2.12 and Figure 3.2.18). At this depth, anhydrite and albite cements are completely absent, while the quantity of quartz and carbonate cements is strongly reduced. Overgrowth of quartz and syntaxial quartz is locally present. In addition, the dissolution of feldspar grains and volcanic fragments vigorously occurs and has led to an enhancement of the porosity.

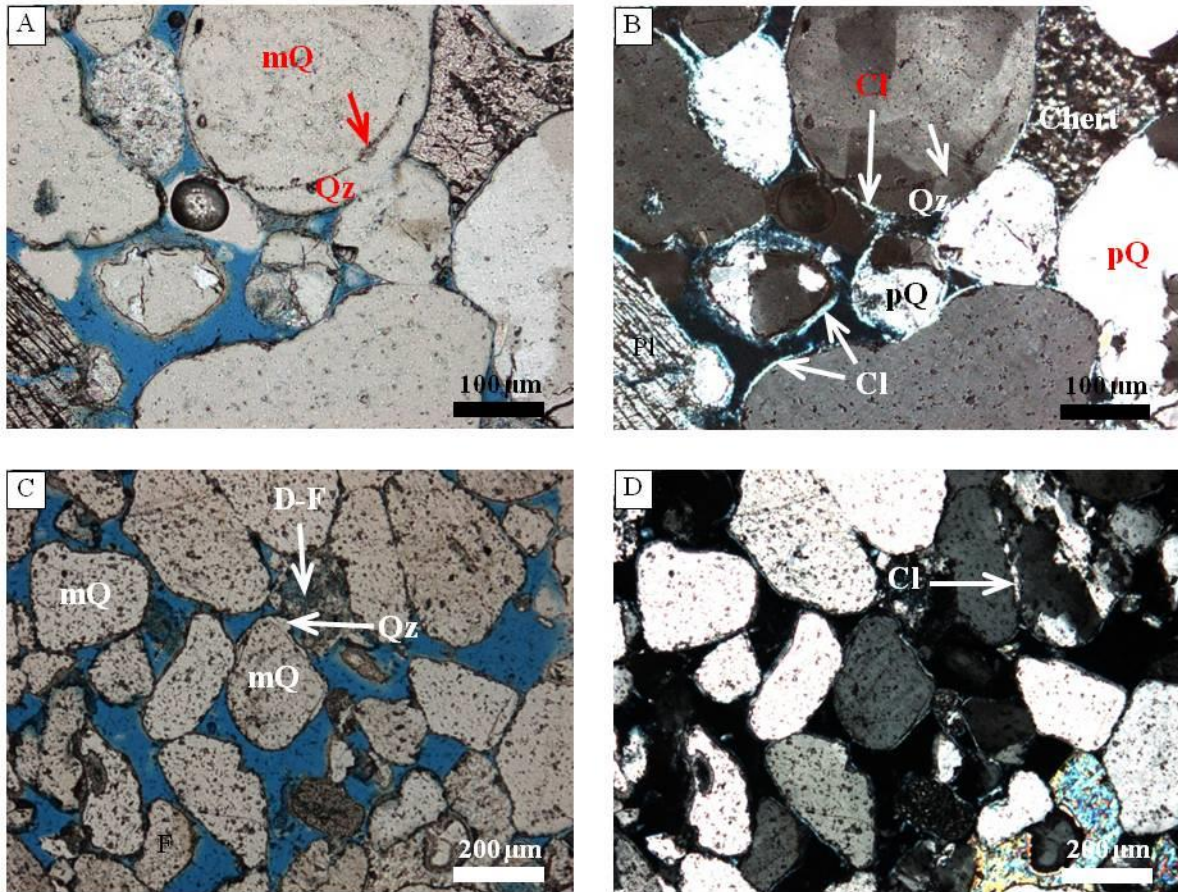


Figure 3.2.12 Well RL_I, sample 5041, photomicrograph, plane polarised light (images A, C), cross polarised light (images B, D).

The main detrital grains of the sandstone are quartz including single crystal quartz with undulose extinction (mQ), polycrystalline quartz (pQ), feldspar (F) and plagioclase grains (Pl), partly altered and dissolved, forming the secondary pores (D-F) within the grains and lithic fragments such as chert. Clay coatings (Cl) with bright colours coat grain surfaces as seen in picture B. Authigenic quartz overgrowths (Qz) grow on the quartz grains. The original quartz surfaces are surrounded by a thin dark rim (arrows). The sandstone porosity shows a high volume with open pores having blue colour.

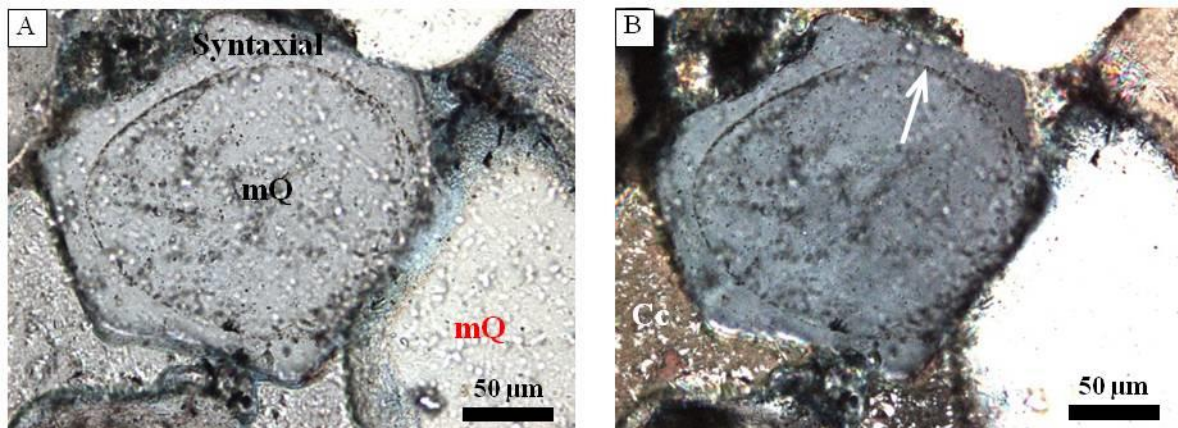


Figure 3.2.13 Well RL_I, sample 4212, photomicrograph, plane polarised light (image A), cross polarised light (image B).

The sandstone is well cemented by calcite (Cc) filling the pores. Quartz in form of syntaxial overgrowth on the quartz grains (mQ) is present as well. The original quartz surface is surrounded by a dark rim of iron oxide (arrow). The overgrowth is well developed; the overall shape of the quartz grain has changed from well rounded to euhedral

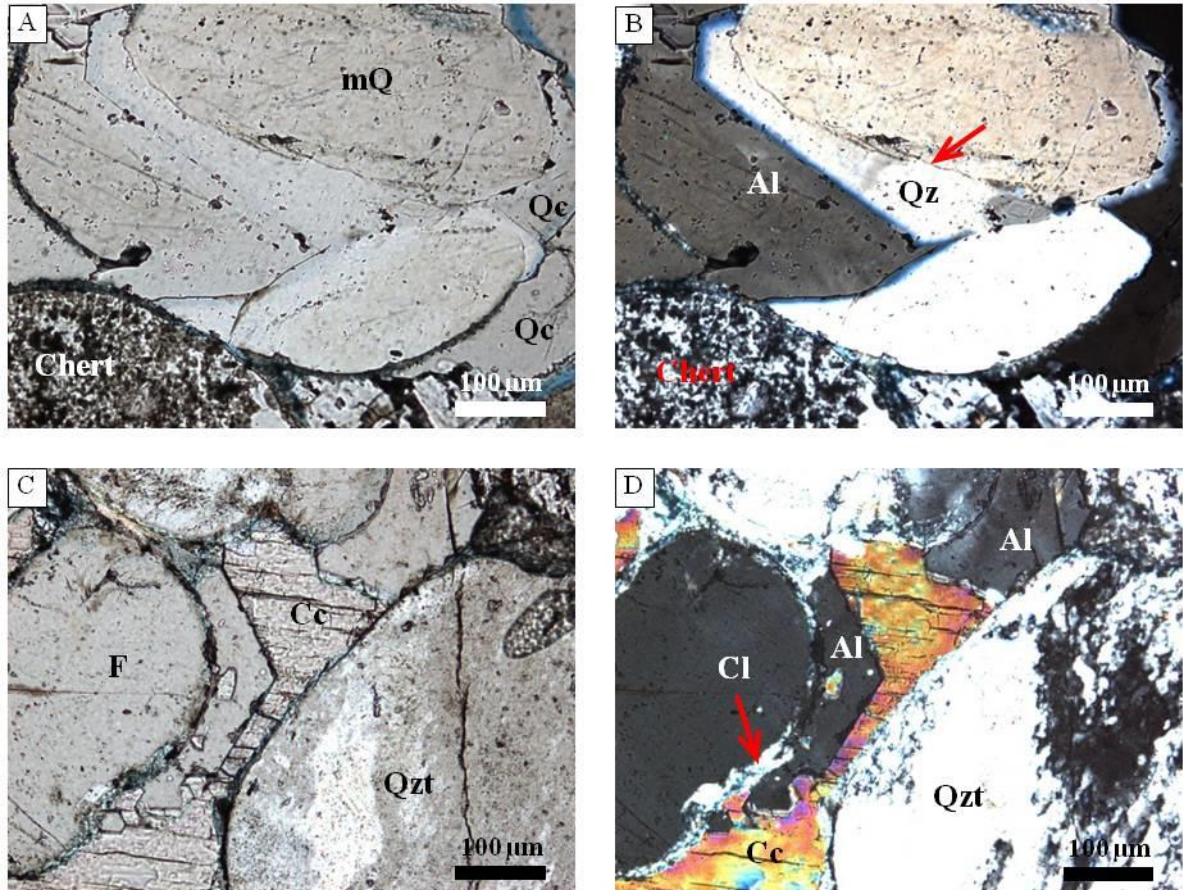


Figure 3.2.14 Well RL_I, sample 4839, photomicrograph, plane polarised light (images A, C), cross polarised light (images B, D).

The quartz (mQ), feldspar (F) grains with clay coating (Cl) and rock fragments of chert, and polycrystalline quartz (Qzt) are very round. The authigenic quartz overgrowth (Qz) coats the quartz grain (images A and B). The surface of the original quartz is surrounded by a thin dark rim. Where the overgrowth is developed, the overall shape of the quartz has changed from very round to subeuhedral. Subsequently, albite (Al) grows over the quartz overgrowth (see pictures A and B) and on the feldspar grain (see pictures C and D). Pore space is filled by calcite (Cc) which shows high interference colours and by albite (Al, in the upper right corner of picture D).

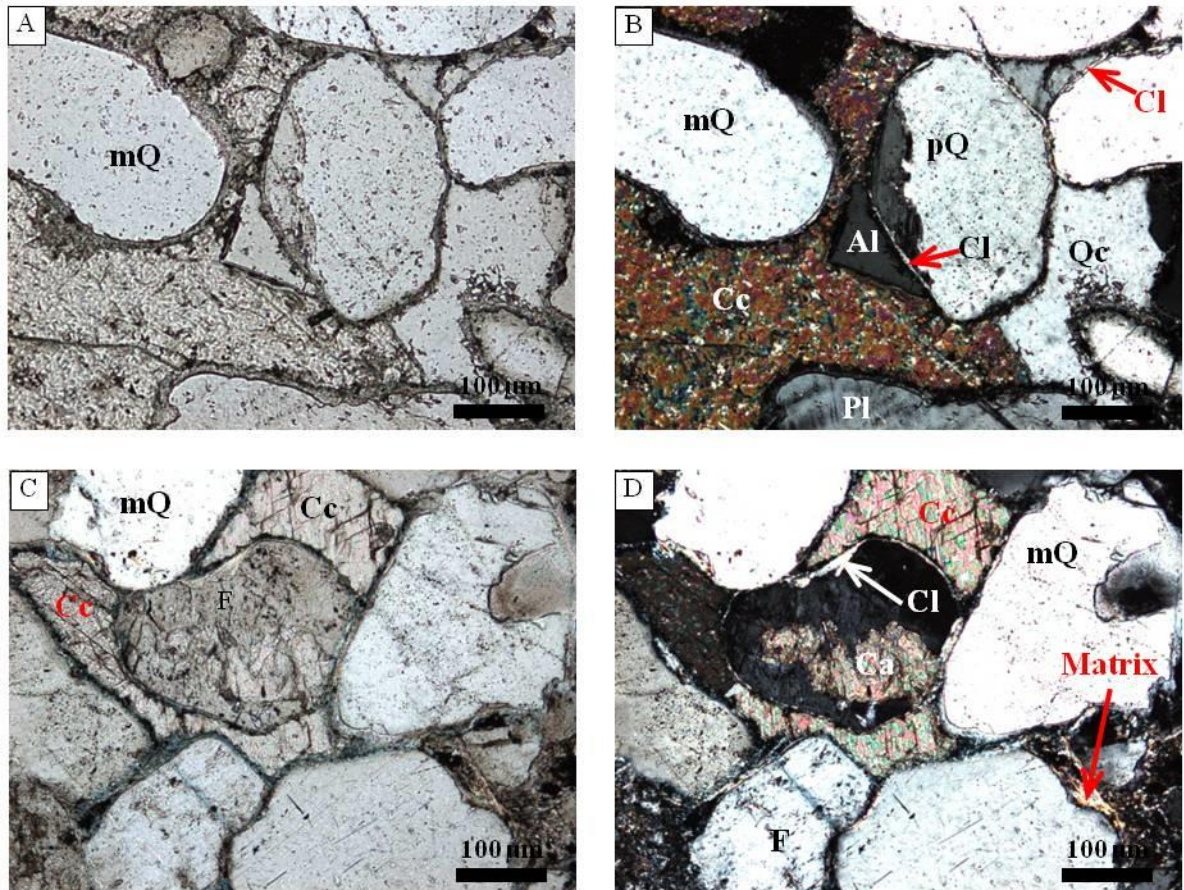


Figure 3.2.15 Well RL_I, sample 4838, photomicrograph, plane polarised light (images A, C), cross polarised light (images B, D).

The sandstone contains rounded quartz grains (mQ, pQ), subrounded rock fragments, feldspar grains (F), plagioclase (Pl) and little clay matrix between the components. Clay coatings are on the grain surfaces (Cl). The feldspar grain in the centre of pictures C, D is replaced by calcite (Ca). The contacts between grains are concavo – convex, sutured and rare long contacts. The detrital grains are well cemented by calcite (Cc) and quartz (Qc) in form of pore – filling and albite (Al) in form of overgrowth on the grain surface.

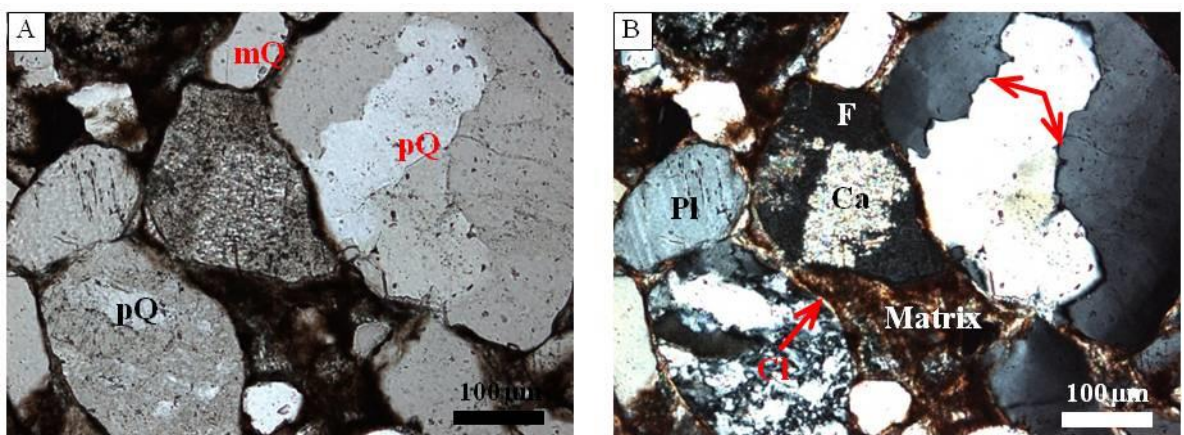


Figure 3.2.16 Well RL_I, sample 4896, photomicrograph, plane polarised light (image A), cross polarised light (image B).

Most of the clastic grains are coated by hematite cement, which makes a brown rim in the images and by clay coatings with bright colour, seen under cross polarised light. The abundant grain component in the sandstone is monocrystalline quartz (mQ) and polycrystalline quartz (pQ) which sutures the boundaries between the crystals (arrows). Less prominent components are feldspar grains (F) replaced by calcite (Ca) and plagioclase grains (Pl), which can be identified by twinning. Additionally, clay matrix can be found seldom between grains.

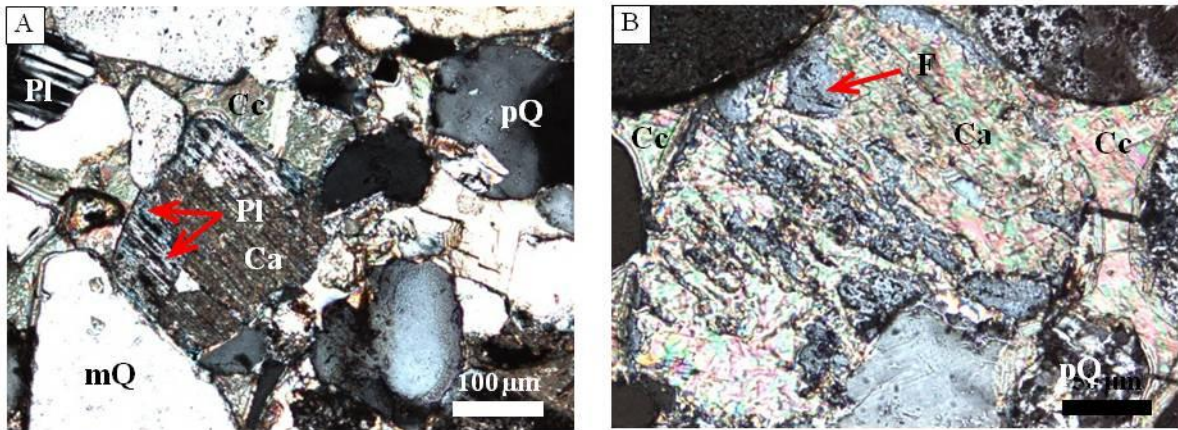


Figure 3.2.17 Well RL_I, sample 4904, photomicrograph, cross polarised light (images A, B).

The detrital constituents of the sandstone are monocrystalline and polycrystalline quartz (mQ, pQ) and plagioclase (Pl), that is easily recognised by multiple twinning, feldspar (F) and seldom lithic fragments. Feldspar grains are drastically replaced by authigenic calcite (Ca). Pores are completely filled by calcite cement.

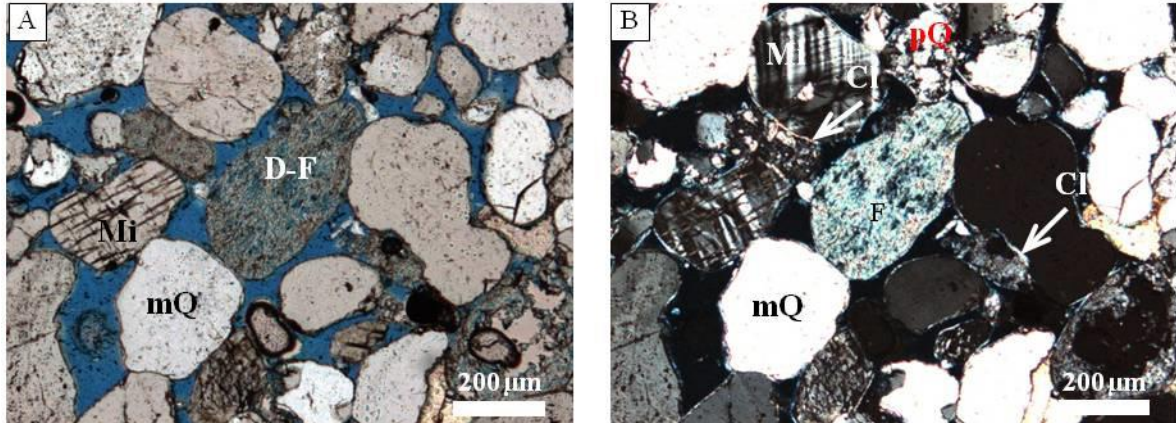


Figure 3.2.18 Well RL_I, sample 5049, photomicrograph, plane polarised light (image A), cross polarised light (image B).

The sandstone mainly contains quartz grains, including single crystals (mQ) and polycrystals, feldspar (F), partly altered and dissolved (D-F), microcline (Mi), identified by cross – hatched twinning and minor lithic fragments. A thin clay rim (Cl) coats the detrital grains. Pore spaces are frequent, as seen in blue colour.

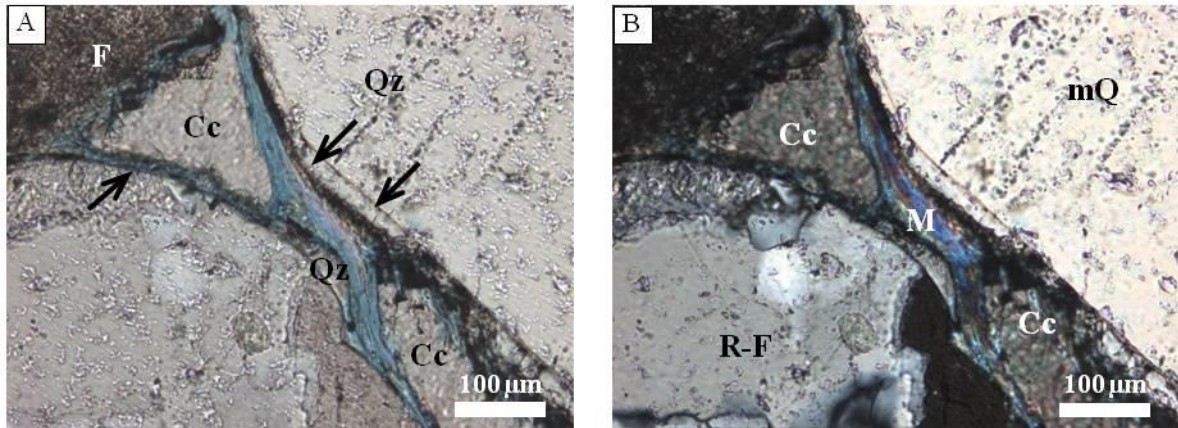


Figure 3.2.19 Well RL_I, sample 4146, photomicrograph, plane polarised light (image A), cross polarised light (image B).

The quartz overgrowth (Qz) covers the clastic grain surfaces. The original grain surfaces show a dark brown rim of iron oxide (arrows). The sandstone contains quartz (mQ), igneous rock fragments (R-F) including quartz, feldspar, weathered feldspar (F) and muscovite (M) with high interference colours seen under cross polarised light. Pore spaces are filled by calcite cement (Cc).

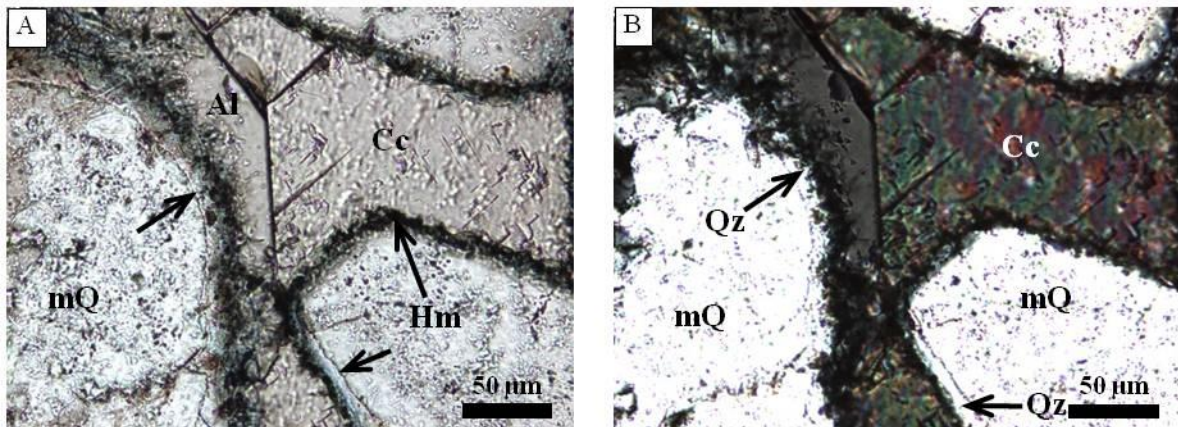


Figure 3.2.20 Well RL_I, sample 2081, photomicrograph, plane polarised light (image A), cross polarised light (image B).

The rounded quartz grains (mQ) are well cemented by calcite (Cc) with high interference colours. Albite (Al) grows over quartz (Qz) overgrowth. The surfaces of the original quartz grains are indicated by a dark brown rim of hematite (arrows, Hm).

3.3 DIAGENESIS

Diagenesis is a process in which sediments have undergone chemical and physical changes which occur during the formation of rocks from loose sediment after its deposition. The term “diagenesis” was introduced by Von Guembel in 1868 to describe sediment alterations that take place during post – depositional processes of lithification and has been used for a wide range of alterations that affect sediments during their progress to become sedimentary rocks (Twenhofel, 1939; Correns, 1950). It however does not include weathering. The concept of

diagenetic regimes is commonly recognised including 3 diagenetic stages as suggested by Choquette et al., 1970: Early diagenesis (eogenesis), burial diagenesis (mesogenesis) and uplift-related diagenesis (telogenesis).

- Eogenesis refers to the early diagenetic stages. All processes occur near the surface with the depths limit ranging from a few metres to tens of metres below the surface. Due to shallow depths, the sediments undergo minor compaction and rearrangement. The interstitial water and pore water are influenced by the depositional environment due to penetrating meteoric water into subsurface. Mineralogical changes and precipitation of new minerals occur during the eogenesis.

- Mesogenesis is mainly related to burial diagenesis. Sediments are strongly compacted resulting in tight grain packing and bed thinning. Besides, due to increasing pressure and temperature in depth, the solubility of grains and chemical reaction rates are increased. Simultaneously, decreasing porosity through cementation occurs by the precipitation of silica or carbonate in pore spaces. In addition, in this process, crystallisation of authigenic minerals takes place due to watery solutions that percolate through the pores between grains. Also, occurrence of mineral replacement may take place due to dissolution of one mineral whereby another mineral fills the space via precipitation or in step by step replacement through fluid penetration, especially of bioclasts. Burial diagenesis occurs at the depth about 100 – 1000 m, sometimes roughly 1 – 2 km.

- Telogenesis: Lithified and diagenetically altered, buried deposits are uplifted and exposed to or close to the surface. Rocks are in contact with meteoric water of the subsurface with low salinity, highly oxidised, CO₂-charged waters, grains and cement are dissolved and porosity is increasing. On the contrary unstable grains such as feldspars alter to clays and ferric mineral oxidation, thus reducing porosity.

Sandstone diagenesis plays a crucial role in petroleum industry or better hydrocarbon enrichment etc... because the diagenesis influences the amount and distribution of porosity and permeability in sandstones. This is an important factor to determine reservoir capacity and fluid flow movement through pore spaces in rocks. Also the source rocks are ruled by diagenesis, buried organic matter has influences of pressure, temperature and compaction. Depending on temperature and kerogen type, the organic material generates gas or oil.

The studied sandstones illustrate multiple diagenetic phases. Many authigenic mineral and cement generations are formed during diagenesis. Additionally, the dissolution and replacement of less stable minerals e.g. feldspars and volcanic fragments, those are weathered and altered by pressure and temperature changes, are found. The diagenesis significantly influences the reduction of porosity and permeability in the sandstones as well as it controls hydrocarbon migration pathways.

3.3.1 Cement and authigenic minerals

In the herein investigated samples, cement and authigenic minerals are mostly present in all the sandstones and mainly consist of calcite, anhydrite and authigenic quartz, albite, clays and hematite. The cement volume is between 10% and 30%. Calcite cement is volumetrically dominant in most of sandstones.

Iron oxides

Hematite or a mixture of hematite and clays are almost omnipresent in the studied sandstones. Hematite occurs as a skin on grain surfaces. The presence of hematite is observed from microscopic investigations. Hematite directly precipitates on the grain surfaces, visible as dark – brown rims on grain surfaces. This suggests that the formation of these grain coatings occurred in the early diagenesis or in eogenesis under the presence of oxygen. In this stage, the chemistry of the interstitial waters was mainly controlled by the depositional environment as demonstrated by Schmidt et al., 1979. As demonstrated in figure 3.2.11, and figure 3.2.16, the thick hematite skins on corroded grains and hematite staining of clastic grains could result from weathering processes. Iron was released during the breakdown of unstable ferromanganese or iron oxide minerals in the sandstones under surface temperature and pressure conditions. Additionally, iron was probably transported into the basin by meteoric waters from weathering of the adjacent areas and precipitated under favourable oxic conditions.

Clay minerals

Clay minerals are ubiquitous in all the sandstones. The most predominant authigenic clays are illite and chlorite, which occur in a number of morphologies in the form of clay coatings on detrital grains and as pore – filling. Smectite is locally present in minor amounts.

Illite and illite - smectite

Illite occurs in distinct forms as grain - tangential illite coatings (Figures 3.3.1; 3.3.2 and 3.3.3), pore – filling and pore - bridging illite ribbons (Figures 3.3.4; 3.3.5 and 3.3.6). Illite coatings are commonly stained by hematite forming dark – red rims surrounding detrital grains, as seen in thin sections. According to Walker, 1976, the grain – coating illite and staining by hematite are typical for the red beds in Rotliegend sandstones. These coatings are predominant filamentous illites probably precipitated from pore water due to supplying of meteoric water into subsurface. Illite – smectite is present in a small fraction in the form of thin fibres as flakes (Figure 3.3.7). The pore – filling and pore - bridging illite ribbons could have been commonly formed later in the burial phase. The illites are linked to extensive grain dissolution, as feldspars, volcanic fragments. Sometimes, illite filaments are released from surfaces at the cost of the authigenic albite, where albite is replaced by illite (Figure 3.3.8). Generally, the appearance of illite and illite – smectite together with authigenic chlorite can complicate the geometry of pore networks and the high resistance to fluid flows through the sandstones, causing a reduce of the permeability.

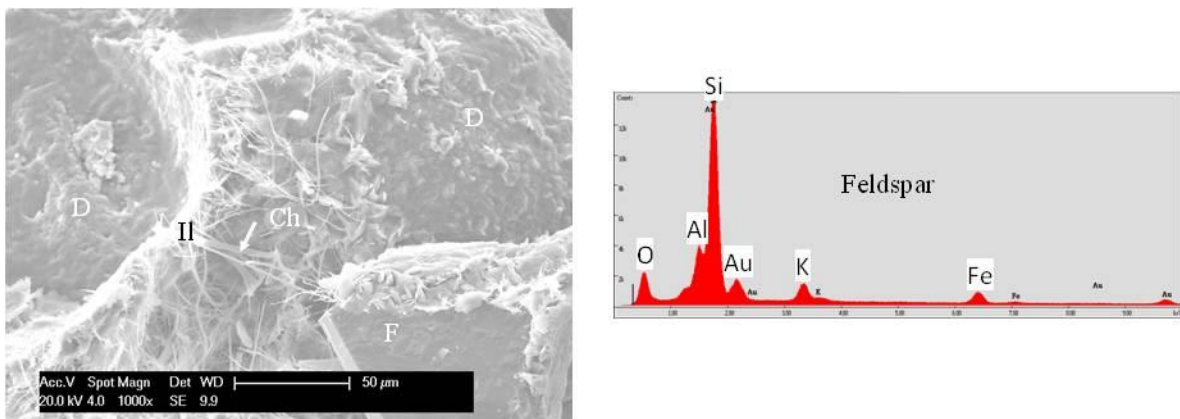


Figure 3.3.1 SEM image showing filamentous authigenic illite (II) forming a mat, coating the detrital grain surface (D) and bridges across a pore (arrow). Chlorite with pseudo hexagonal crystals (Ch) seems to be oriented perpendicular to the detrital grain surface (D) and to fill the pore. Additionally, the pore is narrowed by the overgrowth of authigenic feldspar (F) with euhedral shape. As observed at the lower right corner of the image illite fibers released from the authigenic feldspar are probably formed due to extraction of Al from this feldspar. The authigenic feldspar is identified by EDX analysis showing the major elements O, Al, Si and a minor amount of K. Fe displayed here is not a constituent of feldspar, rather it is a contaminant from adjacent clays such as from chlorite.

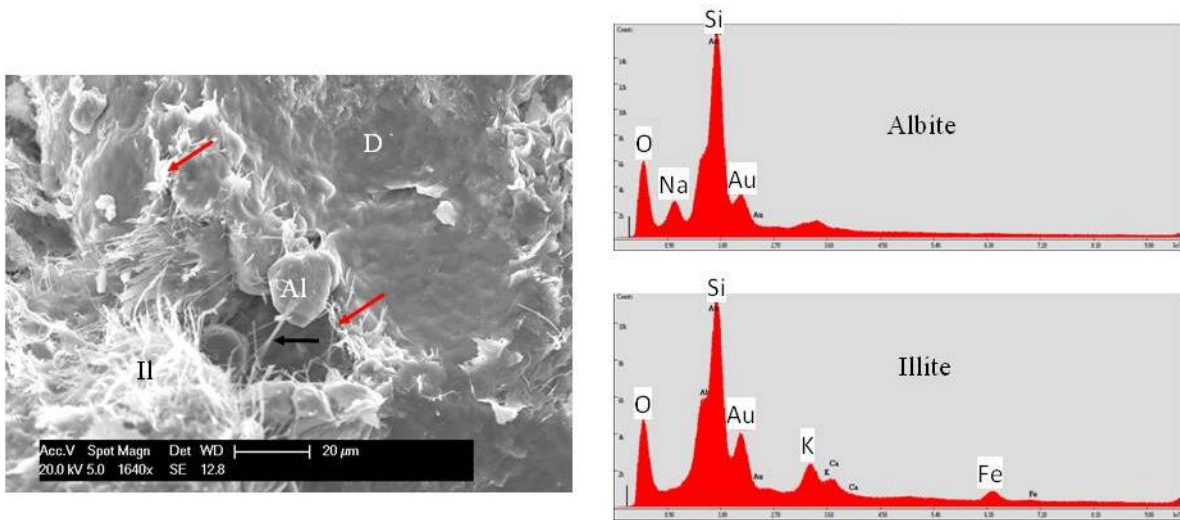


Figure 3.3.2 SEM image shows filamentous illite (II) forming a mat in the pore and coating the detrital grain surfaces (red arrows), while authigenic albite (Al) with euhedral shape grows on a detrital grain (D) facing also into the pore space. Some illite fibres (black arrow) bridge across the pore and cover the authigenic albite. EDX analysis was used to identify illite and albite. The characteristic spectra are given on the right of the image.

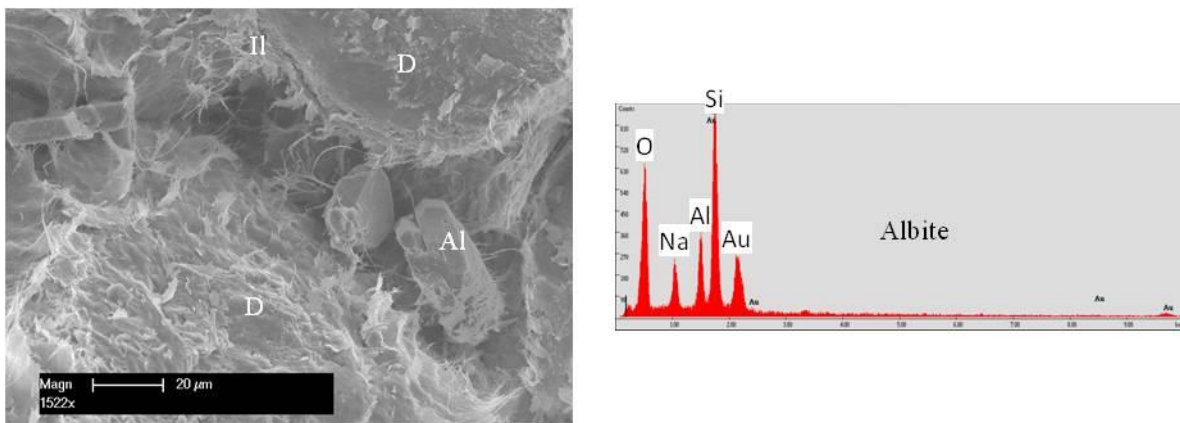


Figure 3.3.3 SEM image shows, that the pore space between detrital grains (D) is partly occluded by pore – lining authigenic illite (II) and pore – filling authigenic albite (Al). Illite filaments form a mat coating the detrital grain surfaces and locally illite fibers are released from the authigenic albite surfaces. The authigenic albite is identified by EDX analysis.

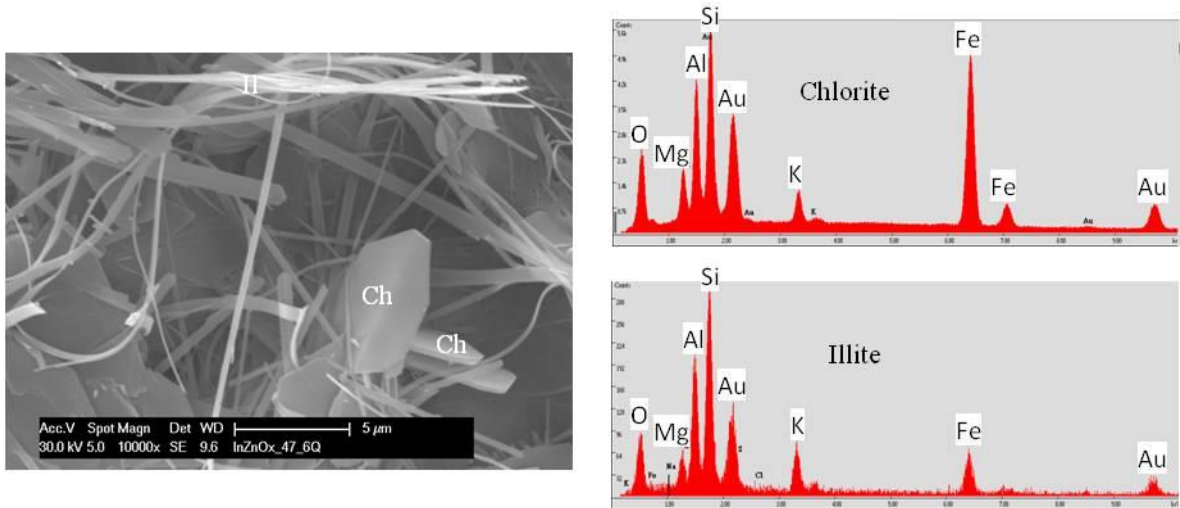


Figure 3.3.4 In the SEM image authigenic illite with the ribbons (II) and chlorite with pseudo hexagonal crystals (Ch) bridge across the pores. Illite is identified by the EDX spectrum showing the major elements of illite: O, Si, Al and K, with a minor amount of Mg. The Fe detected is due to contaminations of the underlying chlorite. Chlorite EDX analysis yields its major elements: O, Si, Al, Mg and Fe. K contaminates the spectrum and results from the adjacent illite.

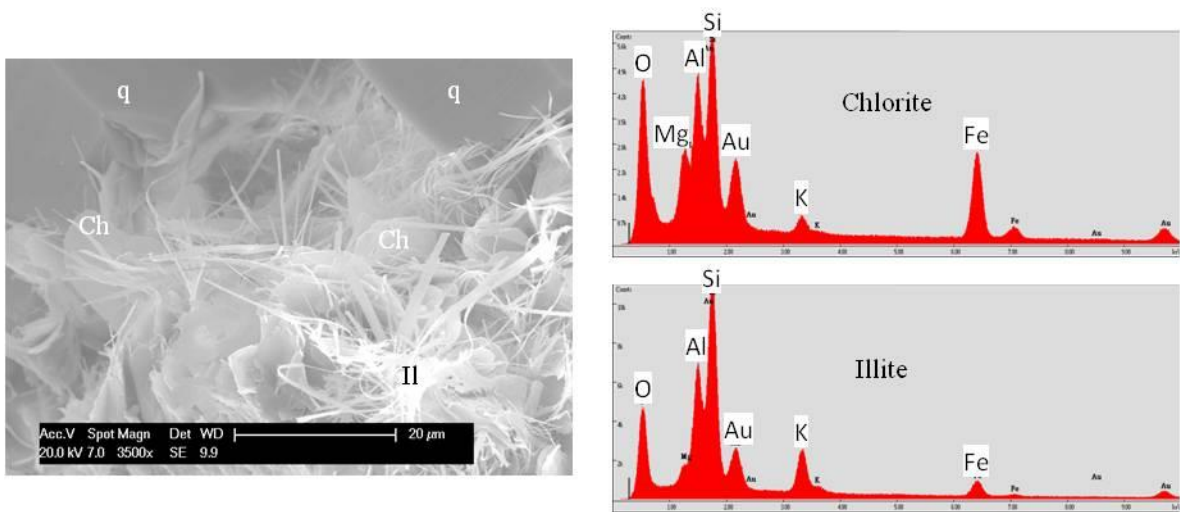


Figure 3.3.5 The authigenic clays illite (II) and chlorite (Ch) are pore fillings. Individual illite ribbons bridge pores and coat the quartz overgrowth (q). Individual chlorite crystals seem to be pseudo hexagonal shape and mixed with illite. Identification of the authigenic clays is carried out by EDX analysis. The illite EDX spectrum contains the major elements: O, Al, Si, K and a minor amount of Fe, which is a contaminant from chlorite, while the chlorite EDX spectrum shows the elements: O, Mg, Al, Si and Fe, where K is a contaminant from illite.

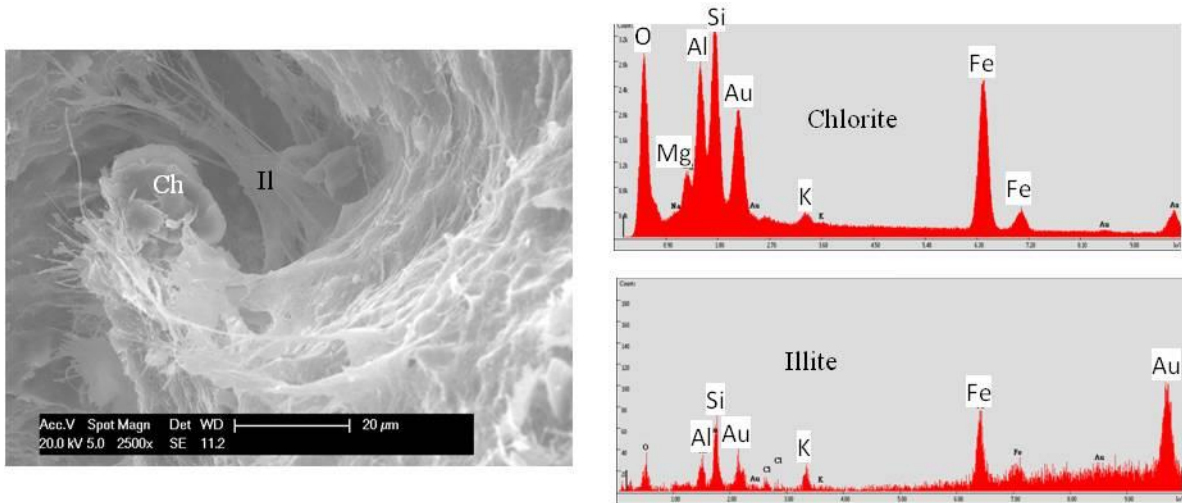


Figure 3.3.6 The pore space is filled with authigenic chlorite and authigenic illite (II) with intertwined filaments bridging across the pore, creating permeability barriers to fluid flows. These minerals were recognised by their morphology and EDX analysis.

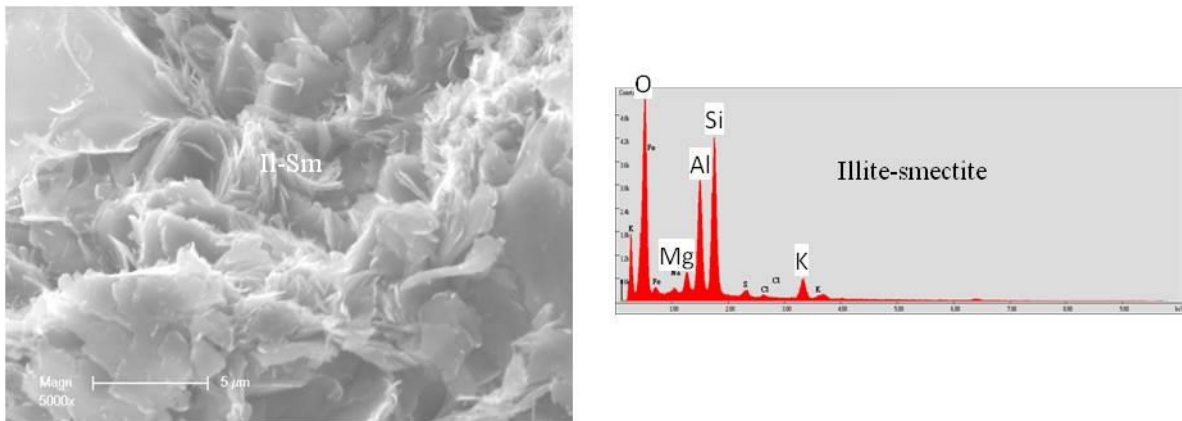


Figure 3.3.7 Mixed illite - smectite clays (II-Sm) appear as a flaky coating on the detrital grain surface. The EDX spectrum yields the major elements O, Si, Al, K, Mg.

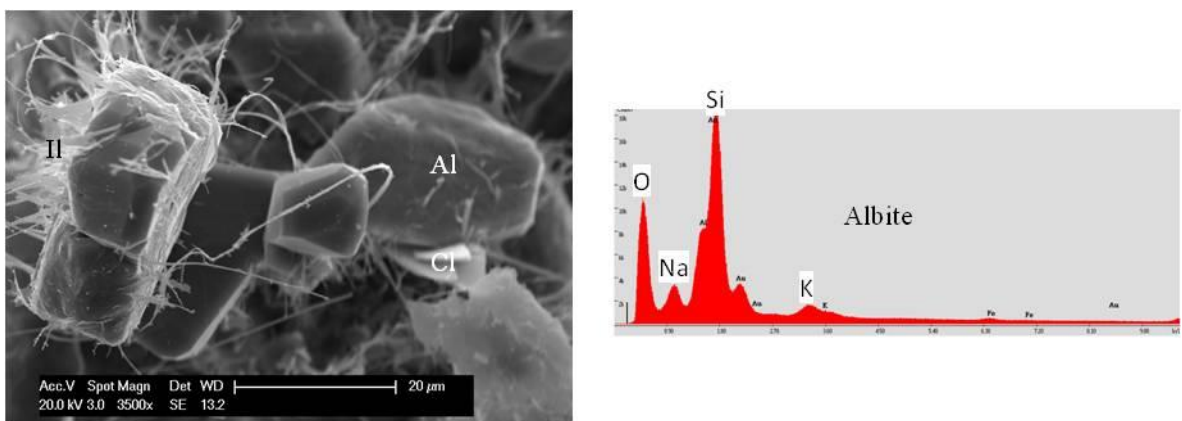


Figure 3.3.8 SEM image shows authigenic albite crystals (Al) with euhedral and subeuhedral shape, which is present in the pore space. Illite filaments (II) are released from the authigenic albite and cross the albite surfaces. The illites could be formed due to the extraction of Al from the authigenic albite minerals. These minerals were determined by the EDX spectra.

Chlorite

Authigenic chlorite is present in some the studied sandstone samples. The chlorites with irregular morphology mix with illite forming grain coatings (Figure 3.3.9). Individual chlorite crystals with euhedral and subeuhedral shapes arranged in rosette pattern are approximately 5 – 15 μm in diameter and less than 1 μm thick. They are perpendicular to the detrital grain surfaces facing into the pore space (Figures 3.3.10 and 3.3.11). This suggests, that the chlorites were formed in the early diagenetic process (eogenesis) as the investigations by Hayes, 1970; Humphreys et al., 1989 demonstrate. These studies show chlorite in form of grain coatings which can precipitate early in diagenesis, but before the onset of metamorphism or weathering. The form of chlorite with subeuhedral crystal plates is present in pore filling cement (Figures 3.3.4; 3.3.5 and 3.3.6). Sometimes the illite - chlorite with small and thin platelets, as flakes, is found in the void filling between the grains (Figure 3.3.12). Probably, the chlorites formed in the burial stage. In this buried diagenesis, the elements Al and Si were released from many dissolved detrital grains and Fe and Mg were supplied from the breakdown of ferromagnesian minerals in the rock fragments and matrix components into pore waters. These formed then the fluid sources to crystallise the authigenic chlorites. The chlorites can be directly precipitated from the pore fluids as investigated by Humphreys et al., 1989. The authigenic grain coating chlorites formed in the early diagenesis, while the pore filling chlorites formed in the burial diagenesis.

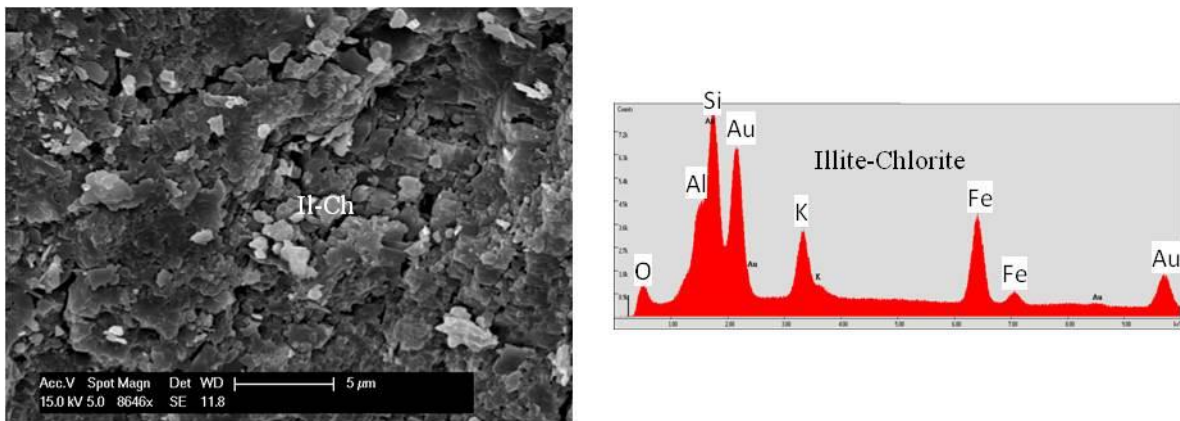


Figure 3.3.9 The jagged overgrowth of a thin authigenic clay layer covers a detrital grain surface (D). The clays are composed of illite with chlorite. The identification of these clays is based on EDX analysis.

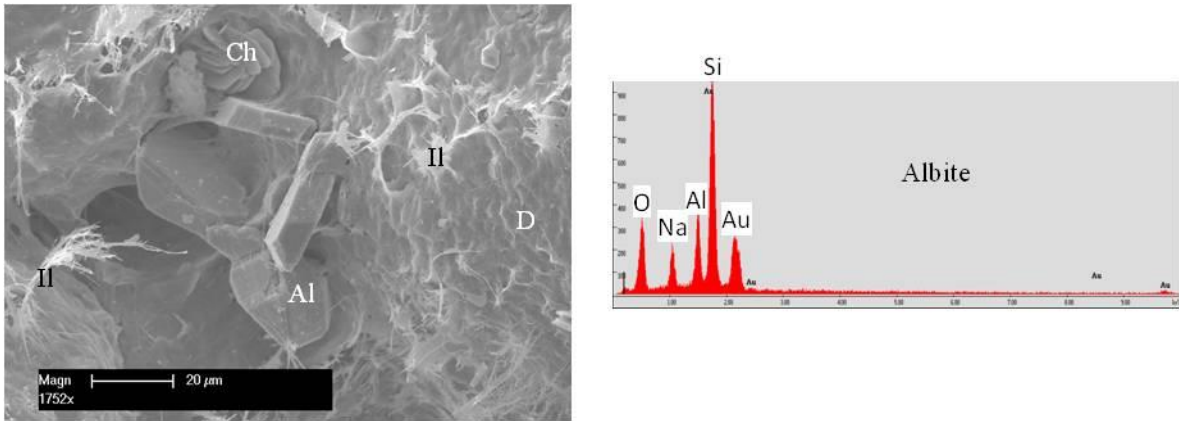


Figure 3.3.10 SEM image reveals, that the intergranular pore is partly occluded by authigenic albite (Al) with subeuhedral and elongated shaped chlorite (Ch). The chlorite is magnified in Figure 3.3.11 and also illite (II) with filamentous flakes. Additionally, the illite filaments coat on a detrital grain surface (D). Precise identification of the albite is possible by EDX analysis.

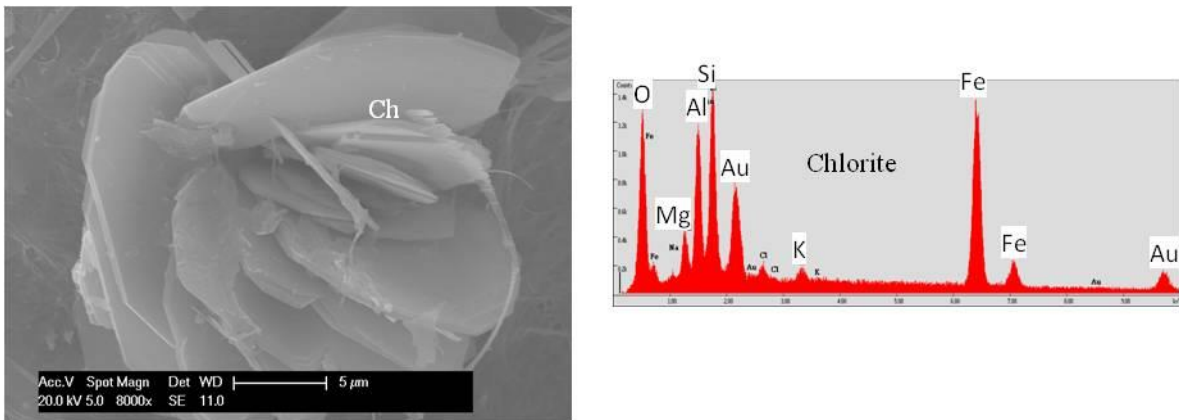


Figure 3.3.11 SEM shows the individual chlorite platelets arranged in a rosette pattern. The euhedral and pseudo hexagonal crystals are roughly 5-15 μm in diameter and less than 1 μm thick. These chlorite crystals form barriers that partly reduce the pore spaces. The EDX spectrum yields an iron – rich chlorite, which contains the elements O, Mg, Si, but also K due to contaminants from adjacent minerals and illite fibers on its surface.

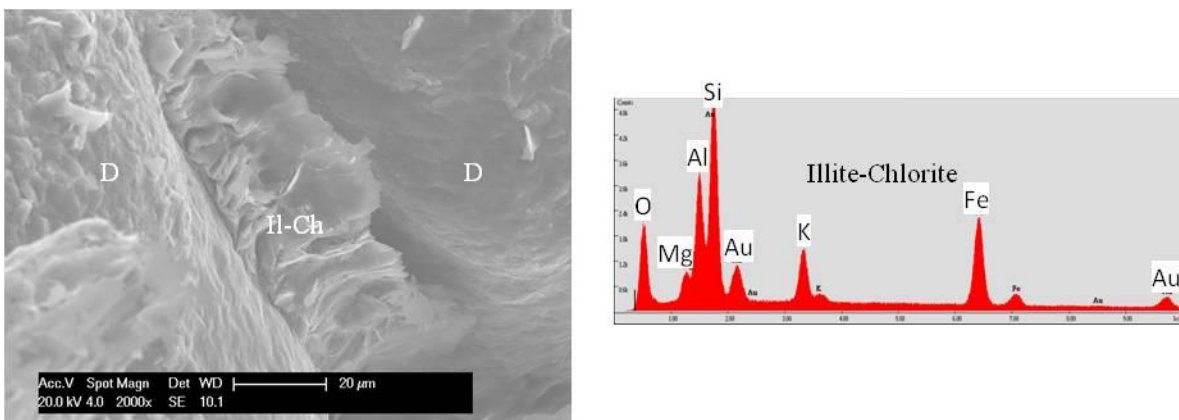


Figure 3.3.12 SEM shows an authigenic clay flake between detrital grains (D). The authigenic clay is mixed illite and chlorite (II-Ch), which were identified by EDX analysis. The EDX spectrum shows all the major

elements of illite and chlorite: O, Si, Al, K, Fe and a minor amount of Mg. The illite – chlorite flake blocks pore throats of connecting pores together leading to isolated pore spaces and reduce permeability.

Anhydrite

Anhydrite cement is present only in a couple of sandstone samples at the depth of 2081 m – 4839 m. The deeper the sandstone is buried the less amount of anhydrite is present. At the depth greater than 4900 m anhydrite is completely absent. Mostly anhydrite forms poikilitic crystals and subhedral laths (Figures 3.2.3; 3.2.4 and 3.2.10) with moderate 15% of volume. Sometimes it has enclosed authigenic quartz as pore – filling cements (Figure 3.3.13), which is a result of the circulation of evaporitic pore waters in the carbonate cements during burial stage derived from the Zechstein sequence.

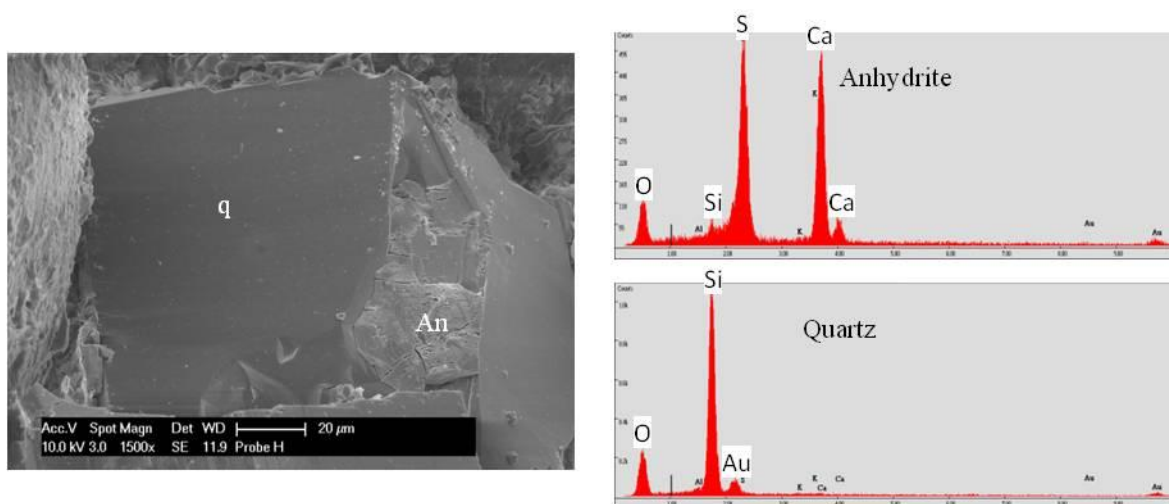


Figure 3.3.13 Authigenic quartz (q) grows in the primary pores. Identification of quartz is based on EDX spectrum analysis showing the major elements of quartz, O and Si. Anhydrite (An) overlays the authigenic quartz surface. The EDX spectrum contains its main elements O, S and Ca.

Authigenic quartz

Quartz cements are less abundant than calcite and precipitate in distinct forms. Authigenic quartz occurs in the form of overgrowth and syntaxial overgrowth on the quartz grain surfaces (Figure 3.2.8; A, B in Figure 3.2.12; Figures 3.2.13; 3.2.14; 3.2.19; 3.2.20 and 3.3.14) with sharp crystal edges. The authigenic quartz with perfect crystal habits has been growing quartz framework surfaces and into pore spaces. The authigenic quartz overgrew the outer rim of clay minerals and/ or hematite skin which separated the quartz frameworks and the authigenic quartz (Figures 3.2.8; 3.2.13). The overgrowth and syntaxial quartz are overlapped by calcite in pore filling cement. This indicates that the first generation cement constitutes clay minerals

and/ or hematite coatings and subsequently the authigenic quartz which formed followed by calcite cement. The overgrowth and syntaxial quartz precipitation are possibly connected to meteoric waters, which took up SiO_2 released from dissolution and chemical weathering processes of less stable minerals. Quartz cement with large crystals in the form of pore – filling (Figures 3.3.13; 3.3.15) precipitates most likely during burial diagenesis or in mesogenesis phase, as quartz cement formation is a significant process only at temperatures greater than about 70-80 $^{\circ}\text{C}$ (Choquette et al., 1970). In general, the authigenic quartz can significantly reduce the size of intergranular pores and pore-throats, leading to a considerable reduction of porosity and permeability of sandstones. Locally, authigenic cristobalite druses with rhomboidal morphology (Figure 3.3.16) scatter on clay layers in pore spaces. The cristobalite crystals also precipitated from the SiO_2 rich pore fluids as did the authigenic quartz but the cristobalite crystallises in higher temperature than the authigenic quartz. In the burial diagenesis, the increasing temperature was responsible for the formation of cristobalite.

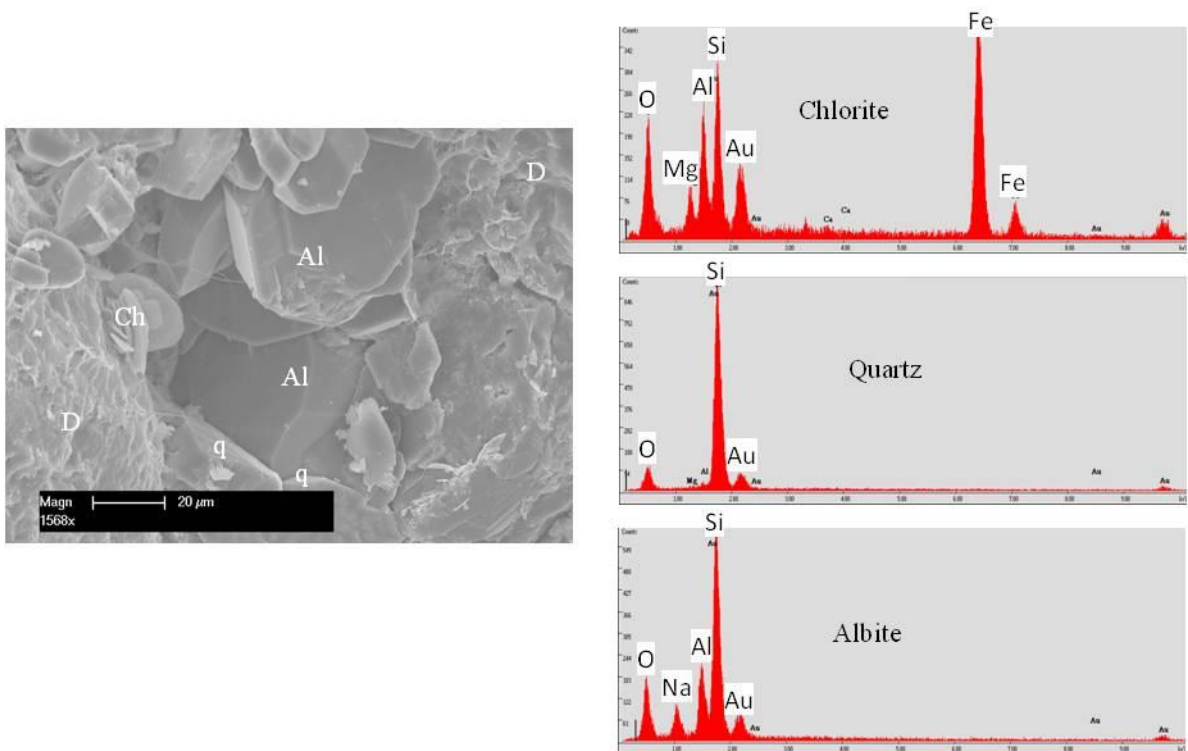


Figure 3.3.14 SEM shows an intergranular pore between detrital grains (D). This pore space is completely occluded by both quartz overgrowth (q) and authigenic albite (Al). Authigenic chlorite (Ch) grows perpendicular to the grain detrital surface. This assembly of the authigenic minerals leads to a strongly reduced porosity and permeability of the rock. The authigenic minerals were identified by the EDX.

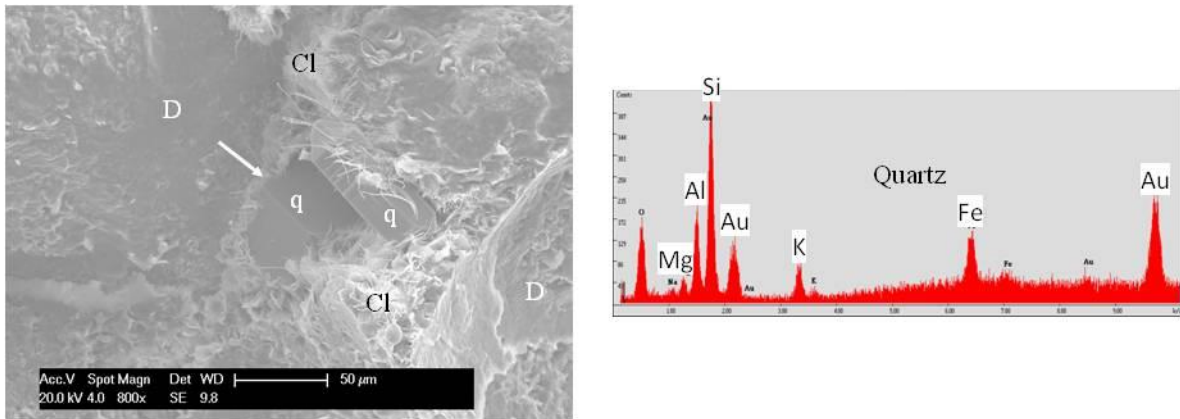


Figure 3.3.15 The intergranular pores and pore throats are occluded by both authigenic quartz (q) and diagenetic clays (Cl). The detrital grain (D) is separated from the quartz overgrowth (q) by a thin layer of clay (arrow). The EDX spectrum contains the major elements O and Si. The detected Mg, Al, K and Fe are contaminants from the surrounding clay coating.

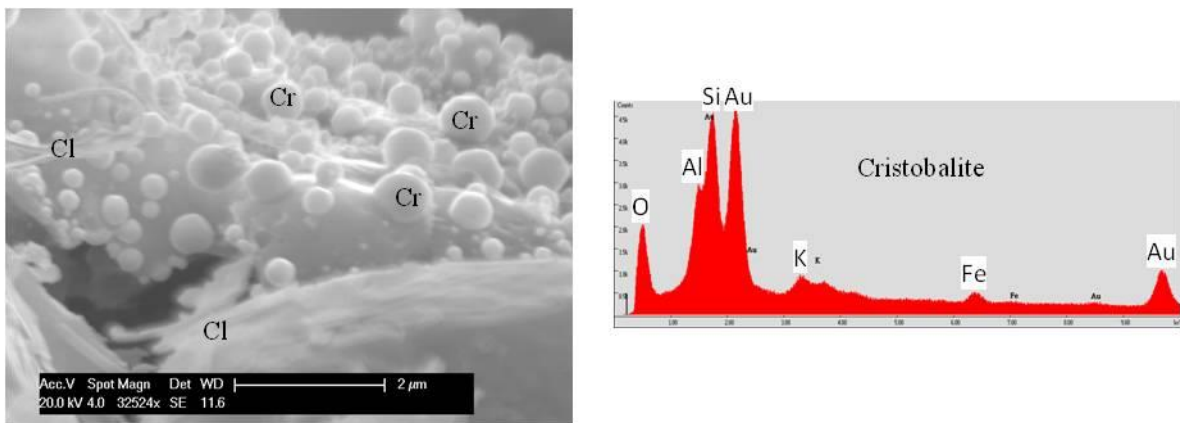


Figure 3.3.16 SEM reveals authigenic cristobalite crystals (Cr) scattered on a clay coating within a pore. The cristobalite crystals are identified by basing on their rounded shape and EDX analysis. The main elements of cristobalite are O and Si but Al, K and Fe detected here are contaminants from the underlying and adjacent clays (Cl). The pore size is partly narrowed by the cristobalite crystals that fill the pore.

Authigenic Feldspar

Authigenic feldspar is known as common cement formed during diagenesis. It forms overgrowths on detrital grains or as pore filling cements. Authigenic albite occurs as a partly throat blocking and pore filling crystal (compare C, D in Figure 3.2.14; A, B in Figure 3.2.15 and Figures 3.2.20; 3.3.2; 3.3.10; 3.3.14; 3.3.17). The albite grows outer clay mineral coatings (Figures 3.2.15 and 3.2.20) indicating that it formed after these clay mineral coatings. The albite is precipitated in the early diagenesis due to the sodium dominated formation water. Subsequently, widespread during burial diagenesis authigenic feldspar occurs as overgrowths on detrital grain surfaces (Figure 3.3.1). A possible reason for the albite formation is that Al

ions which were released from partial dissolved detrital grains re-precipitated at crystallisation nuclei, at favourable diagenetic conditions.

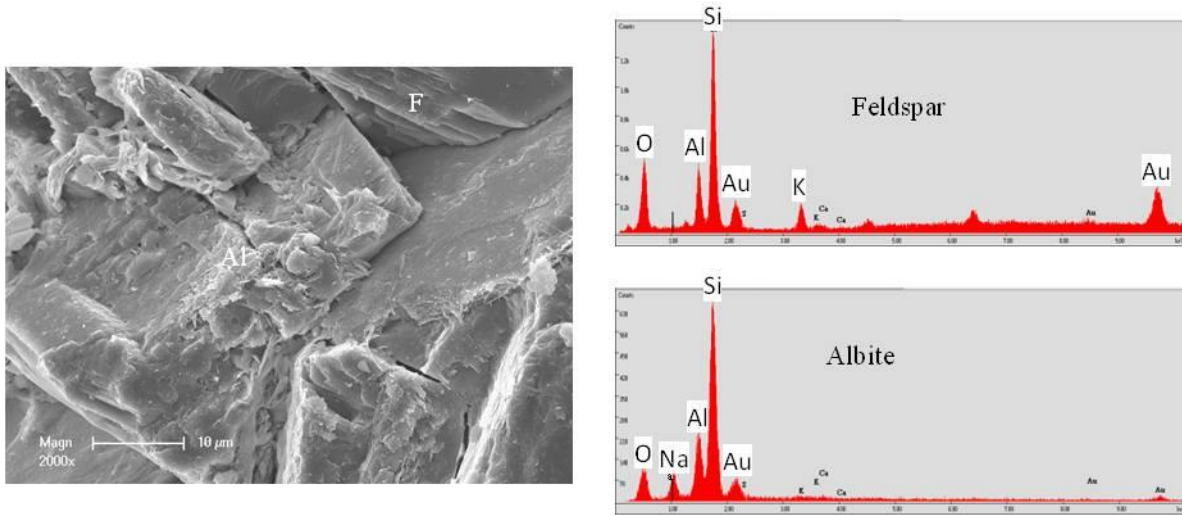


Figure 3.3.17 Authigenic albite (Al) with a jagged surface, overgrowing a pore and a part of detrital feldspar grain (F) is seen in the upper right corner of the image. Precise identification of the minerals is based on EDX analysis. The albite EDX spectrum shows the major elements O, Al, Si and Na, while the feldspar EDX spectrum yields the elements O, Al, Si and K.

Halite

Authigenic cubic halite crystals preferentially precipitate and scatter across clay coatings (Figure 3.3.18). They only locally occur in a couple of the sandstones investigated. Probably the halite crystals can be associated with evaporitic conditions or that a mixture of ground water and brines derived from the overlying Zechstein sequence where the halite could form in the early diagenesis but after the clay coatings.

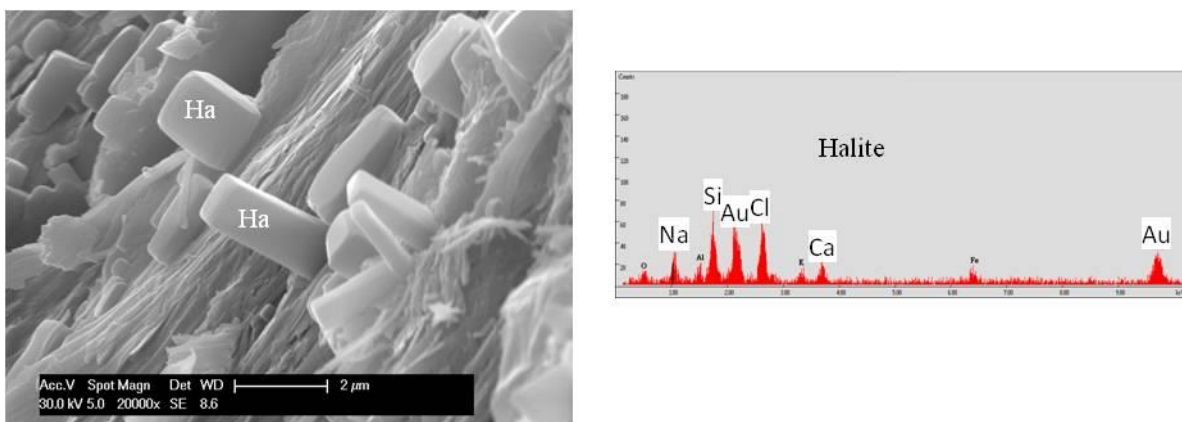


Figure 3.3.18 Small, cubic halite crystals (Ha) scattered across clay coatings of a detrital grain. Identification of halite crystals is due to the cubic morphology and EDX spectrum analysis, which yields the two major elements Na and Cl. Si, and Ca are contaminants from the underlying clay coating.

Siderite

Siderite only occurs in some of the samples investigated. It is present as micro nodules with rhombic habits and is sub euhedral in shape (Figure 3.3.19), like a crust covering the detrital grain surface. Siderite probably took up Fe ions released from the dissolution of Fe ion rich, less stable minerals like feldspars, matrix clays or Fe oxides formed during earlier diagenetic stages and CO_3 ion derived from Zechstein strata. Under reducing conditions siderite was then formed in burial diagenesis. Therefore, siderite formed after the main phase of grain dissolution and clay matrix dissolution typically of chlorite clays during burial diagenesis. Besides, fluids with Fe ion rich form haematite coatings on grain surfaces, as seen in thin sections.

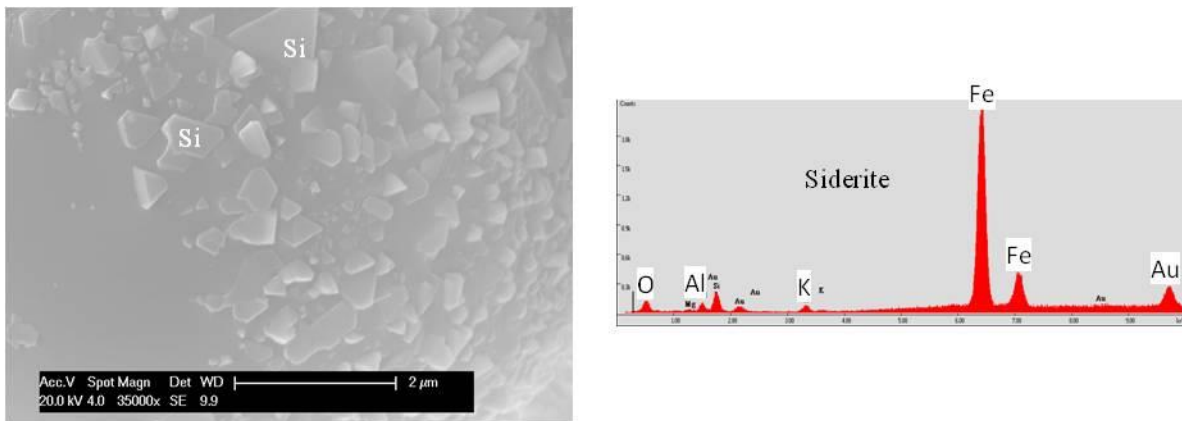


Figure 3.3.19 The surface of the detrital grain is partly covered with authigenic siderite overgrowth (Si) as a coatings. Identification of the siderite crystals is based on its rhombic structure and EDX spectra. The latter contain Fe and a minor amount of O (C is not detected by the EDX system). K and Al are contaminants from the underlying grain and adjacent minerals.

Calcite

Calcite is one of the most abundant cements in sandstones. Calcite typically occludes pore spaces, but also partly replaces detrital feldspars and volcanic rock fragments. Calcite formed during early diagenesis and continued during burial diagenesis. The calcite shows complex textural relations to other diagenetic minerals. In the early diagenesis, calcite forms commonly as pore - filling cements, which precipitated directly on grain surfaces (Figures 3.2.9 and 3.3.20). Sometimes, overgrowth of calcite overlaps on the hematite – clay coatings, albite and quartz overgrowths (Figure 3.2.8, C, D Figure 3.2.14, Figures 3.2.15 and 3.2.20). The calcite formed simultaneously sediment deposits in shallow water environment.

In the burial diagenesis, calcite precipitates locally in pore spaces and replaces the dissolved feldspar grains and volcanic fragments (C, D Figure 3.2.15; Figures 3.2.16 and 3.2.17). The calcite extracted from meteoric water, which primarily derived from the overlying Zechstein sequence and was supplied by marine pore waters due to the Zechstein marine transgression. The replacement only occurs at the depth below than 4900 m. It is possible that acidic fluids extracted from the underlying Carboniferous strata were responsible for the dissolution as investigations by Purvis, 1989; Purvis, 1992, where the Rotliegend sandstone deposits underlain the Westphalian coals and carbonaceous shales (Upper Carboniferous) (Chapter 2). However, a clear determination between calcites of the early and burial diagenesis was not possible for all samples as calcite tends to recrystallise and the textures are difficult to be recognised.

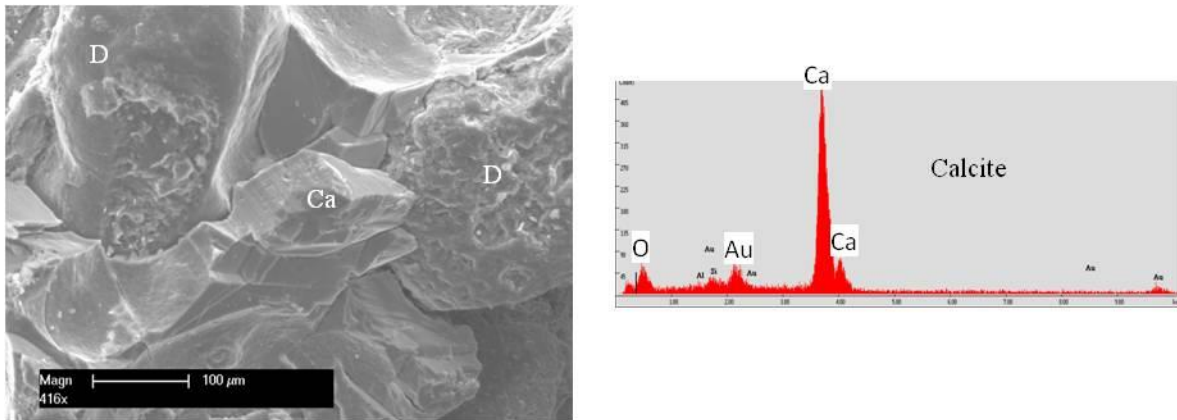


Figure 3.3.20 SEM shows a pore space between grains (D) filled completely by calcite cement. Identification of pore filling calcite is based on the distinctive EDX spectrum showing only Ca and a minor amount of O. Calcite however has also been recognised in thin sections.

3.3.2 Pore network

In general, the analysed sandstones are moderately compacted and they contain a moderate amount of cement and authigenic minerals. However, the distribution of cements and authigenic minerals is heterogeneous and depends on changes of burial depth and grain size. Therefore, the intergranular pores also vary depending on depth. In the interval of 2081 m to 4910 m depth, pore spaces are poor, but well preserved in the interval of 4910 m – 5049 m. In addition, macro/micro pores are also present within the leached feldspar grains (Figures 3.2.12; 3.2.18; 3.3.21). The permeability of sandstones is widely varying from very low to very good (0.25 mD – 53.45 mD, results from the RWE petrological laboratory in Wietze, Table 3.1). This depends on the volume of porosity, the width and the inner roughness of the pore spaces and pore throats, which can be completely blocked by authigenic minerals

especially pore lining clays (consisting mainly of authigenic chlorite, illite with a fraction of illite-smectite), albite and quartz overgrowths. The diagenesis is a main cause that is responsible for the changes of the porosity and the permeability and the varying the pore structure and grain shape. The pore geometry and the grain morphology of the investigated sandstone reservoir rocks are discussed in chapter 4. The grain roughness is formed by the authigenic clays and cements are shown in chapter 5.

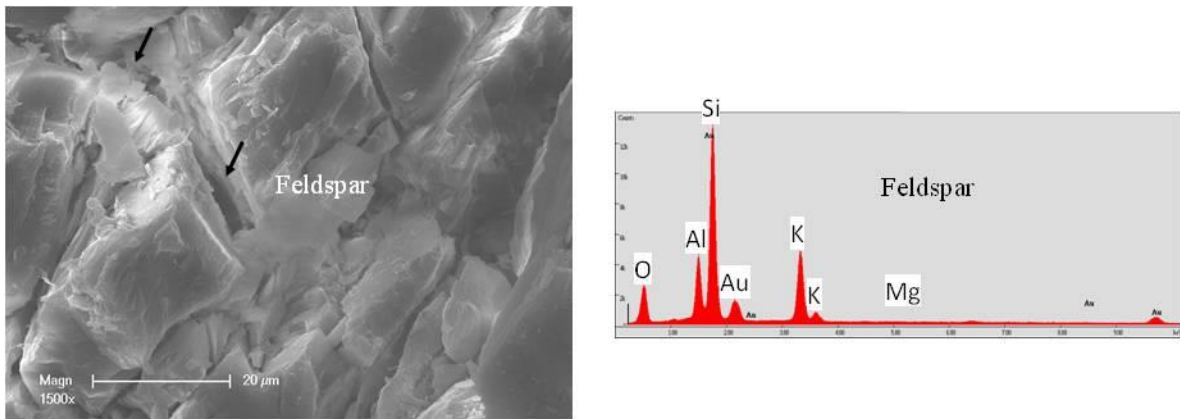


Figure 3.3.21 A detrital K – feldspar grain is dissolved forming a ragged surface with secondary micro pores (arrows) and cracks. The grain was identified by EDX analysis and contains all the major elements O, Al, Si and K.

3.4 DISCUSSION

Most studied sandstones at the interval of 2081 m – 5049 m depth are moderately cemented and compacted. The grains are rounded to very well rounded or poorly rounded, spheroidal, as well as less spheroidal in fine grains. The sorting of grains is moderately to well sorted, however, the sorting is poor in laminated sandstones, where it is varying from laminae to laminae. Such a texture characterises sediments that are accumulated in environments with multiple phases of recycling of fluvial or shallow water, marine and bed load transport. Additionally, most of the sandstones contain a small clay proportion. This suggests that the sediments are in a texturally mature stage according to the classification of Folk, 1951, which based on the contents of clay matrix, the sorting and the roundness of the grains. The constituents of the investigated sandstones, in contrast, are heterogeneous containing a proportion of less stable grains such as K – feldspar, plagioclase grains and metamorphic and volcanic rock fragments. This indicates that the sediments are immature in terms of composition. The composition of the studied sandstones is also an important factor as it indicates source and depositional setting such as volcanic arc or continental margins. However, the provenance aspects were not taken into consideration in this thesis as they are

not significant for the discussed problems. The components are mono and polycrystalline quartz (ca. 50-60%); alkaline feldspar and plagioclase (5-15%) and rock fragments of volcanic clasts, metamorphic (quartzite) and igneous rocks (15% - 25%). The sediments were derived from weathered plutonic and metamorphic rocks. Locally the sandstones contain volcanic clasts with outsized grains (0.8 – 1 mm in diameter) compared with the other fragments and grains, indicating proximal volcanic sources. These results correlate with the investigation by Dickinson, 1985. The Rotliegend sandstones from the northeastern German basin which are quartz rich were derived largely from weathered igneous and metamorphic rocks (gneiss). The sandstones originated from the cratonic source and deposited in a relatively stable tectonic environment (McCann, 1998). The visible porosity in the investigated sandstones is very poor to moderate, widely varying from less than 5% up to 20% in volume and changing with depths. Visible open pores are mainly primary pores with a subordinate proportion of the intragranular porosities, which occur within grains due to dissolution. However, the appearance of the pores is very poor. Almost all the porosities were filled by the precipitation of calcite in burial diagenesis. The pore spaces are increased in correlation with the burial depth, due to the reduction of the large pore filling cements and dissolution. At the depth from 2081 m to 4900 m, the presence of silica fluids flooding the pores is ubiquitous. Hence, most pores are filled by silica cements. In addition, pore spaces are also infiltrated by calcite and anhydrite cements which probably extracted from the overlying Zechstein evaporites. The volume of the cements drastically reduces at the depth from 4910 m to 5049 m. In this depth, most of the cements are in general absent and only locally pores are filled by calcite cement (Figures 3.2.12 and 3.2.18).

The compaction in these sandstone rocks took place down to the burial diagenesis depths, which is indicated by the dissolution of grain boundaries and sutured grain contacts. A factor that widens the pore throats leading to increase the fluid movement through the sandstone reservoir rocks. However, this dissolution occurred locally in the investigated sandstones.

The samples display complex diagenetic stages. Primarily, hematite and/ or clay minerals such as illite, illite – smectite and illite – chlorite were generated in the early stage of diagenesis. The appearance of the clays commonly coats the surrounding grains. These clays precipitated directly from fluids in pore which were supplied from meteoric water into the subsurface. Illite is the dominant authigenic clay mineral. It is ubiquitous in all of the investigated sandstones. The major pore - filling quartz cement and small proportion of authigenic feldspar overgrowth on grains occur. Füchtbauer, 1974 pointed out that albite

precipitates preferentially in evaporitic or marine environments, where halite precipitation led to elevated K/Na ratios. The halite crystals are seen in figure 3.3.18. The diagenetic evolution is in agreement with a previous study (Altermann et al., 2010). The precipitation of calcite and anhydrite also took place at the early diagenetic stage. The calcite and anhydrite crystallised from the pore waters with sulphur and calcium compositions which may have derived from the overlying Zechstein strata. As investigated by Purvis, 1992, petrographic and sulphur isotopic analysis indicate that anhydrite was derived from the Zechstein sequence during diagenesis, as well as the calcite cement was originated from the pore waters which were supplied from the overlying Zechstein sequence due to marine transgression. In the burial diagenetic phase, the precipitation of albite cement in pore spaces was more popular due to highly dissolved feldspars and lithic grains. Besides, the dissolution of the grains leads to the precipitation of illite and chlorite in the form of the pore fillings and locally of siderite. Consequently, some illite fibres were released from albite and feldspar at the expense of dissolved feldspars (Figures 3.3.3 and 3.3.8) at depth in the burial diagenesis as reported by Liêu et al., 2012. According to Platt, 1993, who suggests that illite cementation in the Rotliegend occurred where the Rotliegend contact was closed to the underlying Carboniferous source rocks, which are organic – rich sediments and carbonaceous shales along faults was able lateral flow of fluids out of the Carboniferous strata. Fluids originated from Carboniferous source rocks were responsible for clay formation, grain dissolution and early diagenetic primary calcite dissolution. Clay cementation increased around faults which acted as conduits for fluids flowing into the Rotliegend and mostly took place during tectonic events (Platt, 1993)

In addition, the organic and acidic fluids and the iron released from dissolution of iron-rich minerals favour the formation of pyrite or siderite. The primary factor that determines whether pyrite or siderite will form is the acidity/alkalinity and sulphide availability. Sulphides are produced from sulphate during bacterial decomposition of organic matter. The organic material content is inconsiderable in the studied sandstones hence the source of sulphate probably is insufficient to produce pyrite. Therefore, pyrite is expected to be very rare. In this study no pyrite at all was detected.

However, siderite can form through the combined effects of the dissolved iron and CO_3 ions extracted from Zechstein strata and from fluids which dissolve the early diagenetic calcite cement

Siderite appears as a crust coating on the detrital grains (Figure 3.3.19). The siderite concretions are more popular with increased burial depths and at the expense of leached early diagenetic calcite cement.

Subsequently, the precipitation of calcite cement in burial diagenesis filled into the pore spaces and replaced the dissolved grains. The calcite originated from the overlying Zechstein sequence and was supplied by marine pore waters due to the Zechstein marine transgression as studied by Purvis, 1992.

Table 3.2 Diagenetic characteristic of sandstones at the interval of 2081 m – 5049 m

Diagenetic events	Relative timing	
	Early	Late
Iron oxides	-----	
Precipitation of grain – coating clay (illite/ illite – chlorite/ illite – smectite)	-----	
Quartz cement and albite overgrowths (early diagenesis)	-----	
Anhydrite and calcite cements (early diagenesis)	-----	
Dissolution of feldspar/ volcanic fragments	-----	
Albite overgrowths (burial diagenesis)	-----	
Illite and chlorite in pore – filling and replacing feldspar grains (burial diagenesis)		-----
Precipitation of calcite cements in dissolved minerals and pores (burial diagenesis)		-----

The diagenetic evolution of the Rotliegend sandstone reservoir rocks in Lower Saxony Basin is complex and is the result of fluid-rock interactions subsequent to accumulation from the early to during burial stage. In the early diagenesis, the precipitation of hematite, illite/ illite – chlorite or illite – smectite clays forms grain coatings and the formation of quartz cement is in pores, subsequently, calcite and anhydrite cementation occur in form of pore filling. During the burial stage, the feldspars, predominantly K-feldspar and volcanic fragments are dissolved. The formation of feldspar overgrowth and albite cement in pore spaces is relatively common. The growth of illite and chlorite are in form of pore – filling and replace dissolved grains took place. Finally, the precipitation of the burial calcite cements locally occurred.

4. ANALYSIS OF PORE AND GRAIN GEOMETRY IN SANDSTONE RESERVOIR ROCKS FROM A WELL IN THE NORTH GERMAN BASIN

A major factor leading to the loss of big quantities of hydrocarbons during exploitation is that significant hydrocarbon volumes are embedded in pore spaces and strongly adhere to the grain surfaces of the reservoir rocks. In sandstone reservoir rocks the porosity plays an important role because it affects the total capacity of hydrocarbon uptake within the sandstones. In addition, the grain surface roughness is an essential factor of the reservoir quality, as it relates to the pore surface and the pore shape complexity. This is likely to constrict the fluid flow through rocks. Detailed investigations of the pore morphology and of the grain surface roughness can reveal the fine structure of the pore spaces in rocks. This knowledge can be used to clarify the impact of the grain surface structure on the wetting behaviour and contact area of hydrocarbon fluids in contact with grain surfaces and may finally allow for improving exploitation methods.

The variations of the pore shape and the grain morphology of the investigated sandstone reservoir rocks are directly influenced by diagenetic processes, like re-orientation of grains during compaction, and dissolution and simultaneous or subsequent replacement by authigenic minerals, which are precipitated or recrystallised during the diagenesis in depositional settings. The morphology of pore spaces depends on the grain size distribution, the shape of grains, on packing, and on cementation while the grain surface roughness is influenced by mineralogy, transportation, and the overgrowth by authigenic minerals. The pore geometry and the grain surfaces are usually altered during lithification, beginning with compaction and cementing of loose sediment grains and, finally the conversion into a solid rock.

The quantitative characterisation of the roughness of particles/grains of detrital sediments and of their pore morphology has been the subject of many studies. Various techniques have been developed for that purpose such as e.g. the harmonic wavelet descriptors (HWD) which is based on the harmonic wavelet transform method. With this method, the grain contour and its roughness are analysed at different scales of resolution. Lower resolution levels represent the coarse aspects of the grain contour, while the higher resolution levels represent its increasingly fine structures (Drolon et al., 2000; Drolon et al., 2003). On the other hand the

pore morphology and pore surface roughness in rocks have been investigated using small-angle neutron scattering (SANS) and ultra small angle neutron scattering (USANS) (Triolo et al., 2000; Sen et al., 2002; Drobek et al., 2011).

Also Confocal Laser Scanning Microscopy (CLSM) techniques can be applied to measure the roughness and the pore geometry. Menéndez et al., 2001 performed three dimensional geometry imaging of the pore system of the Fontainebleau sandstone with different degrees of cementation and diagenesis, and also Fredrich et al., 1993 used a CLSM to verify the three dimensional pore of the Fontainebleau sandstone. Chae et al., 2004 analysed the fracture surface roughness of granite by CLSM and Petford et al., 1999 identified three dimensional distributions of pore bodies and pore throats in sandstones with hydrocarbon reservoir potential.

In this study, CLSM is used to analyse the pore morphology and the sediment grain roughness. From the surface topography data, profiles are calculated. 3-D reconstructions and the grain surfaces are analysed by the root mean square roughness parameter to correlate the numerical values. The pore space morphology of the investigated sandstone reservoir rocks is characterised by the features of the clastic grains which are the grain size, the grain surfaces and the growth of authigenic minerals into pore spaces.

4.1 METHODS

4.1.1 Confocal Raman Microscopy

Three samples RL I_2111, RL I_4146, and RL I_5041 derived from sandstone reservoir rock core plugs of the well of the North German Basin were separated into individual grains and small grain groups and mounted on top of a conical sample holder. Subsequently the mineralogical compositions of these grains are characterised with a confocal Raman microscopy (alpha300R; WITecGmbH, Ulm, Germany). The frequency doubled light (532 nm, $P_{max}=22.5$ mW) of a Nd:YAG laser was focused with a 10x objective onto the sample and used for excitation and for the collection of the backscattered light (Appendix II, Raman spectroscopy image). The diffraction-limited lateral resolution was about 300 nm. Due to a confocal microscope setup a resolution of about 1 μm was achieved in depth. Images were generated by scanning the sample and recording a full Raman spectrum at each imaging point.

4.1.2 Confocal Laser Scanning Microscopy (CLSM)

Subsequent to Raman spectroscopy, the grain surface roughness and the pore morphology have been conducted with a digital Confocal Laser Scanning Microscope (CLSM, VK-8700). The laser has a wavelength of 658 nm.

The CLSM delivers digitally sandwiched surface images of the sample, with the quantitative topography of each layer. Four kinds of observation lenses are used for data acquisition: 10x, 20x, 50x and 100x (Appendix II, Confocal Laser Scanning Microscopy). The resolution in Z-direction is 0.5 μm which is the mean distance between two adjacent layers. From the digital data set the roughness parameters were calculated with micrometre size resolution and the morphology of the pores was evaluated from 3-D and profile images. Definitions of the roughness parameters are listed in table 4.1.

Table 4.1 Definition of roughness parameters

Symbol	Description
R_p	highest peak
R_a	arithmetic mean height
R_v	lowest valley
R_z	maximum height
R_q	root mean square height
R_{sk}	skewness
R_{ku}	kurtosis

The surface roughness is usually characterised by one of two statistical height descriptors (American National Standards Institute, ANSI and the International Standardization Organization, ISO, Anonymous, 1975, 1985). These are the arithmetic average of the absolute values of the surface height deviation (R_a) and the root mean square average (R_q) of the height deviations measured from the mean plane. In this study, the root mean square (R_q) expresses the grain surface roughness, as the R_q represents the standard deviation of the distribution of the surface height and is more sensitive to topography changes than the surface height deviation (R_a). The R_a value is defined as

$$R_a = \frac{1}{N} \sum_{j=1}^N |Z_j| \quad (4.1)$$

where Z_j is the current Z value of each data point within the measured area of a scan size of $140 \mu\text{m} \times 105 \mu\text{m}$ and $70 \mu\text{m} \times 50 \mu\text{m}$, respectively with 50x and 100x magnifications, and N is the total number of data points.

To calculate the root mean square roughness (R_q) the background waviness was removed. After an automatic plane tilt correction, the images were flattened, subtracting an appropriate sphere to correct for a spherical surface. The R_q parameter was calculated for all images at 50x and 100x magnifications. This corresponds to a scan size of $140 \mu\text{m} \times 105 \mu\text{m}$ and $70 \mu\text{m} \times 50 \mu\text{m}$ respectively with 1280 x 1024 pixels per image. The root mean square R_q of the height of each point in the region of interest was calculated following the formula below (VK Analyzer. Ver. 2.3 Formanalyse software)

$$R_q = \sqrt{\frac{1}{N} \sum_{n=1}^N Z_n^2} \quad (4.2)$$

here Z_n indicates the height of each point of the analysed surface. N is the number of measured points.

4.2 ANALYTIC RESULTS

4.2.1 Grain roughness measurements

In sedimentology, the shape of grains plays a major role as it influences the capacity of grains to be transported. The morphology of a grain is an indicator of mechanical erosion process due to influence of transportation. The shape of the grains is described by the outline of the grain derived from the sum of the circular functions as Fourier analysis (Clark, 1981; Diepenbroek et al., 1992). It characterises the grains contour indicating the grain property: elongation, angularity, roughness or roundness. Previous studies related grain contour by using the wavelet formalism or using wavelet transform (Newland, 1993), which depends on the scale of observation. The grain shape is shown at multiscale or multiresolution and called wavelet descriptors that provided an efficient method for contour analysis and description of particles. If the observation is in a far distance from a grain, the global form of a grain will be characterised by its elongation or its sphericity. At high resolution and in a close up view the grain will be characterised by its details as its angularity, its roundness or its roughness.

Using the harmonic wavelet transform, Drolon et al., 2000, developed the multiscale roughness descriptor that proves a multiscale roughness descriptor for the description of

particles. With CLSM analysis in this chapter, the morphology of a grain is accessible and is revealed by the 3-D reconstruction, profile and the grain surface roughness is shown by a numerical certain set (Table 4.3).

Particularly, the morphology of the grains of the investigated sandstone reservoir rocks is generated mainly by erosion in transport, compaction and dissolution in diagenesis. Moreover, during diagenesis authigenic minerals and cement did crystallise in pore spaces and overgrew the original grain surfaces. Thus these minerals modify the surfaces of grains. Due to the overlying sediments, the compaction process caused concave imprints and casts on the grains (Appendix II, Confocal Laser Scanning Microscopy).

Depending on the diagenetic phases, different authigenetic minerals were formed causing different roughness (see chapter 3). The grain surfaces display various roughness levels, depending on the scale of observation, i.e. 10x, 20x, 50x or 100x magnification.

Larger areas show the overview of the surface irregularities (50x) while smaller areas (100x) show more details regarding overgrowth and coating. Therefore, at low magnification grain surfaces with high root mean square roughness R_q values have rougher pore spaces than those with low R_q . For the analysis of the surface area at high magnification, the root mean square roughness R_q has been shown to characterise the fractal dimension because it reveals grain surface ruggedness corresponding to numerous curved segments.

The results for a characteristic quartz grain surface roughness show, that the texture and morphology of the grain surfaces were altered during diagenesis due to compaction, cementation and the overgrowth by authigenic minerals.

4.2.1.1 Sample RL I_2111

Four quartz grains of sample RL I_2111 were analysed by Raman spectroscopy (see appendix II.1 – II.4). The quartz surfaces were analysed morphologically by CLSM (see appendix II.11 – II.14). The quartz grains are spheroidal and sub-spheroidal in shape, well rounded and stained by hematite with reddish brown and dark brown colour or covered with organic material, mainly of grey colour.

RL I_2111_Qu_1

The quartz grain is well rounded and sub - spherical in shape, very smooth, and partly coated by organic matter (see appendix II.1). Rarely authigenic minerals have overgrown the surface. The sample surface was analysed at four different magnifications (10x, 20x, 50x and 100x), (Appendix II.11). The quartz grain is approximately 756.79 μm in diameter. Measurements show a small hole on the grain surface, observed at 100x magnification, as shown in images d_1 , d_2 , and profile d_3 (Appendix II.11). The profile is concave, crossing through the hole. The roughness parameters are calculated for the entire surface that is visible at 10x magnification, as displayed in image a_1 (see table 4.3). The quartz surface is the unaltered, original surface. A hole on the surface in the right, image d_1 is probably formed due to struck in transportation or pre-existing in the source rock.

RL I_2111_Qu_2

The quartz grain is well rounded and sub-spherical as displayed in the 2-dimension and 3-dimension images. The profiles a_3 and b_3 show the regular curvature (Appendix II.12). The surface is drastically altered by cementation and overgrowth of authigenic minerals in the diagenetic processes, forming rough surfaces with a lot of high peaks and low valleys. This is clearly observed in images c_2 , d_2 and profiles c_3 and d_3 (Appendix II.12). The quartz grain is approximately 709.83 μm in diameter. The roughness parameters are calculated for the whole surface that is observed at low magnification (see table 4.3). The measurements show that this surface was altered, and overgrown with white cement, which covered the real surface as seen in the images c_2 , d_2 and the curved profile c_3 , d_3 with high peaks and deep valleys. The unaltered surface coating organic matter is of grey colour.

RL I_2111_Qu_3

The quartz surface is partly overgrown by cement minerals in white colour and covered by organic matter. The cement is composed of quartz and organic matter as verified by Raman spectra (Appendix II.3). In the upper left corner of image a_1 , appendix II.13, a non overgrown surface of the grain is visible. The quartz grain is roughly 564.83 μm in diameter (this is also the width of the grain measured in image a_1). The roughness parameters given in table 4.3 were calculated for the whole surfaces as seen in image a_1 . Furthermore, the grain surface roughness is shown by profiles at different magnifications (see profiles in appendix II.13).

RL I_2111_Qu_4

The quartz grain is well rounded and shows a spherical surface completely overgrown by cement minerals with white colour speckles and organic matter in dark grey colour (Appendix II.14). The quartz was identified by Raman spectra (Appendix II.4). The diameter of the grain is about 893.51 μm . The roughness parameters were calculated for the whole surface which was analysed at 10x magnification (Table 4.3). The cement minerals are of euhedral shape, as can be seen in the upper right and left image d₁, they form a rough surface. The surface with dark colour is covered with organic matter. It is also rough in the upper right corner of the image d₁. At 100x magnification the roughness of the quartz surface drastically changes as can be seen in the curved line segments in profile d₃. Both of the properties, overgrowth and organic matter increased the roughness of the grain surface. This is shown in the profiles c₃ and d₃ by the curved segments. In this case, the quartz surface roughness of the original quartz grain is mainly governed by cement mineral overgrowth due to the influence of diagenetic process.

In conclusion, the investigated quartz grains of sample RL I_2111 are commonly well rounded, spherical and sub-spherical in shape. The grain size ranges from 564.83 μm to 893.51 μm . The grain surface roughness is divers and changes from a smooth, unaltered surface (RL I_2111_Qu_1), to a rougher surface, a partly altered surfaces, to a completely altered surface, and to a very rough surface that was overgrown by cement minerals (RL I_2111_Qu_2), totally obliterating the original surface. The roughness of the quartz grains in the RL I_2111 sample is mainly due to the authigenic and cement mineral covering. The coatings are clearly illustrated by the 3D images, the profiles, and the values of the roughness parameters as shown in table 4.3.

The grain surface with the areas covered by authigenic and cement minerals is more complex as shown in profile c₃ and d₃ (Appendix II.12) with many the highest peaks and the lowest valleys. Whereas, the grain surface with the areas covered with organic matter is less change and smooth (Appendix II.12 and II.14). The quartz grain (RL I_2111_Qu_1 see Appendix II.11), with a hematite layer on its surface is less rough. In conclusion, the authigenic cement minerals, which were formed in the diagenetic processes, have an important influence on the characteristics of the surface roughness and thus on pore morphology.

4.2.1.2 Sample RL I_4146

Two quartz grains of sample RL I_4146 were identified by Raman spectroscopy (Appendix II.6 – II.7) and three quartz grains were analysed morphologically by CLSM (Appendix II.15-II.17). The quartz grains have distinct sub-spherical, elongated and round shapes. Their surfaces are partly altered by pressure dissolution and overgrown by cement minerals.

RL I_4146_Qu_1

The quartz grain is sub-angular and sub-spherical and the surface is completely coated by particulate carbon (black colour), as identified by Raman spectroscopy (Appendix II.6). The grain size is approximately 397.73 μm in diameter. The images display, that this surface is quite smooth; showing rarely peaks and valleys as given in the profiles a_3 , b_3 and d_3 (Appendix II.15). Authigenic minerals have rarely overgrown the surface, and with higher imaging magnifications white spots were identified. These are assigned to cement minerals with a size of 31.58 μm in width, as shown in the profiles c_2 and c_3 . However, this surface was probably dissolved in places due to compaction during diagenesis, as shown by concave convex areas in the 3D images: a_2 , b_2 and c_2 (Appendix II.15). The roughness parameters listed in table 4.3 were calculated for the whole surface that was observed at 10x magnification.

RL I_4146_Qu_2

The quartz grain is rounded and of elongated shape with the length of the grain being about twice the width. The surface is shiny and sometimes shows small holes (see appendix II.16). The grain size is roughly 316.25 μm in diameter. The measurements show valleys that were carved into the surface. Images c_1 and c_2 show several white spots which can be cement minerals with 27.15 μm in width overgrowing the surface. At higher magnifications also a sharp peak can be clearly seen (images d_2 and d_3). The roughness parameters were measured for the whole surface at the 10x magnification, as given in table 4.3.

RL I_4146_Qu_3

The quartz grain is rounded and of spheroidal shape, and stained by hematite and coated by organic matter, as determined by Raman spectral results (Appendix II.7). The surface of the grain is pale. The measurements show that the surface is rough with depressions which could have occurred at grain contact positions during compaction (Appendix II.17). A partly

overgrown surface with white colour, is probably composed of cement minerals (image c₂, d₂). The graphs in profiles c₃ and d₃ show vertices. The parameters are shown in table 4.3 representing the surface roughness analysed at 10x magnification. The dimension of the grain is approximately 417.06 µm in width. Comparing these results with the one of quartz grain RL I_4146_Qu_2, it can be observed that this grain is more round and spherical in shape but its surface is also rougher. Moreover, the grain surface shows much more alterations and is therefore interpreted as an obliterated partial surface with cement minerals. In this case, the roughness of the quartz surface is less influenced by overgrown cement minerals, but strongly affected by compaction.

In summary, the quartz grains of sample RL I_4146 are of sub-angular, rounded, sub-spheroidal, spheroidal and elongated shape and stained by hematite as well as coated by carbon and organic matter with dark colour. The surface of the grains is pale, brown colour. The quartz surfaces, that are not coated with cement minerals, have shiny and smooth surfaces sometimes with small holes. Probably, these quartz grains were transported a long distance and deposited far from the sources, and therefore show strongly abraded, impacted and dissolved surfaces.

The values of all roughness parameters are listed in table 4.3. The surface of the overgrown quartz in RL I_4146_Qu_3 sample is the roughest with the vertices and the maximum peak heights of R_p : 173.49 µm. Likewise, in the RL I_4146_Qu_3 sample, compressed quartz is present with the lowest valley with R_v : 204.62 µm. The size of these quartz grains in this sample ranges from 316.25 µm to 417.06 µm. These results lead to the following conclusions:

- The roughness of the grain surfaces is not dependent on the grain size and shape,
- The roughness is not only relative to the abrasion during transportation, but also due to the compaction packing of the grains during diagenesis and processes such as the growth of cement minerals, and pressure solutions.

4.2.1.3 Sample RL I_5041

Three grains of sample RL I_5041 were identified by Raman spectroscopy (Appendix II.8 – II.10). Four grains were imaged with CLSM at different magnifications and their topographies were investigated (Appendix II. 18-II.21).

RL I_5041_Qu_1

The quartz grain is round and sub-elongated and the surface is shiny, with no cement minerals covering the grain as determined by Raman analysis (Appendix II.8). The grain size is 535.83 μm in width and the surface shows tiny holes (Appendix II.18). The values of the calculated roughness parameters at 10x magnification, featuring the entire grain surface, are listed in table 4.3. Cement minerals have rarely overgrown the surface of the grain, and more strongly in the holes, as displayed in the profile in image c₃. This surface is smooth and has white spots (image d₂, profile d₃). At 50x magnification (image c₁), the non-overgrown surface is rough. This could evoke from the fact that the quartz grain was influenced by strong pressure solution at grain contacts.

RL I_5041_Qu_2

The quartz grain is round, of spheroidal shape and with a shiny surface. The composition of the grain was identified by Raman spectroscopy (Appendix II.9). The grain size is approximately 417.06 μm in width (Appendix II.19). The measurements show that partially the surface is rough with distinct vertices (profile a₃, b₃). At larger magnifications a white colour area is observed obliterated by the growth of cement minerals with 29.05 μm in diameter (in the right part of image d₁, and marked in yellow on profile d₃). The surface of the cement minerals is not flat, as shown by the valleys in the profile (profile d₃). The values of the surface roughness parameters are listed in table 4.3. On the non-overgrown surface small holes occurred. This may be regarded as the influence of grain to grain collision during transportation and abrasion on the grain surface during transportation (image a₁, b₁ and the profile a₃, b₃).

RL I_5041_Qu_3

The shape of the grain is sub-angular, sub-flat and its surface is pale, milky colour (Appendix II.20). The composition of the grain is unidentifiable by Raman spectroscopy because of fluorescence. However it has been tentatively identified as a feldspar with the help of binoculars. The grain size is approximately 517.88 μm in width (see profile a₃). The values for the roughness parameters are shown in table 4.3. The surface of the grain is flat, as illustrated in image a₂, b₂ and in the profile a₃, b₃. The profiles show horizontal lines with occasionally small peaks and valleys. This is also clearly observed at the larger magnification in the right part of images c₂ and d₂. Cement minerals have grown on the surface and has a

size of 10 μm in diameter (see profile c_3 , d_3). A part of the surface is slightly pitted, which could be due to abrasion during transportation.

RL I_5041_Qu_4

The quartz surface is indented and overgrown by cement minerals. They created an irregular surface, which was also coated by organic matter as identified by Raman spectra (Appendix II.21). The roughness measurements show that the white areas are rough and high, probably of cement minerals which masked the surface, while the brown colour areas (hematite) are low (depressions). The grain size is 476.65 μm , and the roughness parameters are shown in table 4.3. Comparing this grain with the above described quartz grains (RL I_5041_Qu_2 and RL I_5041_Qu_3) of the same sample RL I_5041, this quartz grain is drastically altered, due to the impact of compaction and cementation. The quartz grain is maybe cemented in the first phase and subsequently compacted in the following phases, in which the grains were re-arranged and tightened. The quartz was also dissolved at contacts, leading to the appearance of concave convex areas and to small holes (bottom of image b_2).

The analytical data and the thin section analysis show that the composition of the RL I_5041 sample is dominated by clastic quartz and subordinated other clastic grains, and feldspar with pale surfaces. The quartz surface is coated by organic matter. The shape of the grains is sub-angular-round, sub-flat, and sub-elongated. The grain size ranges from 417.06 to 535.83 μm , and their roughness parameters are given in table 4.3. The surfaces of the grains are commonly shiny and locally masked by cement and organic matter (RL I_5041_Qu_4). In general all grains have rough surfaces. The size of the cement minerals range from 10 to 30 μm as measured at the largest magnification (100x). The quartz grain surfaces were altered due to transportation and the diagenetic processes (pressure solution). Compared with the sample RL I_2111 and RL I_4146, this sample could have been more strongly affected by compaction than by cementation.

Additionally, many grains were taken from the three samples RL I_2111, RL I_4146 and RL I_5041 to determine the surface roughness. The roughness was calculated for 50x and 100x magnifications as shown by the root mean square roughness, R_q parameter in table 4.2.

Table 4.2 Root mean square roughness R_q calculated at 50x and 100x magnifications

Order	Sample	R_q (μm)		Sample	R_q (μm)		Sample	R_q (μm)	
		50x	100x		50x	100x		50x	100x
1	RL I_2111_1	5.48	2.02	RL I_4146_1	9.9	3.59	RL I_5041_1	9.46	6.12
2	RL I_2111_2	8.53	6.48	RL I_4146_2	5.83	1.87	RL I_5041_2	4.52	1.57
3	RL I_2111_3	5.97	2.52	RL I_4145_3	9.29	9.2	RL I_5041_3	8.22	3.06
4	RL I_2111_4	6.61	4.83				RL I_5041_4	10.09	3.23
5	RL I_2111_5	5.59	5.34				RL I_5041_5	6.83	1.61
6	RL I_2111_6	9.04	2.64				RL I_50441_6	5.22	2.31
7	RL I_2111_7	3.5	2.54				RL I_50441_7	13.02	6.38
8	RL I_2111_8	11.5	3.14				RL I_5041_8	8.72	3.76
9	RL I_2111_9	6.32	3.44						
10	RL I_2111_10	6.27	4.46						
11	RL I_2111_11	9.99	8.25						
12	RL I_2111_12	4.33	2.86						
13	RL I_2111_13	8.59	5.04						
14	RL I_2111_14	13.47	5.32						
15	RL I_2111_15	4.18	3.67						
16	RL I_2111_16	8.99	1.36						

The root mean square roughness R_q depends on the analysed area of the grain surface. At 50x magnification, corresponding to a relatively large observation area, the grain surface profile changes in a wide range leading to a large value of R_q . At 100x magnification (smaller observation area) the analysed surface area shows more details and finer features can be observed. The grain surface profile only varies slightly, hence leading to small R_q value. As shown in table 4.2, on the same analysed surface the root mean square R_q at 100x magnification is always smaller than that at 50x magnification for different observation areas. However, decreasing the analysed surface area by a factor of 2 does not decrease R_q by the same factor.

4.2.2 Pore space morphology

Although fluid flow through sedimentary rocks is directly related to the porosity, it depends critically on the geometry of the pore space such as pore connectivity, pore throat size distribution, tortuosity and pore shape as the investigation by Pape, 1999 has demonstrated. Permeability prediction is based on fine internal structure of pores as the growth of authigenic and cement minerals facing into pores leads to increased roughness of pore walls and pore spaces become narrower. Therefore, fluid flow through the pore spaces is largely inefficient.

The description of the pore structure of sedimentary rocks in this study is thus critical to evaluate the permeability.

The morphology of the pores of the investigated sandstone reservoir rocks was characterised by the size of the detrital grains, by the grain surfaces as well as by the presence of authigenic minerals. The primary pore morphology is modified by both, cementation and authigenic mineral growth in the pores and on the clastic grain surfaces. These form the roughness of the pores and complicate the pore morphology. The effect of the pore tortuosity as protrusions of crystal facets that reach into the pores (Figures 4.1; 4.3 and 4.5) leading to reducing pore spaces. Likewise, the pore throat radii of connecting pores are decreased or blocked, leading to pore isolation and a decreased fluid flow through pores in rocks (Figure 4.4).

The pore space of sample RL I_2111 was filled with precipitated authigenic mineral, as shown in figure 4.1. The mineral has subhedral shape pointing towards albite. Albite was also found in other samples and confirmed by EDX and SEM measurements and by thin section microscopy (Chapter 3). The surface of the albite is slightly altered, showing small inclusions (rectangles in figure 4.1A). The minerals surrounding the albite crystal are authigenic calcite cements and/or calcite inclusions (arrows and circle). The albite is displayed in the 3-D image of figure 4.1B.

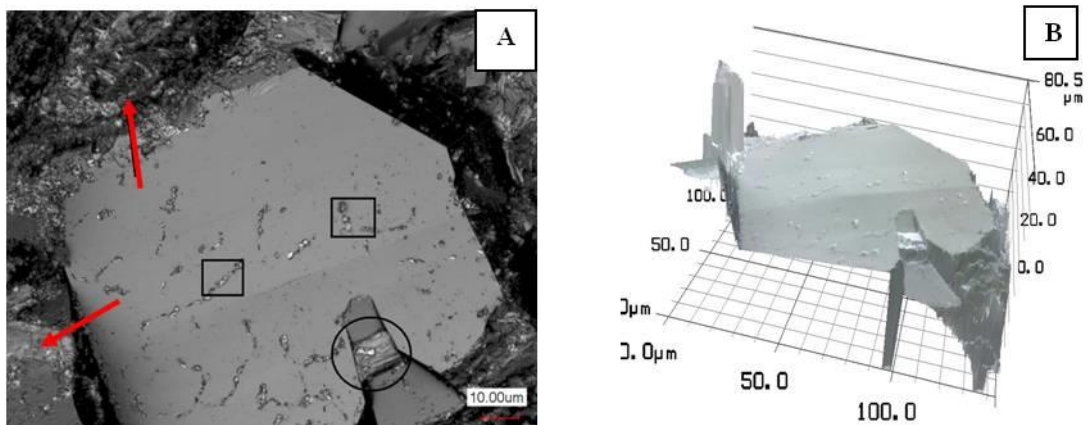


Figure 4.1 CLSM image (A) taken at 100x magnification showing an albite authigenic mineral grown in the pore space of sample RL I_2111. Image (B) shows the 3-dimensional reconstruction of the roughly 60 μm high albite mineral.

The observed pore network in sample RL I_4146, shown in figure 4.2, exhibits the pore geometry which was formed and altered due to the influence of diagenesis. As displayed, an open pore space is formed by rhombohedral packing, which occurs when detrital grains are re-arranged. They formed a triangular pore space (pore, figure 4.2A) and a connection to the

neighbouring pores by a pore throat as shown by the arrow in figure 4.2A. Subsequently, the precipitation of calcite cement filled the pores. The calcite cleavage planes are visible in the centre of figure 4.2A and its surface roughness is displayed by the line profile in figure 4.2B. The profile is quite rough with the presence of many high sharp peaks and deep valleys. In figure 4.3 another pore is shown, which was drastically altered due to the growth of different authigenic minerals and the dissolution of minerals (Figure 4.3A). Albite blades, as indicated by the arrow, are visible. In the centre of the pore needle-shaped crystals of illite (circle) grow into the pore space and overgrow the clastic grain. Some of the needles seem also to have grown from the altered feldspar surface (rectangle). Partially this feldspar was dissolved, forming intragranular micro pores. The profile in figure 4.3B shows the ruggedness of the pore space morphology. Likewise, the pore throats were also altered and narrowed by overgrowth as shown in figures 4.2 and 4.3. In figure 4.4 the pore throat of sample RL I_4146 is blocked by a cement filling (arrow). The filling caused the isolation of the pores, the formation of closed pore spaces, and a reduction of the permeability of the rocks (see table 3.1, chapter 3). In addition, the grain surface displays pockets or casts that probably result from collisions with other grains during transportation or from dissolution during compaction (line mark, Figure 4.4). In the diagenetic stage authigenic minerals (circle, Figure 4.4) grew on this surface, which modified the original grain roughness and resulted in rough pore walls.

Abrasion and dissolution of grains by different mechanisms during transport and diagenesis has been investigated in detail by Kempe et al., 2004; Kempe et al., 2005. The studies show the discrimination of erosion due to aeolian and aquatic transport mechanisms in sedimentary paleoenvironments or due to bioerosion. The grain morphology and pore geometry of sandstone have been studied by Altermann et al., 2011. The work reveals a change of grain surfaces and pore shapes due to diagenetic alterations.

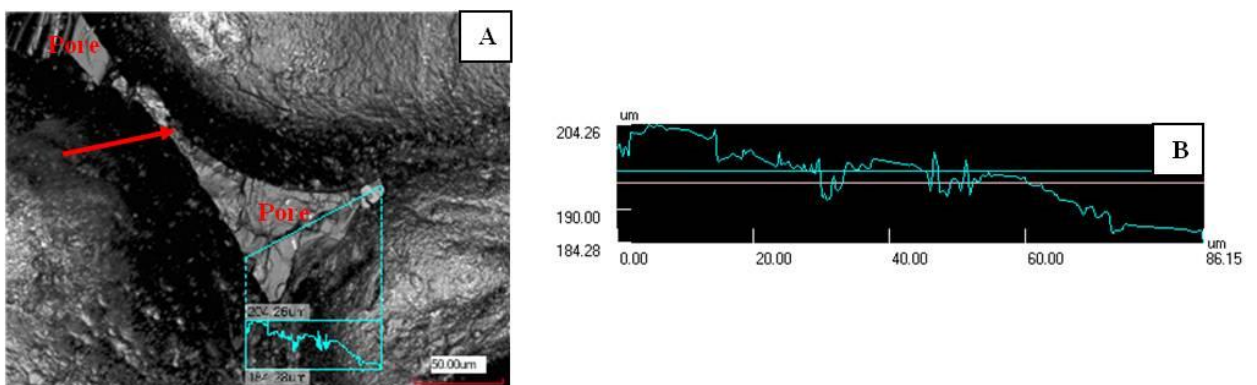


Figure 4.2 CLSM image showing the structure of a pore, taken at 50x magnification. Image (A) shows a

triangular shaped pore space which was formed between three detrital grains. A pore throat, indicated by the arrow, is the connection to a neighbouring pore. Image (B) displays the topography of the pore ground.

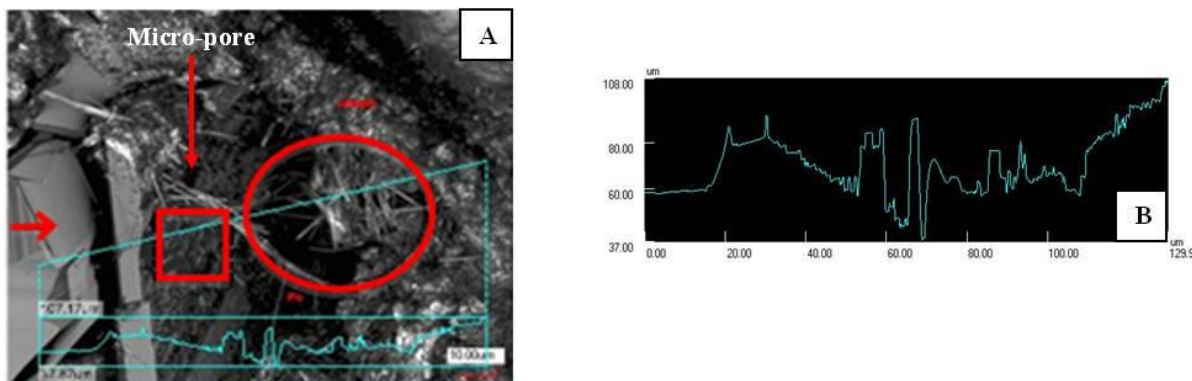


Figure 4.3 CLSM image of authigenic minerals grown in pores. Image (A) taken at 100x magnification shows albite blades (indicated by arrows) and needle-shaped crystals of illite (indicated by the circle), which have grown in the pore space. Image (B) shows the corresponding surface roughness within the pore.



Figure 4.4 Grain surface and pore throat of sample RL I_4146 imaged by CLSM at 50x magnification. The surface of the grain is sculptured by micro-pits (line mark) and overgrown by authigenic minerals (circle). The pore throat is blocked by cement filling (arrow).

The sample RL I_5041 had the highest porosity (15%) out of the three investigated samples. Most of the pores seemed to be connected by pore paths, as demonstrated in petrography analysis (see chapter 3). The pore body and pore throats of this sample are shown in the 3-D reconstruction in figure 4.5. In figure 4.5A the structure of a pore space forms the boundary between the grains (G). Some visible apparent illite barriers inside the pore divide the pore space into many micro pores, constructing micro-walls and increasing the contact surfaces. The authigenic illite mineral was attested with SEM (Figure 4.5C and D) and by EDX (Figure 4.5E). The profile in figure 4.5B displays the roughness of the pore surface and one of the illite barriers with 17 μm width. The marked illite barrier partly blocks the flow ability of fluids. The permeability is primarily associated with the porosity, pore sizes and their connectivity. In this sample the pore throats connected the open pores between two grain

surfaces, which were rather smooth and the pore path width was about 20 μm , as seen in figure 4.6. Thus the potential possible flow of fluids through the pores was much better than in the other samples (see figure 4.4).

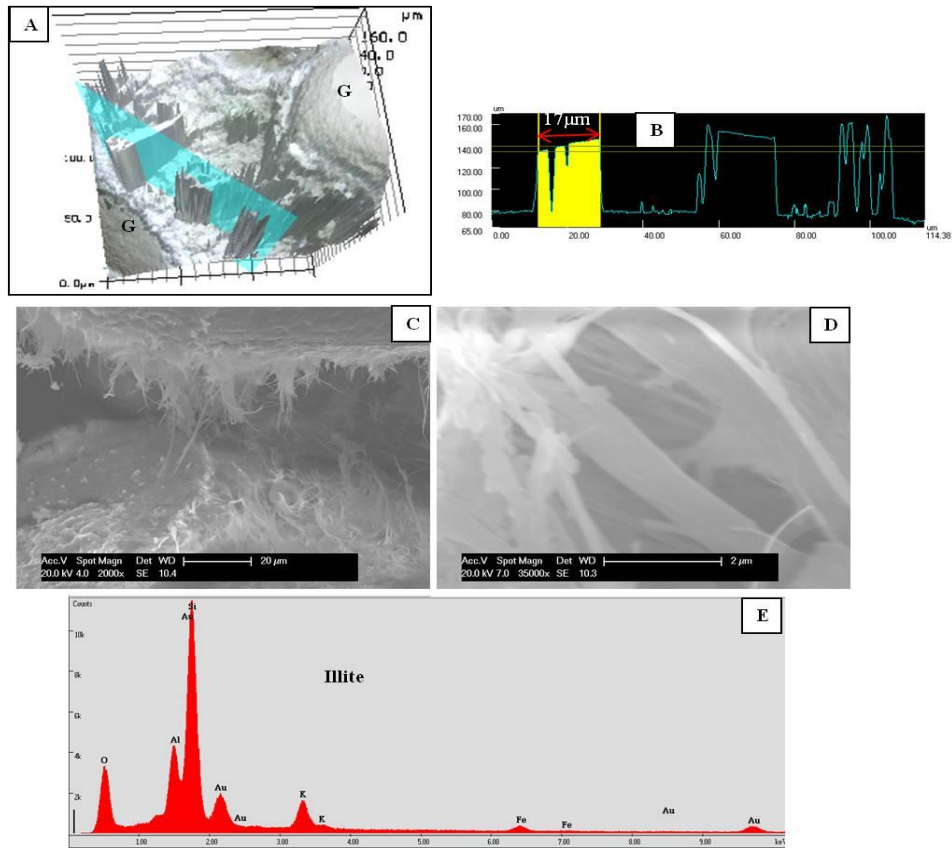


Figure 4.5 CLSM image showing a pore structure in 3-D (A) and the roughness profile (B) of the pore surface. Images C and D are SEM photographs which display fibrous illites growing into the pore and coating the grain surface. In image (E) the corresponding EDX spectrum is shown indicating the presence of illite.

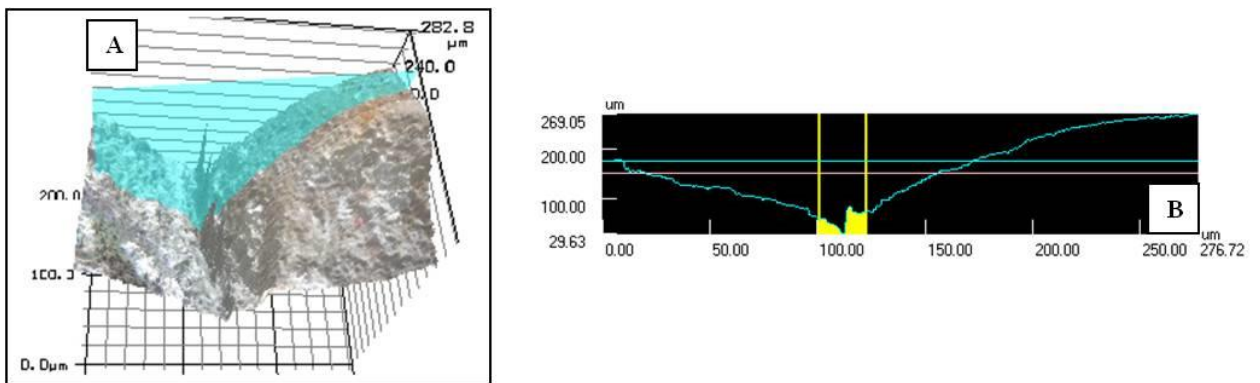


Figure 4.6 Three-dimensional CLSM image (A) and its profile (B) of a pore throat.

In summary, the pore characteristics of the investigated sandstone reservoir rocks are associated firstly, with the packing of detrital grains; and secondly, with the alteration of the pore geometry through diagenetic processes, which are the most relevant for a potential fluid

flow. This is demonstrated by the various pore spaces that are filled by cements and authigenic minerals e.g. in sample RL I_2111, of figure 4.1A. Similarly, in samples RL I_4146 and RL I_5041 of figure 4.3 and figure 4.5 respectively, the pores are partly cemented by calcite and overgrown by illite and albite, probably representing the first stage of diagenesis. The pores and pore throats are filled by cement and authigenic minerals that form the rough pore structure and lead to a decrease of the effective porosity and permeability of the sandstone reservoir rocks (see figures 4.1; 4.3). Below the 4910 m depth, with decreasing amount of cementation (see chapter 3), the pore space is less filled by cement and some illite minerals crystallised in pores during burial diagenesis (see figures 4.5 and 4.6). The pore geometry is subdivided by such illite crystallites into smaller compartments but is not fully blocked.

4.3 CONCLUSION

In the analysed sandstone samples, the major component is quartz (see chapter 3). The quartz grain surface topography widely changes during the diagenesis as the analysis of surfaces of RL I_2111 grains shows. The grains are completely covered by cement minerals, and RL I_4146 grains are both, coated with cement and slightly compacted. In case of RL I_5041 the grains show strong compaction characteristics and are overgrown with cement minerals. Thus in the RL I well, the roughness of the sandstone grains is not similar and varies a lot. The characteristics of the grain surfaces are expressed by the parameters which are listed for each whole grain investigated at 10x magnification in table 4.3.

A comparison of these parameters, which were measured at the same magnification, analytic conditions and filter process for each grain, was carried out. It shows that the RL I_2111 sample has the largest overview values, the highest peaks with R_p : 162.80 to 225.79 μm , the lowest valleys with R_v : 268.23 to 440.95 μm , the maximum height of R_z : 666.74 μm , the average height of the grain roughness R_a : 90.11 μm , the root mean square height R_q : 67.85 to 111.37 μm , the kurtosis R_{ku} : 3.81 and the asymmetry of height distribution R_{sk} : -0.87. The grain surfaces of the RL I_2111 sample are very rough with very high peaks and low valleys while the RL I_4146 and RL I_5041 samples show values of roughness parameters with, in general, slightly smaller values, and fewer deviations (Table 4.3). However, the R_{ku} parameter of RL I_5041 is larger than of RL I_2111, which means that the RL I_5041 grains have more sharp peaks. Since in the lower/depressed areas cement minerals have grown more frequently, the roughness characteristics of the grains in the RL I_5041 sample show higher irregularities

than the grains in the RL I_2111 sample. The parameters also show that the roughness characteristics of the investigated grains are independent from the grain size and shape, but significantly related to the real/original surface, the overgrowth of cement minerals, and to the kind of authigenic minerals. All these parameters in table 4.3 show the grain surface characteristics, which are the highest peak, lowest valley, maximum height and the roughness.

Table 4.3 Values of roughness parameters_Rotliegend RL I well, at 10x magnification

Sample	R_p (μm)	R_v (μm)	R_z (μm)	R_a (μm)	R_q (μm)	R_{sk}	R_{ku}
RL I_2111_Qu_1	225.79	440.95	666.74	90.11	111.37	-0.75	3.05
RL I_2111_Qu_2	180.70	352.13	532.83	70.43	85.23	-0.56	2.57
RL I_2111_Qu_3	168.29	268.23	436.52	69.82	89.38	-0.87	3.71
RL I_2111_Qu_4	162.80	278.83	441.63	53.28	67.85	-1.15	3.81
RL I_4146_Qu_1	109.46	185.89	295.35	46.44	55.64	-0.30	2.53
RL I_4146_Qu_2	108.46	192.48	300.94	38.13	46.66	-0.7109	3.2423
RL I_4146_Qu_3	173.49	204.62	378.10	60.96	72.23	-0.44	2.35
RL I_5041_Qu_1	136.96	286.70	423.66	47.40	59.80	-1.1384	4.1821
RL I_5041_Qu_2	173.48	204.62	378.10	60.96	72.23	-0.44	2.35
RL I_5041_Qu_3	110.65	200.65	311.30	34.82	46.92	-1.42	5.79
RL I_5041_Qu_4	159.64	246.59	406.23	63.09	76.16	-0.77	2.67

As given in table 4.2, the grain surface roughness was determined at 50x and 100x magnifications. At 50x magnification the grain surfaces of sample RL I_2111 have larger R_q values than those of sample RL I_4146 and RL I_5041, which show the smallest values. The pore surfaces of sample RL I_2111 are rougher. At 50x and 100x magnifications, the R_q values of the grain surface roughness of sample RL I_5041 are the smallest, thus the pore surfaces are the smoothest and so the permeability of this sample is the highest (Table 3.1, Chapter 3). On the contrary, the samples RL I_2111 and RL I_4146 show larger R_q values, therefore more rough pore surfaces and hence less permeability is present in this sample as shown in the table 3.1, chapter 3. The grain roughness is not the only criterion to restrict the permeability of sandstone rock but is a factor reducing the permeability. The permeability of rock depends on the connection of pores together.

A comparison of the root mean square roughness (R_q) values and permeability analysis values with fractal dimension D values derived from Small Angle Neutron Scattering experiments (Drobek et al., 2011) are in good agreements. The fractal dimension D is a description on self-similarity of an object having exactly or approximately similar in appearance of fractal geometry under different magnifications to a part of itself (Mandelbrot, 1967) and is an index

characterising complicated geometric forms. The index is 1 for sets describing lines; 2 for sets describing surfaces and 3 for sets describing volumes (3-dimensional objects having length, width, and height). This publication shows values of D ranging from 2.2 up to 3, for the samples RL I_5041, RL I_4146 and RL I_2111. The grain surfaces of the sample RL I_2111 with a D value close to 3 have a more complex structure than those of the samples RL I_4146 and RL I_5041 with D values lower than 3. A low R_q corresponds to a decreased D with an increased porosity and permeability. The higher permeability (RL I_5041) implies a higher fluid flow through the rocks compared to samples (RL I_2111 and RL I_4146) with the lower permeability. The pore spaces in sample RL I_2111 are completely filled by cements while in samples RL I_4146 and RL I_5041 the pores are partly cemented by quartz, calcite and overgrown by illite and albite. The pore throats of sample RL I_5041 are less constricted, enabling a higher fluid flow through the pore spaces compared to a more restricted flow in the samples RL I_2111 and 4146.

5. ROUGHNESS OF AUTHIGENIC MINERAL SURFACES OF SANDSTONE RESERVOIR ROCKS FROM A WELL IN THE NORTH GERMAN BASIN

The grain surface roughness is a characteristic of the texture of a grain surface. It is defined by the vertical deviations from the horizontal imaginable average level line of a grain surface (Chapter 4). The variations in the height of a grain surface determine the degree of irregularities of a grain surface (Cai et al., 2010). The surface is rough if large height deviations occur or smooth if small deviations appear on the same horizontal distance. The grain roughness depends on the grain surface coating that is the degree of the authigenic mineral crystallisation during the diagenesis (Chapter 3). The grain surface roughness affects the properties of a grain surface like the contact area between the grain surface and hydrocarbon fluid and the surface wettability which can be wetting or non-wetting.

Many investigations have demonstrated roughness effects on grain surface properties. Wetting phenomena were studied by Good et al., 1952; Hazlett, 1992. The rough surface in general, is wetted more rapidly than the smooth one. The interfaces between the grain surface and liquid were investigated by Butt et al., 2003 based on Young's equation (Young, 1805), to study the influences of surface roughness in regard to the intensity of surface energy and wetting action. Such in a measured unit area, a rough surface shows higher surface energy than in the same measured unit area on a smooth surface. In rock hydrocarbon reservoirs, the characterisation of the grain surface roughness is revealed as the contact area, the adhesion of hydrocarbon on the grain surfaces and impacts the permeability of rocks.

The studies by Blunt, 1998; Taylor et al., 2006 characterised the effects of surface roughness on fluid flow through the pores. The flow is constricted due to decreasing flow diameter caused by surface roughness. As a consequence the surface area is increased which leads to a higher adhesion with the fluid. These characterisations are extremely important for the petroleum industries in order to improve oil recovery and estimate the adhesion of hydrocarbon on the grain surface.

The herein investigated sandstone reservoir rocks are composed predominantly of quartz, subordinate feldspar and lithic fragments, as shown in chapter 3. The global form of grains was revealed by roughness parameters and 3-D reconstruction in chapter 4. The grain roughness and the fine grain surface structure that is formed by the authigenic minerals are

not observed with CLSM analysis because the minerals are tiny, with nanometre size. Thus, the individual grain roughness analysis was carried out downing to nanometre size, with AFM and combined with SEM. The analytic results reveal the roughness of the investigated authigenic minerals, for individual grain and for each sample.

5.1 METHODS

With CLSM analysis (Chapter 4) the features of the grain roughness are shown at micrometre size, so the roughness of the grain surface which is formed by authigenic mineral coatings with smaller than micrometre size cannot be recognised.

Therefore, the roughness of the authigenic mineral surfaces and the pore space morphology of the samples were investigated with Atomic Force microscopy (AFM, Dimension Icon Scanning Probe Microscope) at the nanometre size. Images with resolutions from a few micrometres down to nanometres were taken. Experiments on various samples with different surface roughness were conducted on individual grains and grain groups.

The analysis of the surface roughness was carried out by operating the Atomic Force microscope in tapping mode, in air. Silicon cantilevers (PPP-ZEHR) with a length of 225 μm , a width of 57 μm , a thickness of 5 μm , a resonance frequency of 130 kHz, a force constant of 27 N/m, and a tip radius smaller than 10 nm were used. Images were taken at a free oscillation amplitude of the cantilever $A_{\text{free}} \sim 55$ nm and a relative amplitude set point ratio of $A_{\text{sp}}/A_{\text{free}} \sim 0.8$. Image processing of the 256 x 256 pixel comprising data was carried out using Nanoscope Analysis 1.2 (Veeco, USA). The resolution and image size chosen depend on the surface roughness of each grain, therefore the scale is not similar for all grains of the specimens. The surface roughness is expressed by the R_q parameter as defined in equation (4.2, Chapter 4).

A second-order polynomial plane correction was used to remove the tilt and bow of the surface and to eliminate unwanted features from scan lines (e.g. noise, bow and tilt), which appear as horizontal shifts or stripes in the image, caused during scanning. Subsequently the flattening operation was used to level the mean plane with the zero height. The root mean square (R_q) surface roughness parameter was calculated for all images for an area size of 1 μm x 1 μm and a scan rate of 0.1 Hz.

Additionally, some areas were measured with varying area sizes ranging from 850 nm to 5 μm in order to image authigenic mineral structures, which are overlain on the original grain surfaces.

Finally, the authigenic mineral features that caused the roughness of the grain surfaces and cement surfaces at an area size of 1 μm x 1 μm , were examined morphologically with the scanning electron microscopy (SEM) and an element analysis was carried out by an Energy dispersive X-ray system (EDX). The SEM and EDX analytic method is described in chapter 3.

5.2 ANALYTIC RESULTS

The analysis of the sandstone reservoir rocks with the AFM and SEM revealed authigenic mineral surface characteristics and pore topographies at the nanometre size. The AFM results are displayed in height images with the height scale shown as a colour bar on the right side of the image, as 3D images and by the root mean square roughness (R_q) parameter of sample RL I_2111 (Table 5.1 – 5.3), sample RL I_4146 (Table 5.4 – 5.6) and sample RL I_5041 (Table 5.7 – 5.9). The SEM and EDX results show the authigenic mineral morphology and its element spectra.

5.2.1 Sample RL I_2111

Four quartz grains RL I_2111_Qu_1, RL I_2111_Qu_2, RL I_2111_Qu_3 and RL I_2111_Qu_4 were analysed by AFM and SEM measurements according to their investigations with the confocal Raman microscope and the CLSM. The samples (RL I_2111_A to RL I_2111_E) were only analysed with AFM and SEM.

RL I_2111_Qu_1

On the quartz grain, five spots (Figure 5.1) were analysed with the AFM. Images with a scan size of 1 μm x 1 μm , as marked by the numbers I to IV (Figure 5.1), were taken. The area of number V (Figure 5.1) was imaged with a scan size of 5 μm . The authigenic mineral composition of the quartz surface was verified with SEM and EDX corresponding to AFM measurements from points I to IV (Figure 5.2).

The quartz surface is heterogeneous and rough as seen at the nanometre scale. The roughness is due to the growth of authigenic minerals which have blade, nodule (Images Ia, IIa and IIIa in figure 5.1), flower-like (Image IVa, figure 5.1) and sub-rhomboidal and square shapes

(Image Va, figure 5.1). Similar detailed structures could not be observed at the micrometre scale as measured by CLSM (Chapter 4). In image Ia the height of the quartz surface varies from 0 nm to 57.7 nm and authigenic minerals with blade-like shape are visible in the lower right corner. In image IIa and image IIIa the quartz surface seems to be composed of a pellet-blade aggregation. In image IVa the rough quartz face is rather inhomogeneous and the height difference is quite distinct, widely ranging from 0 nm up to 126 nm. Corresponding to the AFM images measured at points I to IV (Figure 5.1), the authigenic minerals, which cover the grain surface are illite-chlorite, as identified by their morphology and EDX spectra (Figure 5.2). In image Va (Figure 5.1) the quartz surface is however, overgrown by authigenic minerals with sub-rhomboidal and square shapes. The surface seems to be less rough compared to the area in image IVa. One of the authigenic minerals has a dimension from 1 μm to 1.2 μm , as marked in image Va. The quartz surface roughness is displayed by the root mean square roughness (R_q) calculated for the measured surface areas of 1 μm x 1 μm scan size. For images Ia to IVa (Figure 5.1) the corresponding R_q values are 7.01 nm; 10.5 nm; 15 nm and 16.3 nm (Table 5.1).

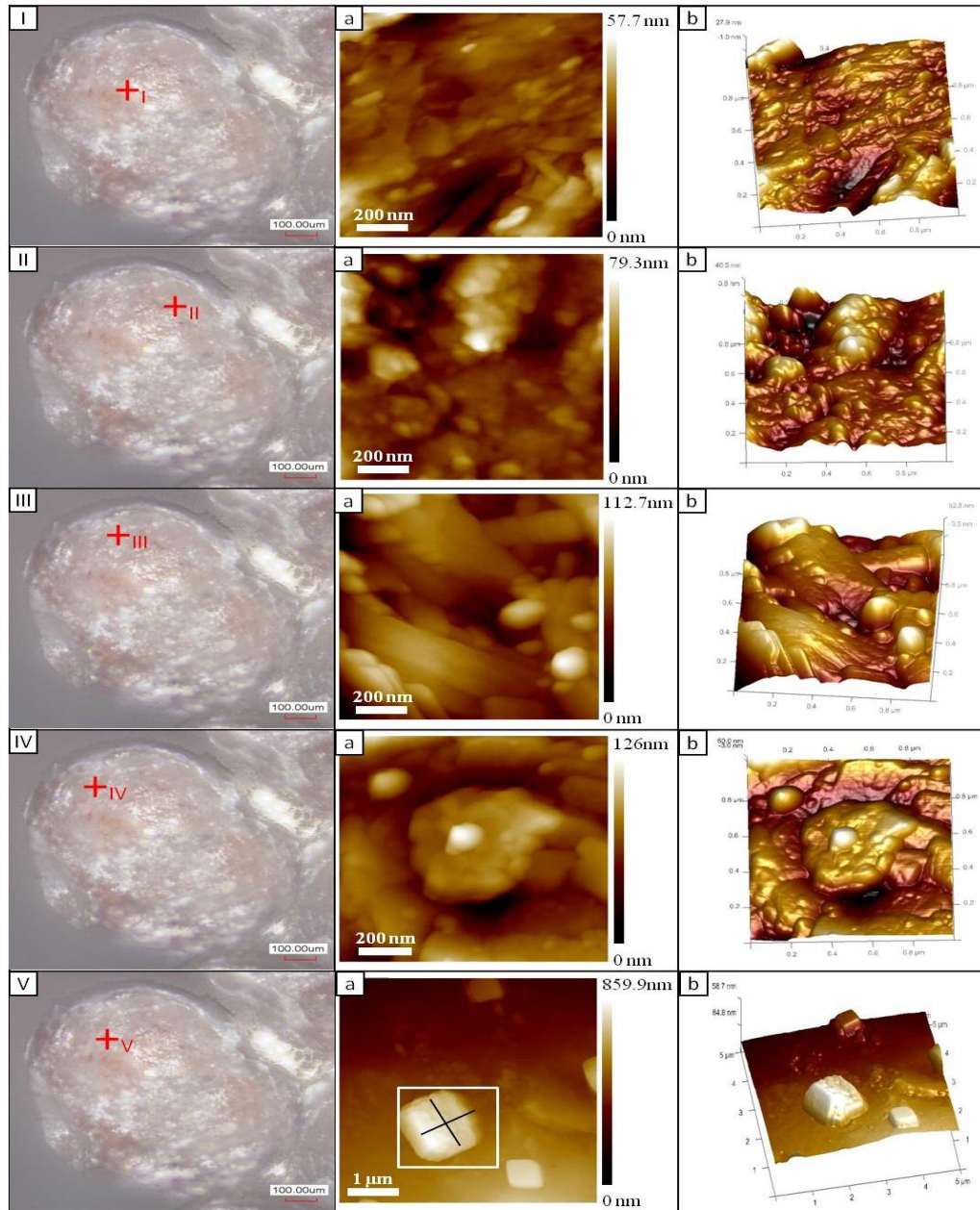


Figure 5.1 Sample RL I_2111_Qu_1, CLSM and AFM images. CLSM images show an overview of the quartz surface at 10x magnification. The red crosshairs mark the spots where AFM and SEM measurements were taken. Images Ia - IVa show the corresponding AFM images taken with a scan size of 1 μm x 1 μm. Image Va is imaged with a scan size of 5 μm x 5 μm. Images Ib – Vb are the corresponding 3D illustrations.

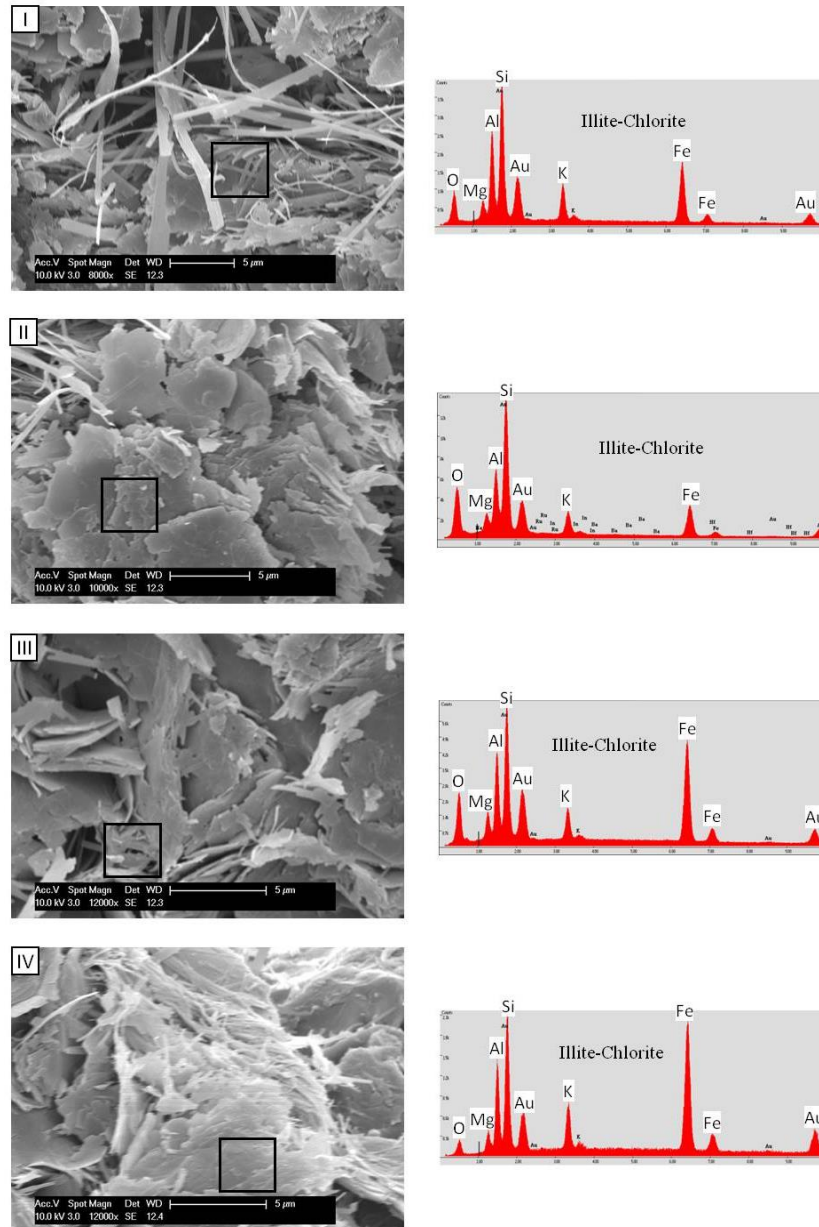


Figure 5.2 Sample RL I_2111_Qu_1. SEM images show the authigenic mineral morphology corresponding to the positions I to IV of the AFM measurements. Illite-chlorite in ribbons, thin filaments, and in euhedral shape, coats the quartz surface and forms micro pores. The minerals are distinguished by EDX spectra taken at the box areas.

RL I_2111_Qu_2

The quartz surface was imaged with the AFM at five different points, at scan sizes ranging from 850 nm to 1 µm. The R_q roughness parameter was only calculated for the surfaces with the same scan size of 1 µm x 1 µm (Images Ia to IVa in figure 5.3). Also the mineral morphology and element analysis with SEM and EDX (Figure 5.4) of the corresponding surface was only carried out at areas with 1 µm x 1 µm scan size. For point V, the image Va

(Figure 5.3) shows a smaller scanned surface with the grain surface overlain by authigenic minerals with different morphologies.

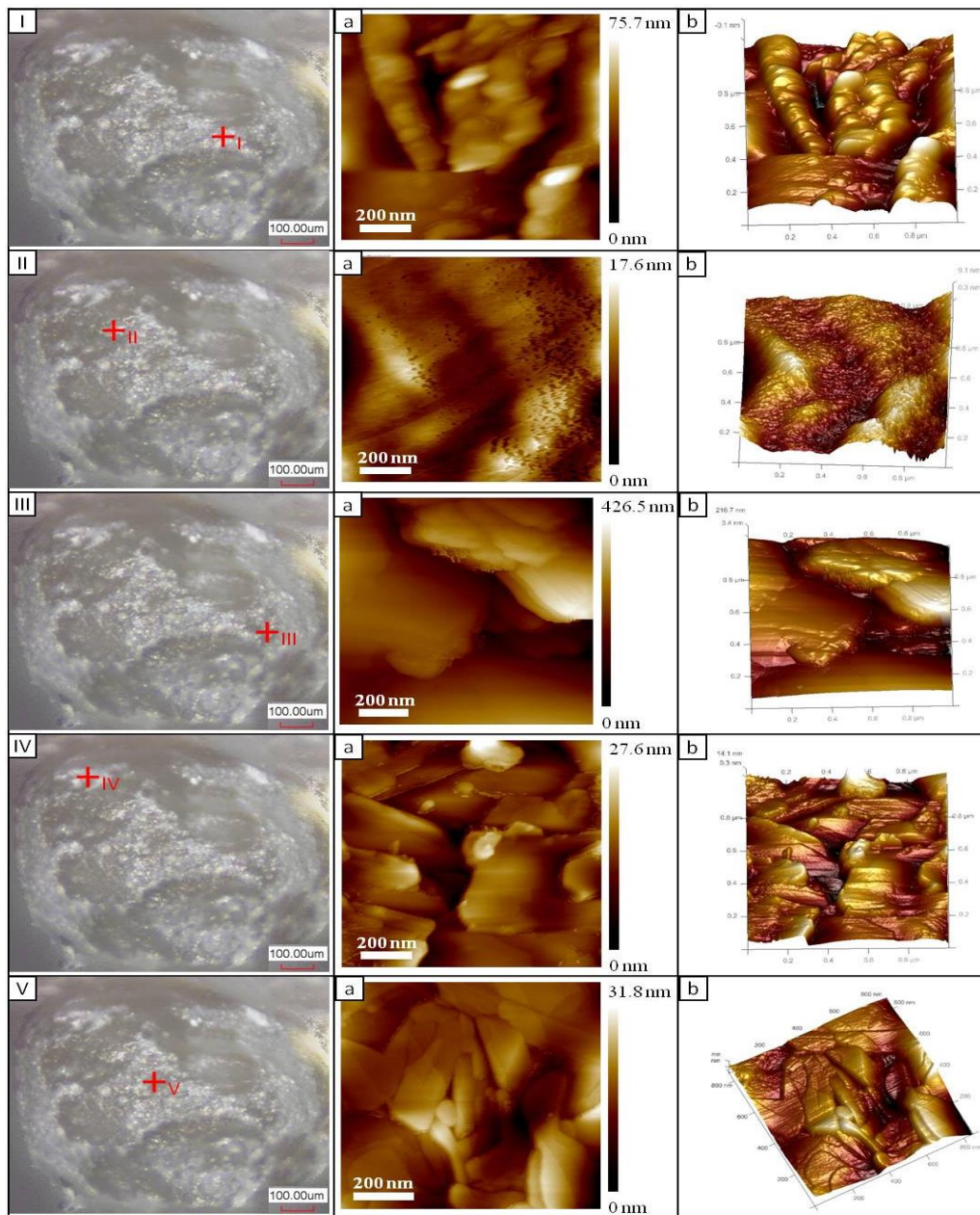


Figure 5.3 Sample RL I_2111_Qu_2. An overview image of the quartz surface was taken with CLSM. The marked spots are analysed with AFM and SEM. Images Ia – IVa show the quartz surface analysed with AFM at $1 \mu\text{m} \times 1 \mu\text{m}$ scan size and image Va the surface imaged with a scan size of 850 nm. Images Ib – Vb display the corresponding quartz surface in 3D.

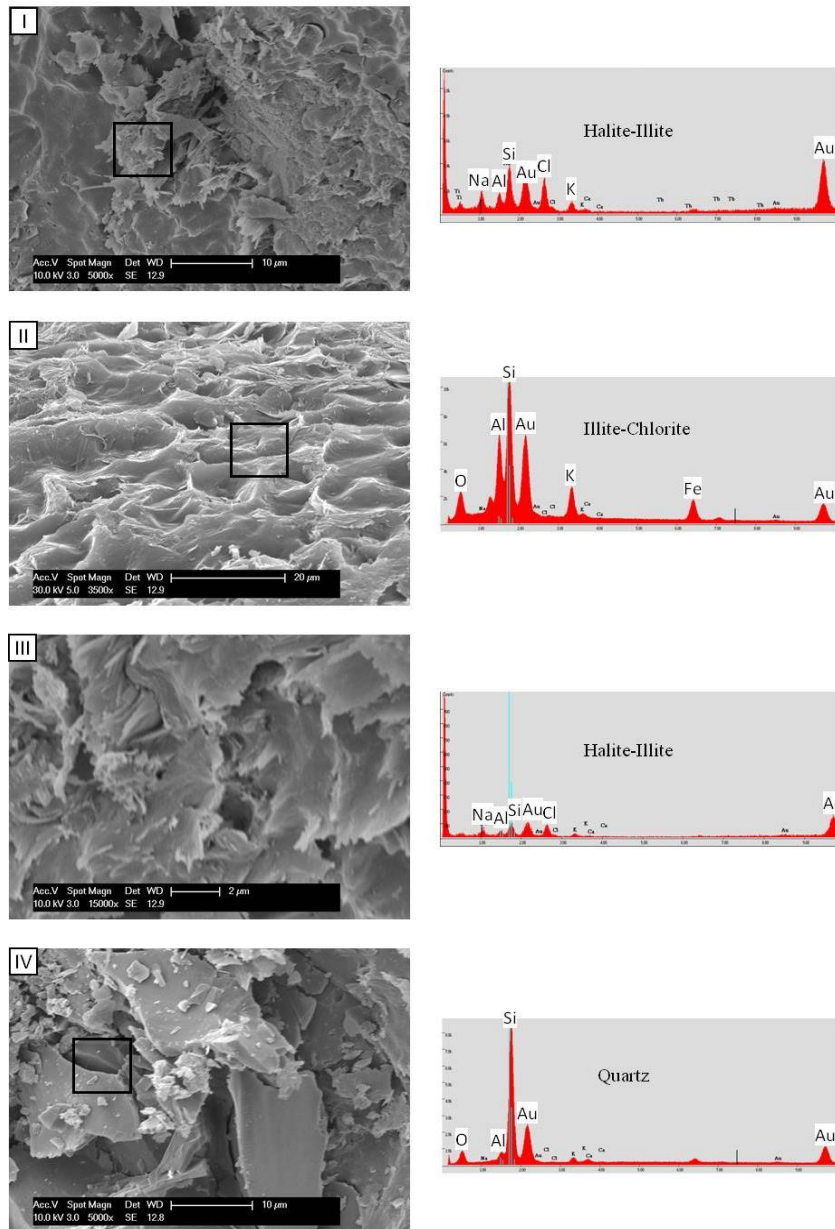


Figure 5.4 Sample RL I_2111_Qu_2. SEM images show that authigenic minerals are halite-illite, illite-chlorite and quartz, which overgrow the original quartz face at points I to IV (analogous to the AFM analysed surfaces from images Ia to IVa). EDX spectra represent the whole area of image III and the marked box in images I, II, IV.

As the CLSM image (Figure 5.3) of the quartz grain shows, the areas with dark colours are commonly at lower positions than those with bright colours. AFM measurements could not be taken from the darker areas, because it was not possible to reach into the valleys with the AFM tip, without touching the surface of the grain with the AFM head before. Therefore, the AFM results only display the elevated quartz surfaces with bright colours. All measured AFM spots show that the roughness of the quartz surface is quite diverse (Table 5.1). The quartz surface is covered by authigenic minerals with many various shapes, as shown in images Ia,

IIIa, IVa, and Va (Figure 5.3). However, at point II (Image IIa, Figure 5.3) the quartz surface has numerous micro pores. As proved in SEM images and EDX spectra, the quartz surface is overlain by halite-illite, illite-chlorite and authigenic quartz at the spots I, II, III and IV (Figure 5.4). The R_q values calculated at these points from I to IV (Figure 5.3), are 10.5 nm, 2.42 nm, 61.5 nm and 40.4 nm. The quartz surface has its roughest at point III and shows the lowest roughness at point II.

RL I_2111_Qu_3

On this quartz grain four spots were analysed with AFM and SEM as marked by the numbers I to IV in the CLSM image (see appendix III.1). Each area scanned had a scan size of $1 \mu\text{m} \times 1 \mu\text{m}$. The SEM images show the mineral morphology and its element spectra (see appendix III.2).

The overview image of the quartz grain, taken with the CLSM at 10x magnification (Appendix III.1), shows that the quartz surface is probably fractured and covered by hematite, in brown colour (see also chapter 4). The AFM measurements were taken at areas with different colours: brown and white. The result of the AFM analysis show that there is a difference in roughness at all measured points on the quartz face. At point I and II (Images Ia and IIa in appendix III.1) the areas seem to represent an authigenic mineral accumulation like an arrangement of tilted booklets and inter booklets in its gaps. At these points the vertical height is 183.9 nm and 208.3 nm. On the other hand, at point III and IV, the roughness of the quartz surface is governed by rounded pellets as seen in images IIIa and IVa (Appendix III.1). The surface of the pellets is rough as shown in the corresponding 3-image IIIb (Appendix III.1) and a groove is surrounding the pellets in image IVb (Appendix III.1). The quartz surface roughness given by the root mean square value (R_q) at points I and III is 21.2 nm and 21.3 nm respectively. The R_q value is extremely large at point II with 29.3 nm and the smallest at point IV with 3.62 nm (Table 5.1). At points I and III, the quartz surface is covered by illite-chlorite, while points II and IV are a quartz surface which was not overgrown, as identified by SEM and EDX (Appendix III.2).

RL I_2111_Qu_4

The quartz surface is heterogeneous in colour with dark and bright areas. Five areas were measured with AFM and SEM. Each point had the same scan size of $1 \mu\text{m} \times 1 \mu\text{m}$ (see

appendix III.3). The root mean square roughness parameters calculated illustrate the quartz surface roughness at the analysed AFM and SEM areas.

An overview image of the quartz grain taken with the CLSM at 10x magnification is shown in appendix III.3. The quartz surface is dark and bright in colour, similar to the quartz grain RL I_2111_Qu_2 (Figure 5.3). The AFM results show that the quartz surface is non-uniform, varying from a flat smooth surface (Image IIa, appendix III.3) to a flat surface with many small pores (Image IVa, appendix III.3) and to rough surfaces (Images Ia, IIIa and Va in appendix III.3). The mineral covering the quartz surface of samples RL I_2111_Qu_4 (Appendix III.3) and RL I_2111_Qu_2 (Figure 5.3) has morphological similarities to the images Ia (see appendix III.3) and IIIa (Figure 5.3). It shows illite-chlorite with layered structures as analysed with EDX spectra. At points II and III the minerals are illite and at points I, IV and V are illite-chlorite (see appendix III.4). The root mean square roughness parameters are calculated at points I to V with R_q : 47.4 nm, 6.73 nm, 26.2 nm, 3.55 nm and 23.4 nm, respectively (Table 5.1).

RL I_2111_A

On the quartz grain, three points (see figure 5.5) were analysed with AFM and SEM. The AFM measurement was limited to 1 μm x 1 μm scan size. The R_q roughness parameter was calculated for all images.

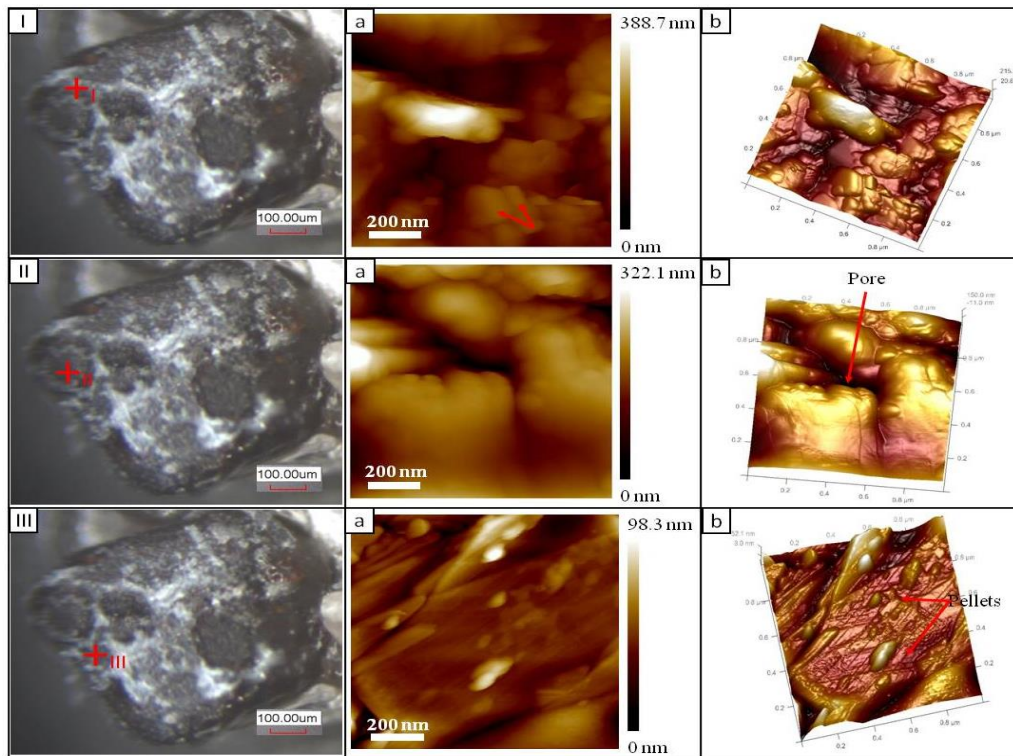


Figure 5.5 Sample RL I_2111_A. Overview CLSM image showing the grain surface at 10x magnification with the crosshairs labelling the spots that were subsequently analysed by AFM and SEM. AFM images show the roughness of the quartz surface in images Ia – IIIa. The corresponding 3D illustrations are shown in images Ib – IIIb.

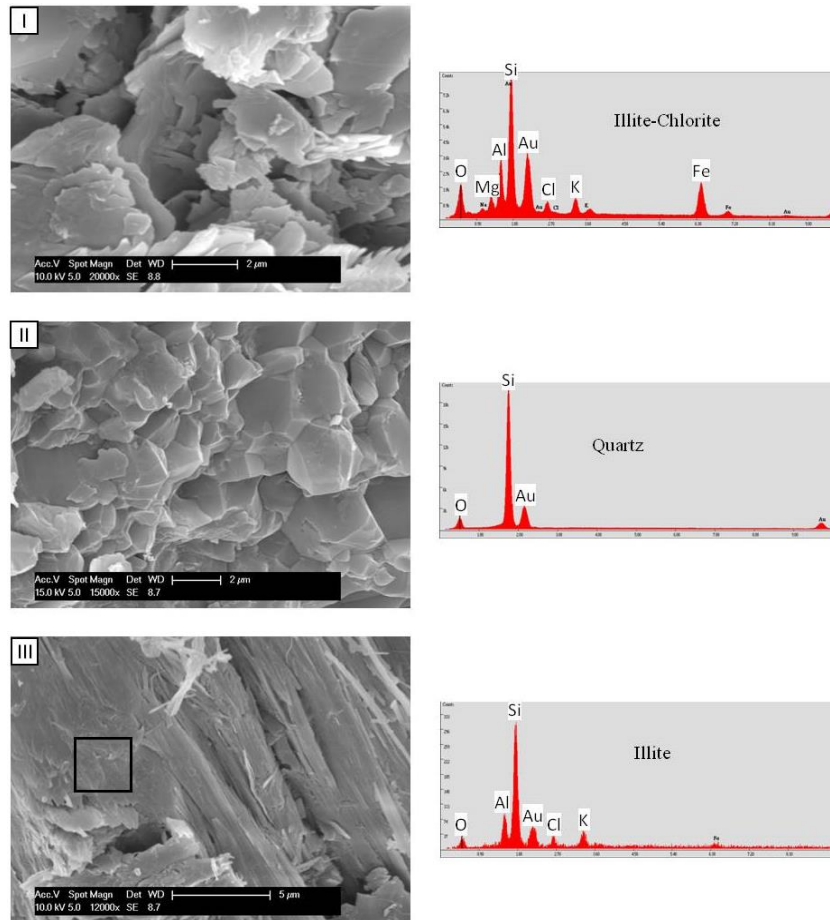


Figure 5.6 Sample RL I_2111_A. SEM images show that illite-chlorite with thin plates, authigenic quartz with crystals and illite with filaments overlay the quartz surface at spots I to III. EDX spectra are taken for the entire image areas at position I, II and the marked rectangle in image III.

The AFM images of the sample RL I_2111_A show the partial grain surface, as marked in figure 5.5. The grain surface differs at the measured areas as shown in the AFM images. At point I (Figure 5.5) the rough surface is composed of illite-chlorite minerals with euhedral shapes (arrow marks in image Ia, figure 5.5), as displayed by morphology in image I and the EDX spectrum (Figure 5.6). At point II the grain surface is overgrown by well developed euhedral quartz with clear crystal shape in image II (Figure 5.6), forming micro pore (Image IIb, figure 5.5). Point III features a flat surface, covered with a filamentous illite mat (Image III, figure 5.6), which is sometimes overgrown by authigenic minerals with rounded pellets as pointed out by the arrows in image IIIb (Figure 5.5). The R_q values calculated at point I, II and III are 52.09 nm, 44.1 nm and 11.8 nm, respectively (Table 5.1).

RL I_2111_B

A grain group contains individual grains and cements (Appendix III.5). The surface roughness measurement with AFM and the authigenic mineral determination with SEM were taken on the grain surface at point I and on the cement surfaces at points II – VI (Appendix III.5).

The AFM measurements were taken of the grain surface at point I and of the cement surfaces at points II to VI (Appendix III.5). The scan size was limited to 1 μm x 1 μm . At point I the grain surface is covered by thin flakes as indicated by an arrow in image Ia (Appendix III.5). The flakes are authigenic illite ribbons as shown by morphological and spectral analysis in image I (Appendix III.6). The cement surfaces are heterogeneous as shown in the AFM images IIa – VIa (Appendix III.5), but they have clearly visible different shapes. At points II and IV they show minerals with blade shapes. Additionally, the cement surfaces are quite rough with the presence of pores and striations, as pointed out by the arrows in images IIIa, Va and VIa (Appendix III.5). As analysed with SEM and supported by EDX spectra, the results show that the diagenetic minerals are illite-chlorite at points II, IV, anhydrite at points III, V and halite at point VI (Appendix III.6 and III.7). The R_q parameters were calculated at all areas separately. The corresponding values are 13.1 nm (Table 5.1), 37.8 nm, 28.4 nm, 22 nm, 20.7 nm and 40.5 nm (Table 5.2) for points II to VI.

RL I_2111_C

On this sandstone sub sample, four points marked (Appendix III.8) including grain and cement surfaces were imaged with the AFM. Each spot measured had a scan size of 1 μm x 1 μm . SEM analysis was also carried out on the corresponding AFM areas.

The AFM results show that the grain surface is rather flat at point I (Appendix III.8) but it is not uniform due to the presence of low and high terrains (arrows in image Ia, appendix III.8). At this point, the grain surface is covered by calcite (see image I and spectrum in appendix III.9). At point II the grain surface is overlain by illite-chlorite with sharp structures as shown in the SEM image II in appendix III.9.

The cement surfaces are not similar in structure because they are formed by authigenic minerals with various shapes. This can be seen by the authigenic mineral structures displayed in the AFM images IIIa and IVa (Appendix III.8). The minerals are illite-chlorite as analysed with the SEM and EDX (Images III, IV in appendix III.9). At points I and II, the R_q values are

89 nm and 23.8 nm (Table 5.1) and on the cement surfaces at points III and IV the corresponding R_q values are 75 nm and 68 nm (Table 5.2).

RL I_2111_D

On this grain group, two areas were investigated with the AFM and the SEM, as marked (see appendix III.10). The analysed areas were cement surfaces and scan sizes of $1\ \mu\text{m} \times 1\ \mu\text{m}$ were evaluated. The SEM analysis (see appendix III.11) was taken at the same points as the AFM images.

AFM images reveal that the cement surfaces are quite rough and have a number of micro pores, as pointed out by arrows (Image Ia, appendix III.10). The cement minerals are formed by illite-chlorite authigenic minerals with ribbons and multi-thin flakes with sub euhedral shape. At point I, these minerals have ribbon-like and fibrous shapes and layered flakes (Image Ia, appendix III.10 and image I, appendix III.11). In image IIa (appendix III.10) they are layered euhedral crystals (arrow) as also visible in the morphology image II in appendix III.11. The corresponding root mean square roughness values are 32 nm and 40 nm (Table 5.2).

RL I_2111_E

On the sample RL I_2111_E, four different spots with scan sizes of $1\ \mu\text{m} \times 1\ \mu\text{m}$ were examined with the AFM (Appendix III.12). The root mean square roughness parameters of the cement surfaces were calculated for the analysed areas separately (Table 5.2). The authigenic minerals that form a cement layer were identified by morphology and chemical element analysis with SEM and EDX (Appendix III.13).

The overview image of the sample was taken with the binocular at 5x magnification (Appendix III.12) and shows that the cement surfaces are composed of authigenic quartz and illite-chlorite minerals as verified by the SEM and EDX spectra (Appendix III.13). They look like pellets (arrows, image IIb in appendix III.12) and have similar shapes to those observed in the AFM images IIa, IIIa and IVa (Appendix III.12). At point I however, the cement surface is formed by authigenic minerals with multi layered structures as indicated by the arrow in image Ia (Appendix III.12). The corresponding SEM and the element spectrum analysis reveal that the minerals are a mixture of illite and chlorite with shapes of filaments and euhedral crystals. Therefore the roughness of the cement surface in point I is very high

with the largest R_q value of 134 nm, compared to the R_q values at points II - IV of 16.5 nm, 27.7 nm, and 8 nm (Table 5.2).

Interpretation

For sample RL I_2111 AFM and SEM measurements were taken on 9 sub samples at several points, including single grains and grain groups. On the grain surfaces 23 different areas and on the cement surfaces 13 points with 1 μm x 1 μm scan size were analysed. The root mean square roughness (R_q) values of the grain surface and cement surface were only calculated for scan sizes of 1 μm x 1 μm to compare the distinct surface roughness for all the AFM measurements. The root mean square roughness (R_q) average values were calculated for each grain surface, for the common authigenic minerals which are illite-chlorite and illite, and authigenic quartz covering on the grain surface and for the whole sample. The R_q average values are shown in table 5.3. The calcite, halite and anhydrite authigenic minerals are less common in this sample and therefore their R_q mean values are less accurate.

The various morphologies of illite-chlorite are clearly visible in ribbon, filament, plate, platelet, and euhedral structures. The illite-chlorite complexes arrange themselves in pore spaces and on grain surfaces. They are oriented as plates forming parallel layers (Image Ia, appendix III.1 and image IIa, appendix III.10), piled platelets and plates (Image II, figure 5.2 and image I, figure 5.6), ribbon mats (Image Ia, appendix III.11), intersected ribbons (Image III, figure 5.2) and mixtures of chaotic platelets creating micro to nano pores (Image I, appendix III.13). These arrangements cause a diverse range of roughness values. The R_q value of sample RL I_2111_Qu_2, at point II for example (Image IIa, figure 5.3) is 2.42 nm, but 134 nm for the sample RL I_2111_E at point I (Image Ia, appendix III.12). The R_q average value of illite-chlorite, which covers the grain surface, is 22.9 nm (Table 5.3).

Authigenic illite shows interweaved filaments (Image III, figure 5.6) and ribbons (Images II and III appendix III.4) like a mat coating the grain surface. It resembles fewer pores on the coating. The R_q values therefore change slightly from 6.73 nm to 26.2 nm. The R_q average value of illite, which covers the grain surface, is 13.78 nm (Table 5.3).

In some areas, halite precipitates on illite. Illite shows plate-like structures with fringed edges (Images I and III, figure 5.4). The halite is only identified by EDX spectra in images I and III (Figure 5.4). At these points, the R_q values change from 10.5 nm (Image Ia, figure 5.3) to 61.5

nm (Image IIIa, figure 5.3). The root mean square roughness (R_q) values of the surface vary less than those of illite-chlorite.

For calcite and anhydrite, authigenic minerals are less common such as in the sample RL I_2111. They only exist occasionally in some areas as shown in the AFM and SEM results. The anhydrite surface is smooth with occurrence of numerous micro pores and striations, as can be seen in images IIIa and Va (Appendix III.5). The roughness of anhydrite is low with the calculated R_q values varying from 20.7 nm to 28.4 nm. In contrast to anhydrite, the roughness of calcite is quite high with a R_q value of 89 nm due to its laminated rough surface (see in images Ia, appendix III.8 and I, appendix III.9).

The surface roughness values of authigenic quartz and original quartz without covering authigenic minerals surfaces differ distinctly. The authigenic quartz is less common than illite-chlorite and illite. Its roughness depends on the crystallised quartz degree. The authigenic quartz is well developed as euhedral quartz with crystal shapes (Image II, figure 5.6). The crystal assembly creates a rough coating on the grain surface while the authigenic quartz, covered with pellets (Image II to image IV, appendix III.13), is less rough. The R_q values strongly differ from 16.5 nm (Image IIa, appendix III.12) to 44.1 nm (Image IIa, figure 5.5) at a mean value of 42.25 nm. The real quartz surface roughness with its micro pores is affected by erosion (see images II and IV, figure 5.4). At point II (Figure 5.3), the real quartz surface is heavily eroded compared to that at point IV, so the R_q values are quite large at this point. The calculated R_q values are 29.3 nm and 3.62 nm. The roughness of all the authigenic and cement surfaces is evidenced by the root mean square roughness (R_q) parameter (Table 5.1 and 5.2).

The AFM and SEM analysis of the grain surfaces, points out that the illite-chlorite and illite authigenic minerals, covering the grain surfaces, are quite widespread and frequent in occurrence. The authigenic quartz with high roughness is less widespread, therefore the main minerals forming the sample roughness are illite-chlorite and illite. The illite-chlorite shows higher roughness than illite, as given by the R_q average values. The chlorite is hardly detectable in this sample at the various measurement points. The R_q average value of the sample RL I_2111 is 26.70 nm (see in table 5.3).

Table 5.1 Root mean square roughness (R_q) values of mineral coatings on grain surfaces with 1 μm scan size, sample RL I_2111

Order	Sample	Name	Figure/ Appendix	Image	Root mean square (R_q) (nm)	Height scale (nm)		Mineral
						Min	Max	
1	RL I_2111	RL I_2111_Qu_1	5.1	Ia	7.01	0	57.7	illite-chlorite
2				IIa	10.5	0	79.3	illite-chlorite
3				IIIa	15	0	112.7	illite-chlorite
4				IVa	16.3	0	126	illite-chlorite
5		RL I_2111_Qu_2	5.3	Ia	10.5	0	75.7	halite-illite
6				IIa	2.42	0	17.6	illite-chlorite
7				IIIa	61.5	0	426.5	halite-illite
8				IVa	40.4	0	27.6	authigenic quartz
9		RL I_2111_Qu_3	III.1	Ia	21.2	0	183.9	illite-chlorite
10				IIa	29.3	0	208.3	quartz
11				IIIa	21.3	0	145.7	illite-chlorite
12				IVa	3.62	0	282.7	quartz
13		RL I_2111_Qu_4	III.3	Ia	47.4	0	419.4	illite-chlorite
14				IIa	6.73	0	73.4	illite
15				IIIa	26.2	0	173.9	illite
16				IVa	3.55	0	25.6	illite-chlorite
17				Va	23.4	0	159.9	illite-chlorite
18		RL I_2111_A	5.5	Ia	52.9	0	388.7	illite-chlorite
19				IIa	44.1	0	322.1	authigenic quartz
20				IIIa	11.8	0	98.3	illite
21		RL I_2111_B	III.5	Ia	13.1	0	98.5	illite
22		RL I_2111_C	III.8	Ia	89	0	680.7	calcite
23				IIa	23.8	0	163.9	illite-chlorite

Table 5.2 Root mean square roughness (R_q) values of cement surfaces with 1 μm scan size, for sample RL I_2111

Order	Sample	Name	Figure/ Appendix	Image	Root mean square (R_q) (nm)	Height scale (nm)		Mineral
						Min	Max	
1	RL I_2111	RL I_2111_B	III.5	IIa	37.8	0	276.7	illite-chlorite
2				IIIa	28.4	0	252.8	anhydrite
3				IVa	22	0	219	illite-chlorite
4				Va	20.7	0	158.2	anhydrite
5				VIa	44.5	0	303	halite
6		RL I_2111_C	III.8	IIIa	75	0	357.4	illite-chlorite
7				IVa	68	0	442.3	illite-chlorite
8		RL I_2111_D	III.10	Ia	32	0	157.7	illite-chlorite
9				IIa	40	0	271.9	illite-chlorite
10		RL I_2111_E	III.12	Ia	134	0	888.6	illite-chlorite
11				IIa	16.5	0	123.1	authigenic quartz
12				IIIa	27.7	0	223.9	authigenic quartz
13				IVa	18	0	98.3	authigenic quartz

Table 5.3 Root mean square roughness (R_q) average values of grain surfaces with 1 μm scan size, sample RL I_2111

Name	Root mean square roughness (R_q) (nm) average values					
	grain	sample	illite-chlorite	illite	chlorite	authigenic quartz
RL I_Qu_1	12.2	26.70	22.9	13.78	no data	42.25
RL I_Qu_2	28.7					
RL I_Qu_3	18.85					
RL I_Qu_4	21.45					
RL I_Qu_A	36.26					
RL I_Qu_B	13.1					
RL I_Qu_C	56.4					

5.2.2 Sample RL I_4146

Two grains RL I_4146_Qu_1 and RL I_4146_Qu_2, of sample RL I_4146 were analysed with AFM, SEM and EDX to investigate the grain surface roughness, to locate authigenic minerals and to compare these results to those of CLSM analysis. Additionally, five samples, (RL I_4146_A to RL I_4146_E) including individual grains and grain groups were examined with AFM, SEM and EDX to identify the grain, cement and authigenic mineral surface roughness, which covers the grain surfaces and forms the cements.

RL_4146_Qu_1

On the quartz grain, six spots with numbers I to VI (Figure 5.7) were analysed with the AFM at a scan size of 1 μm x 1 μm , and with SEM and EDX. The roughness of the quartz surface was calculated for all analysed spots separately and illustrated by the root mean square R_q roughness parameter (Table 5.4).

According to the CLSM results, the quartz surface is smooth with concave areas and probably intended, where grain surfaces are dissolved. It is not covered by cement. The nanometre scale AFM measurements of the spots (see figure 5.7) show that the quartz surface is covered by authigenic minerals with various shapes. These minerals were not observed at the micrometre scale in the previous CLSM analysis.

The quartz surface is heterogeneous (see images Ia – VIa, figure 5.7). It is overgrown by illite authigenic mineral at spots I and IV, as identified by SEM and the EDX spectra in figure 5.8 and 5.9. The minerals are lath assemblages, with euhedral shape as marked by the arrows in images Ia, and IVa (Figure 5.7). At point III calcite with euhedral crystal flakes, deposits on the illite surface can be found (see image IIIa, figure 5.7 and image III, figure 5.8). In image VIa the quartz surface looks like a fibrous shaped lattice. Along these fibers and at intersecting areas, pores appear (arrows, image VIa, figure 5.7). At these areas, illite-chlorite, in ribbons, is overlaying the quartz surface (see image VIa, figure 5.7). At points II and V, in the lower part of image Va, the quartz surface is smooth. The upper part of image Va shows rough quartz in pellets. The quartz surface has a varying roughness, which is illustrated by the R_q values 9.44 nm, 17.3 nm, 12 nm, 20.1 nm, 70 nm and 38.3 nm corresponding to points I to VI (Table 5.4).

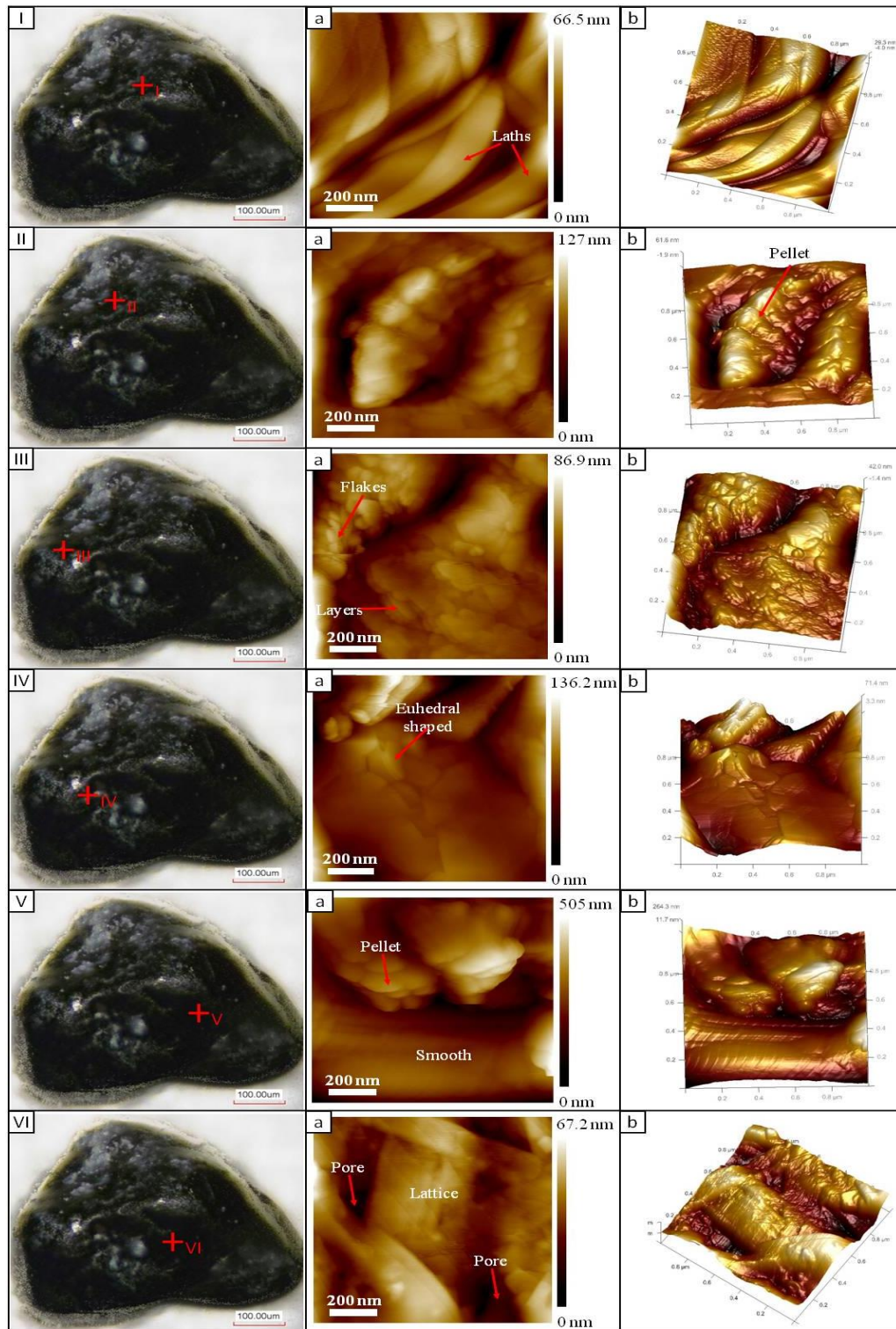


Figure 5.7 Sample RL_4146_Qu_1. The CLSM images show an overview picture of the quartz surface at 20x magnification. Crosshairs I to VI mark the areas where AFM measurements were taken. Images Ia – VIa are the corresponding AFM images of the quartz surface. Images Ib- VIb are 3D illustrations, respectively.

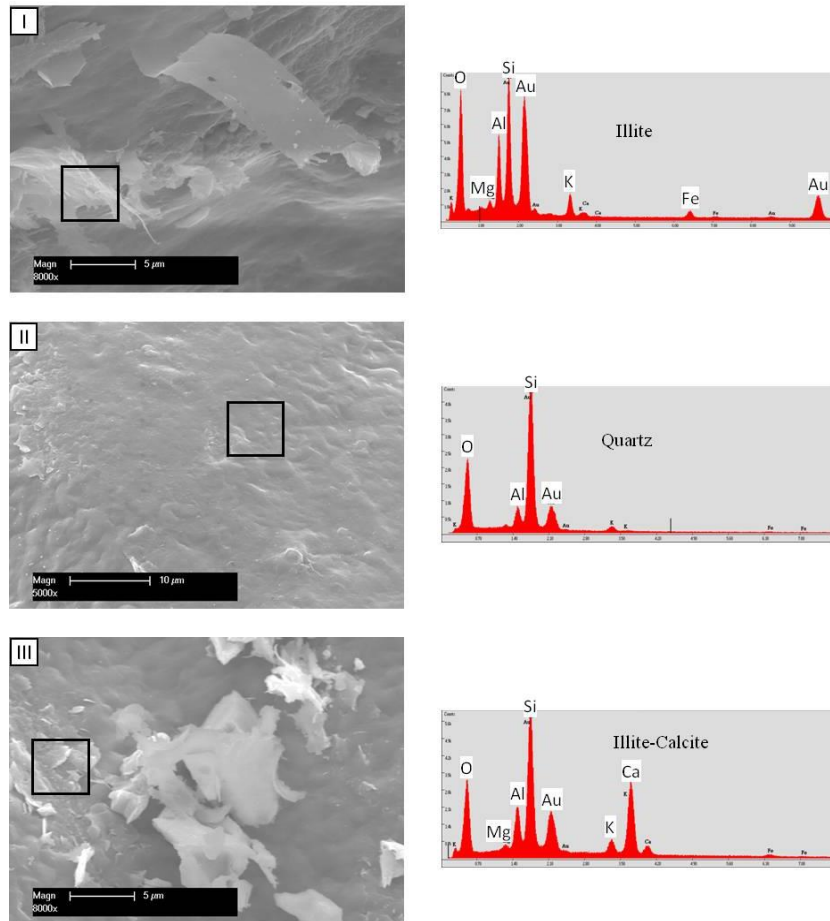


Figure 5.8 Sample RL_4146_Qu_1. SEM images and EDX spectra of sample positions I to III. The quartz grain surface is overgrown by authigenic minerals: illite, calcite precipitated on illite at points I and III and non-overgrown quartz surface at point II. The minerals were detected with EDX within the marked rectangles (images I – III).

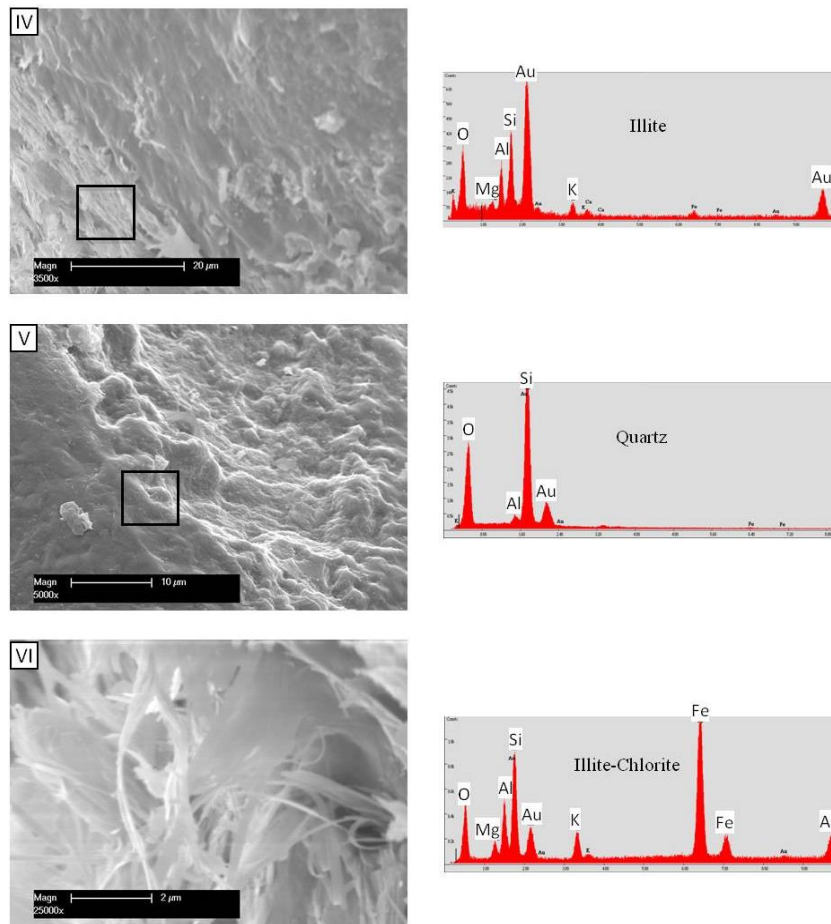


Figure 5.9 Sample RL_4146_Qu_1. SEM images and element spectra of sample positions IV to VI. The quartz grain surface is overgrown by authigenic minerals: illite and illite-chlorite at points VI and IV. The quartz surface is uncovered at point V. The minerals were detected with EDX within the marked rectangles (images IV and V). In image VI the entire image area was analysed.

RL_4146_Qu_3

On the quartz grain RL_4146_Qu_3 AFM measurements were taken at six spots with a scan size of $1\ \mu\text{m} \times 1\ \mu\text{m}$, as indicated by the crosshairs I to VI (Appendix III.14). SEM images and EDX spectra (Appendix III.15 and 16) were taken at the corresponding AFM areas. The root mean square roughness parameter was calculated at each measured area separately (Table 5.4).

In the CLSM overview image (Appendix III.14) the quartz grain was imaged with 20x magnification. The quartz surface is probably stained by hematite (CLSM image) with brown colour and has many hollow areas that could represent dissolved grain contact areas. The AFM measurements show the different quartz topographies at the various measured points. At points I, II and V (Images Ia, IIa and Va, appendix III.14) the quartz surface features a concave area with the height difference changing approximately from 17.5 nm to 338.4 nm, as

shown in the height images Ia, IIa and Va. In images IIIa, IVa, and VIa (Appendix III.14) the quartz surface is covered by authigenic and/or cement minerals. They show higher roughness and more micro pores. The minerals have shapes such as: pellets (see image IIIa), multi-blade (Image IVa) and polygons with around 300 nm in diameter as marked in image VIa. SEM and EDX analysis (Appendix III.15 and 16) show that for all examined points, the quartz surface is entirely covered by an illite layer. Illite roughness is calculated and represented by the root mean square parameter (R_q) which results in 34.9 nm, 2.24 nm, 12.5 nm, 27.2 nm, 10.5 nm and 39.4 nm at the positions I to VI (Appendix III.14) respectively. The quartz surface is relatively smooth at point II with the smallest R_q value, while at the other analysed points the quartz surface is rougher with R_q values larger than 10 nm due to overgrowth of different authigenic minerals with complicate morphologies.

RL I_4146_A

The quartz grain RL I_4146_A was analysed with the AFM at four areas with a scan size of $1 \mu\text{m} \times 1 \mu\text{m}$, as marked with numbers I to IV in appendix III.17. The roughness is represented by the R_q value which was calculated for each analysed area (Table 5.4). SEM and EDX analysis (Appendix III.18) were conducted at the same areas.

The results of the AFM analysis at four points show that the quartz grain surface is rather smooth in the right part of image IIa (Appendix III.17) and concave at the left side. At this point and at point I, the quartz face is not overgrown (see images I and II, appendix III.18). However, at the other analysed points the quartz surface is very rough, covered with authigenic minerals. At points III and IV the quartz surface is coated by a thin layer of illite and illite-chlorite authigenic minerals. They have different shapes, e.g. also laths and euhedral shaped (Images IIIa and IVa). The areas I – IV are analysed with SEM and EDX (Appendix III.18). Illite and illite-chlorite with ribbons and euhedral shaped coat the quartz surface at points III and IV. That signifies that the quartz surface is heterogeneous at the analysed areas, which is also represented by the R_q values I to IV. The R_q values are calculated to: 16.8 nm, 23.3 nm, 14.9 nm and 24.6 nm respectively. Comparing the roughness at all the measured spots of this grain surface, it reveals that the surface is very rough at points II and IV and less rough at points I and III (Table 5.4).

RL I_4146_B

Sample RL I_4146_B represents a medium sandstone sample. The sandstone is often larger than 0.5 mm in grain size. AFM and SEM analyses were carried out on the grain surfaces at three points from I – III and on the cement surface at point IV (Appendix III.19). AFM measurements were limited to a scan size of 1 μm x 1 μm . The roughness of the grain and cement faces was determined by the R_q values represented in table 5.4 and 5.5.

As can be seen in appendix III.19 the areas I to III are coated by hematite (brown colour) and the analysed area IV is composed of cement (white colour). As observed at point I the grain surface shows low and high terraces. At this point the quartz surface is not overgrown, while at points II and III the surface is overgrown by authigenic minerals. The minerals are illite and illite-chlorite as determined by morphology and EDX analysis in appendix III.20. They look like nodules or needles (arrows in images IIa and IIIa, appendix III.19). Their surface roughness is determined by their R_q value: 10.5 nm, 10 nm and 4.46 nm at points I to III. The roughness parameter calculated at the cement surface has a R_q value of 51 nm.

RL I_4146_C

The sample was scanned with the AFM with a 1 μm x 1 μm scan size at four different areas. Points I to III are on the grain surfaces and point IV is on the cement surface. Authigenic minerals which covered the grain surfaces and formed cement are recognised by morphology (SEM) and chemical element analysis (EDX). The roughness of the measured surfaces is calculated and listed in table 5.4 and 5.5.

As shown in the CLSM image (appendix III.21), the grain surface roughness is verified at three different areas, marked I to III. The AFM images Ia – IIIa show mineral structures with visible shapes: nodule (see arrows in images Ib and IIa) and thin blade shaped. One of them is approximately 250 nm in width as revealed from image IIa. In image IVa the cement surface is also formed by the authigenic minerals with different euhedral shapes. The scanned AFM areas are covered by illite and illite-chlorite. This is proved by SEM and EDX analysis as shown in appendix III.22. The R_q values are calculated at points I to III as: 3.3 nm, 18.6 nm and 13.2 nm, and the R_q value at point IV on the cement surface is 56.3 nm.

RL I_4146_D

On sample RL I_4146_D, the surface roughness analysis with AFM and the authigenic mineral identification with SEM and EDX were carried out on one point of the grain surface (I, appendix III.23) and on two spots (II and III, appendix III.23) of the cement surface. All AFM images were 1 μm x 1 μm in area.

The overview image of the sample, taken with binoculars at 5x magnification (Appendix III.23), shows that at point I (Image Ia) the grain surface is stained by hematite (brown coloured regions). As observed in the AFM image the presence of high (bright colour) and low (dark colour) areas reveal that the surface is not smooth. The cement faces (Image IIa and IIIa) are built by layered authigenic minerals with clearly visible euhedral shapes as shown in image IIa. However, at point III (Image IIIa) the cement surface is quite rough with striations (indicated by the arrows). The areas verified with SEM show flaky illite, illite-chlorite and quartz covering the grain (Image I) and cement surfaces (Image II and III in appendix III.24). The R_q values are as follows: 46.1 nm (Table 5.4), 44.6 nm and 92 nm (Table 5.5).

RL I_4146_E

Four areas were analysed with AFM and SEM on sample RL I_4146_E including two points on the grain surface at points I and II and the points III – IV on the cement surface (Figure 5.10). The revealed roughness parameters are listed in table 5.4 and 5.5.

As observed in the AFM images, the grain and cement surface structures are composed by authigenic minerals. These minerals have different shapes and sizes. As seen in images Ia and IIa, the minerals are blade and euhedral shaped (arrows), with multi layers (arrow in image IIIa). They are also lath shaped with width of around 193 nm (Image IVa). The lath shaped minerals are randomly ordered and display pores as shown by the arrow marks in image IVb. These minerals are illite and illite-chlorite, as verified by their morphology and spectra in figure 5.11. The corresponding root mean square surface roughness, represented by the R_q values are 32.8 nm and 43.1 nm (points I and II) on the grain surfaces and 5.26 nm and 12.3 nm (points III and IV) on the cement surfaces.

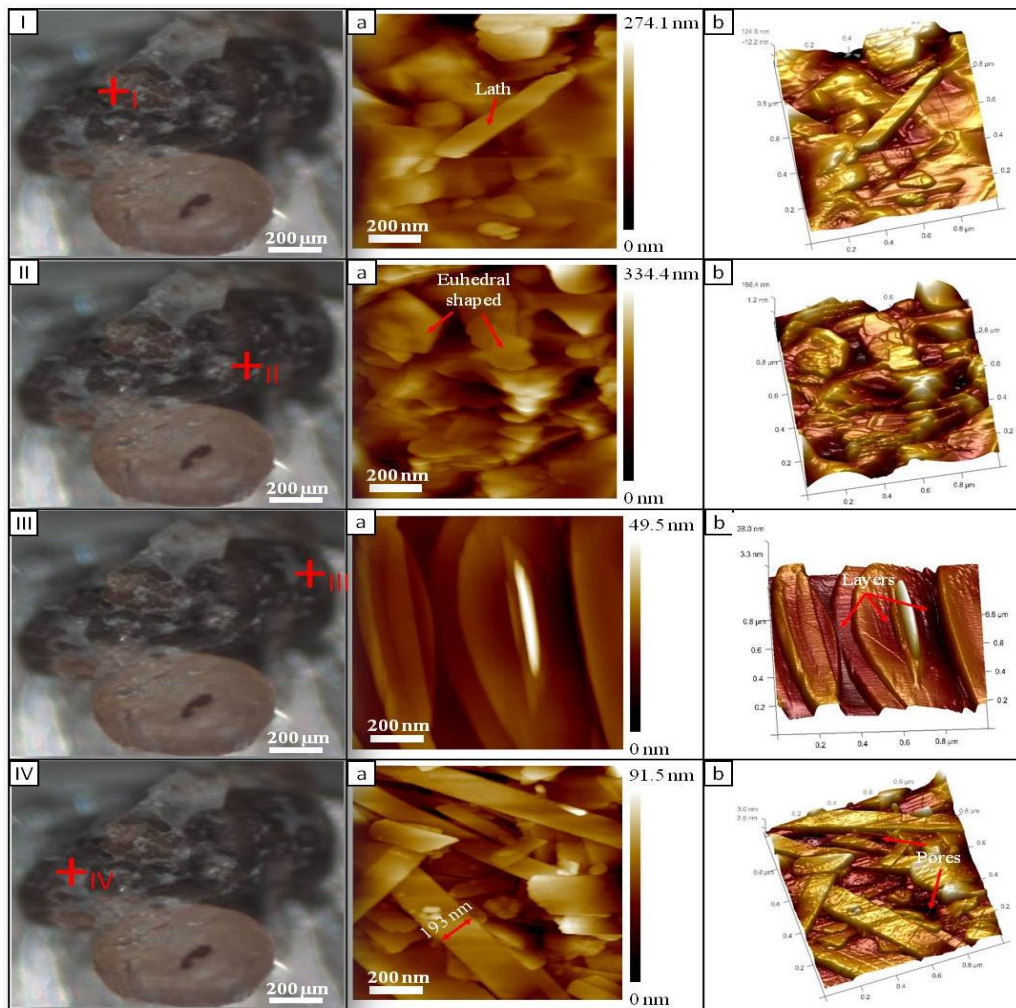


Figure 5.10 Sample RL I_4146_E. The image shows the sample pictured with binoculars at 5x magnification. The red crosshairs indicate the areas analysed by the AFM and SEM. The surface roughness is displayed in AFM height images (Ia – IVa) and as a 3D (images Ib- IVb).

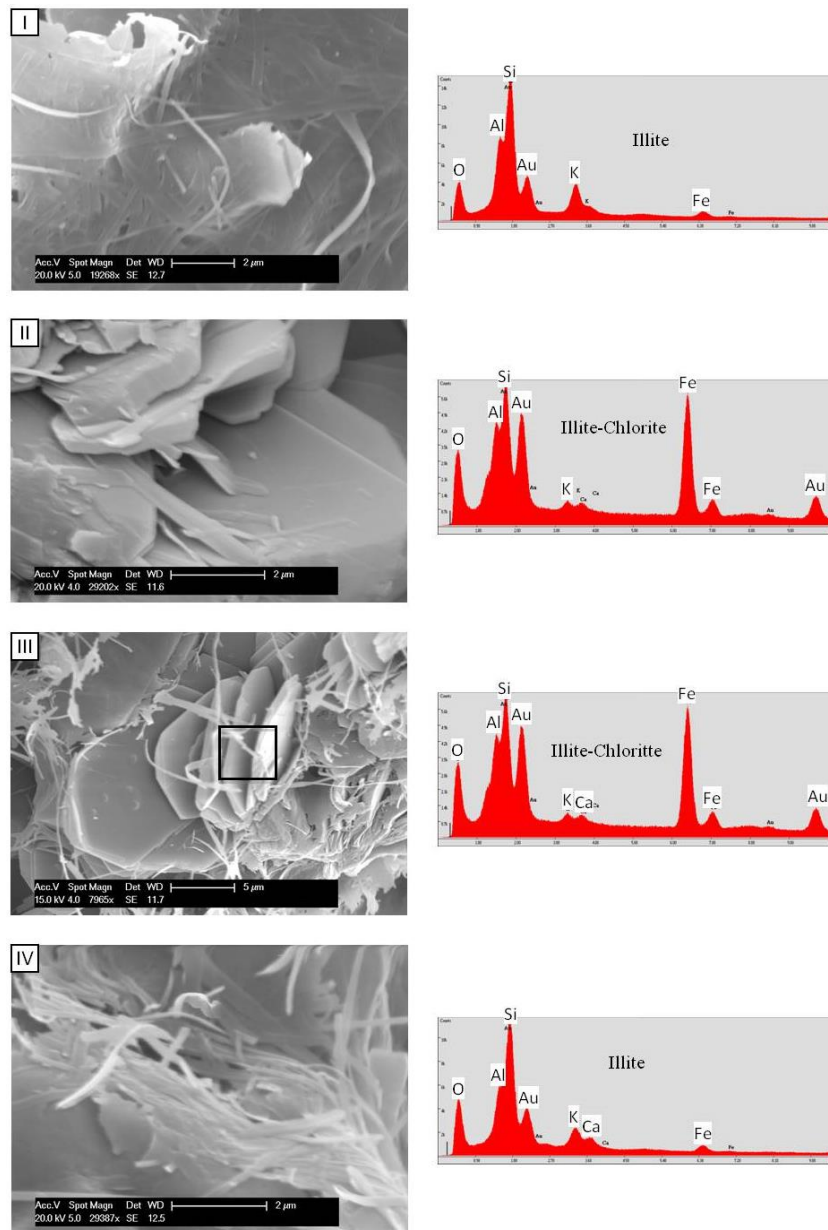


Figure 5.11 Sample RL I_4146_E. SEM images show illite ribbons and chlorite platelets. EDX spectra approve the chemical element composition of the minerals for the entire image areas I, II, IV and the marked area in image III.

Interpretation

For the sample RL I_4146 AFM measurements were carried out on 7 specimens with a total of 25 analysis points on the clastic grain surfaces and 6 areas on cement surfaces. The rough grain and cement surfaces are formed by overlaying authigenic minerals with various shapes and different structures, as observed in the AFM images. The mineral content was verified with SEM and EDX analysis. The roughness at each point of the authigenic minerals is given by the root mean square (R_q) roughness parameter (Table 5.4 and 5.5). Likewise, the

roughness of each grain surface, of the entire sample and of the dominant authigenic minerals of illite-chlorite and illite is represented by the R_q mean values (Table 5.6). These values show the different roughness of the grain surface due to the characteristics of the authigenic minerals.

The authigenic minerals are mainly illite. Illite has diverse morphologies but most commonly forms ribbons, laths, and fibers that intertwine and generate pores along the intersecting areas. Illite with euhedral shapes, arranging in parallel layers and parallel grooves (Image Ia, appendix III.23) also coats the grain surface. Therefore, the roughness of illite has a wide range of 2.24 nm to 46.1 nm. The R_q mean value of illite coating the grain surface is 21.9 nm (Table 5.6).

Authigenic illite-chlorite minerals are quite frequent in this sample. Chlorite has various shapes, commonly platelet, pseudo hexagonal and euhedral mixtures of fibrous illite coating surrounding the grains. The roughness values of its surface vary from 5.26 nm to 56.3 nm. The average roughness value R_q is 22.72 nm, which is small compared with the R_q average value of the sample RL I_2111.

Calcite cannot be directly observed by AFM and SEM analysis, perhaps only few spots scattering. With EDX however, the spectrum reveals a high peak of Ca elements. Probably, the calcite has precipitated over illite hence it is a subordinate factor to forming the rough grain surface. The R_q value is 12 nm.

The R_q values of authigenic quartz surfaces are varying in the range of 17.3 nm to 92 nm. This range is larger than for sample RL I_2111 because of the authigenic quartz grooves and striations (Image IIIa, appendix III.23). The roughness of the non overgrown quartz surface (Images IIa and Va, figure 5.7) changes from 10.5 nm to 23.3 nm. This value is slightly higher compared to that of the sample RL I_2111 because the quartz surface is heavily eroded, producing a number of micro pores.

The (R_q) roughness parameter is calculated for all 31 points as given in table 5.4 and 5.5.

The roughness of the whole sample of illite-chlorite and illite is shown by the R_q average values in table 5.6. The grain surface that is overgrown by illite-chlorite is rougher than that overgrown only by illite.

Table 5.4 Root mean square roughness (R_q) values of mineral coatings on grain surfaces with 1 μm scan size, sample RL I_4146

Order	Sample	Name	Figure/ Appendix	Image	Root mean square (R_q) (nm)	Height scale (nm)		Mineral
						Min	Max	
1	RL I_4146	RL I_4146_Qu_1	5.7	Ia	9.44	0	66.5	illite
2				IIa	17.3	0	127	authigenic quartz
3				IIIa	12	0	86.9	illite-calcite
4				IVa	20.1	0	136.2	illite
5				Va	70	0	505	authigenic quartz
6				VIa	38.3	0	67.2	illite-chlorite
7		RL I_4146_Qu_3	III.14	Ia	34.9	0	256.8	illite
8				IIa	2.24	0	17.5	illite
9				IIIa	12.5	0	91.5	illite
10				IVa	27.2	0	177.2	illite
11				Va	10.5	0	388.4	illite
12				VIa	39.4	0	279.6	illite
13		RL I_4146_A	III.17	Ia	16.8	0	130.8	quartz
14				IIa	23.3	0	181.7	quartz
15				IIIa	14.9	0	113.3	illite
16				IVa	24.6	0	189.1	illite-chlorite
17		RL I_4146_B	III.19	Ia	10.5	0	66.6	quartz
18				IIa	10.0	0	49.1	illite-chlorite
19				IIIa	4.46	0	39.3	illite
20		RL I_4146_C	III.21	Ia	13.3	0	92.6	illite
21				IIa	18.6	0	165.8	illite
22				IIIa	13.2	0	147.1	illite-chlorite
23		RL I_4146_D	III.23	Ia	46.1	0	375.6	illite
24		RL I_4146_E	5.10	Ia	32.8	0	274.1	illite
25				IIa	43.1	0	334.4	illite-chlorite

Table 5.5 Root mean square roughness (R_q) values of cement surfaces with 1 μm x 1 μm scan size of sample RL I_4146

Order	Sample	Name	Figure/ Appendix	Image	Root mean square (R_q) (nm)	Height scale (nm)		Mineral
						Min	Max	
1	RL I_4146	RL I_4146_B	III.19	IVa	51	0	467.4	illite-chlorite
2		RL I_4146_C	III.21	IVa	56.3	0	389.1	illite-chlorite
3		RL I_4146_D	III.23	IIa	44.6	0	327.9	illite-chlorite
4				IIIa	92	0	619.8	authigenic quartz
5		RL I_4146_E	5.10	IIIa	5.26	0	49.5	illite-chlorite
6				IVa	12.3	0	91.5	illite

Table 5.6 Root mean square roughness (R_q) average values of grain surfaces with 1 μm x 1 μm scan size of sample RL I_4146

Name	Root mean square roughness (R_q) (nm) average values					
	grain	sample	illite-chlorite	illite	chlorite	authigenic quartz
RL I_Qu_1	27.85	25.18	22.72	21.9	no data	43.65
RL I_Qu_3	21.12					
RL I_Qu_A	19.9					
RL I_Qu_B	8.32					
RL I_Qu_C	15.03					
RL I_Qu_D	46.1					
RL I_Qu_E	37.95					

5.2.3 Sample RL I_5041

Three sub samples, RL I_5041_Qu_1, RL I_5041_Qu_2 and RL I_5041_Qu_4 of sample RL I_5041 were analysed with AFM and CLSM (Chapter 4). Samples RL I_5041_A to RL I_5041_F were only analysed by AFM, SEM and EDX.

RL I_5041_Qu_1

The quartz grain sample RL I_5041_Qu_1 was analysed with the AFM at 9 spots. The areas marked with numbers I to V were scanned with scan sizes of 1 μm x 1 μm (Figure 5.12) and additionally analysed with SEM and EDX (Figure 5.14). The areas marked with numbers VI to IX had scan sizes ranging from 1.3 μm x 1.3 μm to 3 μm x 3 μm . The area marked in image IXa is shown enlarged in images a1 and b1 (Figure 5.13) which show clearly authigenic mineral structure with layering.

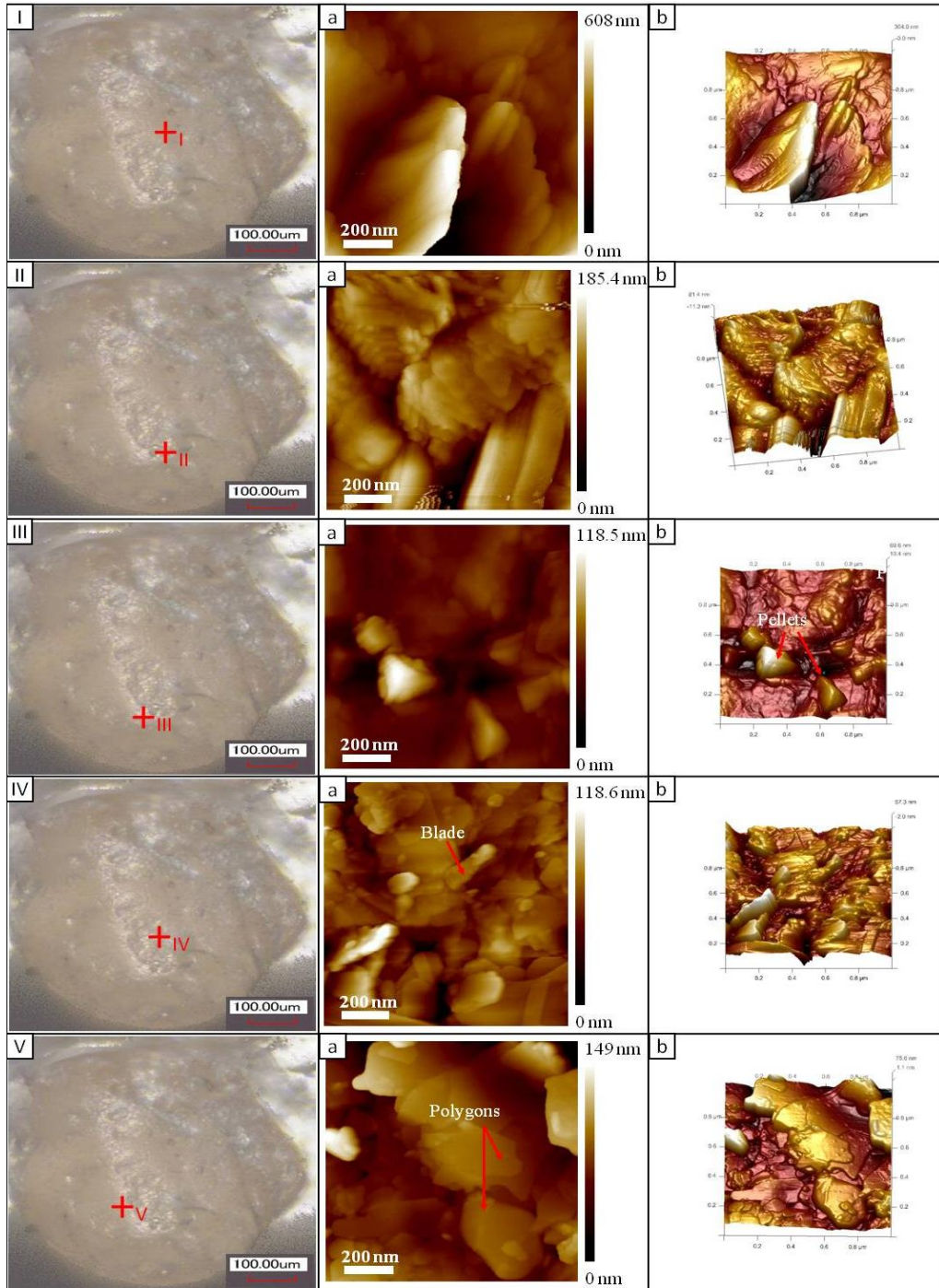


Figure 5.12 Sample RL_I_5041_Qu_1. Overview CLSM image of the quartz surface at 10x magnification. Crosshairs indicate the spots that were analysed with AFM and SEM. The AFM images Ia – Va show areas with scan sizes of 1 µm x 1 µm. Images Ib-Vb are 3D representations of the same scans.

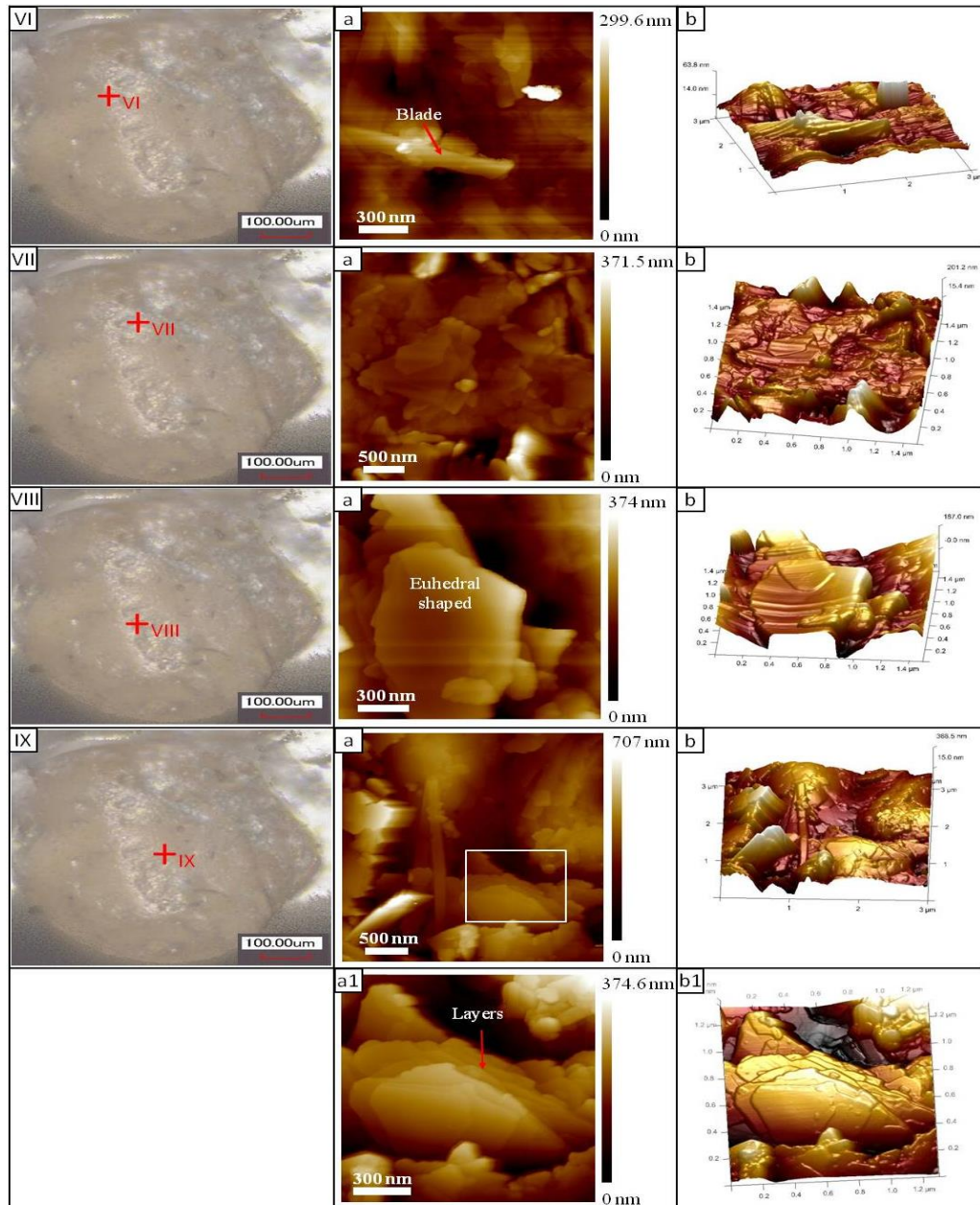


Figure 5.13 Sample RL I_5041_Qu_1. CLSM, AFM topography, and 3D images of RL I_5041_Qu_1. The CLSM image is an overview picture of the quartz surface at 10x magnification. The red marked spots VI to IX label the positions where AFM measurements were taken. Images correspond to $3\ \mu\text{m} \times 3\ \mu\text{m}$ (images VIIa and IXa), $1.5\ \mu\text{m} \times 1.5\ \mu\text{m}$ (images VIa and VIIIa) and $1.3\ \mu\text{m} \times 1.3\ \mu\text{m}$ (image a1). Images VIb – b1 are the corresponding 3D illustrations.

The CLSM analysis of the quartz surface RL I_5041_Qu_1 shows a very smooth surface (Figure 5.12 and 5.13). At the nanometre scale the AFM measurements of all 9 sample areas indicate that the quartz surface is very rough. The quartz surface is covered by a thin layer of authigenic minerals with many different shapes: blade, pellet, lath, euhedral and polygon shaped. These minerals are illite and chlorite, as identified by SEM and EDX analysis (Figure 5.14). Sometimes, the mineral aggregations are layered, as seen in image a1 (Figure 5.13).

The R_q parameter is calculated for the areas of images Ia – Va in figures 5.12. The corresponding R_q values are 89.7 nm, 23.9 nm, 12.6 nm, 14.3 nm, and 20.7 nm (Table 5.7). The value of R_q is the largest at point I, a region covered by illite-chlorite (Image Ia). Images VI – IX in figure 5.13 with scanned size of $1.5 \mu\text{m} \times 1.5 \mu\text{m}$ and $3 \mu\text{m} \times 3 \mu\text{m}$ show that the quartz surface could be covered by chlorite authigenic minerals with multi-morphologies: layered polygon and euhedral shaped. One of the layered structures is magnified in image a1, figure 5.13.

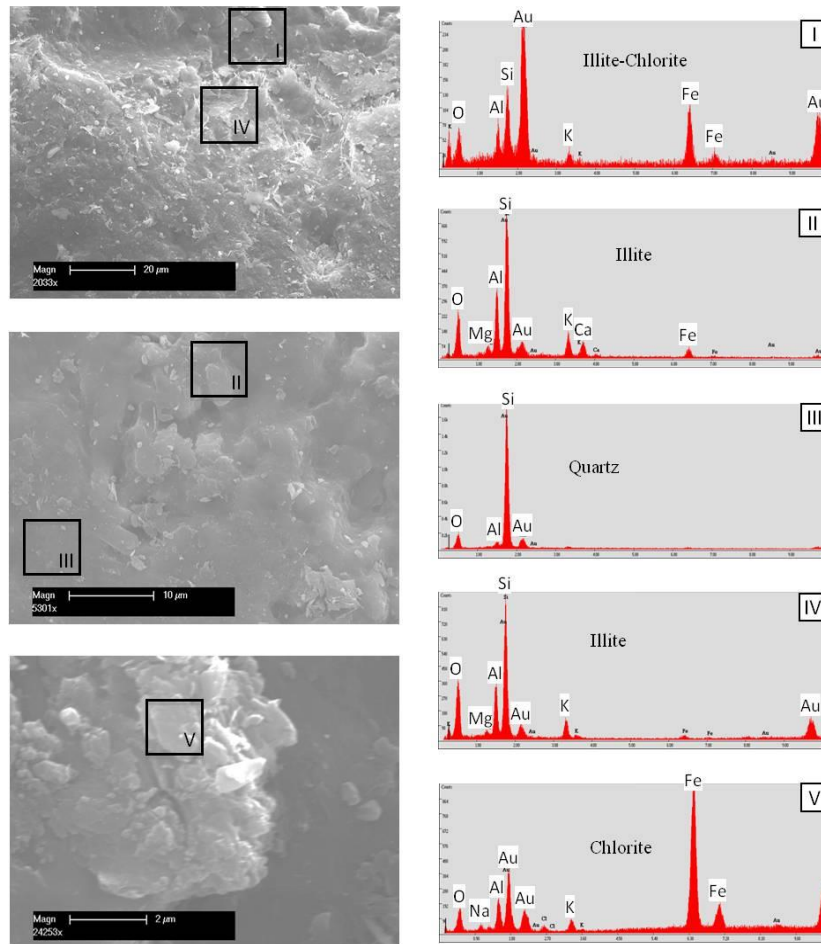


Figure 5.14 Sample RL I_5041_Qu_1. SEM images with the corresponding show the illite and illite-chlorite authigenic minerals which grow on the quartz surface. The analysed regions I – V are similar to the areas imaged with the AFM in figure 5.12.

RL I_5041_Qu_2

On the quartz grain RL I_5041_Qu_2, the marked spots I to III (Appendix III.25) were analysed with AFM (scan size of $1 \mu\text{m} \times 1 \mu\text{m}$), SEM and EDX. The roughness of the areas is represented by the R_q roughness parameter in table 5.7.

The overview CLSM image of the quartz grain shows similarities to that of the sample RL I_5041_Qu_1 (Figure 5.12). The CLSM picture shows a smooth, round surface. The AFM measurements nevertheless, reveal that the quartz surface is very rough at nanometre scale. It is coated by authigenic chlorite minerals with many various shapes such as blade, pellet, lath and euhedral shape. These minerals have an arrangement in disordered leading to building pores as indicated by the arrows in images Ia – IIIa, appendix III.25. The roughness of the quartz surface is evidenced by the R_q values: 28.2 nm, 21.2 nm and 30 nm (Table 5.7).

RL I_5041_Qu_4

The surface of the quartz grain RL I_5041_Qu_4 has different colours which change in gradients from white to brown. On this grain surface, four different areas were imaged with the AFM. Scan sizes of 1 μm x 1 μm were used. These areas were subsequently analysed with SEM and EDX at the positions marked by the crosshairs in figure 5.15. The roughness parameter was calculated for all surfaces separately (Table 5.7).

The overview image of the quartz grain (Figure 5.15) shows that the quartz surface is partly covered by a white coloured cement layer. The covered areas appear a little higher than the areas with brown colour. SEM and element spectra analysis (Figure 5.16) at the white coloured areas reveal that the cement layer is composed of illite, calcite and in some places precipitated halite (Image II). AFM measurements were taken of the areas with authigenic minerals, of white colour and of the primary quartz face with brown colour (marked areas in figure 5.15). The quartz surface structure strongly varies at all measured points. At point I, on the real quartz surface with non overgrown and at point III, on the quartz surface coated by illite, the surface is partly smooth but with grooves or striations, as marked by the arrows in image Ib and IIIb (Figure 5.15). The quartz surface covered by illite - halite and calcite at point II and IV (see images II and IV, figure 5.16) in contrast, is built up by cubic-shaped halite (arrow, image IIa) and tilted multi layers (arrow, image IVa, figure 5.15) that are clearly visible in the middle. of image IVa. The quartz surface topography is defined by the R_q value of 18.9 nm, 17 nm, 15.1 nm, and 32.9 nm corresponding to points I to IV. It turns out that the surface has the highest roughness with the largest root mean square at point IV.

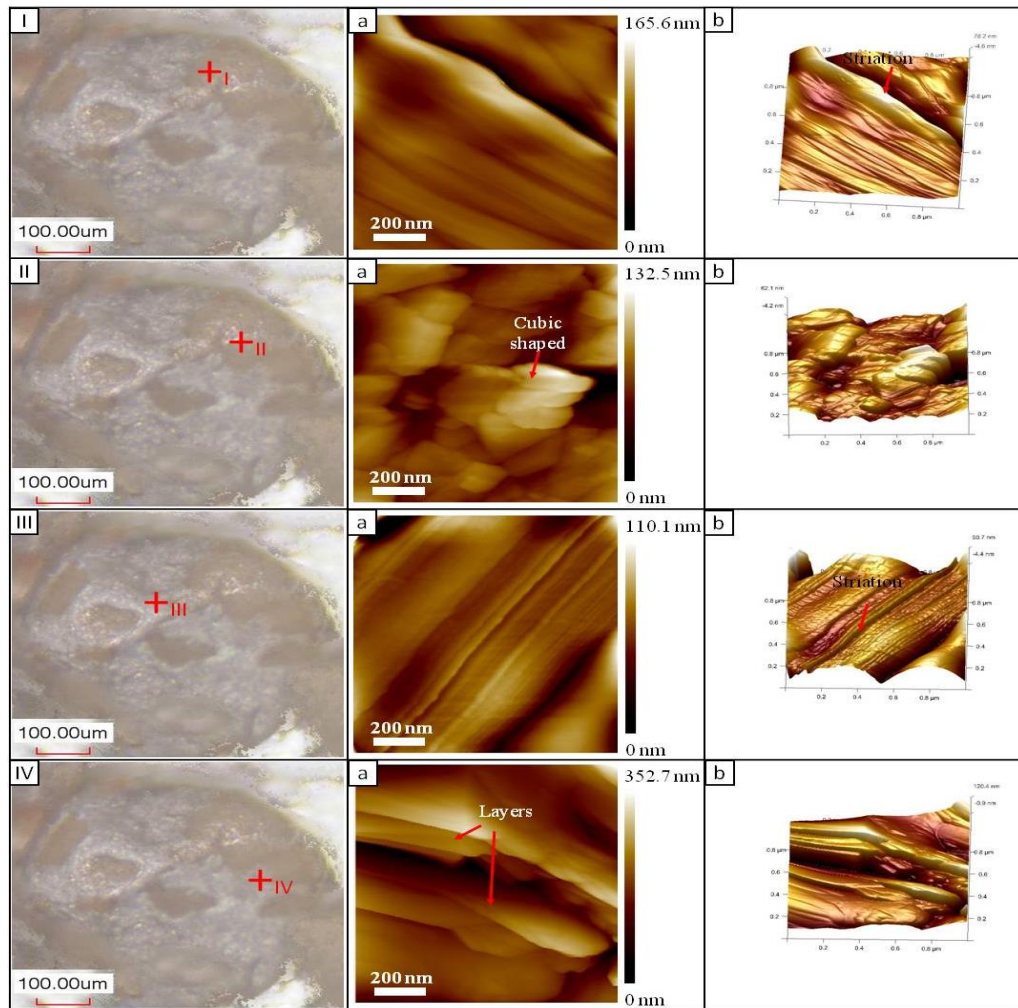


Figure 5.15 Sample RL I_5041_Qu_4. The CLSM image shows an overview picture of the quartz surface at 10x magnification. The red crosses mark the spots where AFM measurements were taken. AFM scan sizes were $1 \mu\text{m} \times 1 \mu\text{m}$. The quartz surface is displayed in height images Ia – IVa and in 3D reconstructions Ib - IVb.

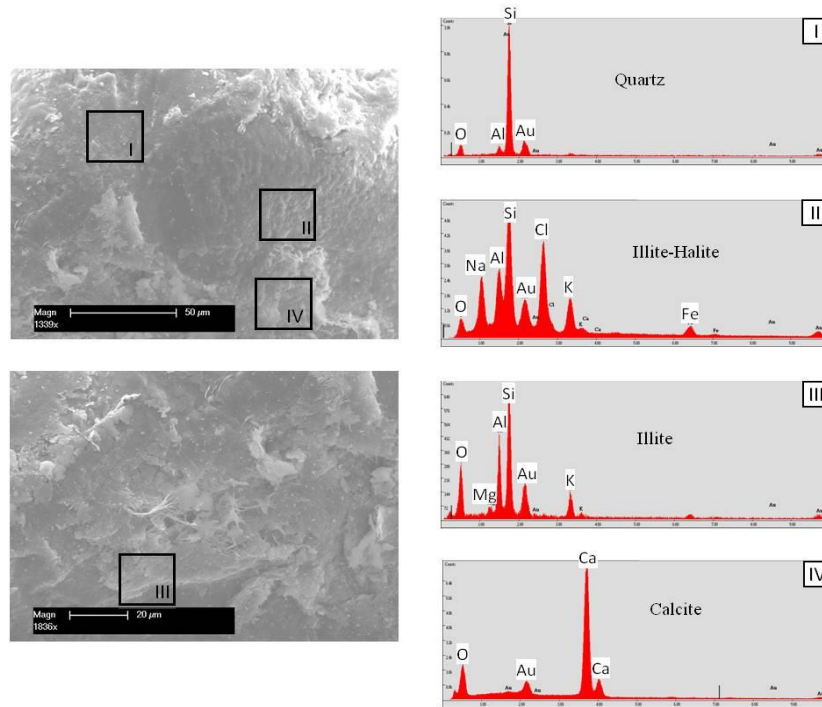


Figure 5.16 Sample RL I_5041_Qu_4. SEM images and EDX spectra I – IV taken at the marked boxes, the same areas as used for AFM analysis. At points II – IV the quartz surface is covered by illite-halite, illite and calcite authigenic minerals.

RL I_5041_A

The quartz grain RL I_5041_A was analysed with AFM and SEM at 6 areas, as marked by numbers I to VI (Appendix III.27). The scan size was limited to $1\ \mu\text{m} \times 1\ \mu\text{m}$. The quartz surface roughness was calculated from the same regions as those imaged by AFM areas. The results are listed in table 5.7.

The overview CLSM image (Appendix III.27) of the quartz surface shows similarities to the quartz grain sample RL I_5041_Qu_4 (Figure 5.15). In the CLSM picture the areas with white colour are commonly elevated compared to those with brown colour. AFM measurements were not taken at the low areas because the AFM head would crush into the sample surface while the AFM tip would not reach the grain surface. The AFM images, in contrast to the CLSM image, show that the surface of sample RL I_5041_A is different to that of the grain sample RL I_5041_Qu_4. The coatings on the quartz surface of sample RL I_5041_Qu_4 are illite, calcite, and sometimes halite, while on sample RL I_5041_A the surface covering film is authigenic illite, chlorite, chlorite-illite and quartz. At point I, the roughness of the quartz surface is governed by authigenic quartz with pellets. Otherwise, the areas from point II to point VI are covered by illite, illite-chlorite, and chlorite authigenic

minerals as analysed with SEM and EDX (Appendix III.28). They have tangled lath-like and plate like shapes (Images IVa and Va). At these positions, the quartz surface has micro pores as pointed out by the arrows in the images. Additionally, there are possibly other authigenic minerals growing over the plate like shaped minerals, which are also pellet shaped with roughly 100 nm size, as marked in the image VIa. They could have been formed after the lath-like and plate-like shaped minerals, at a later stage of diagenesis. The corresponding R_q values are: 17.7 nm, 24.7 nm, 33 nm, 18.6 nm, 14.6 nm and 6.22 nm, for points I to VI (Table 5.7).

RL I_5041_B

On the quartz grain RL I_5041_B three spots were measured with the AFM at a $1\ \mu\text{m} \times 1\ \mu\text{m}$ scan size, as marked by numbers I to III (Appendix III.29). All these points were also imaged with the SEM coupled with chemical element analysis EDX (Appendix III.30) and the surface roughness R_q values were calculated as listed in table 5.7.

In the overview image of the quartz grain (Appendix III.29) shiny areas are the highest and roundest surfaces. AFM measurements were only taken of these higher regions (see crosshairs), because at too low areas or steep sidewalls the cantilever already touched the surrounding walls while the AFM tip was not in contact to the surface. The structure of the quartz surface is varying a lot and has various shapes in all areas. Most common are plate-like and lath- or pellet-like structures. One of the pellets is around 100 nm in size, as determined in image IIa. Only at point III the quartz face is coated by calcite whereas at point I and II the original quartz grain surface is exposed (see appendix III.30). In the left of image IIIa, a scratch occurred, which is a measuring artefact. The quartz surface roughness parameters calculated at points I - III are: 5.72 nm, 5.38 nm and 15.4 nm (Table 5.7).

RL I_5041_C

RL I_5041_C is a sample group of grains that contains cement and clastic grains. The AFM measurements were taken on grain surfaces at points I and II and on cement surfaces at points III and IV (Appendix III.31) with scan sizes of $1\ \mu\text{m} \times 1\ \mu\text{m}$. The roughness of all these areas was calculated and is listed in table 5.7 and table 5.8 and element analysis was conducted with SEM and EDX (Appendix III.32).

The AFM images of the grain surface at positions I and II show a rather rough surface topography with micro pores and pellets, as indicated by the arrows in images Ia and IIa

(Appendix III.31). The grain surfaces are overgrown by illite as determined by EDX analysis (Appendix III.32). The surface of the cements is overgrown by illite and chlorite authigenic minerals with clearly visible laths and pellet like shapes. Additionally, there are probably other minerals growing on the lath mineral bed, maybe halite crystals as assigned by the arrows in the 3D images IIIb and IVb. The R_q values calculated at points I to IV are: 14 nm, 40.8 nm (Table 5.7), 25.9 nm and 30.7 nm (Table 5.8).

RL I_5041_D

On the sample RL I_5041_D, two regions of the grain surface were scanned with AFM coupled with SEM and EDX analysis. The examined areas are marked as I – II (Figure 5.17). The grain surface roughness was determined and the corresponding R_q values are given in table 5.7.

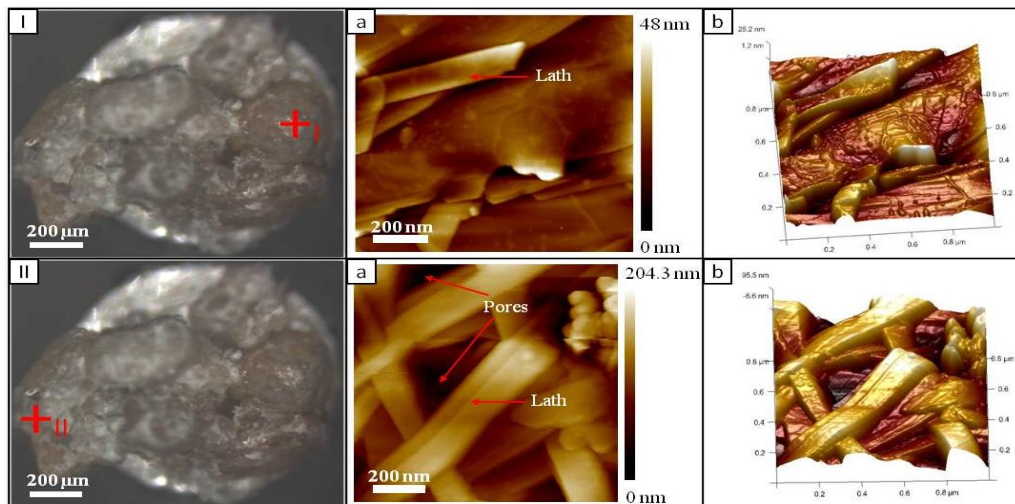


Figure 5.17 Sample RL I_5041_D. Binocular overview images show the sample and the spots analysed by the AFM. The AFM images display the topography of a 1 μm x 1 μm grain surface area.

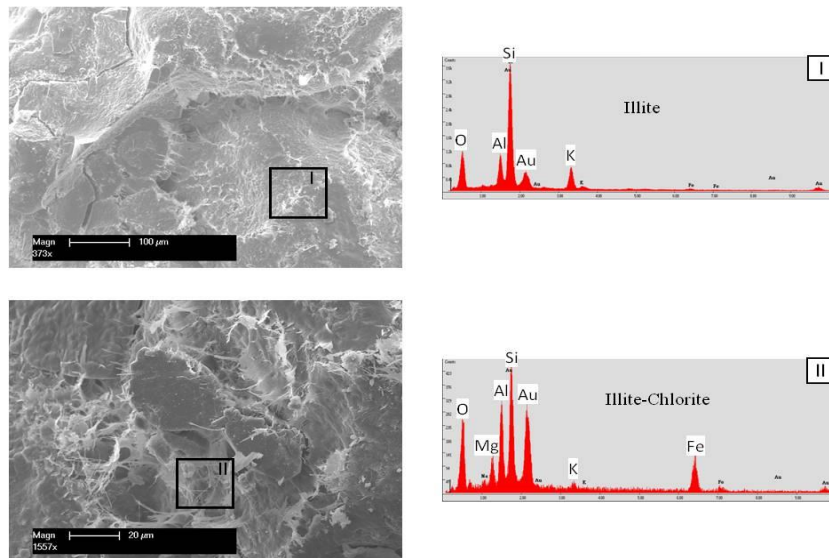


Figure 5.18 Sample RL I_5041_D. SEM images indicate that illite and illite-chlorite overgrow the grain surfaces. The EDX element spectra taken at the areas indicated in the SEM images prove this.

The AFM images show that the grain surfaces are coated by authigenic minerals. The minerals are illite, and illite-chlorite, as observed with SEM and EDX (Figure 5.18). These minerals are lath shaped (arrows, figure 5.17) and show a chaotic arrangement. Therefore, they build a rough grain surface with many interstitial pores (arrows, figure 5.17) and large height differences. The root mean square roughness value is 5.83 nm and 32.5 nm corresponding to points I and II.

RL I_5041_E

On sample RL I_5041_E only one point was scanned with the AFM as pointed out by the mark. SEM analysis and the grain surface roughness (R_q) calculation were taken at this area. The grain surface is overlain by calcite authigenic mineral layers (Image Ia, appendix III.33) as verified by the EDX analysis in appendix III.34. The calcite seems to be arranged in titled layers as indicated by the arrow in image Ia, and they form a surface with elevations and slots. The surface roughness has a R_q value of 45.2 nm.

RL I_5041_F

AFM measurements were taken on the grain surface of sample RL I_5041_F at points I – IV and on the cement surface at point V (Appendix III.35) with a scan size of 1 µm x 1 µm. All the spots were additionally examined with SEM and EDX (Appendix III.36) and the surface roughness was determined as shown in table 5.7 and 5.8.

An overview of the imaged AFM areas is shown in appendix III.35. Images were taken of the grain and the cement surface. At points I - IV, the grain surfaces seem to have a similar structures. They are covered by illite and chlorite-illite minerals with filaments (Appendix III.36). At point I, the AFM image Ia (Appendix III.35) shows that the grain surface is covered by lath like shaped chlorite minerals with parallel (arrow) and crossed arrangements (see the top of the image). The chlorite minerals have individual platelets, as seen in image I (Appendix III.36). The cement surface is rough and composed of illite-chlorite as shown in image Va and image V (Appendix III.35 and appendix III.36). The R_q parameter values are: 19.8 nm, 17.3 nm, 5.15 nm, 19.9 nm (Table 5.7) and 14.1 nm (Table 5.8) corresponding to points I to V.

Interpretation

For the sample RL I_5041, 9 sub samples with 33 points including 30 points on the grain surfaces and 3 points on the cement surfaces were analysed with the AFM. Scan sizes of $1\ \mu\text{m} \times 1\ \mu\text{m}$ and 5 points with scan sizes changing from $1.3\ \mu\text{m} \times 1.3\ \mu\text{m}$ to $3\ \mu\text{m} \times 3\ \mu\text{m}$ were used. The roughness of each measurement point on the grain and cement surfaces is illustrated by the root mean square (R_q) parameter as given in table 5.7 and 5.8. Also the morphology and chemical composition of the authigenic minerals were determined with SEM and EDX corresponding to analysed AFM points. The roughness of the individual grain, of the entire sample and the illite-chlorite, illite and chlorite authigenic minerals, which dominantly cover the grain surfaces, are shown by the R_q average values in table 5.9.

The roughness of the grain and cement surfaces is predominantly governed by the mineral illite, which shows different structures as observed in AFM and SEM images. The structures and morphologies are commonly blade, lath and ribbon like. They often arrange in crossed and intersected structures with many pores at the intersection places. The surface roughness (R_q) values of the illite are in a range from 5.15 nm to 40.8 nm. Due to the chaotic arrangement of illites, the large difference between the highest peak and the lowest points, e.g. the vertical scale of image IIa (Appendix III.31) can be explained. Values vary from 0 nm to 348 nm. Therefore, the roughness (R_q) value reaches the largest value of 40.8 nm in this image whereas, the R_q value is the smallest with 5.15 nm in image IIIa (Appendix III.35), where the height scale only ranges from 0 nm to 44.3 nm. The R_q mean value for illite is 16.9 nm (Table 5.9). Rarely halite precipitated on the illite crystals. The halite crystals have cubic

shaped (Image IIa, figure 5.12 and image IIIa, appendix III.31), lying above the illite, so that the resulting surfaces are rougher and the R_q values are larger (17 nm and 25.9 nm).

Chlorite is also a popular mineral that overlays the grain surface and it is also a component of the cement in this sample. The chlorite mineral features a variety of morphologies and structures. Common shapes are blade, euhedral, pseudo hexagonal (Figure 5.12), individual platelet (Image Ia, appendix III.35 and image I, appendix III.36) and polygon like (Image VIa, appendix III.27). The aggregation of the crystals forms the rough facial structures. The surface roughness (R_q) values vary from 6.22 nm to 30.7 nm. The chlorite, which coats the grain surface, has an average R_q value of 18.3 nm (Table 5.9). The value is higher than that of illite, thus the grain surfaces covered by chlorite are rougher than those coated only by illite. The chlorite is almost absent in the samples RL I_2111 and RL I_4146.

Illite-chlorite occurs in nearly all of the analysed samples (RL I_2111, RL I_4146 and RL I_5041). In sample RL I_5041 the illite-chlorite is less common. It only occurs in a couple of analysed points. Its structures are of lath and euhedral shapes. The R_q values are 14.1 nm to 89.7 nm. The R_q average value is 43.1 nm (Table 5.9).

Authigenic quartz appears only in sample RL I_5041_Qu_1 and RL I_5041_A with the R_q values varying from 12.6 nm to 17.7 nm. The authigenic quartz has no sharp shapes and was tested by EDX analysis. The original grain quartz surface roughness has R_q values from 5.72 nm to 18.9 nm. These R_q values are smaller than those of the quartz grain surface covered by authigenic quartz. Thus the non overgrown quartz surface is less rough than the quartz surface covered by authigenic quartz.

Authigenic calcite was also not frequently observed and only found at 3 points (samples RL I_5041_Qu_4, RL I_5041_B and RL I_5041_E). The R_q values are quite large. They range from 24.4 nm to 52.6 nm. Calcite shows layered structures. This affects and increases the surface roughness.

Table 5.7 Root mean square roughness (R_q) values of mineral coatings on the grain surface of sample RL I_5041 (scan sizes analysed 1 μm x 1 μm)

Order	Sample	Name	Figure/ Appendix	Image	Root mean square (R_q) (nm)	Height scale (nm)		Minerals
						Min	Max	
1	RL I_5041	RL I_5041_Qu_1	5.12	Ia	89.7	0	608	illite-chlorite
2				IIa	23.9	0	185.4	illite
3				IIIa	12.6	0	118.5	authigenic quartz
4				IVa	14.3	0	118.6	illite
5				Va	20.7	0	149	chlorite
6		RL I_5041_Qu_2	III.25	Ia	28.2	0	229.7	chlorite
7				IIa	21.2	0	164	chlorite
8				IIIa	30	0	239.8	chlorite
9		RL I_5041_Qu_4	5.15	Ia	18.9	0	165.6	quartz
10				IIa	17	0	132.5	illite-halite
11				IIIa	15.1	0	110.1	illite
12				IVa	32.9	0	352.7	calcite
13		RL I_5041_A	III.27	Ia	17.7	0	116.2	authigenic quartz
14				IIa	24.7	0	180.8	illite
15				IIIa	33	0	253.5	illite-chlorite
16				IVa	18.6	0	137.4	illite
17				Va	14.6	0	117.2	illite
18		VIa	6.22	0	53.7	chlorite		
19		RL I_5041_B	III.29	Ia	5.72	0	43.5	quartz
20				IIa	5.38	0	42.5	quartz
21				IIIa	15.4	0	195.3	calcite
22		RL I_5041_C	III.31	Ia	14	0	107.1	illite
23				IIa	40.8	0	348.3	illite
24		RL I_5041_D	5.17	Ia	5.83	0	48	illite
25				IIa	32.5	0	204.3	illite-chlorite
26		RL I_5041_E	III.33	Ia	45.2	0	305	calcite
27		RL I_5041_F	III.35	Ia	19.8	0	170.8	chlorite
28				IIa	17.3	0	134.6	illite-chlorite
29				IIIa	5.15	0	44.3	illite
30				IVa	19.9	0	133.3	illite

Table 5.8 Root mean square roughness (R_q) values of cement surfaces with 1 μm x 1 μm scan sizes analysed on sample RL I_5041

Order	Sample	Name	Figure/ Appendix	Image	Root mean square (R_q) (nm)	Height scale (nm)		Mineral
						Min	Max	
1	RL I_5041	RL I_5041_C	III.31	IIIa	25.9	0	227.1	illite-halite
2				IVa	30.7	0	229.4	chlorite
3		RL I_5041_F	III.35	Va	14.1	0	114	illite-chlorite

The authigenic minerals feature morphological differences that cause the different roughness, as expressed by the R_q average values in table 5.9. The grains covered by illite-chlorite are rougher than those covered only by illite or chlorite. Therefore, depending on the authigenic mineral coatings, the single grain roughness is widely changing. The average roughness value for the entire sample is 23.88 nm.

Table 5.9 Root mean square roughness (R_q) average values of grain surfaces with 1 μm x 1 μm scan size of sample RL I_5041

Name	Root mean square roughness (R_q) (nm) average values					
	grain	sample	illite-chlorite	illite	chlorite	authigenic quartz
RL I_Qu_1	32.24	23.88	43.1	16.9	18.3	15.15
RL I_Qu_2	26.46					
RL I_Qu_4	20.97					
RL I_Qu_A	19.13					
RL I_Qu_B	8.83					
RL I_Qu_C	27.4					
RL I_Qu_D	19.16					
RL I_Qu_E	45.2					
RL I_Qu_F	15.53					

5.3 CONCLUSION

The grain and cement surface roughness of the sandstone samples from the Rotliegend RL I well, were evaluated with AFM, investigating 78 areas on the grain surfaces and 22 areas on the cement surfaces. Most of the grain surfaces are overgrown by authigenic minerals. All the imaged AFM points were subsequently identified with SEM and analysed for their element spectra by EDX, to determine their morphology and authigenic mineral composition. The authigenic minerals show flake, euhedral, blade, polygon, lath, square shape, and rounded pellet morphologies, often arranged in multi layers. The minerals are without preferential arrangement, forming micro pores on the grain surfaces. Sometimes the grain surfaces are

covered by unstable minerals which were dissolved and which left behind micro pores or pits on the grain surface. Likewise, the cements were also formed from authigenic minerals or precipitated from fluids during diagenesis. The most common authigenic minerals covering the grain surfaces are illite-chlorite, illite, and chlorite. Less common minerals are quartz, calcite and also rarely halite or calcite precipitates on illite. With AFM analysis, haematite is not detected probably, only stains on grain surface. However, the chlorite was only found in the sample RL I_5041 by nano-methods. It is nevertheless abundantly visible in thin petrographic sections.

The roughness of the grain surfaces covered by illite-chlorite was higher compared to those covered by illite and/or chlorite and the roughness of chlorite was higher than that of illite as shown by the R_q average values for sample RL I_5041 (Table 5.9). Conversely, the authigenic minerals forming cement are mainly illite-chlorite, while illite, chlorite and quartz are very rare and anhydrite is very seldom, occurring only at two measured points. The roughness of all authigenic mineral coatings on both, the grain and cement surfaces is expressed by the mean values of the root mean square (R_q) parameter (see table 5.10). The roughness of illite-chlorite is the highest with the largest R_q mean value of 32.28 nm, also showing a wide range with a standard deviation of 26.62 nm. The roughness of chlorite and illite is less variable and features lower roughness. The authigenic minerals such as quartz, anhydrite, calcite, halite precipitated on illite, and calcite precipitated on illite are present at one or a couple of points so that the data are insufficient to display their general roughness degree. Figure 5.19, a diagram plotted all root mean square roughness values shows an overview of the changes of the roughness of all the mineral surfaces which were analysed from the Rotliegend well.

Table 5.10 Root square mean roughness (R_q) values of the minerals

Order	Type	Mean value (nm)	Standard deviation (nm)	Min value (nm)	Max value (nm)
1	illite-chlorite	34.03	27.88	2.42	134
2	chlorite	22.4	8.49	6.22	30.7
3	illite	18.44	11.31	2.24	46.1
4	authigenic quartz	35.63	26.62	12.26	92
5	quartz	14.19	9.37	3.62	29.3
6	calcite	45.62	31.39	15.4	89
7	halite-illite	28.72	22.74	10.5	61.5
8	anhydrite	24.55	5.44	20.7	28.4

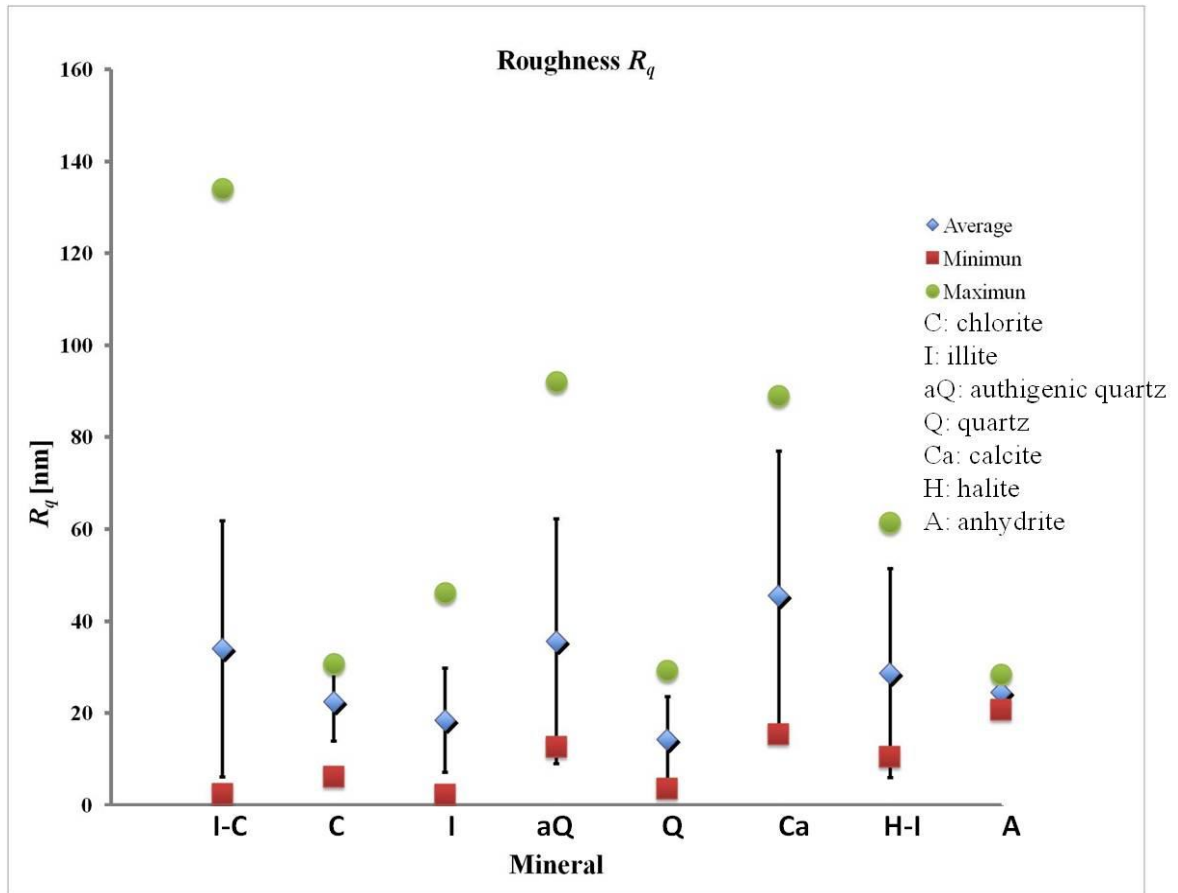


Figure 5.19 Diagram displaying the change of the root mean square roughness values of the minerals.

The R_q value difference of the minerals is due to distinct crystal habits coating on grain surface. Such illite and chlorite with multi shapes, mixture of together, their R_q values range in a wide field (2.42 nm – 134 nm) compared with roughness of other minerals e.g chlorite, illite, halite-illite, quartz or anhydrite. The R_q values of the authigenic quartz and calcite have a largely various change due to that the authigenic quartz is a crystal cluster with distinct crystal surface arrangement and calcite surface is dissolved.

The results in table 5.11 show that the R_q average value of the sample RL I_2111 is the largest and the smallest R_q average value is found for the sample RL I_5041. This means that the grain surfaces of the sample RL I_2111 have the highest roughness and sample RL I_5041 shows the lowest roughness of all samples. This is caused by the illite - chlorite surface layer which has a high roughness and is quite abundant in sample RL I_2111. On the other hand, the illite with lower roughness is popular in the samples RL I_4146 and RL I_5041. Additionally, in the sample RL I_4146 the authigenic quartz with high roughness is more common than in the sample RL I_5041, leading to the higher roughness of the sample RL I_4146.

The porosity, permeability and the roughness of the investigated samples are listed in table 5.11.

Table 5.11 Porosity, permeability and roughness of the investigated samples

Sample	Porosity (%)	Permeability (mD)	Grain density	Average R_q (nm)	Formation factor
RL I_2111	4.4	0.25	2.670	26.7	126
RL I_4146	8.7	4.04	2.656	25.18	43
RL I_5041	15	53.45	2.645	23.88	25

The results show that the difference in permeability of the investigated samples is quite large, while the roughness distribution is rather close. Sample RL I_2111 with rough grain surfaces shows low permeability. Conversely sample RL I_5041, that has a lower roughness shows high permeability. These results are consistent with previous studies performed on the fractal dimension D derived from Small Angle Neutron Scattering Analysis, formation factor F (Drobek et al., 2011) and the roughness R_q analysed with CLSM (Chapter 4). Perhaps the larger porosity allows for more authigenic minerals and permeability still remains good. The sample RL I_5041 with a low grain surface roughness R_q (CLSM and AFM) corresponds to a decreased D with an increased porosity and permeability and a low F . The formation factor F is the ratio between the electric resistivity of the rock filled with water only and the brine water. In contrast, the sample RL I_2111 with a high grain surface roughness corresponds to a low permeability and a high formation factor F (see table 5.11). Furthermore, the grain surface roughness is an important factor in sandstone reservoir rocks because it influences the contact area between the grain surface and the fluid and the wetting properties and surface tension on the nanoscale. The contact area can be expressed by contact angle measurements (Butt et al., 2003). For good wetting properties, a high grain surface roughness involves a large contact area. The roughness also affects adhesive force of liquids on the grain surface (Kamusewitz et al., 2003). The determination and parameterisation of the surface roughness is fundamental for a better understanding of surface wetting and adhesion and hence important factors to improve oil recovery.

6. DISCUSSION

The investigations described in this thesis were carried out to determine the processes of diagenesis, the grain morphology, the pore geometry and the grain surface roughness of Rotliegend sandstone reservoir rocks taken from the Lower Saxony Basin in northern Germany. The petrography and diagenesis of Rotliegend sandstones as discussed in chapter 3, show the influences of diagenesis on the pore networks. The grain morphology and pore geometry are described in chapter 4, where the variety of the grain surfaces and pore spaces due to the influence of diagenesis are examined. The grain roughness was treated in chapter 5, which demonstrates that the roughness distinction can be attributed to the authigenic minerals of the investigated samples.

6.1 THE DIAGENESIS

Clay minerals in the early phase of diagenesis are predominantly illite, which surrounds the grains and precipitated from pore waters. The cements in pore – fillings are commonly quartz, calcite, subordinated anhydrite and albite. Quartz cements precipitated from silica - rich fluids which probably largely originated from fluvial settings. Illite grain coatings were formed in continental deposits as in continental meteoric water (Wilson, 1992; Platt, 1994; Schöner, 2006). Also, the occurrence of calcite and anhydrite cements shows that it is likely that cements precipitated from the overlying Zechstein evaporates (Purvis, 1992). Locally the precipitation of halite indicates that the water was increasingly saline. It is likely that authigenic albite was associated with sandstones of marine origin (Rasmussen et al., 1996) or invaded by marine brines and was trapped by Zechstein deposits (Purvis, 1989). Authigenic albite is largely widespread at burial depth, due to the fact that Na^+ was released from extensively dissolved unstable grains, mostly feldspars and volcanic fragments. The dissolution was responsible for the crystallisation of illite and chlorite in pore - fillings. The latest cement is calcite, which precipitated in local pores and in pits of dissolved grains. It is possible that the fluids dissolved the unstable grains, forming illite and chlorite in pores occurred in Rotliegend sandstones which were nearby or adjacent to the underlying Carboniferous sequence. The fluids derived from the Carboniferous deposits (Platt, 1991; Platt, 1993).

The diagenetic alteration had a large impact on the grain morphology and the pore geometry.

6.2 THE GRAIN MORPHOLOGY, GRAIN ROUGHNESS AND PORE GEOMETRY

Three Rotliegend sandstone samples were analysed with a CLSM and an AFM systems. The characterisations of the grain surface were revealed by parameters (R_p , R_v , R_z , R_a , R_q , R_{sk} , R_{ku} and R_q see chapter 4 and 5). The grain surfaces of RL I_2111 are completely coated by authigenic and cement minerals. Those of RL I_4146 are covered by authigenic and cement minerals and slightly dissolved. For sample RL_I 5041 the surfaces of the grains are both, strongly dissolved and overgrown with authigenic and cement minerals, as shown in 3-D images. The roughness parameter values of sample RL I_2111 are the largest while those of samples RL I_4146 and RL I_5041 are small at low resolution (10x magnification with CLSM), giving the morphology of the grains. The grain surfaces of sample RL I_2111 vary largely in their roughness. They are more complex due to large distances between the highest peak and deepest valley, showing a wide height deviation of the surface and strong asymmetry of the height distribution. On the other hand, for samples RL I_4146 and RL I_5041, the grain surfaces are less complex.

At high resolutions (50x and 100x magnifications) of the CLSM analysis, the grain roughness is characterised in details for the analysed surface area. On the same analysed area, the surface roughness observed at 100x magnification is always of lower roughness than that at 50x magnification (Chapter 4). At the nanometre size resolution with AFM analysis, the roughness features are ruled by the authigenic and cement minerals. The analysed roughness at the different scales of observation reveals that decreasing the analysed surface area by a factor of 2 does not decrease R_q by the same factor. The decrease deeply depends on the kind of authigenic and cement minerals covering the grain surfaces, such as the R_q value of sample RL I_2111_Qu_4 is 6.61 μm ; 4.83 μm and 26.7 nm, of sample RL I_4146_Qu_3: 9.29 μm ; 9.2 μm and 21.12 nm and of RL I_5041_Qu_2: 5.42 μm ; 1.57 μm and 26.46 nm respectively, using CLSM at 50x and 100x magnification and using AFM it is difficult to follow which values are CLSM and which are AFM. Decreasing the analysed surface area by a factor is not correlative to decrease the R_q by the same factor. The diagenetic coating of the sample RL I_2111_Qu_4 is predominantly of illite-chlorite and illite, of the sample RL I_4146_Qu_3, it is illite and of the sample RL I_5041_Qu_2, it is chlorite. The roughness of illite-chlorite is higher than that of illite or chlorite and the roughness of chlorite is higher than of illite, as shown by the (R_q) average values (Chapter 5).

The authigenic minerals and cements overlapping on the grain surfaces, which are facing into the pore space (Figure 4.3 and 4.5), built an irregular pore structures as shown by the R_q values at the different observations. The pore structures are similar to a model, which describes the natural appearance of pore spaces in sedimentary rocks, the so – called “pigeon – hole” model (Pape et al., 1987a) (see figure 6.1).

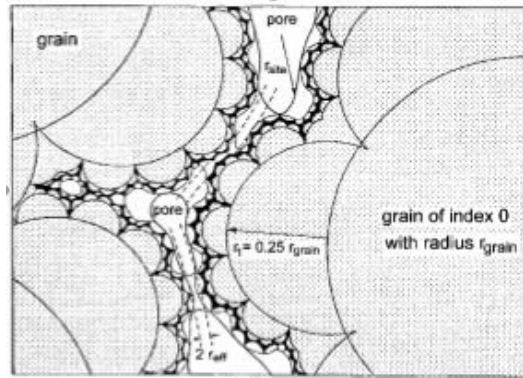


Figure 6.1 A sedimentary rock according to the “pigeon hole” model showing pore space geometry with radii r_{site} and hydraulic model capillaries with effective radii r_{eff} (Pape et al., 1987a).

A comparison of the root mean square roughness (R_q) values (CLSM and AFM) and the fractal dimension D values with the formation factor F values shows good agreements with the work by (Drobek et al, 2011). The D value close to 3 shows the grain surfaces with a complex structure found in sample RL I_2111 with a large R_q value, high roughness and a large formation factor F . In contrast, when the D value is lower than 3, it is showing the grain surfaces with a less complex structure, as visible in sample RL I_5041, with a small R_q value, low roughness (Chapter 4) and a small formation factor F (Chapter 5).

The roughness of the grain surfaces is a factor which restricts fluid flow through pores, determines the adhesion forces of the fluid to the pore wall and thus is related to the amount of hydrocarbon kept on the mineral/grain surfaces and in pore spaces. Enabling fluid flow between connected pores via pore throats in sandstones is of great interest in petroleum extraction. As stated above, the grain roughness has also a significant impact on the wetting and adhesion forces of fluids on the mineral surfaces. The characterisations of adhesion and wetting will be studied in further investigations.

7. CONCLUSION

The sediments of Rotliegend sandstone reservoir rocks from a well of the Lower Saxony Basin in northern Germany, taken a depth of 2081 m – 5049 m, were sourced from weathered plutonic and metamorphic rocks with predominant quartz, alkaline feldspar and plagioclase and subordinately contain rock fragments of volcanic clasts. The detrital fragments were deposited in fluvial or shallow water environments and underwent bed load transport with multiple phases of recycling. The porosity and permeability of the sandstones largely varies depending on the burial depth and the volume of the pore filling cements. The porosity is increasing in concordance with the burial depth because the deeper the sediment was buried and the less cement it contains in the pore spaces the higher is the porosity and permeability of the sandstones. These are two essential factors for the accumulation and the flow of hydrocarbons through rocks. Moreover, the geometry of the internal pore spaces and the rugged connection paths which are caused by the surface roughness, are crucial factors in sandstone reservoir rocks because of the effect of reduced flow diameters. The main cause for changes of the flow diameters are the growth of authigenic minerals on grain surfaces in post depositional stages.

The sediments analysed were affected by a complicated diagenetic alteration. Authigenic minerals and cements were formed in the form of pore fillings and grain coatings during diagenesis, leading to a decrease in porosity, permeability and a change of the grain shape, grain surface and pore geometry. In the early stage of diagenesis, illite, illite – smectite and illite – chlorite growth took shape surrounding the grains and small proportions of authigenic feldspar overgrowth on grains occurred. The predominantly quartz cement filled pore spaces and calcite, anhydrite and halite cements also precipitated at this stage. In the burial diagenetic phase, highly dissolved (corrosion) feldspars and lithic grains caused the widespread precipitation of albite cement and illite and chlorite in pore spaces. Subsequently, calcite cement filled into the pore spaces and further replaced the dissolved grains.

During diagenesis the crystallisation of authigenic minerals and the precipitation of cements in pores and on grain surfaces of the investigated sandstone reservoir rocks (Chapter 3) resulted in the change of grain morphology, grain roughness and pore geometry. Three investigated samples of RL I_2111, RL I_4146 and RL I_5041 reveal the characteristics of

the grain surface which base on the calculated parameters R_p , R_v , R_z , R_a , R_q , R_{sk} , R_{ku} derived from CLSM analysis and R_q extracted from CLSM and AFM analysis.

The three sandstone samples contain predominantly quartz grains. The morphology of the quartz grains has changed during diagenesis. The grain surfaces of sample RL I_2111 are completely covered by authigenic and cement minerals, which are very rough, displaying the largest parameter values. The grain surfaces of sample RL I_4146 are both coated with authigenic and cement minerals and are slightly dissolved. The grain surfaces of sample RL I_5041 are strongly intended by dissolution and overgrown with authigenic and cement minerals showing less roughness with the smaller parameter values. The investigated grain roughness characteristics are significantly connected to the original grain surface, the overgrowth of cement minerals, and to the kind of authigenic minerals crystallised during the diagenesis. For the analysis and characterisation of the grain surface roughness at high magnifications (50x, 100x), as analysed with CLSM, the root mean square roughness values (R_q) are used. They characterise the grain surface ruggedness, which formed the roughness of the pore walls and of the pore throats. The R_q values of the grain surfaces of sample RL I_5041 are the smallest and show the lowest roughness. Therefore, the fluid flow through the pore spaces in this sample was the highest as supported also by permeability measurements (Table 3.1, chapter 3). In contrast, the samples RL I_2111 and RL I_4146 feature larger R_q values and rougher pore surfaces and hence a restricted fluid flow. To identify the distinction of grain roughness due to the overgrowth of the different authigenic minerals on grain surfaces, their roughness was analysed on nanometre scale with AFM.

The analysis and authigenic mineral determination with SEM moreover revealed, that most of the grain surfaces are coated by authigenic minerals forming micro pores without preferential arrangement. The dominant authigenic minerals covering the grain surfaces are illite - chlorite, illite and chlorite. The roughness of illite - chlorite is the highest with the largest R_q compared to chlorite and illite, while the roughness of chlorite is higher than that of illite. The illite - chlorite is common in sample RL I_2111 and the illite is predominant in samples RL I_4146 and RL I_5041. Therefore, the roughness of the grain surfaces of the sample RL I_2111 is higher than those of the samples RL I_4146 and RL I_5041. Additionally, in the sample RL I_4146, the authigenic quartz with high roughness is more frequent than in the sample RL I_5041 so that the roughness of the grain surfaces in the sample RL I_4146 is higher. Authigenic quartz, anhydrite, calcite, halite and calcite precipitated on illite minerals

are less common in the three investigated samples. Their R_q values are therefore insufficient to show their roughness

A high surface roughness results in a large interface between the grain surfaces and fluids. Therefore, depending on surface tension and viscosity of the fluid, the grain surfaces of the sample RL I_2111 may have a larger contact area with fluids than those of the samples RL I_4146 and RL I_5041. The grain surfaces of the sample RL I_2111 may have an extensive wetting behaviour and higher adhesion forces compared to the other samples. On the contrary, the grain surfaces of the samples RL I_4146 and RL I_5041 may have less wetting and adhesive force. These results show the strong influence of the nano-scaled grain roughness on the surface wetting and adhesion properties of sandstones.

Additionally, the pore geometry of the three studied samples is altered due to the filling of cements and authigenic minerals. Almost all pore networks in sample RL I_2111 are filled by cements. Pore spaces in sample RL I_4146 are partly filled by quartz, calcite cements and albite and illite minerals, and pore throats are also blocked by these cements. Open pores are connected and less occupied by cement and authigenic minerals in sample RL I_5041. Therefore, the capacity of storage and fluid flow through the pores in the sample RL I_5041 is high compared to the constricted flow in the samples RL I_2111 and 4146. The permeability of the sample RL I_5041 is the highest of the three investigated samples.

The characterisation of grain surface and pore geometry of the investigated sandstone reservoir rocks can provide a better understanding of the storage capacity and fluid flow through pore spaces in rocks. The parameters R_p , R_v , R_z , R_a , R_q , R_{sk} , R_{ku} are essential for showing the global grain morphology and the pore geometry. Particularly the roughness of the pore walls and of the pore throats is shown in detail by the R_q parameter analysed at high magnifications (50x, 100x) with CLSM. The R_q parameter which is analysed downing to nanometre scale (AFM), reveals the ruggedness of the authigenic and cement minerals growing into pore spaces and the pore throats. The analysed grain roughness at the different micrometre scales downing to nanometre scale, shows the grain surface irregularity at distinct observed scales. These grain surfaces form a pore structure that is similar to the pigeon-hole model. Additionally, the features of the grain surface roughness can significantly influenced the grain surface wetting behaviours and adhesion properties. The results are an additional factor in order to calculate new models in exploitation and to enhance oil recovery.

REFERENCES

- Adams, A. E., MacKenzie, W. S. and Guilford, C., 1988. Atlas of sedimentary rocks under the microscope. Great Britain, Longman Group UK Ltd.
- Aigner, T. and Bachmann, G.-H., 1992. Sequence-stratigraphic framework of the German Triassic. *Sedimentary Geology* 80, 115-135.
- Almon, W. R., 1981. Depositional environment and diagenesis of Permian Rotliegendes sandstones in the Dutch sector of the Southern North Sea.– In: Longstaffe, F.J. (ed.), *Clays and the Resource Geologist, Mineral. Association Canada Short Course Handbook 7*, 119-147.
- Altermann, W., Drobek, T., Frei, M., Heckl, W. M., Kantioler, M., Lieu, K. P., Stark, R. W. and Strobel, C., 2010. Surface and Wetting Properties of Diagenetic Minerals and Sedimentary Grains in Reservoir Rocks (NanoPorO). *Geotechnologien Science Report* 16, 65-75.
- Altermann, W., Stark, R. W., Drobek, T., Frei, M., Lieu, K. P. and Strobel, J. (2011). Nanomorphology and Wetting Properties of Sediment Grain and Porespace Surfaces (NanoPorO), Ludwig-Maximilians-Universität München, Department für Geo- und Umweltwissenschaften.
- Bachmann, G.-H. and Hoffmann, N., 1997. Development of the Rotliegend Basin in Northern Germany. *Geologisches Jahrbuch D103*, 9-31.
- Baldschuhn, R., Best, G. and Kockel, F., 1991. Inversion tectonics in the north-west German Basin. In: Spencer, A.M. (Ed), *Generation, Accumulation and Production of Europe's Hydrocarbons*. Special Publication of the European Association of Petroleum Geologists. Oxford University Press, Oxford 1, 149-159.
- Benek, R., Kramer, W., McKann, T., Scheck, M., Negendank, J. F. W., Korich, D., Heubscher, H. and Bayer, U., 1996. Permo-Carboniferous magmatism and relate subsidence of the NE German Basin. *Tectonophysics* 206, 379-404.
- Betz, D., Führer, F., Greiner, G. and Plein, E., 1987. Evolution of the Lower Saxony Basin. *Tectonophysics* 137, 127-170.
- Betz, D., Führer, F., Greiner, G., Plein, E., 1987. Evolution of the Lower Saxony Basin. *Tectonophysics* 137, 127-170.
- Blunt, M. J., 1998. Physically based network modeling of multiphase flow in intermediate-wet media. *Petroleum Science and Engineering* 20, 117-125.
- Brink, H.-J., Dürschner, H. and Trappe, H., 1992. Some aspects of the late and post-Variscan development of the Northwestern German Basin. *Tectonophysics* 207, 65-95.
- Butt, H. J., Graf, K. and Kappl, M., 2003. Chapter 7 Contact angle phenomena and wetting Wiley-VCH Verlag & Co.KGaA.
- Cai, J. C., Yu, B. M., Zou, M. Q. and Mei, M. F., 2010. Fractal Analysis of Surface Roughness of Particles in Porous Media. *Chinese Physics Letters* 27(2/024705), 1-4.
- Chae, B. G., Ichikawa, Y., Jeong, G. C., Seo, Y. S. and Kim, B. C., 2004. Roughness measurement of rock discontinuities using a confocal laser scanning microscope and the Fourier spectral analysis. *Engineering Geology* 72, 181-199.

- Choquette, P. W. and Pray, L. C., 1970. Geologic nomenclature and classification of porosity in sedimentary carbonates. *Bulletin-American Association of Petroleum Geologists* 54(2), 207-250.
- Clark, M. W., 1981. Quantitative shape analysis: a review *Math. Geology* 13(4), 303-320.
- Collinson, J. D., Jones, C. M., Blackburn, G. A., Besly, B. M., Archard, G. M. and McMahon, A. H., 1993. Carboniferous depositional systems of the southern North Sea, in Parker, J.R., ed., *Petroleum geology of northwest Europe*. Geological Society, London, *Petroleum Geology Conference series*.
- Cornford, C., 1998. *Source rocks and hydrocarbons of the North Sea*. London, Blackwell Scientific Publishers.
- Correns, C. W., 1950. Zur Geochemie der Diagenese. *Geochimica Cosmochimica Acta* 1, 49-54.
- Dickinson, W. R., 1985. Interpreting detrital modes of greywack and arkose. *Sedimentary Research* 40(2), 695-707.
- Diepenbroek, M., Bartholomä, A. and Ibbeken, H., 1992. How round is round? A new approach to the topic "roundness" by Fourier grain shape analysis. *Sedimentology* 39, 411-422.
- Donaldson, E. C., Chilingarian, G. V. and Yen, T. F., 1985. *Enhanced oil recovery, I fundamentals and analyses*. Netherlands, Elsevier Science.
- Drobek, T., Kantioler, M., Lieu, K. P., Altermann, W., Frei, M., Strobel, J. and Stark, R. W., 2010. Pore surface topography in sandstone reservoirs. *Schriftenreihe Deutsche Gesellschaft Geowissenschaften (SDGG)*. 145-146.
- Drobek, T., Strobel, J., Park, S., Lieu, K. P., Altermann, W., Lemmel, H., Lindner, P. and Stark, R. W., 2011. Small Angle Neutron Scattering Analysis of Porous Reservoir Rocks. *International Symposium of the Society of Core Analysts, Austin, Texas, USA*.
- Drolon, H., Druaux, F. and Faure, A., 2000. Particles shape analysis and classification using the wavelet transform. *Pattern Recognition Letters* 21, 473-482.
- Drolon, H., Hoyez, B., Druaux, F. and Faure, A., 2003. Multiscale roughness analysis of particles: Application to the classification of detrital sediments. *International Association for Mathematical Geology*.
- Drong, H. J., Plein, E., Sannemann, D., Schuepbach, M. A. and Zimdars, J., 1982. Der Schneverdingen-Sandstein des Rotliegenden - eine äolische Sedimentfüllung alter Grabenstrukturen. *Zeitschrift der Deutschen Geologischen Gesellschaft* 133, 699-725.
- Falke, H., 1976. Problems of the continental Permian in the Federal Republic of Germany.- In: Falke, H. (ed.), *The Continental Permian in Central, West, and South Europe*. Dordrecht (Reidel). 38-52.
- Folk, R. L., 1951. Stages of texture maturity on sedimentary rocks. *Sedimentary Research* 21, 127-130.
- Folk, R. L., 1974, 1980. *Petrology of Sedimentary Rocks*. Austin, Texas 78703, Hemphill Publishing Company.
- Fredrich, J. T., Greaves, K. H. and Martin, J. W., 1993. Pore geometry and transport properties of Fontainebleau sandstone. *International journal of rock mechanics and mining sciences & geomechanics abstracts*.

- Füchtbauer, H., 1974. Zur Diagenese fluviatiler Sandsteine. *Geologische Rundschau* 63, 904-924.
- Gast, R. E., 1988. Rifting im Rotliegenden Niedersachsens. *Geowissenschaften* 4(6), 115-122.
- Gast, R. E., 1991. The Perennial Rotliegend Saline Lake in NW Germany. *Geologisches Jahrbuch Reihe A* 119, 25-59.
- Gaupp, R., 1996. Diagenesis types and their application in diagenesis mapping.– *Zbl. Geologie und Paläontologie* 1, 1994(11/12), 1183-1199.
- Gaupp, R., Gast, R. and Forster, C., 2000. Late Permian Playa Lake Deposits of the Southern Permian Basin (Central Europe).– In: Gierlowski-Kordesch, E.H. and Kelts, K.R. (eds.), *Lake basins through space and time. AAPG Studies in Geology* 46, 75-86.
- Gaupp, R., Matter, A., Platt, J., Ramseyer, K. and Walzebeck, J.P. , 1993. Diagenesis and Fluid Evolution of Deeply Buried Permian (Rotliegende) Gas Reservoirs, Northwest Germany. *AAPG Bull* 77(7), 1111-1128.
- Gautier, D. L., 2003. Carboniferous-Rotliegend Total Petroleum System Description and Assessment Results Summary. U.S. Geological Survey Bulletin 2211.
- Gebhardt, U., Helmuth, H.-J., Kleditzsch, O. and Süßmuth, S., 1995. Havel-Subgroup.– In: Plein, E. (ed.), *Norddeutsches Rotliegendbecken, Rotliegend-Monographie Teil II*, Courier Forschungsinstitut Senckenberg 183, 110-121.
- George, G. T. and Berry, J. K., 1993. A new palaeogeographic and depositional model for the Upper Rotliegend, offshore The Netherlands. *First Break* 12, 147-158.
- George, G. T. and Berry, J. K., 1997. Permian Upper Rotliegend synsedimentary tectonics, basin development and palaeogeography of the southern North Sea, in Ziegler, P., Turner, P., and Daines, S.R., eds., *Petroleum geology of the southern North Sea. Geological Society of London Special Publication* 123, 31-61.
- Glennie, K. W., 1972. Permian Rotliegendes of Northwest Europe Interpreted in Light of Modern Desert Sedimentation Studies. *AAPG Bulletin* 56(6), 1048-1071.
- Glennie, K. W., 1986. Development of NW Europe's Southern Permian gas basin, in Brooks, J., Goff, J., and van Hoorn, B., eds., *Habitat of Palaeozoic gas in northwest Europe. Geological Society of London Special Publication* 23, 3-22.
- Glennie, K. W. and Buller, A. T., 1983. The Permian Weissliegend of NW Europe: the partial deformation of aeolian dune sands caused by the Zechstein transgression. *Sedimentary Geology* 35, 43-81.
- Glennie, K. W., Mudd, G. and Nagtegaal, P. J. C., 1978. Depositional environment and diagenesis of Permian Rotliegendes sandstones in Leman Bank and Sole Pit areas of the UK southern North Sea. *Geological Society* 135, 25-34.
- Goes, S., Loohuis, J. J. P., Wortel, M. J. R. and Govers, R., 2000. The effect of plate stresses and shallow mantle temperatures on tectonics of northwestern Europe. *Global and Planetary Change* 27, 23-38.
- Good, R. J. and Am, J., 1952. A Thermodynamic Derivation of Wenzel's Modification of Young's Equation for Contact Angles; Together with a Theory of Hysteresis. *Chemical Society* 74, 5041-5042.
- Goodchild, M. W. and Whitaker, J. H. M., 1986. A petrographic study of the Rotliegendes Sandstone reservoir (Lower Permian) in the Rough Gas Field. *Clay Mineral* 21, 459-477.

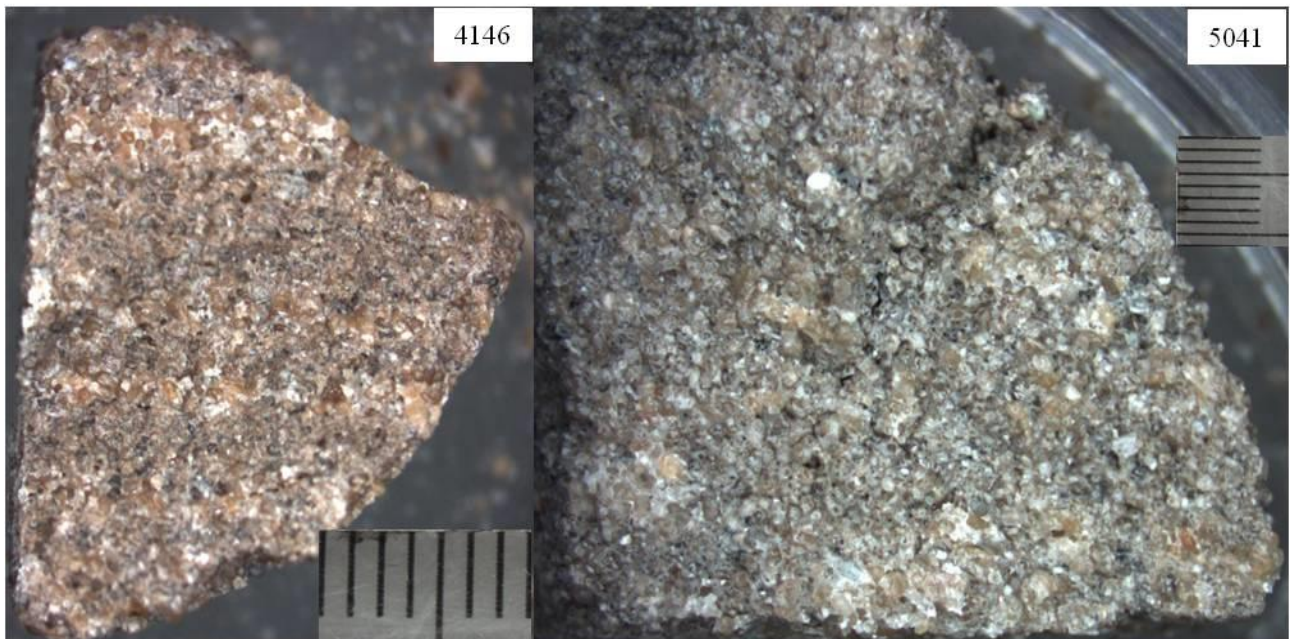
- Gramann, F., Heunisch, C., Klassen, H., Kockel, F., Dulce, G., Harms, F.-J., Katschorek, T., Mönning, E., Schudack, M., Schudack, U., Thies, D. and Weiss, M., 1997. Das Niedersächsische Oberjura-Becken - Ergebnisse interdisziplinärer Zusammenarbeit. *Zeitschrift der Deutschen Geologischen Gesellschaft* 148, 165-236.
- Hancock, N. J., 1978. Possible causes of Rotliegend sandstone diagenesis in northern West Germany. *Geological Society* 135, 35-40.
- Hayes, J. B., 1970. Polytypism of chlorite in sedimentary rocks. *Clay Mineral* 18, 285-306.
- Hazlett, R. D., 1992. On surface roughness effects in wetting phenomena. *Adhesion Science and Technology* 6(6), 625-633.
- Humphreys, B., Smith, S. A. and Strong, G. E., 1989. Authigenic chlorite in late Triassic sandstones from the Central Graben, North Sea. *Clay Mineral* 24, 427-444.
- Kamusewitz, H. and Possart, W., 2003. Wetting and scanning force microscopy on rough polymer surfaces: Wenzel's roughness factor and the thermodynamic contact angle. *Applied Physics A76*, 899-902.
- Kempe, A., Jamitzky, F., Altermann, W., Baisch, B., Markert, T. and Heckl, W. M., 2004. Discrimination of Aqueous and Aeolian Paleoenvironments by Atomic Force Microscopy - A Database for the Characterisation of Martian Sediments. *Astrobiology* 4(1), 51-64.
- Kempe, A., Wirth, R., Altermann W., Stark R.W., Schopf, J. W. and W.M., H., 2005. Focussed Ion Beam Preparation and in situ Nanoscopic Study of Precambrian Acritarchs. *Precambrian Research* 140(36-54).
- Kiersnowski, H., Paul, J., Peryt, T. M. and Smith, D. B., 1995. Facies, Paleogeography, and Sedimentary History of the Southern Permian Basin in Europe.- In: Scholle, P.A., Peryt, T.M. and Ulmer-Scholle, D.S. (eds.), *The Permian of Northern Pangea, Sedimentary Basins and Economic Resources*. Berlin (Springer) 2, 119-136.
- Leeder, M. R. and Hardman, M., 1990. Carboniferous geology of the southern North Sea Basin and controls on hydrocarbon prospectivity, in Hardman, R.F.P., and Brooks, J., eds., *Tectonic events responsible for Britain's oil and gas reserves*. Geological Society of London Special Publication 55, 87-105.
- Leveille, G. P., Primmer, T. J., Dudley, G., Ellis, D., and Allinson, G. J., 1997. Diagenetic controls on reservoir quality in Permian Rotliegendes sandstones, Jupiter Fields area, southern North Sea.- In: Ziegler, K., Turner, P. and Daines, S.R. (eds.), *Petroleum geology of the Southern North Sea: Future and Potential*. Geological Society London Special Publications 123, 105-122.
- Liêu, K. P., Altermann, W., Stark, R. W., Drobek, T. and Frei, M., 2012. Characteristics of sandstone reservoir rocks from a well of the Northern German Basin. *PetroVietnam* 09, 21-25.
- Lieu, K. P., Drobek, T., Altermann, W. and Stark, R. W., 2010. Pore surface topography in sandstone reservoirs. *Proceedings International Symposium Hanoi Geoengineering, Vietnam National University*.
- Mälzer, H., Hein, G. and Zippelt, K., 1983. Height changes in the Rhenish Massif: determination and analysis. In: Fuchs, K., von Gehlen, K., Mälzer, H., Murawski, H., Semmel, A (Eds), *Plateau Uplift: The Rhenish Shield-A Case History*. Springer-Verlag, Berlin, 164-176.

- Mandelbrot, B., 1967. How long is the Coast of Britian? Statistical self-similarity and fractional dimension. *Science* 156(3775), 636-638.
- McCann, T., 1996. Pre-Permian of the north-east German Basin. *Geology* 31, 159-177.
- McCann, T., 1998. Sandstone composition and provenance of the Rotliegend of the NE German Basin. *Sedimentary Geology* 116, 177-198.
- Menéndez, B., David, C. and Nistal, A. M., 2001. Confocal scanning laser microscope applied to the study of pore and crack networks in rocks. *Computer and Geosciences* 27, 1101-1109.
- Menning, M., 1995. A Numerical Time Scale for the Permian and Triassic Periods: An Integrated Time Analysis.– In: Scholle, P.A., Peryt, T.M. and Ulmer-Scholle, D.S. (eds.), *The Permian of Northern Pangea. Paleogeography, Paleoclimates, Stratigraphy*, Berlin (Springer) 1, 77-97.
- Newland, D. E., 1993. Harmonic wavelet analysis. *Proceedings The Royal Society London A*(443), 203-225.
- Pape, H., 1999. Fractal geometry and fractal "music of the Earth" (according to a term of H. Cloos). *Zentralblatt Fur Geologie Und Palaontologie I*(9/10), 969-979.
- Pape, H. and Schopper, J. R., 1987a. Fractal description of the Falkenberg granite microfissure system as derived from petrophysical and microscopical investigations. *Geologie Jahrbuch E39*, 149-166.
- Petford, N., Davidson, G. and Miller, J. A., 1999. Pore structure determination using confocal scanning laser microscopy. *Physics and Chemistry of the Earth* 24(7), 563-567.
- Pettijohn, F. J., 1975. *Sedimentary rock*, Harper & Row.
- Pettijohn, F. J., Potter, P. E. and Siever, R., 1972. *Sand and sandstone*, Springer-Verlag Berlin.Heidelberg.
- Platt, J., 1991. The Diagenesis of Early Permian Rotliegend deposits from northwest Germany. *Dissertation, Bern University*. 367
- Platt, J., 1993. Controls on clay mineral distribution and chemistry in the early Permian Rotliegend of Germany. *Clay Mineral* 28, 393-416.
- Platt, J., 1994. Geochemical evolution of pore waters in the Rotliegend (Early Permian) of northern Germany. *Marine and Petroleum Geology* 11(1), 66-78.
- Plein, E., 1978. Rotliegend-Ablagerungen im Norddeutschen Becken. *Zeitschrift der Deutschen Geologischen Gesellschaft* 129, 71-97.
- Plein, E., 1993. Bemerkungen zum Ablauf der paläogeographischen Entwicklung im Stefan und Rotliegend des Norddeutschen Beckens. *Geologisches Jahrbuch A*(131), 99-116.
- Plein, E., 1995. Norddeutsches Rotliegendbecken, Rotliegend-Monographie Teil II.-Cour.Forsch. Institute Senckenberg-Frankfurt a.M, 183-193.
- Purvis, K., 1989. Zoned authigenic magnesites in the Rotliegend Lower Permian, southern North Sea *Sedimentary Geology* 65, 307-318.
- Purvis, K., 1992. Lower Permian Rotliegend sandstones, southern North Sea: a case study of sandstone diagenesis in evaporate – associated sequences. *Sedimentary Geology* 77, 155-171.

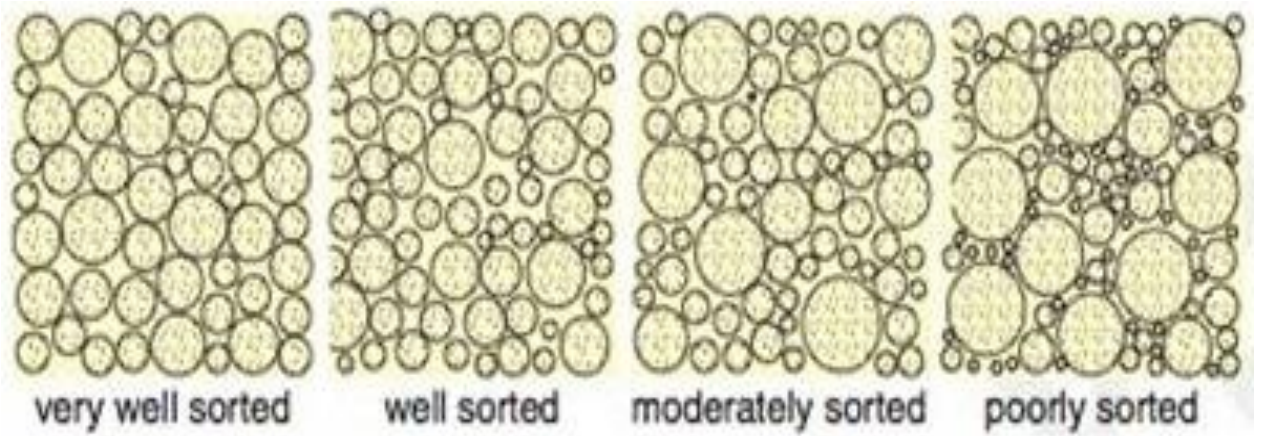
- Pye, K. and Krinsley, D. H., 1986. Diagenetic carbonate and evaporite minerals in Rotliegend aeolian sandstones of the southern North Sea: Their nature and relationship to secondary porosity development. *Clay Mineral* 21, 443-457.
- Rasmussen, B. and Glover, J. E., 1996. Fluid evolution interpreted from diagenetic assemblages and salinity data in Permo-Triassic sandstone, northern Perth Basin, Western Australia *Sedimentary Research* 66(3), 492-500.
- Rossel, N. C., 1982. Clay mineral diagenesis in Rotliegend aeolian sandstones of the southern North Sea. *Clay Mineral* 17, 69-77.
- Sannemann, D., Zimdars, J. and Plein, E., 1978. Der basale Zechstein (Al-T,) zwischen Weser und Emss. *Zeitschrift der Deutschen Geologischen Gesellschaft* 129, 33-69.
- Scheck, M. and Bayer, U., 1997. Configuration of the crust below the intracratonic Northeast German Basin: preliminary modelling results. *Europrobe Tesz, Alfred-Wegener-Stiftung, Köln*.
- Scheck, M. and Bayer, U., 1999. Evolution of the Northeast German Basin — inferences from a 3D structural model and subsidence analysis. *Tectonophysics* 313, 145-169.
- Schmidt, V. and McDonald, D. A., 1979. The role of secondary porosity in the course of sandstone diagenesis.— In: Scholle, P.A. and Schluger, P.R. (eds.), *Aspects of diagenesis*. SEPM Special Publications 26, 175-207; Tulsa.
- Schneider, J. and Gebhardt, U., 1993. Litho- und Biofaziesmuster in intra- und extramontanen Senken des Rotliegend (Perm, Nord- und Ostdeutschland). *Geologisches Jahrbuch - Reihe A* 131, 57-98.
- Schöner, R., 2006. Comparison of Rotliegend sandstone diagenesis from the northern and southern margin of the North German Basin, and implications for the importance of organic maturation and migration. *Dissertation, Jena University*. 230.
- Schröder, L., Plein, E., Bachmann, G. H., Gast, R. E., Gebhardt, U., Graf, R., Helmuth, H.-J., Pasternak, M., Porth, H. and Süßmuth, S., 1995. Stratigraphische Neugliederung des Rotliegend im Norddeutschen Becken. *Geologisches Jahrbuch - Reihe A* 148, 3-23.
- Seemann, U., 1982. Depositional facies, diagenetic clay minerals and reservoir quality of Rotliegend sediments in the Southern Permian Basin (North Sea). *Clay Mineral* 17, 55-67.
- Sen, D., Mazumder, S. and Tarafdar, S., 2002. Pore morphology and pore surface roughening in rocks: a small-angle neutron scattering investigation. *Materials Science* 37, 941-947.
- Taylor, J. B., Carrano, A. L. and Kandlikar, S. G., 2006. Characterisation of the effect of surface roughness and texture on fluid flow-past, present, and future. *International Journal of Thermal Sciences* 45, 962-968.
- Triolo, F., Triolo, A., Agamalian, M. M., Lin, J.-S., Heenan, R. K., Lucido, G. and Triolo, R., 2000. Fractal approach in petrology: combining ultra small angle, small angle and intermediate angle neutron scattering. *Applied Crystallography* 33, 863-866.
- Twenhofel, W. H., 1939. *Principles of sedimentation*, New York, London, McGraw-Hill Book Company.
- Van Wees, J. D., Stephenson, R. A., Ziegler, P. A., Bayer, U., McCann, T., Dadlez, R., Gaupp, R., Narkiewicz, M., Bitzer, F. and Scheck, M., 2000. On the Origin of the Southern Permian Basin, Central Europe - Mar. *Marine and Petroleum Geology* 17, 43-59.

- Walker, T. R., 1976. Diagenetic origin of continental red beds.- In: Falke, H. (ed.), The continental Permian in Central, West and South Europe. NATO Advance Study Institute C(22), 240-282.
- Wilson, M. D., 1992. Inherited grain-rimming clays in sandstones from eolian and shelf environments: Their origin and control on reservoir properties.- In: Houseknecht, D.W and Pittman, E.D. (eds.), Origin, Diagenesis, and Petrophysics of Clay Minerals in Sandstones SEPM Special Publications 47, 209-225; Tulsa.
- Young, T., 1805. An essay on the cohesion of fluids. Philosophical Transactions of the Royal Society of London 95, 65-87.
- Ziegler, P. A., 1982. Geological Atlas of Western and Central Europe. Amsterdam, Elsevier.
- Ziegler, P. A., 1990. Geological Atlas of Western and Central Europe.- Shell Intern. Amsterdam (Elsevier).
- Ziegler, P. A., 1992. European Cenozoic rift system. Tectonophysics 208, 91-111.

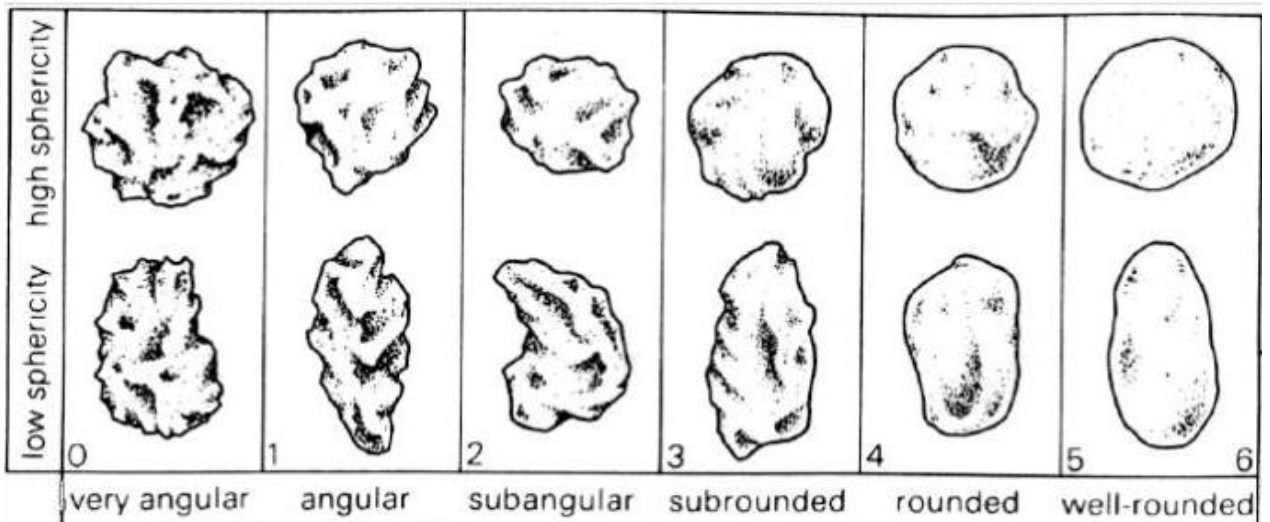
Appendix I: Macro samples, diagrams for estimation of grain sorting, categories of roundness for grains and grain size classification



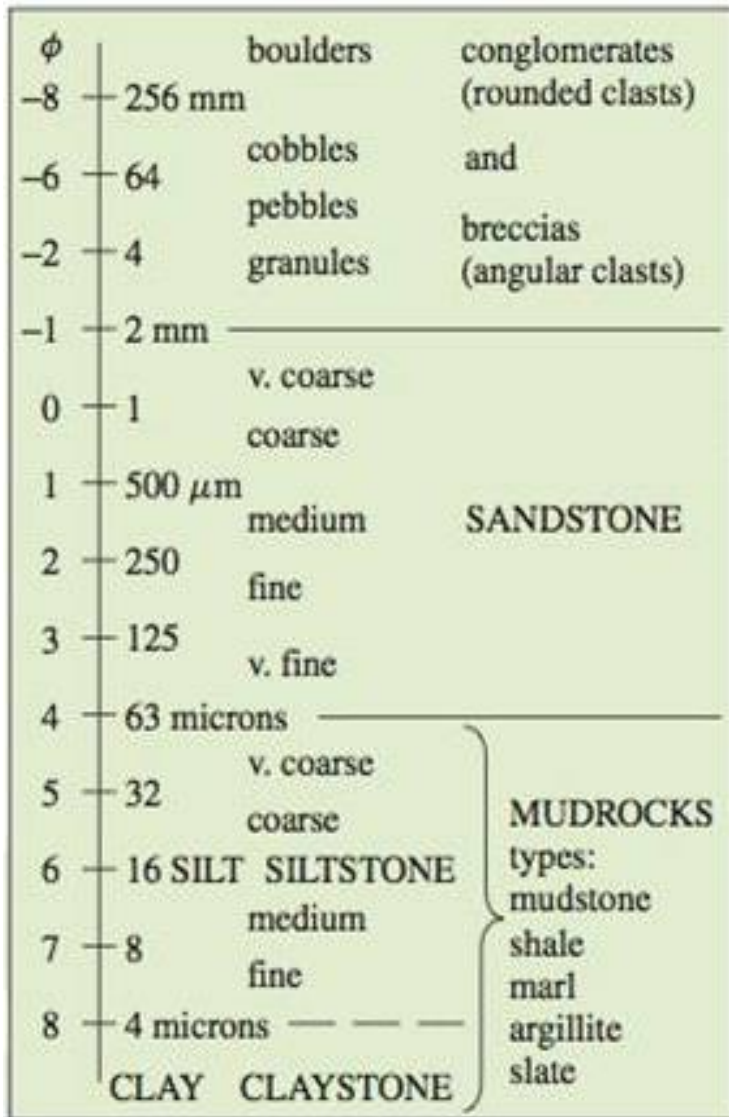
Appendix I.1: Samples RL I_2111, RL I_4146 and RL I_5041 are taken by binoculars.



Appendix I.2: Sorting diagrams using thin sections (after Pettijohn et al. 1973)



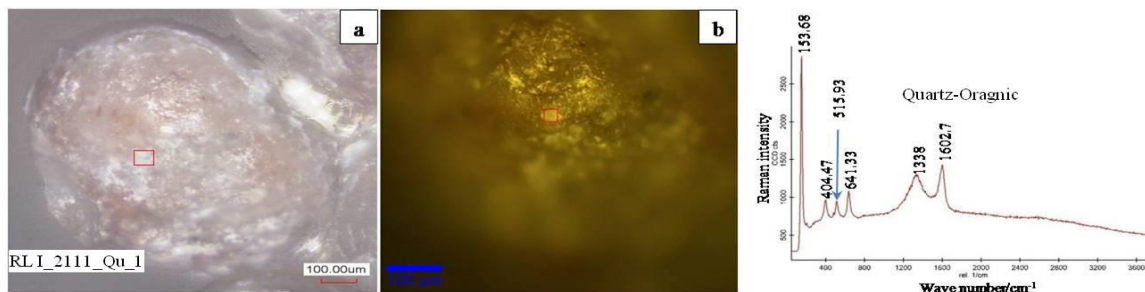
Appendix I.3: Categories of roundness for grain of low and high sphericity (after Pettijohn et al. 1973)



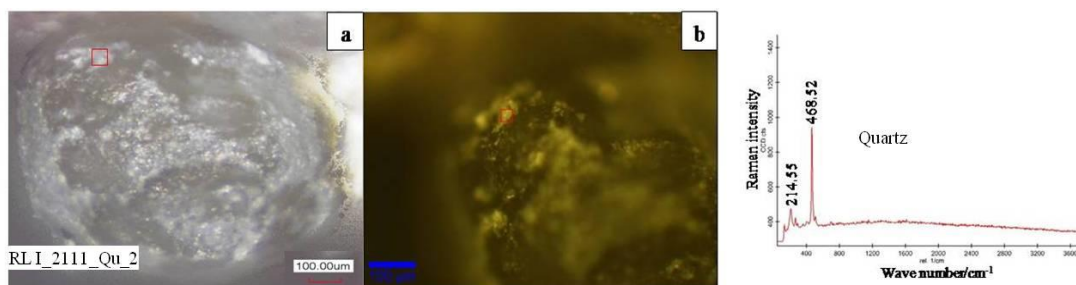
Appendix I.4: Grain size classification of sediments (Udden - Wentworth scale)

Appendix II: Raman spectroscopy spectra and Confocal Laser Scanning Microscope image

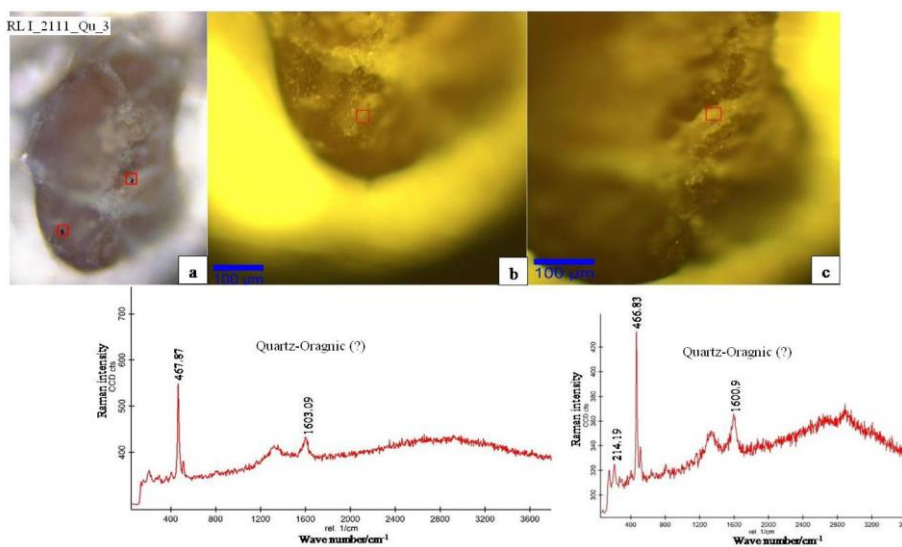
Raman spectroscopy image



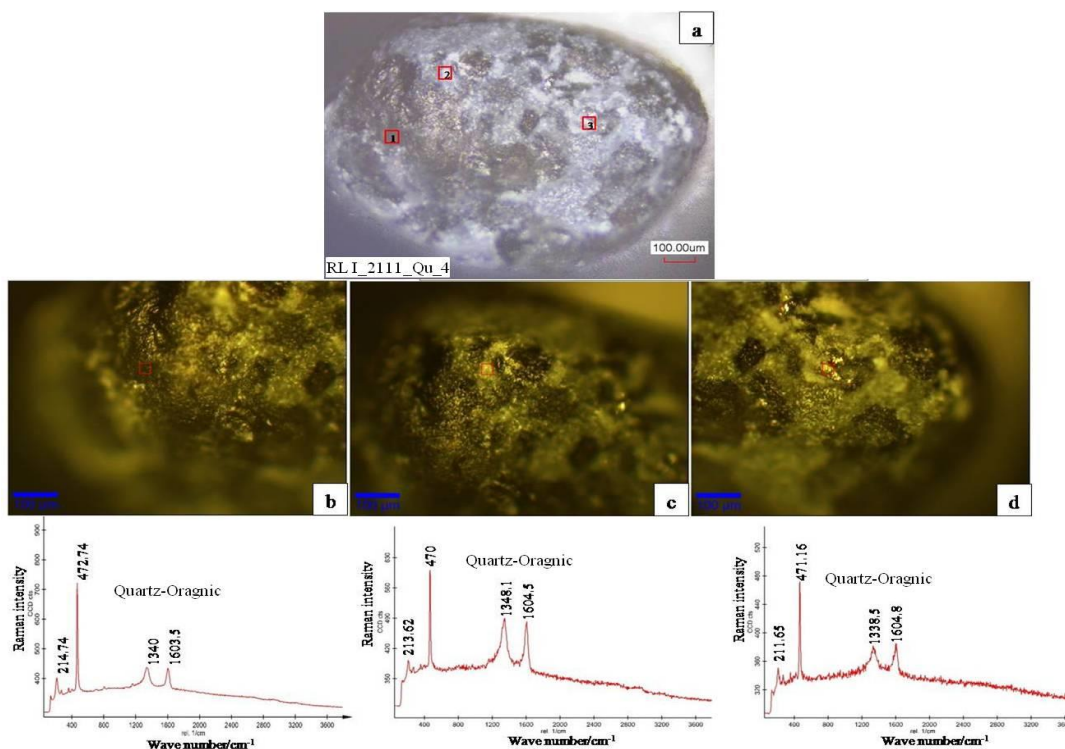
Appendix II.1: Sample RL I_2111_Qu_1, the Raman spectroscopy result shows the spectrum of quartz and organic matter with the present peak values of quartz: 153.68cm^{-1} ; 404.47cm^{-1} ; 515.93cm^{-1} and 614.33cm^{-1} and the peak values of coal: 1338cm^{-1} ; 1602.7cm^{-1} .



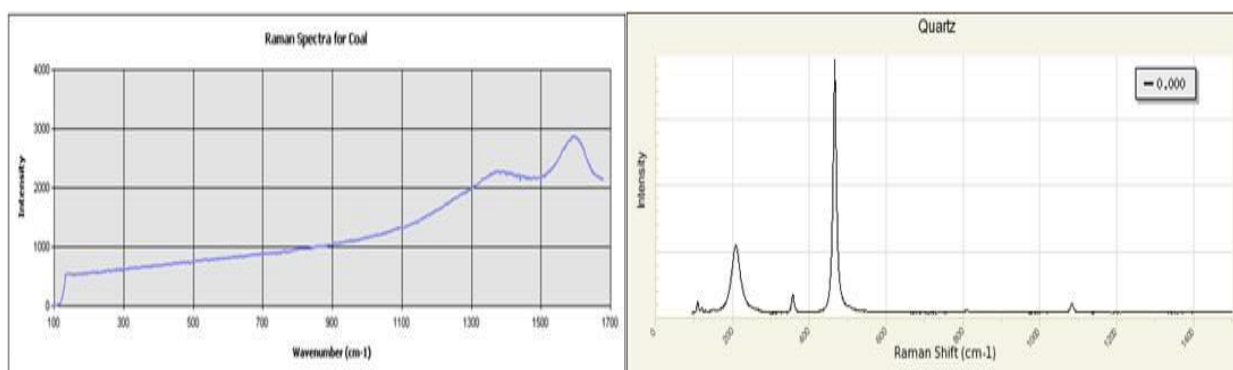
Appendix II.2: Sample RL I_2111_Qu_2, the Raman spectroscopy result is the spectrum of quartz with the present peak values of quartz: 214.55cm^{-1} ; 468.52cm^{-1} .



Appendix II.3: Sample RL I_2111_Qu_3, the Raman spectroscopy results show the spectra of quartz and organic matter with the present peak values of quartz: 214.19 cm^{-1} ; 466.83 cm^{-1} ; 467.87 cm^{-1} and the peak values of coal: 1603.09 cm^{-1} ; 1600.9 cm^{-1}



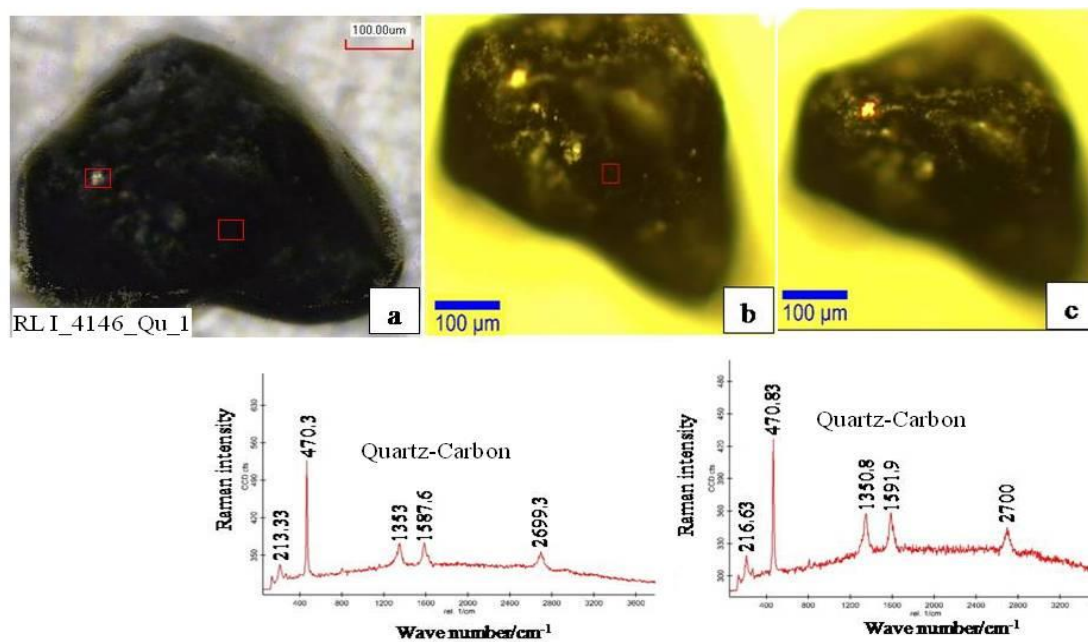
Appendix II.4: Sample RL I_2111_Qu_4, the Raman spectroscopy results are the spectra of quartz and organic matter with the present peak values of quartz: ranging 211.63-214.74 cm^{-1} and 470-472.74 cm^{-1} and the peak values of coal: ranging 1338.3-1349.1 cm^{-1} and 1603.5-1604.8 cm^{-1} .



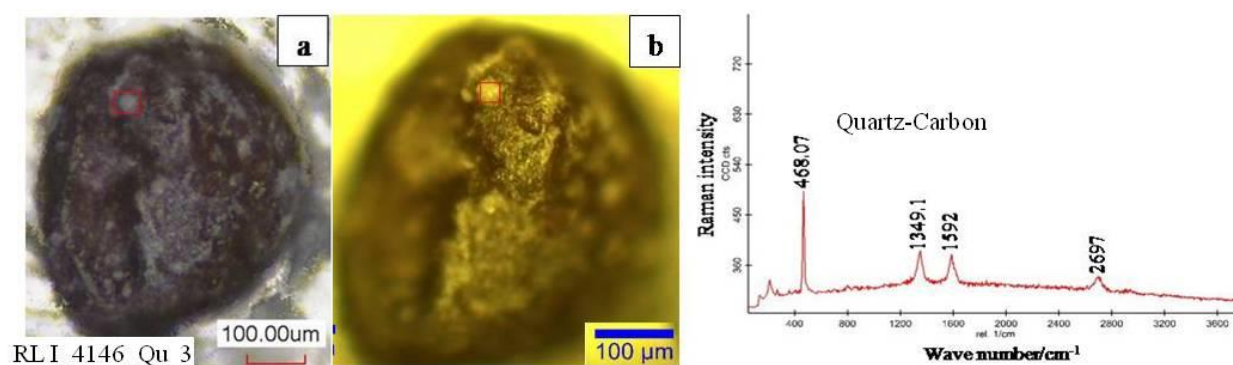
Appendix II.5: Reference of the Raman spectral database for quartz and coal

Appendix II.1-II.4: a). RL I_2111_Qu_1, RL I_2111_Qu_2, RL I_2111_Qu_3 and RL I_2111_Qu_4 samples showing images of grain overview, with CLSM images at 10x magnification. b, c and d images show the Raman spectroscopy images at 10x magnification and Raman spectra results. Red rectangles are spots analysed with Raman spectroscope. Appendix II.5 is the Raman spectra database for quartz and coal, maybe carbonaceous organic matter because of only grayish dark spots, grown over quartz surface. Coal and carbonaceous organic matter have the same primary composition, so the peak values are similar, the present peak values of quartz are

fundamental vibrations at $206\text{-}215\text{cm}^{-1}$; $463\text{-}472\text{cm}^{-1}$, and coal ranging $1300\text{-}1350\text{cm}^{-1}$; $1600\text{-}1650\text{cm}^{-1}$. The RL I_2111_Qu_2 Raman spectrum shows the presence of quartz through the peak values 214.55 and 468.32cm^{-1} .

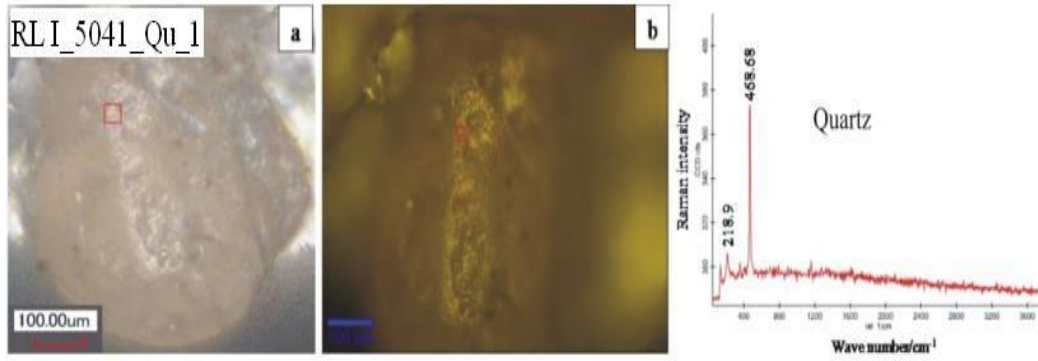


Appendix II.6: Sample RL I_4146_Qu_1, the Raman spectra show two peak values of quartz, ranging from $213.33\text{-}216.63\text{cm}^{-1}$ and $470.3\text{-}470.83\text{cm}^{-1}$ and of carbon $1350.8\text{-}1353\text{cm}^{-1}$ and $1587.6\text{-}1591.9\text{cm}^{-1}$.

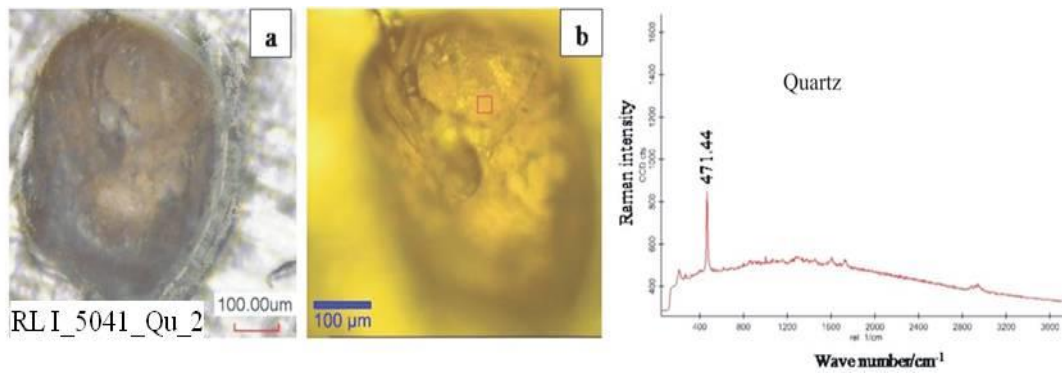


Appendix II.7: Sample RL I_4146_Qu_3, the Raman result shows the peak value of quartz at 468.07cm^{-1} , and carbon at $1349.1\text{-}1592\text{cm}^{-1}$.

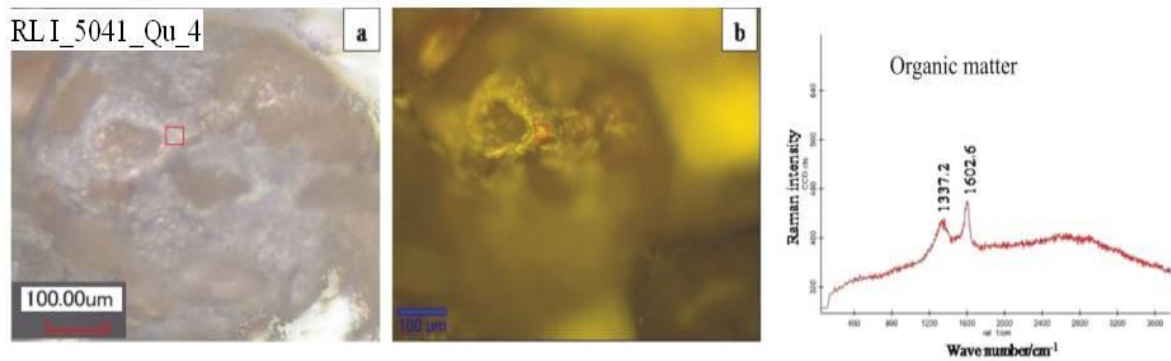
The figures (appendix II.6 and II.7) show the CLSM images of RL I_4146_Qu_1, RL I_4146_Qu_3 samples (a), Raman spectroscopy (b) (c) at 10x magnification and the corresponding Raman spectra, the red squares are the spots that are analysed for their mineralogy by Raman spectroscopy.



Appendix II.8: Sample RL I_5041_Qu_1, the Raman spectroscopy result is a spectrum of quartz with the present peak values at 218.9cm^{-1} and 468.68cm^{-1} .



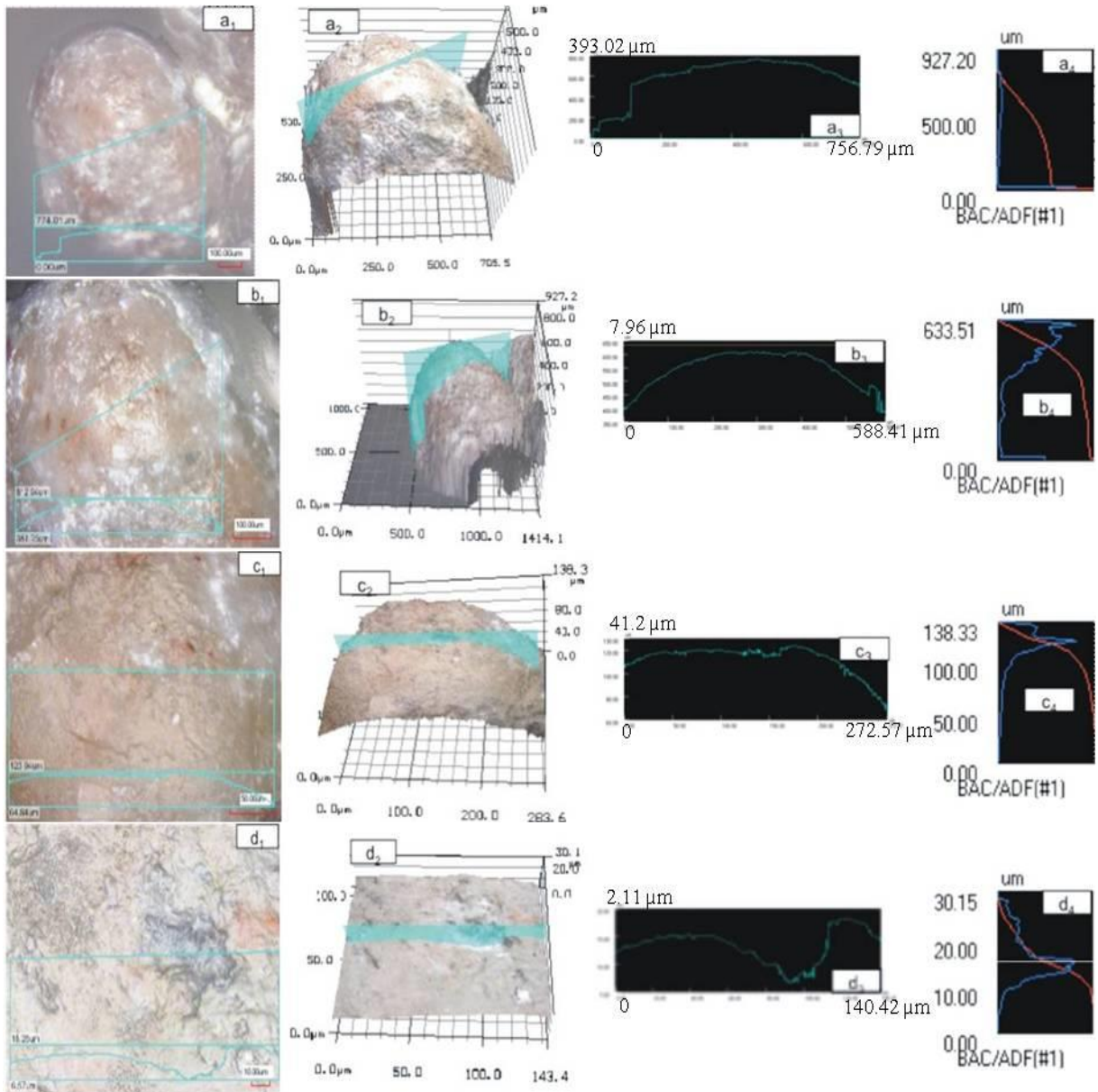
Appendix II.9: Sample RL I_5041_Qu_2, the Raman spectroscopy result shows a spectrum of quartz with the presence of only one peak value at 471.44cm^{-1} .



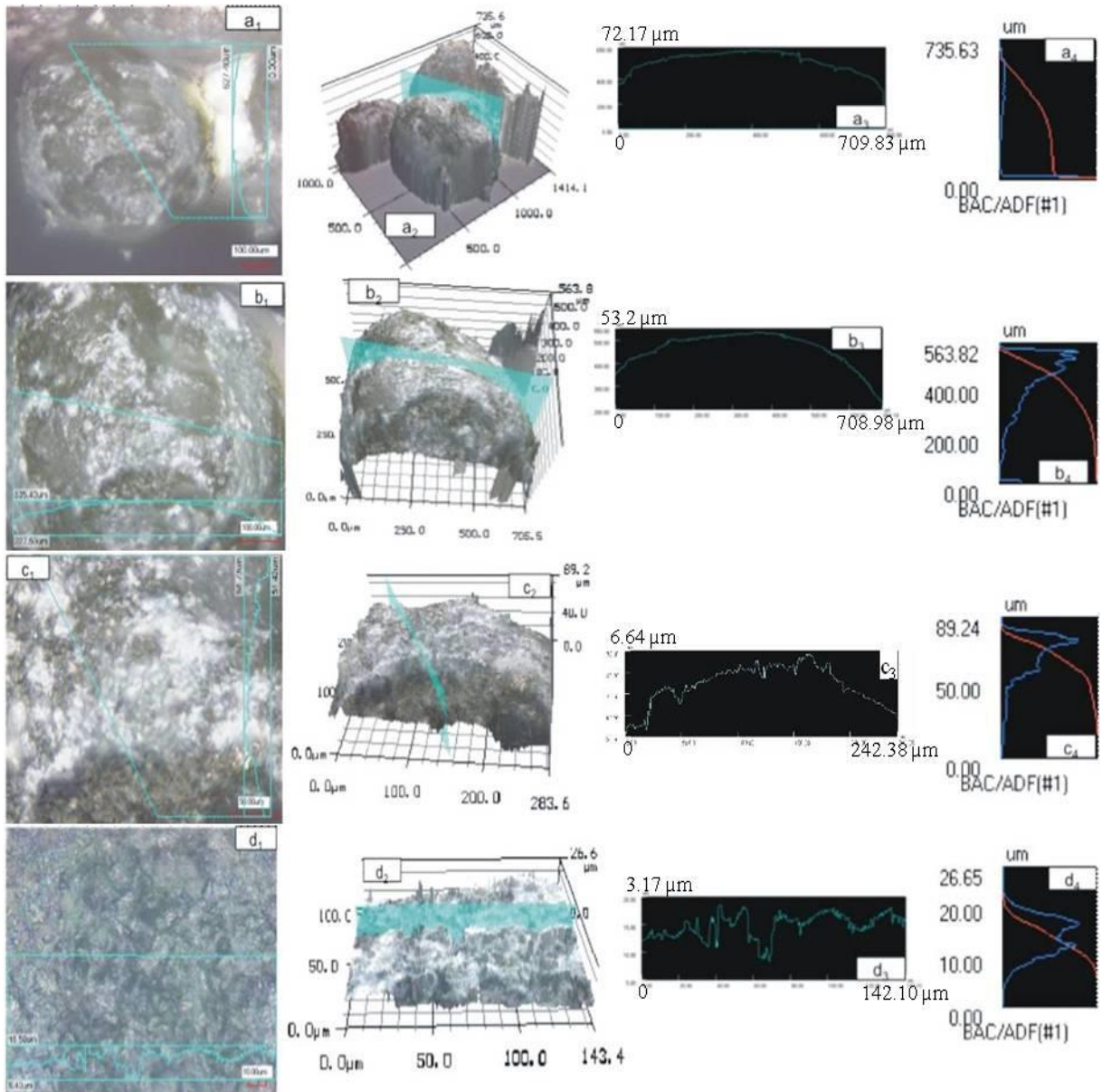
Appendix II.10: Sample RL I_5041_Qu_4, the Raman spectroscopy results in a spectrum with the present peak values at 1337.2cm^{-1} and 1602.6cm^{-1} representing organic matter.

Images of RL I_5041_Qu_1, RL I_5041_Qu_2, RL I_5041_Qu_4 grains are taken with the digital camera CLSM (a), the Raman spectroscopy (b) at 10x magnification and the Raman spectral results; the red rectangles are the spots that are analysed by Raman spectroscopy.

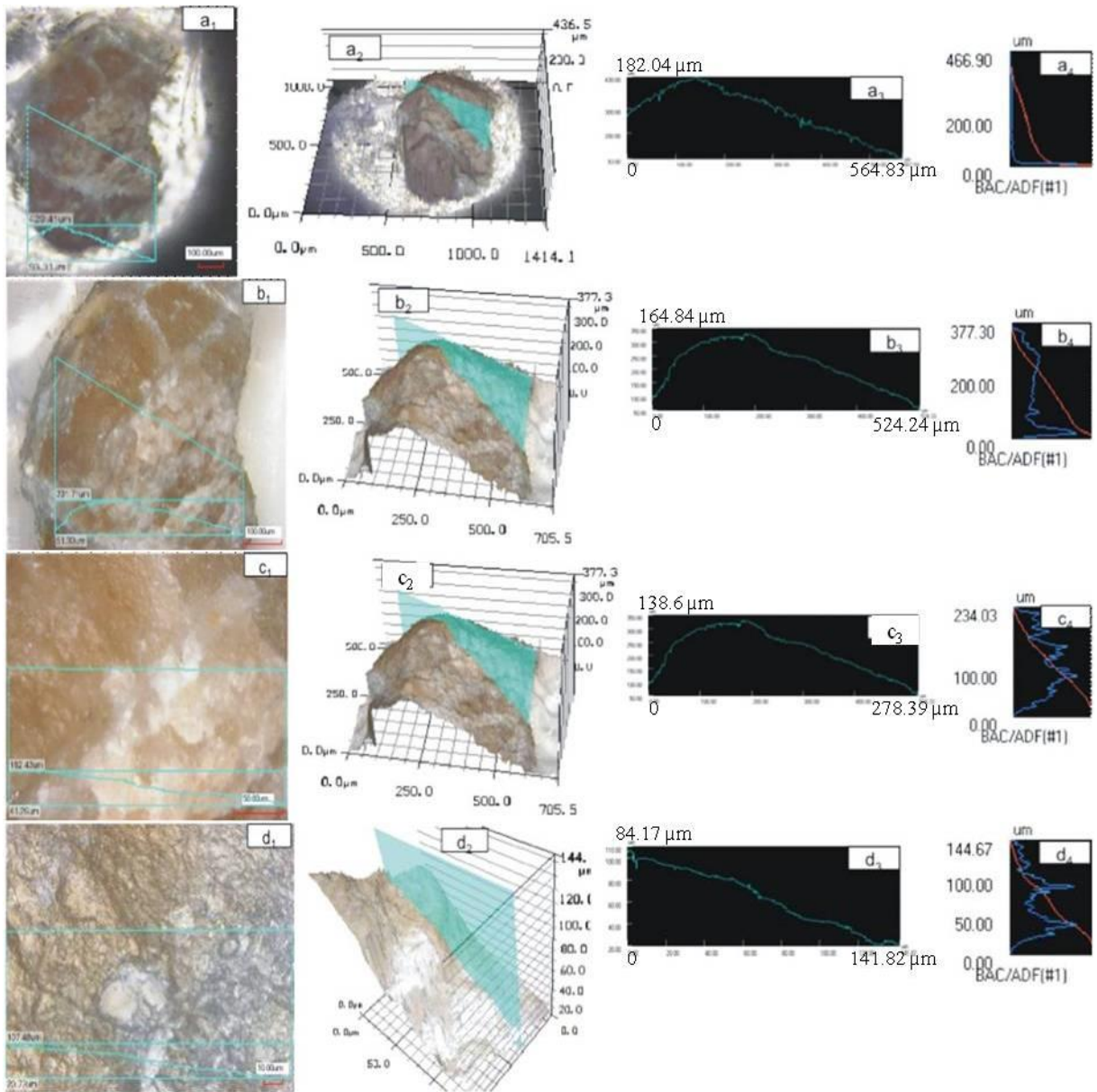
Confocal Laser Scanning Microscopy (CLSM)



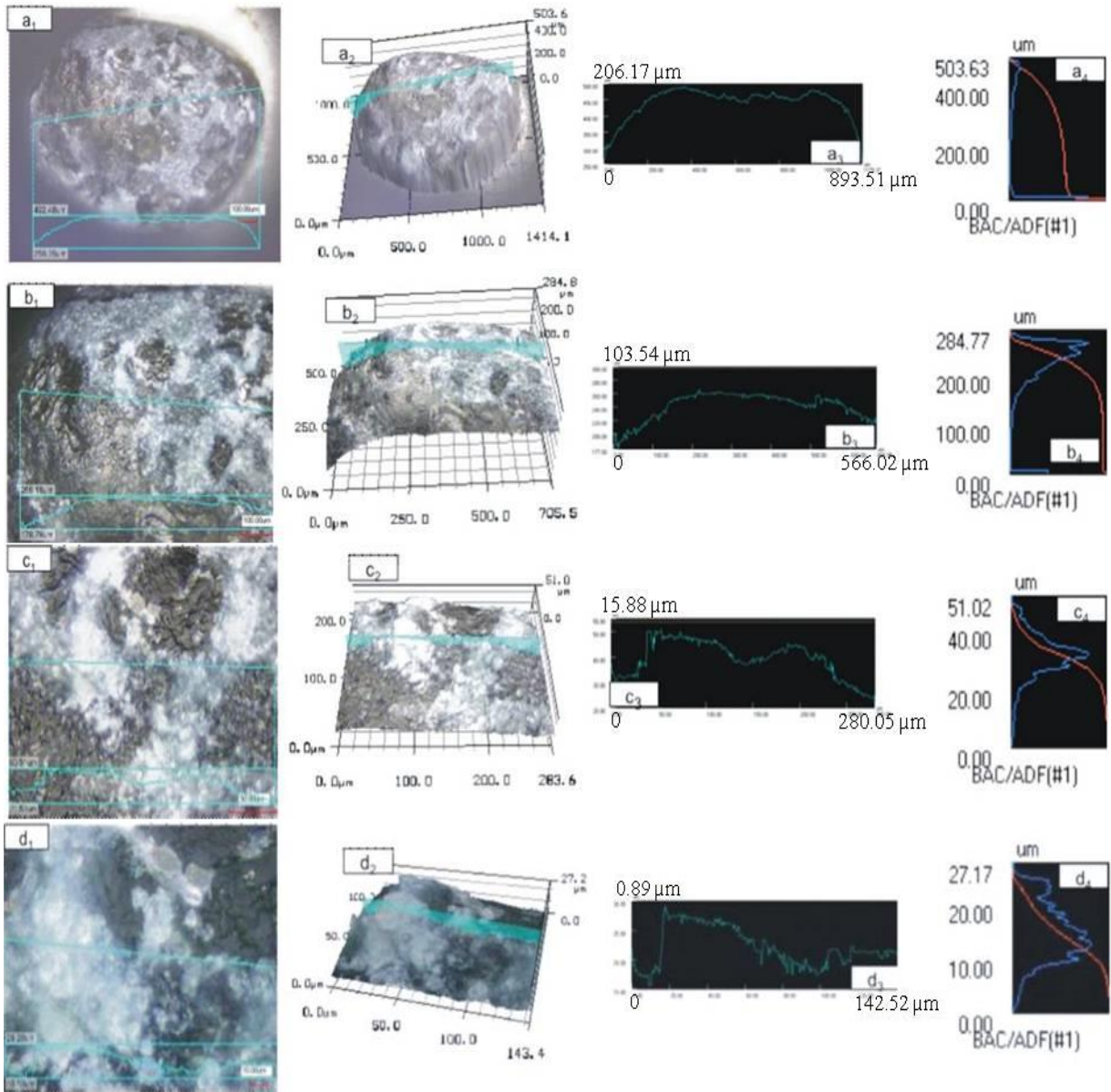
Appendix II.11: Sample RL I_2111_Qu_1, CLSM image shows a quartz grain analysed at 4 different magnifications a: 10x; b: 20x; c: 50x and d: 100x; a₁-d₁: 2D image; a₂-d₂: 3D image; a₃-d₃: profile and a₄-d₄: roughness profile. The quartz surface is shiny, sub-spheroid in shape, stained with hematite brown spots. The large magnification, image d₁, d₂ shows a small hole on the quartz grain surface, displayed a valley on d₃ line profile.



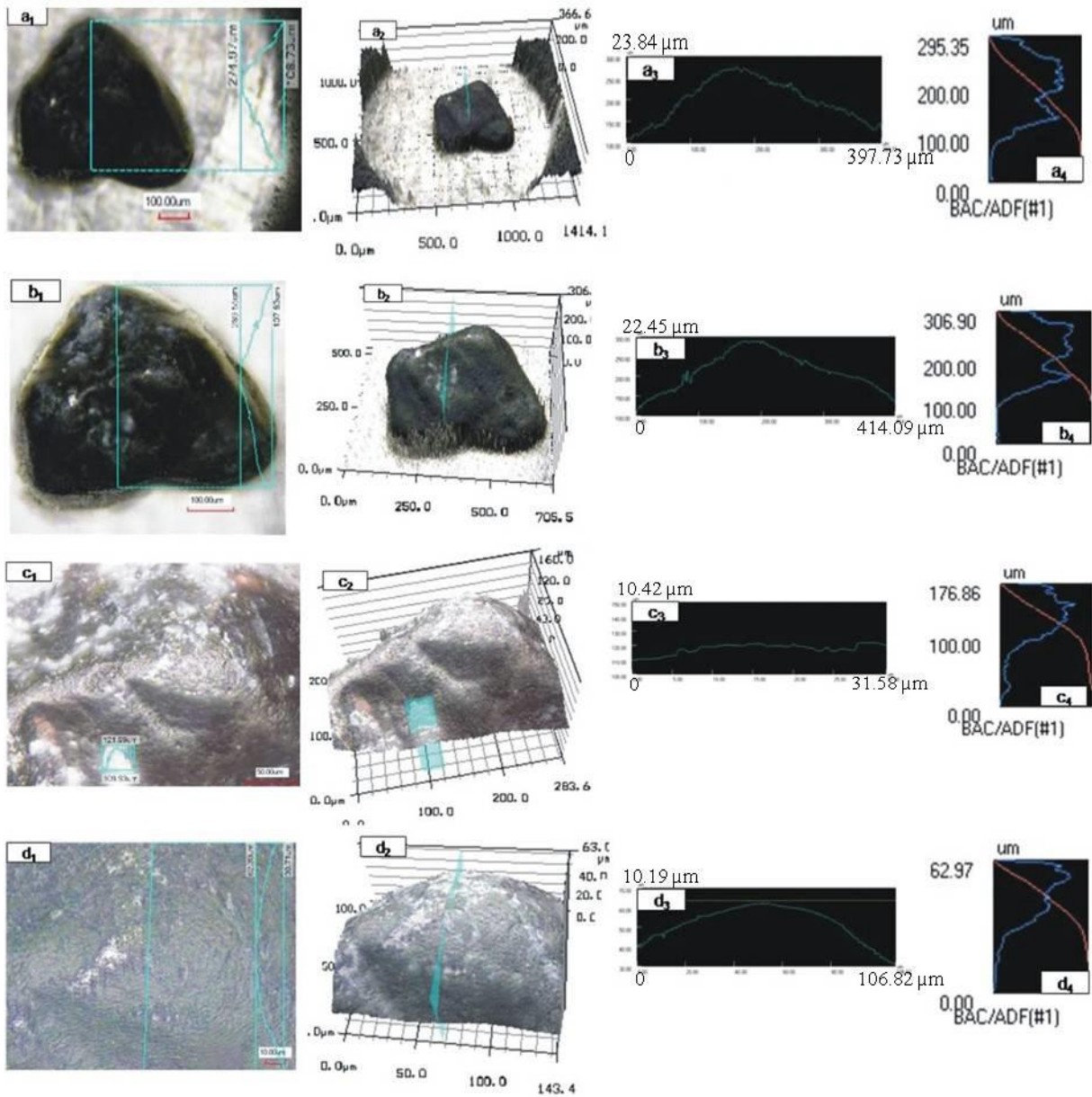
Appendix II.12: Sample RL I_2111_Qu_2, CLSM image of a quartz grain taken at 4 different magnifications a: 10x; b: 20x; c: 50x and d: 100x; a₁-d₁: 2D image; a₂-d₂: 3D image; a₃-d₃: profile and a₄-d₄: roughness profile. The quartz grain is well rounded and sub-spherical. The surface is coated by cement minerals so this surface is very rough as illustrated in the c₃, d₃ profiles taken at high magnifications (50x, 100x).



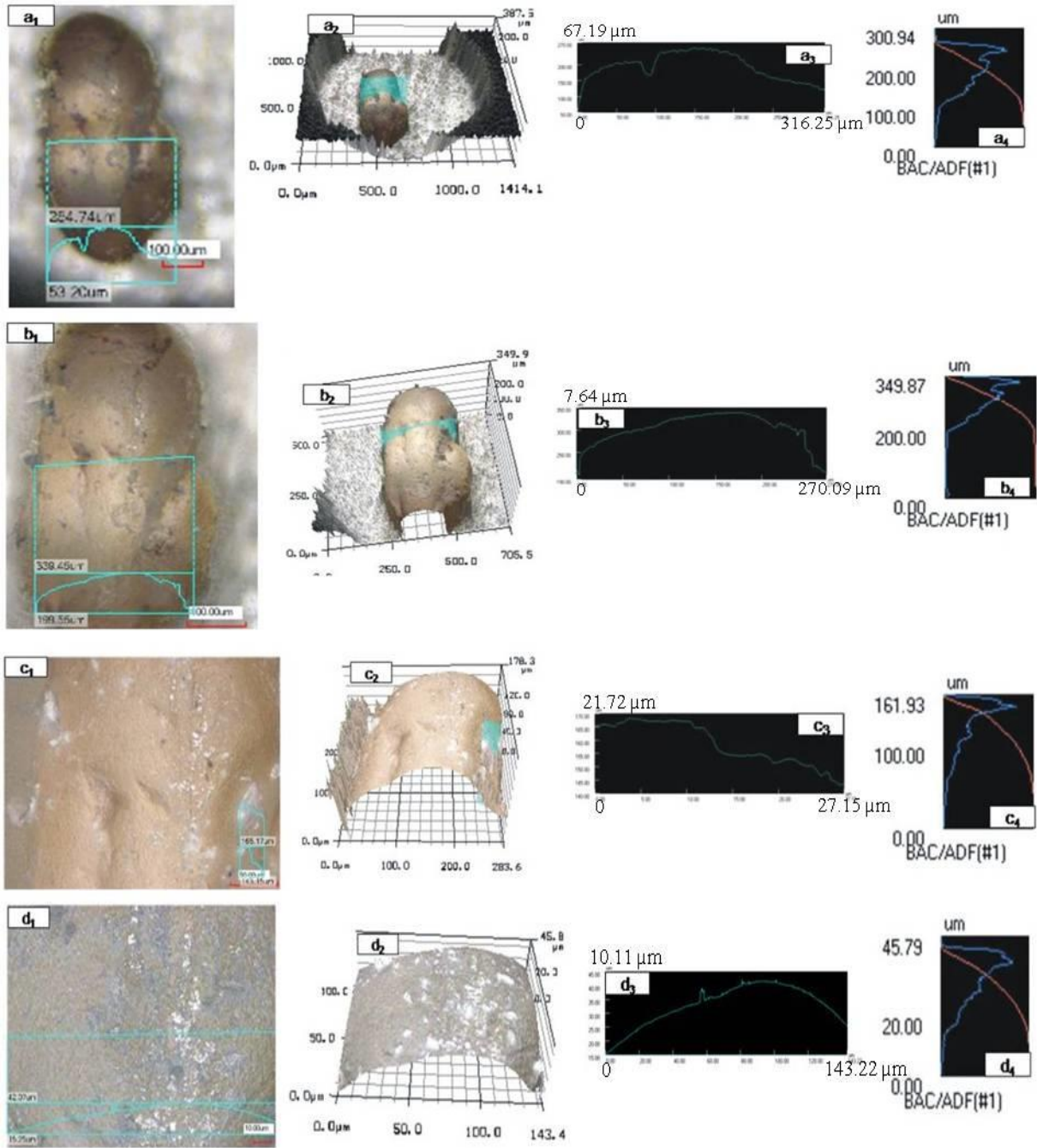
Appendix II.13: Sample RL I_2111_Qu_3, CLSM image of a quartz grain taken at 4 different magnifications a: 10x; b: 20x; c: 50x and d: 100x; a₁-d₁: 2D image; a₂-d₂: 3D image; a₃-d₃: profile and a₄-d₄: roughness profile. Cement minerals of white colour have grown on the quartz surface in the right images. This surface is very rough, and profile is lots peaks and valleys. The area with brown colour shows the non-overgrown surface of the grain.



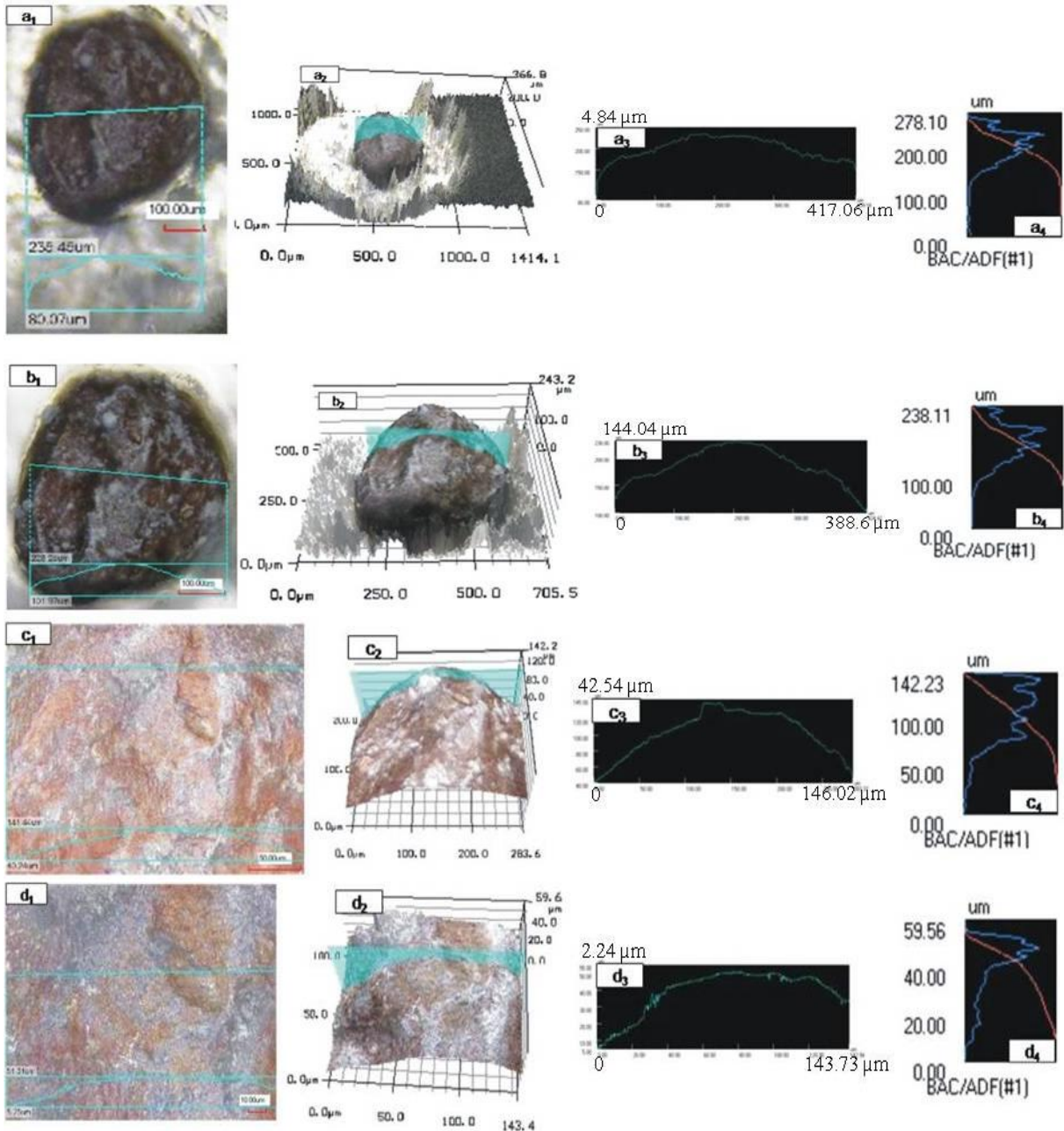
Appendix II.14: Sample RL I_2111_Qu_4, CLSM image of a quartz grain taken at 4 different magnifications a: 10x; b: 20x; c: 50x and d: 100x; a₁-d₁: 2D image; a₂-d₂: 3D image; a₃-d₃: profile and a₄-d₄: roughness profile. The quartz grain surface overview is unsmooth with the appearance of cement minerals, white colour areas and the dark colour part is the real surface, covered with organic matter. The cement mineral crystals grow over the quartz grain surface in left image d₁. The profile d₃ displays the quartz grain surface roughness with lots of high peaks and valleys.



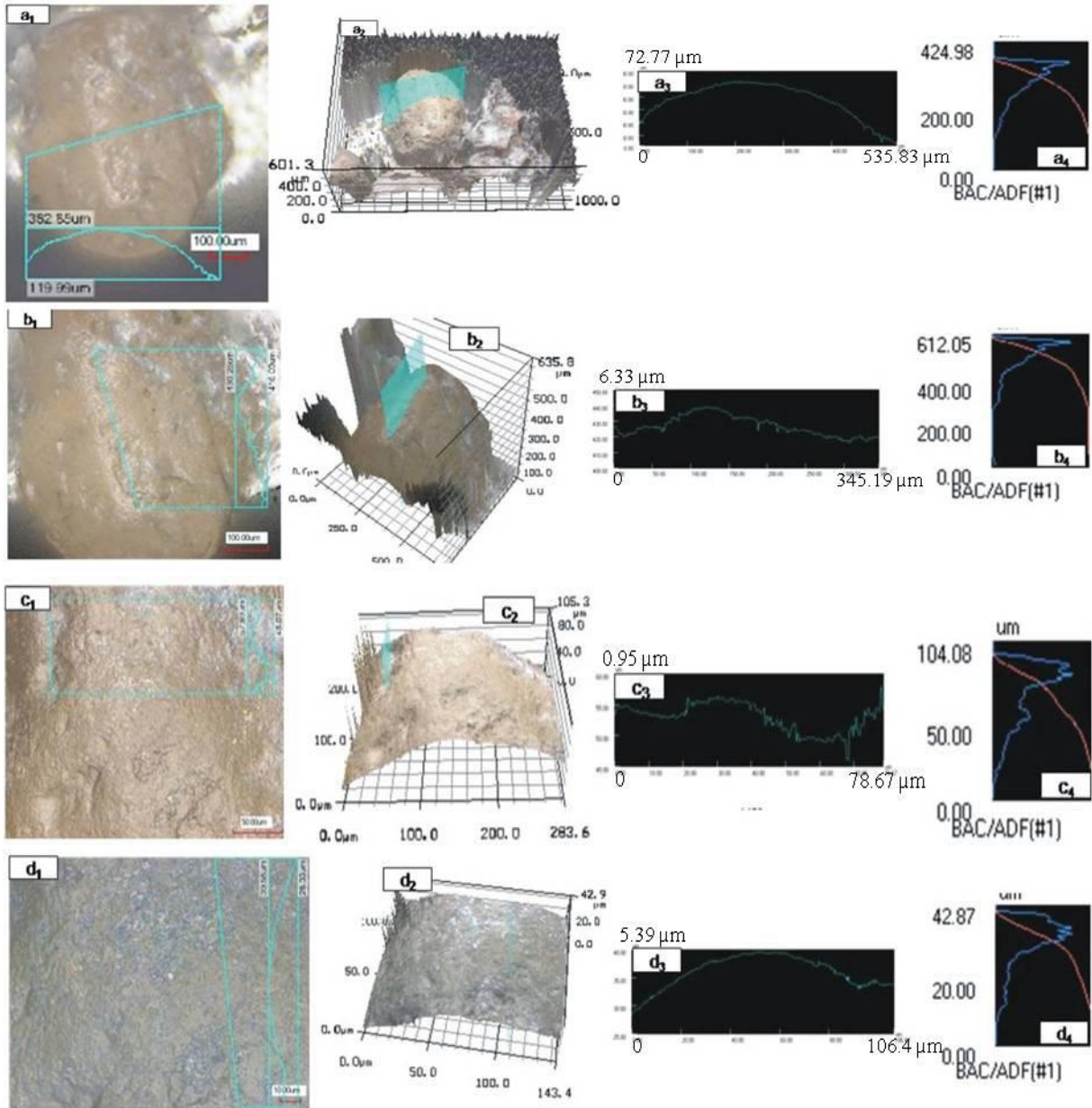
Appendix II.15: Sample RL I_4146_Qu_1, CLSM image of a quartz grain taken at 4 different magnifications a: 10x; b: 20x; c: 50x and d: 100x; a₁-d₁: 2D image; a₂-d₂: 3D image; a₃-d₃: profile and a₄-d₄: roughness profile. The quartz is completely coated by carbon of black colour and is engraved with holes, obvious in the bottom of the image c. The surface is concave-convex, as displayed in profiles with a lot of peaks and holes.



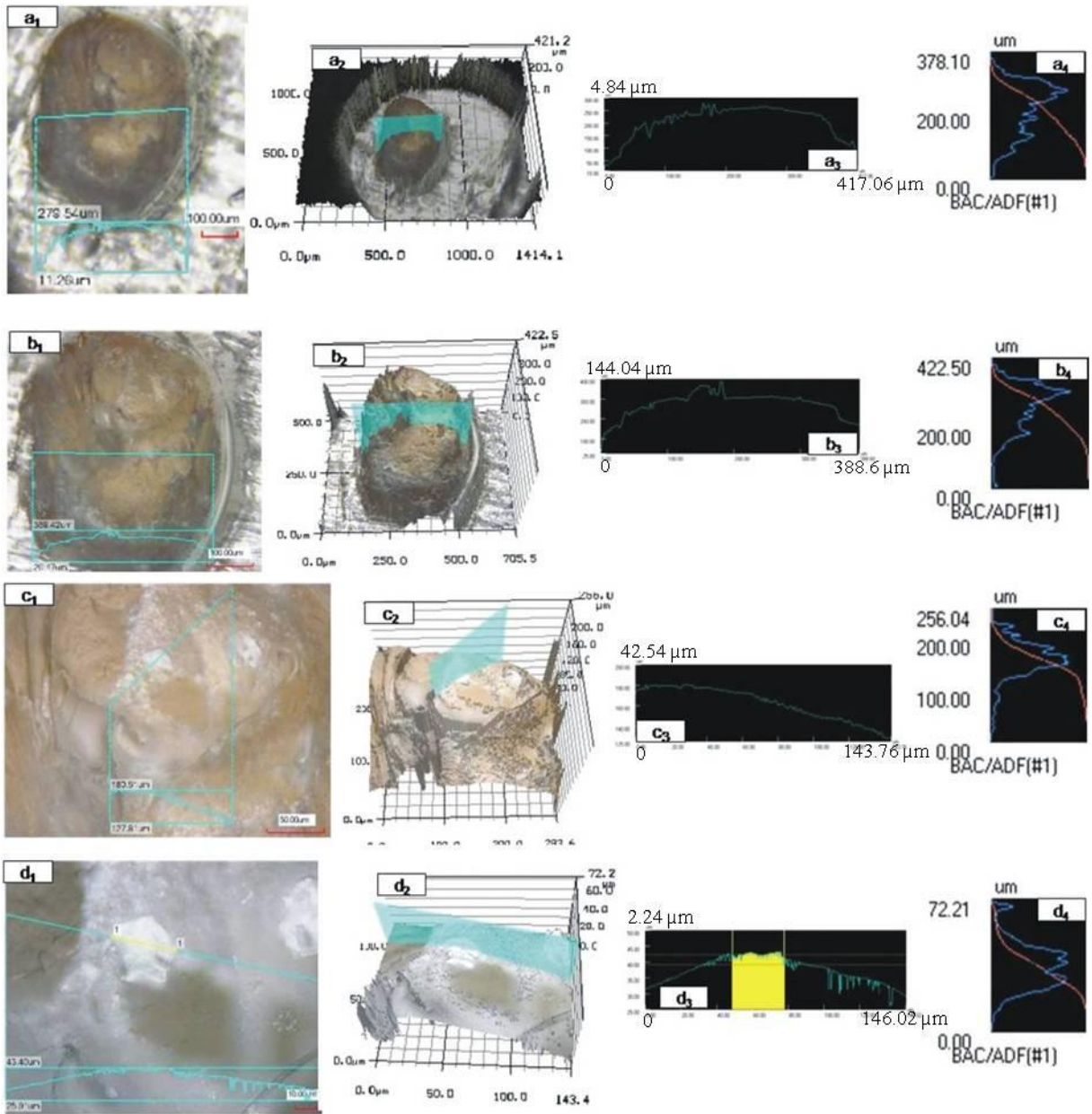
Appendix II.16: Sample RL I_4146_Qu_2, CLSM image of a quartz grain taken at 4 different magnifications a: 10x; b: 20x; c: 50x and d: 100x; a₁-d₁: 2D image; a₂-d₂: 3D image; a₃-d₃: profile and a₄-d₄: roughness profile. The quartz is rounded and of elongated shape, and the surface is fresh and shiny. The surface shows small holes (image c₁), and is scattered with white spots which are probably cement minerals (image d₁).



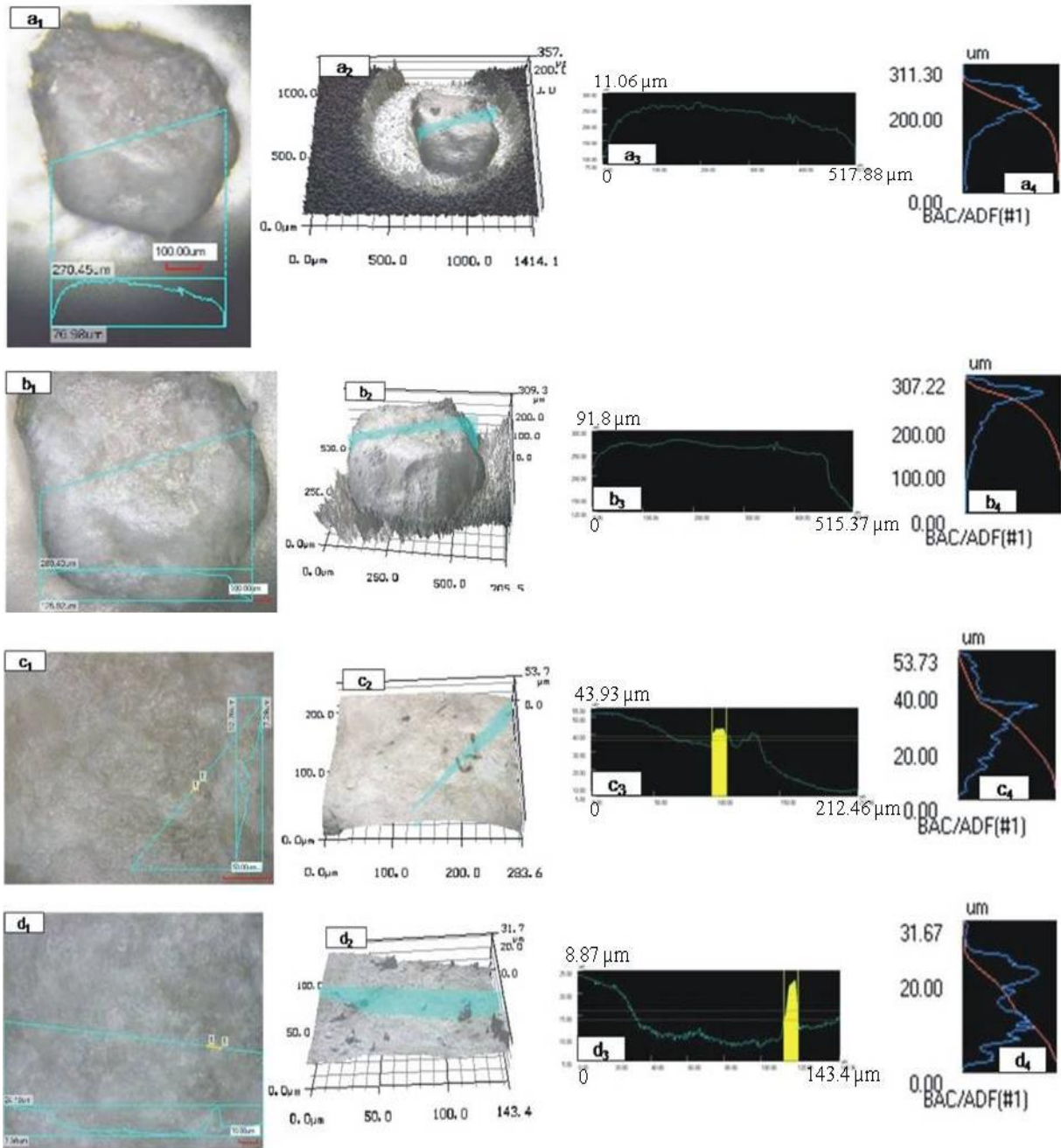
Appendix II.17: Sample RL I_4146_Qu_3, CLSM image of a quartz grain taken at 4 different magnifications a: 10x; b: 20x; c: 50x and d: 100x; a₁-d₁: 2D image; a₂-d₂: 3D image; a₃-d₃: profile and a₄-d₄: roughness profile. The quartz grain is a pale surface. The surface shows depressed areas with small holes, and scattered white spots which are probably cement minerals clearly seen in the c₂ image.



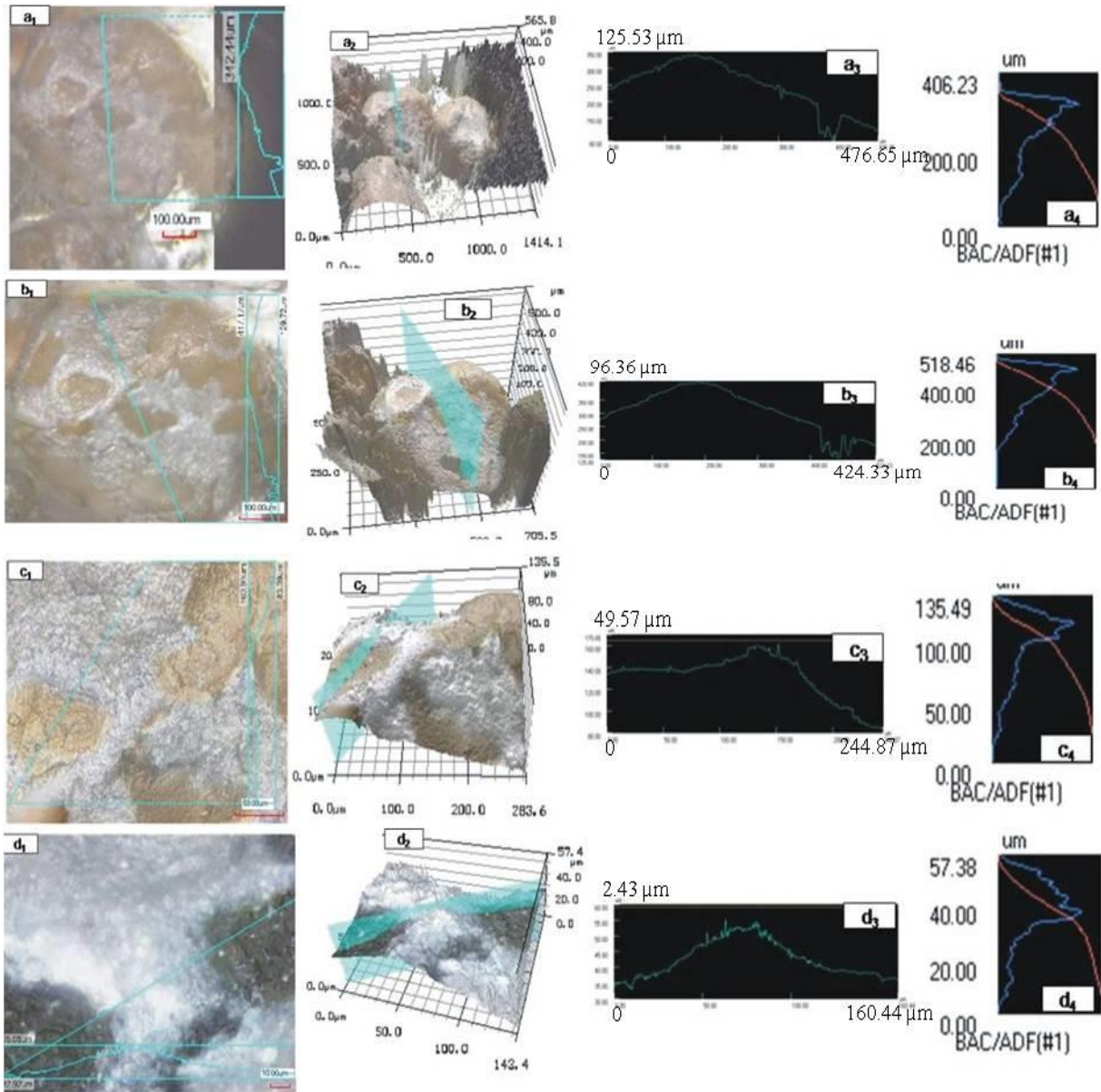
Appendix II.18: Sample RL I_5041_Qu_1, CLSM image of a quartz grain taken at 4 different magnifications a: 10x; b: 20x; c: 50x and d: 100x; a1-d1: 2D image; a2-d2: 3D image; a3-d3: profile and a4-d4: roughness profile. The surface of the quartz is shiny, with worked in holes, unsmooth. The surface is rough, typically the profiles b3, c3 show very rough curvature, which are irregular with high peaks and low valleys.



Appendix II.19: Sample RL I_5041_Qu_2, CLSM image of a quartz grain taken at 4 different magnifications a: 10x; b: 20x; c: 50x and d: 100x; a₁-d₁: 2D image; a₂-d₂: 3D image; a₃-d₃: profile and a₄-d₄: roughness profile. The quartz surface is shiny, locally pale due to a coating with cement minerals, which can be observed at the largest magnification in image d₁. The size of the mineral is 29.05 μm, marked yellow and the surface with tiny holes is displayed in the profile in d₃.



Appendix II.20: Sample RL I_5041_Qu_3, CLSM image of a quartz grain taken at 4 different magnifications a: 10x; b: 20x; c: 50x and d: 100x; a₁-d₁: 2D image; a₂-d₂: 3D image; a₃-d₃: profile and a₄-d₄: roughness profile. The feldspar surface is recessed and cement minerals grow on it, which can be seen as small crystals in d₂ and marked yellow in d₃ profile

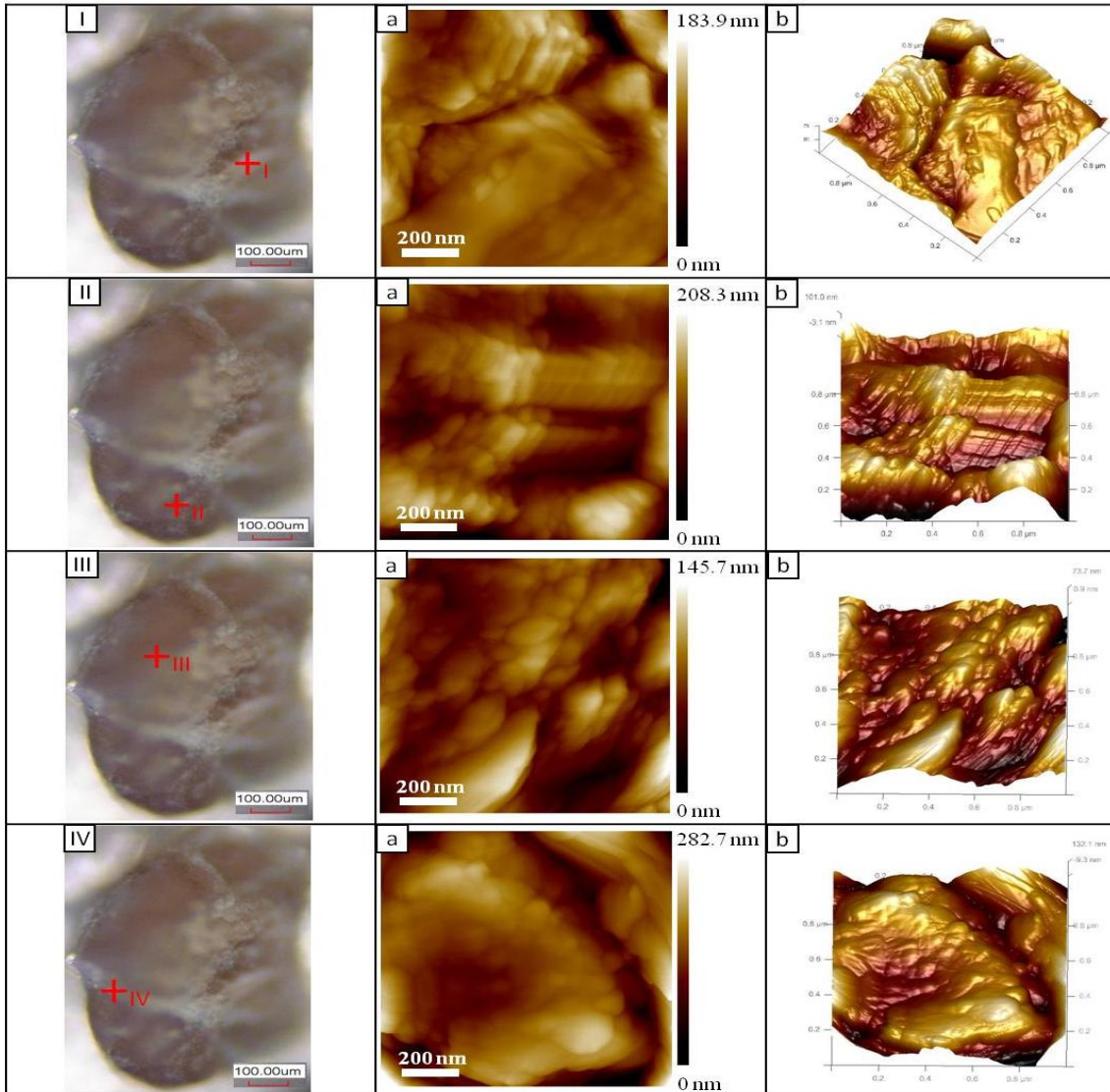


Appendix II.21: Sample RL I_5041_Qu_4, CLSM image of a quartz grain taken at 4 different magnifications a: 10x; b: 20x; c: 50x and d: 100x; a₁-d₁: 2D image; a₂-d₂: 3D image; a₃-d₃: profile and a₄-d₄: roughness profile. The quartz grain is round, of sub-spheroidal shape and the surface is rough. At a close view (image d₁) at the cement minerals they are quite rough, and the non-overgrown grain surface in the dark areas is also not smooth, which can be seen at the curvature with sharp peaks in d₃ profile.

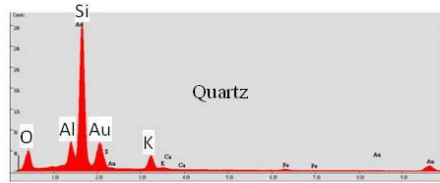
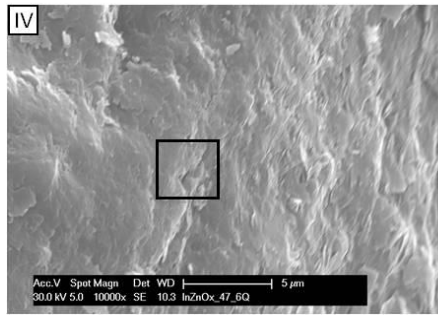
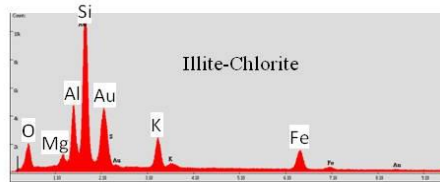
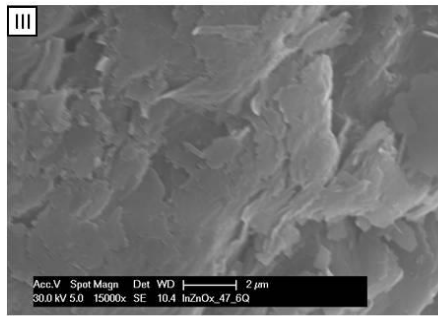
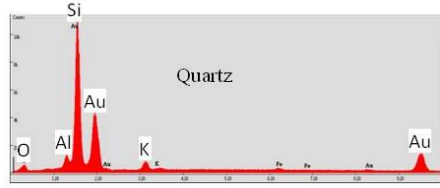
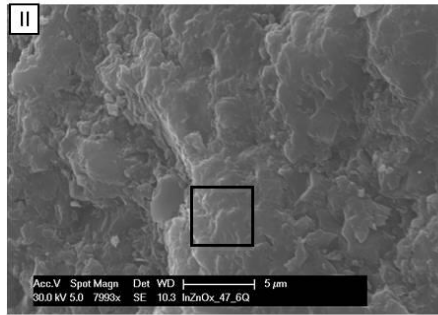
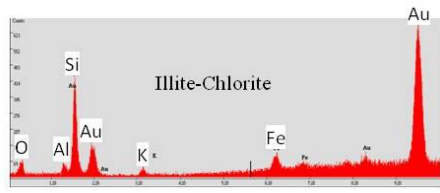
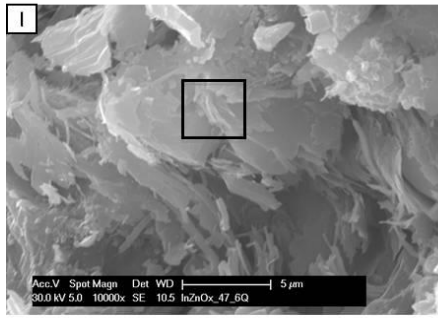
Appendix III: Atomic Force Microscope, Scanning Electron Microscope images and Energy dispersive X-ray spectra

RL I_2111

RL I_2111_Qu_3

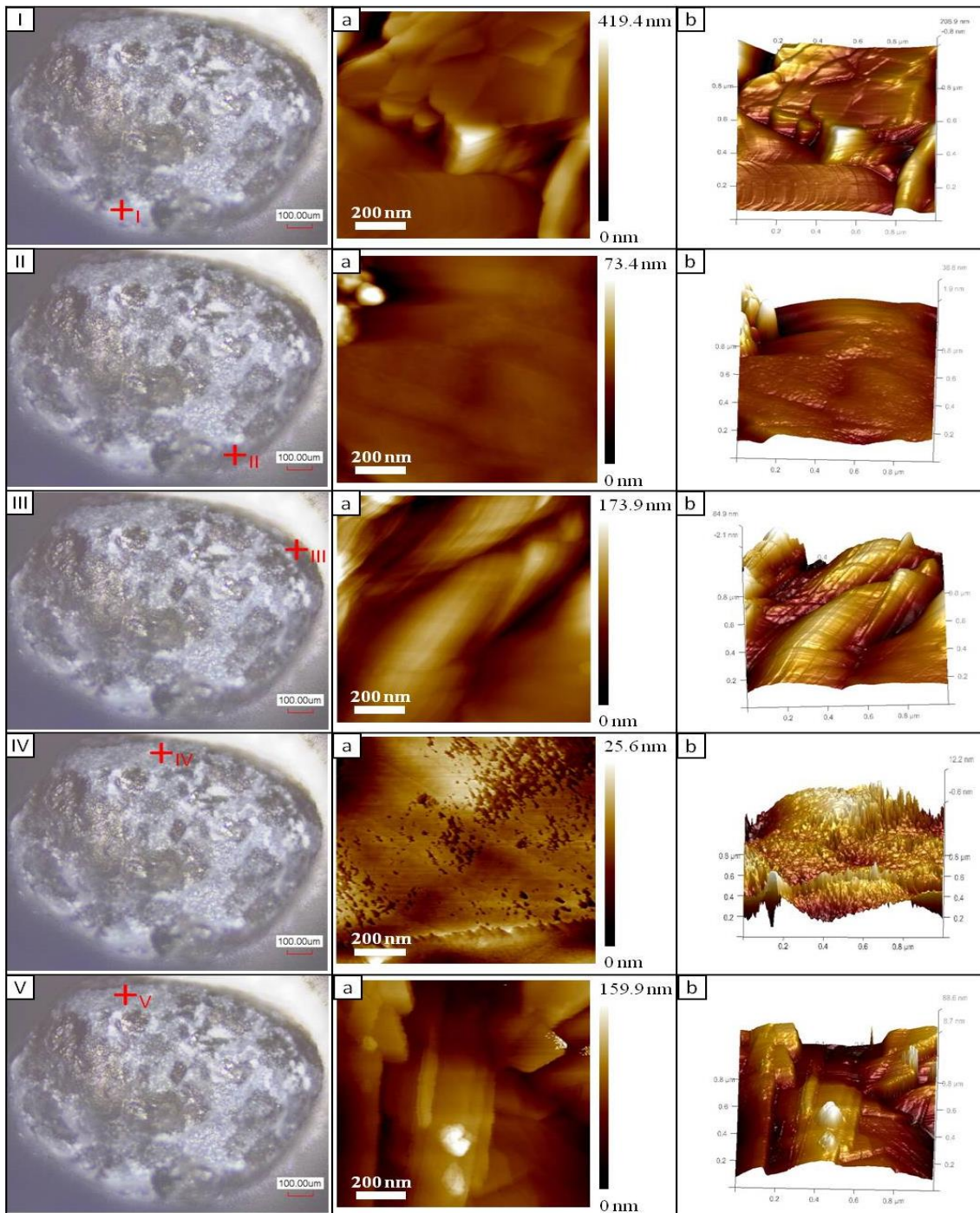


Appendix III.1: Sample RL I_2111_Qu_3. CLSM images showing an overview of the quartz surface at 10x magnification with crosshairs indicating the spots that were analysed with AFM and SEM. The AFM images Ia - IVa show the roughness of the quartz grain surface, measured with scan sizes of 1 μm x 1 μm. Images Ib -IVb display the quartz grain surface in 3D.

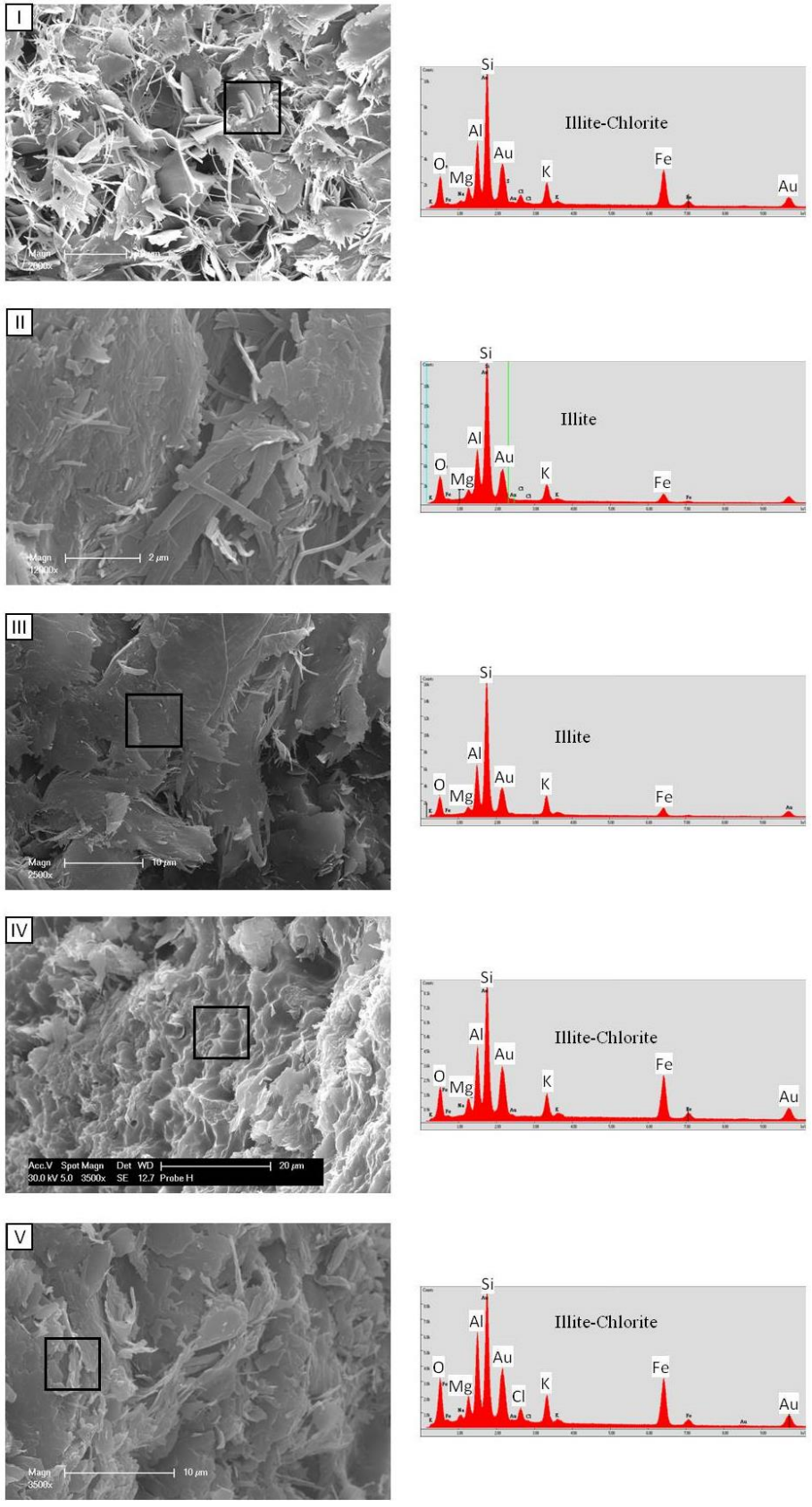


Appendix III.2: Sample RL I_2111_Qu_3. SEM images displaying an illite-chlorite mat with filaments and thin plates at points I and III while points II and IV show a quartz surface. The minerals are identified by EDX spectra taken at the marked rectangles in images I, II, IV, and the entire area in image III.

RL I_2111_Qu_4

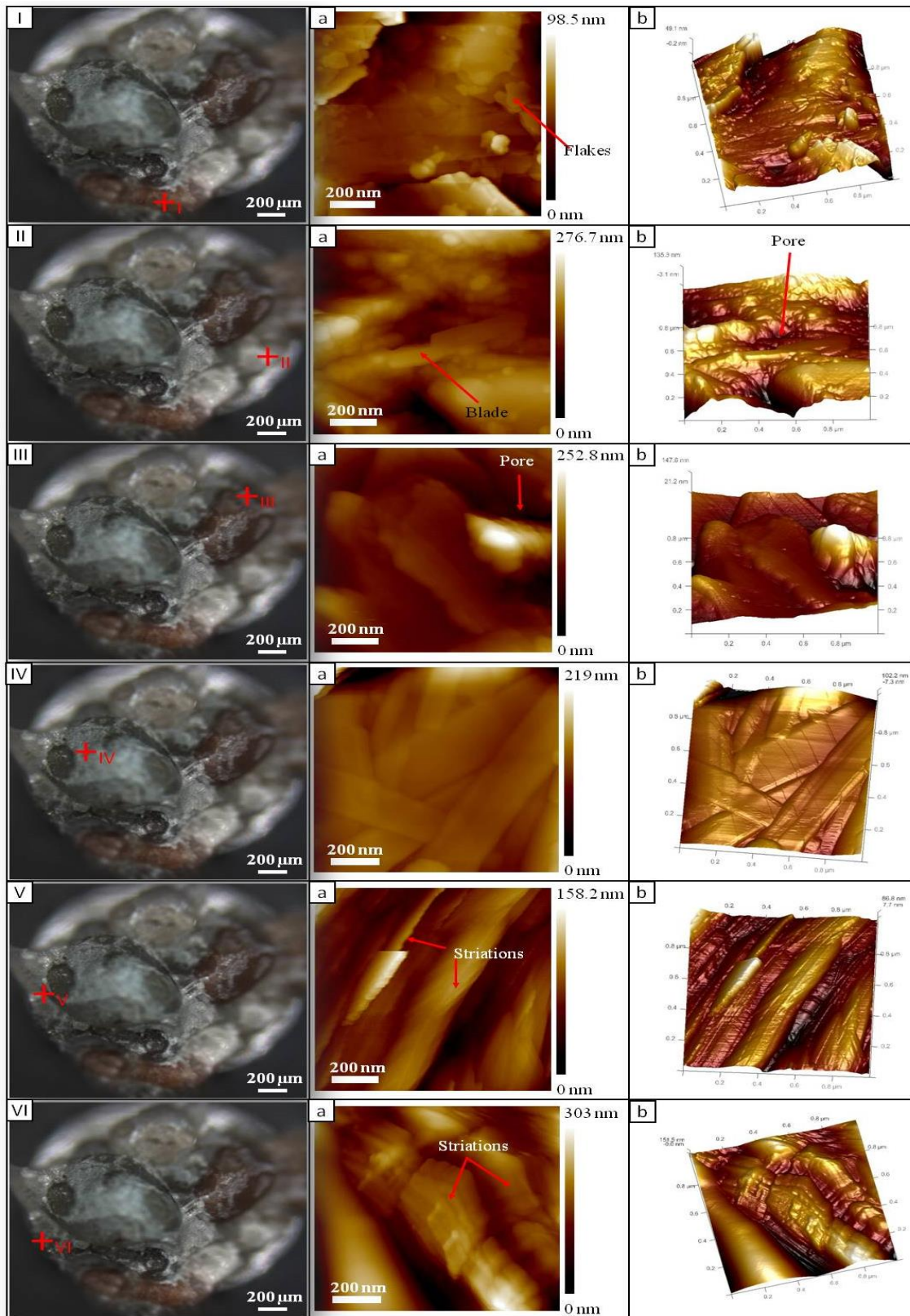


Appendix III.3: Sample RL I_2111_Qu_4. CLSM image showing an overview of the quartz surface taken with 10x magnification. AFM and SEM images were taken and analysed at the 5 spots as marked. Images Ia – Va are AFM images showing the quartz grain surface. Images Ib – Vb are 3D of the corresponding areas.

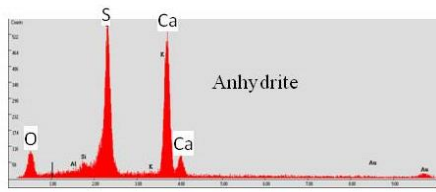
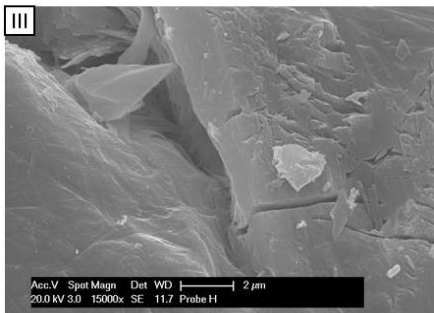
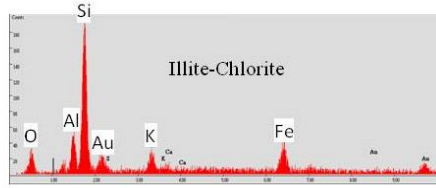
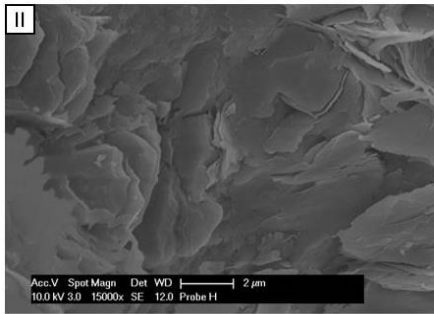
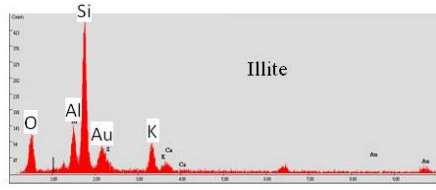
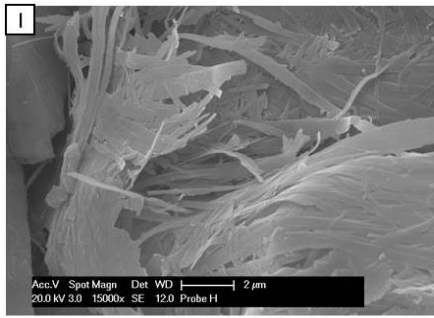


Appendix III.4: Sample RL I_2111_Qu_4. SEM images showing authigenic morphology. Filamentous authigenic illite and chlorite with pseudo hexagonal crystals form a mat that coats the quartz surface. EDX spectra are extracted from the rectangles as marked in images I, II, III, V, and from the complete image area IV.

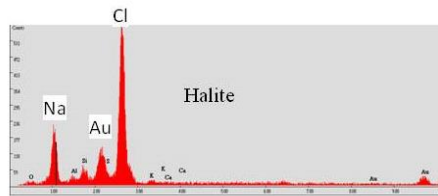
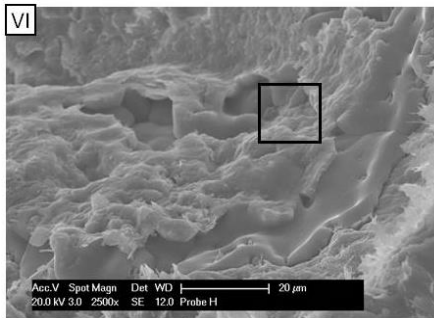
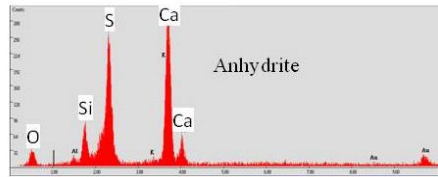
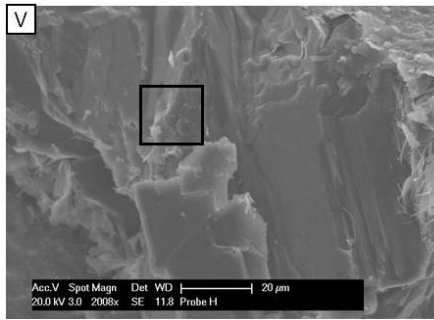
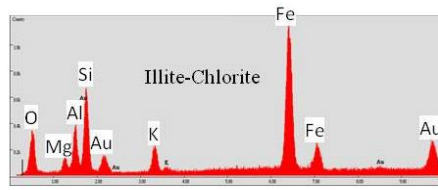
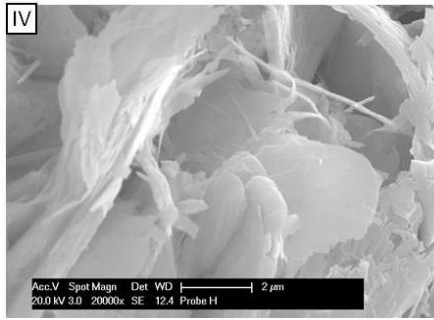
RL I_2111_B



Appendix III.5: Sample RL I_2111_B. The image shows a binocular overview picture of the sample. Spots I -VI where subsequently imaged and analysed with AFM and SEM. AFM images Ia – VIa display the surface of the grains and cements. Images Ib – VIb are the 3D displays.

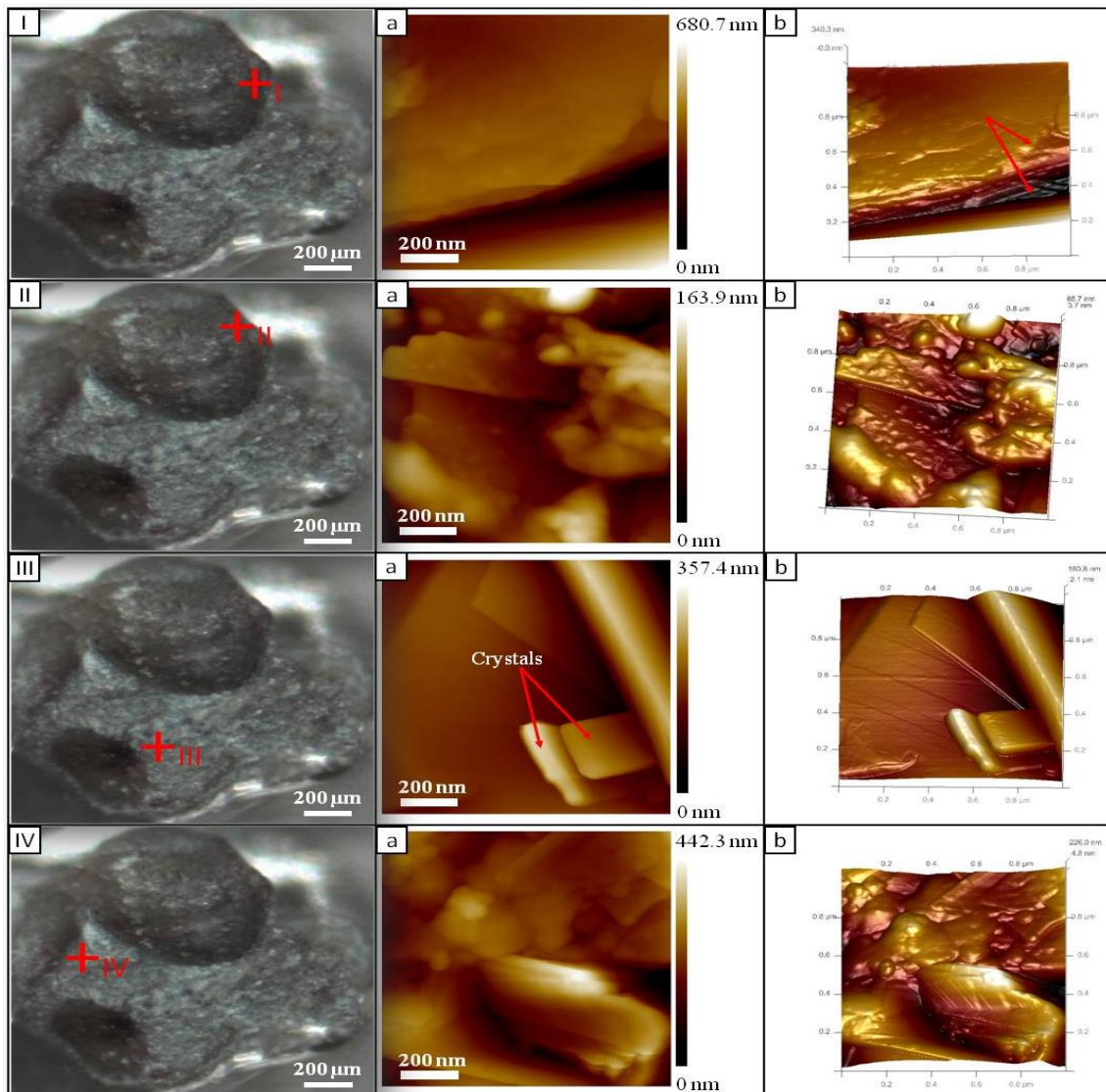


Appendix III.6: Sample RL I_2111_B. EDX spectra and SEM images of the authigenic minerals show illite ribbons, chlorite euhedral crystals, and anhydrite with cracks and micro pores at points imaged with AFM respectively.

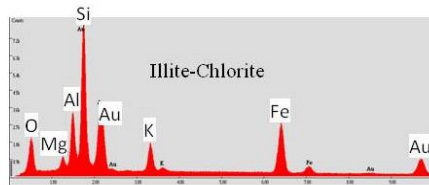
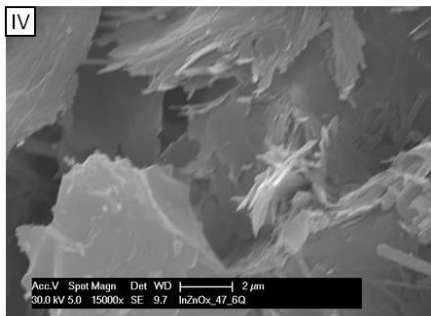
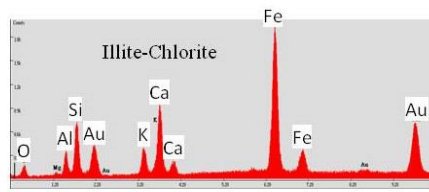
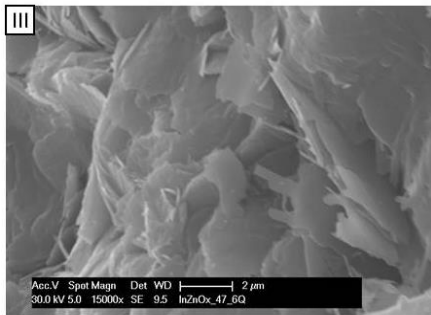
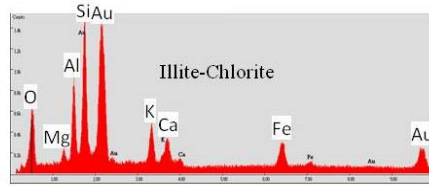
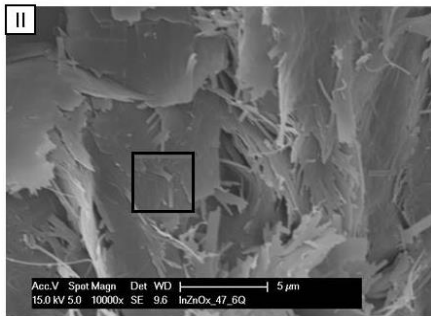
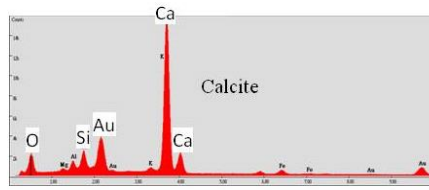
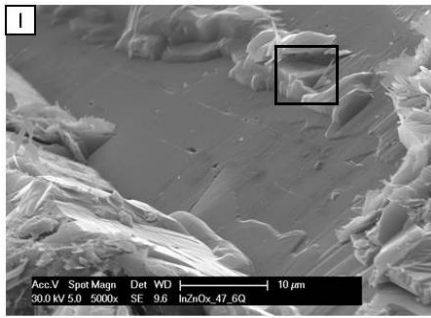


Appendix III.7: Sample RL I_2111_B. EDX spectra and SEM images of the authigenic minerals showing illite ribbons, chlorite euhedral crystals, anhydrite and halite in small crystals at points imaged with AFM respectively.

RL I_2111_C

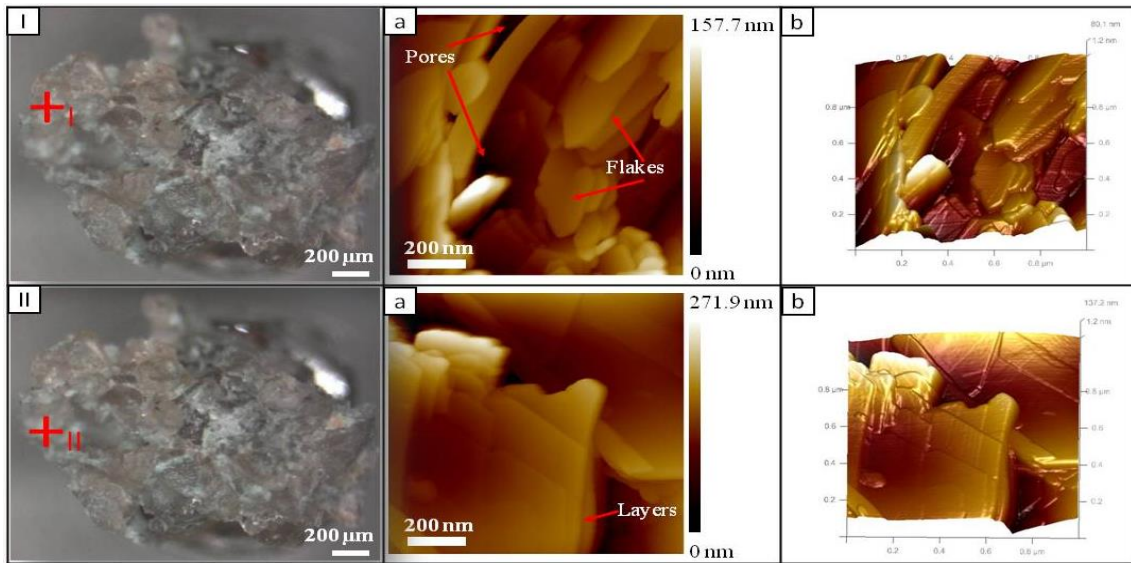


Appendix III.8: Sample RL I_2111_C. An overview image of the sample surface taken with binoculars with a 5x magnification. Marks indicate the spots analysed with the AFM and SEM. Images Ia – IIa are taken on grain surfaces at dark coloured areas and cement surfaces at bright coloured areas as shown in images IIIa – IVa. Images Ib – IVb are the associated 3D images.

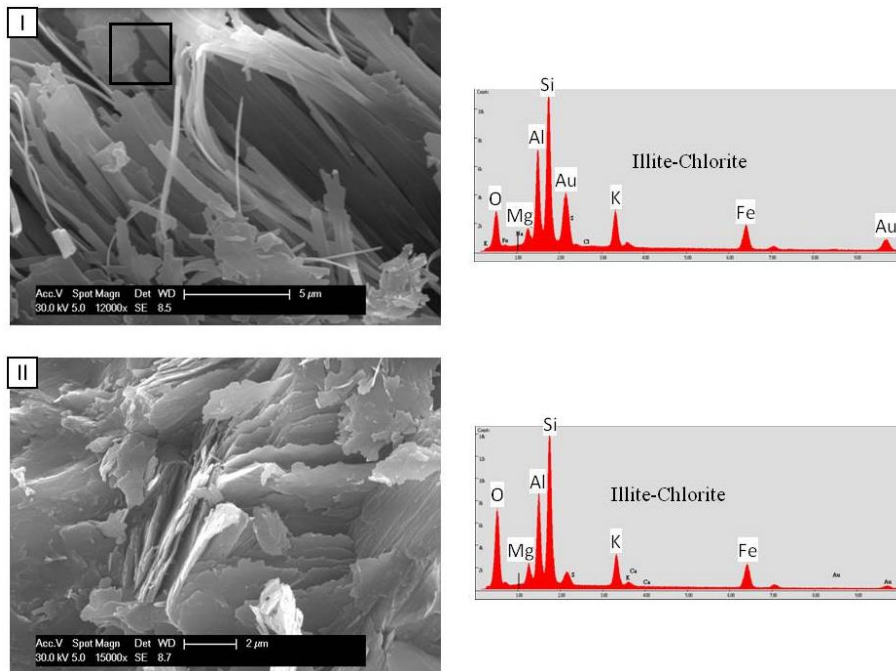


Appendix III.9: Sample RL I_2111_C. SEM images show calcite at point I and illite-chlorite with filaments and thin blades at points II to IV. Element spectra are analysed at the rectangles marked in images I, II and for the whole areas in images III, IV.

RL I_2111_D

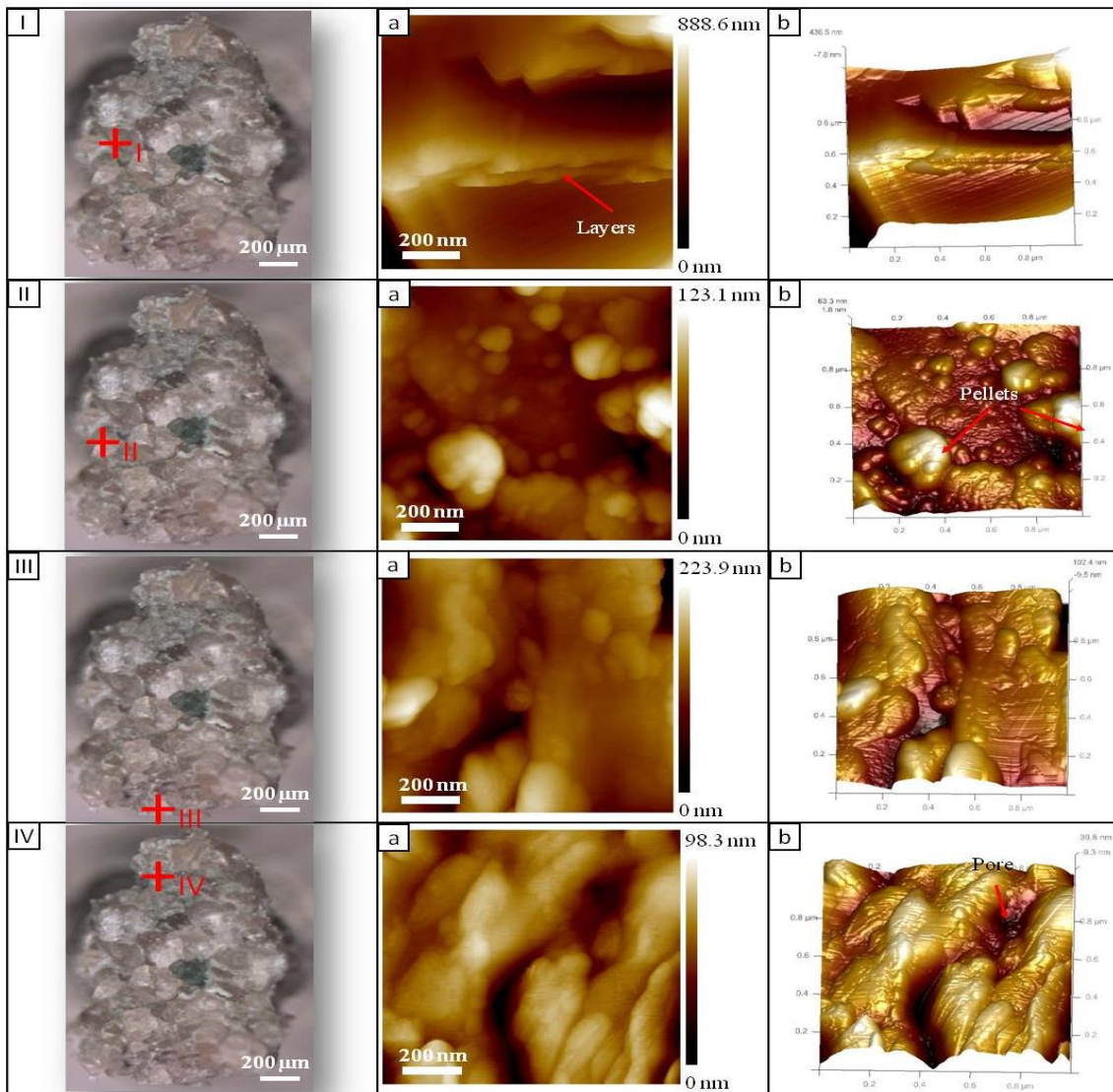


Appendix III.10: Sample RL I_2111_D. A binocular overview image of the sample with the crosshair marking the position analysed with the AFM and the SEM. AFM images show the cement surfaces in height images Ia – IIa and in 3D images Ib – IIb.

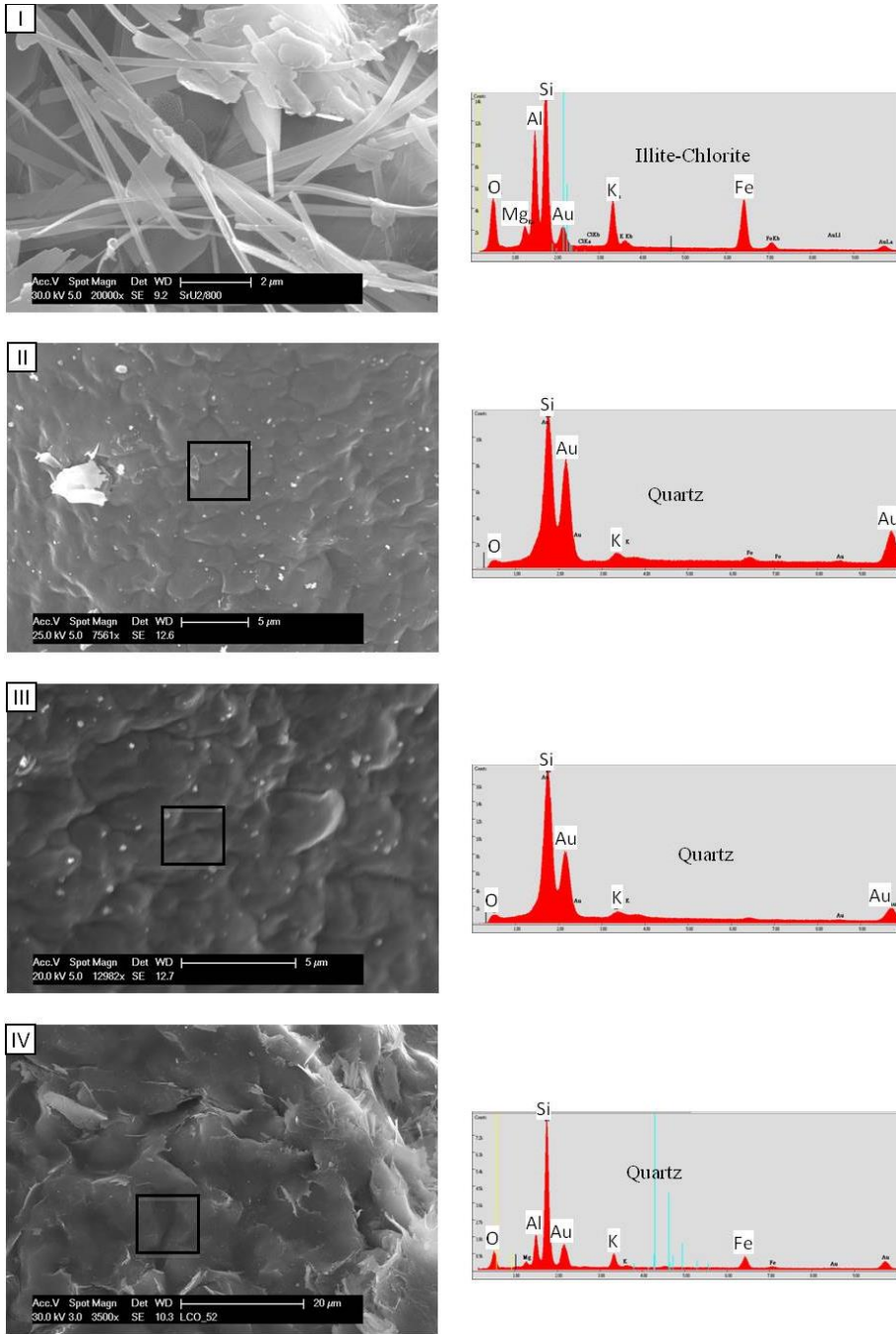


Appendix III.11: Sample RL I_2111_D. SEM images of point I and II show illite-chlorite with ribbons and multi-thin flakes. The corresponding EDX spectra are taken at the indicated rectangle in image I and of the complete area in image II.

RL I_2111_E



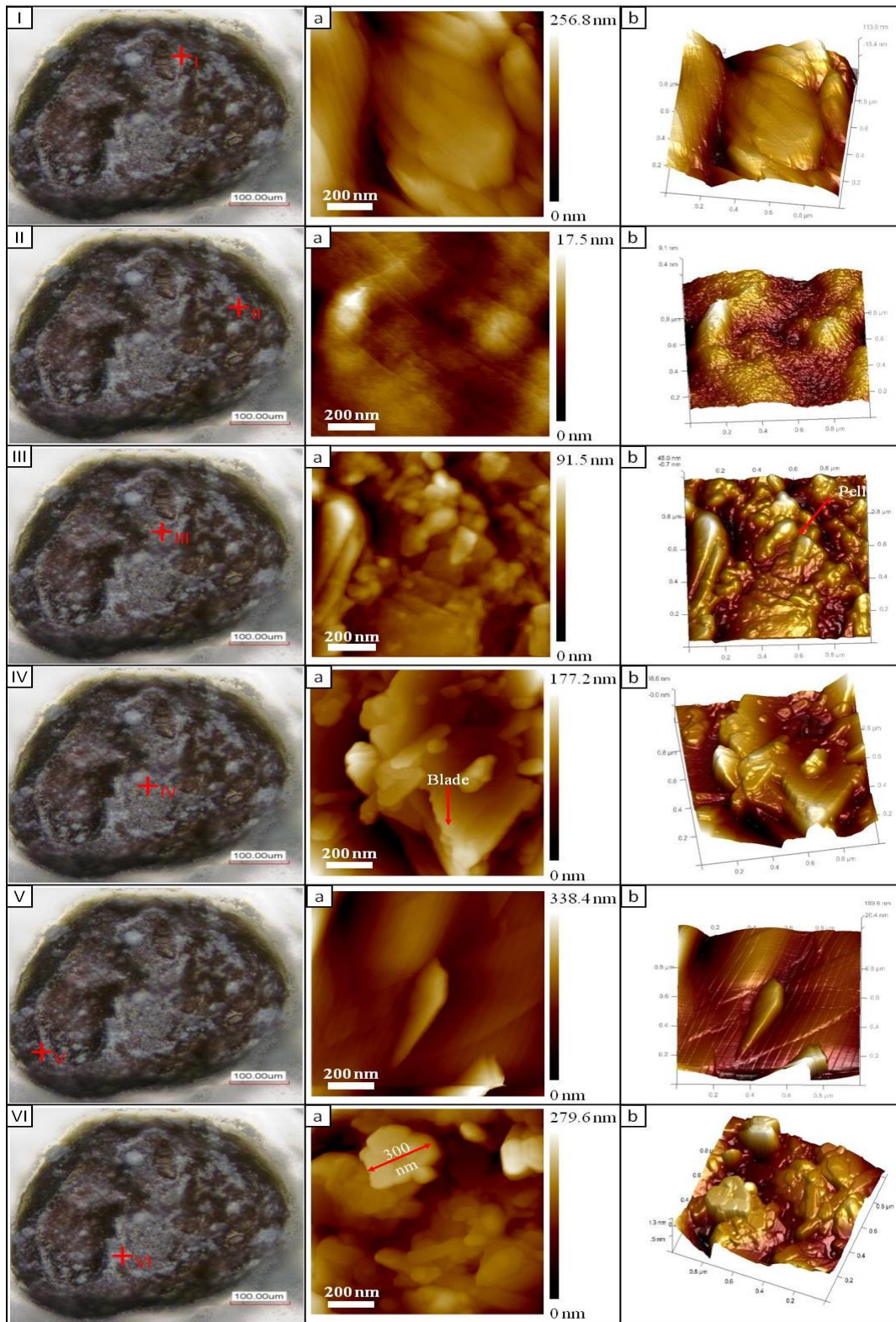
Appendix III.12: Sample RL I_2111_E. A binocular image showing an overview image of the sample and the marks indicating the spots at which AFM and SEM analysis was carried out. Images Ia – IVa show the roughness of the cement surfaces, measured with the AFM at different areas. Images Ib – IVb are 3D images of the same areas.



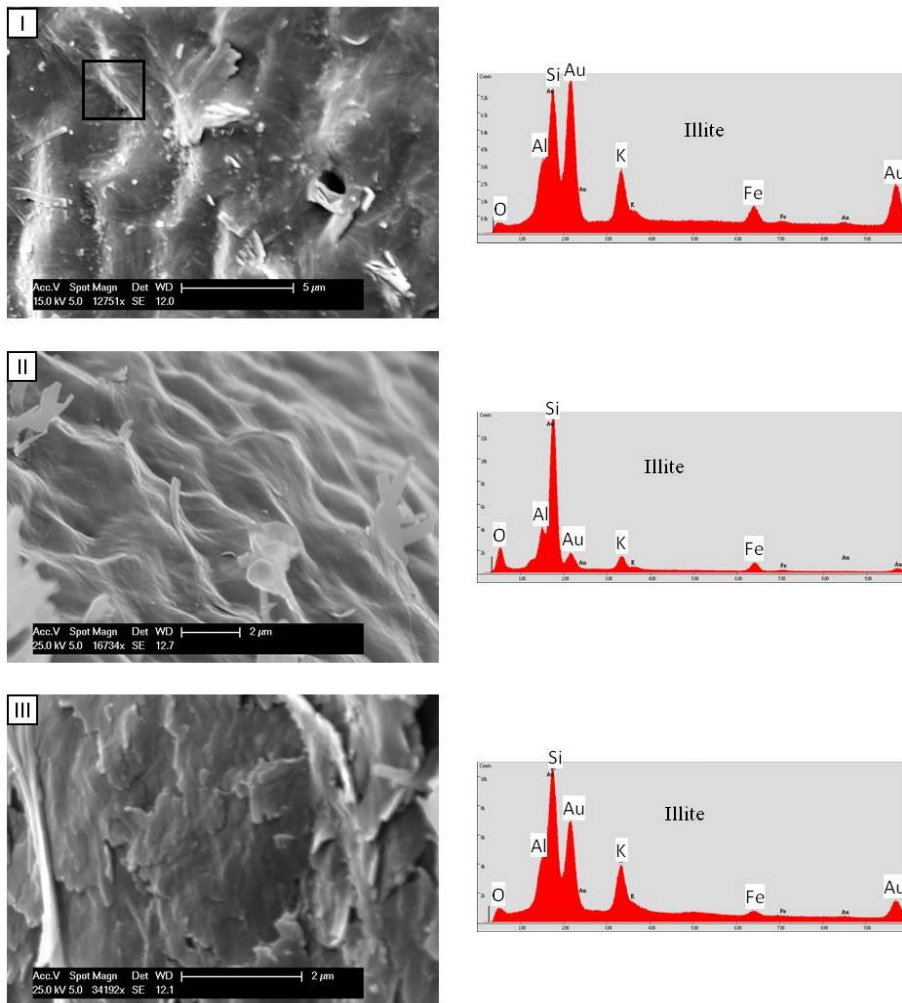
Appendix III.13: Sample RL I_2111_E. SEM images show illite-chlorite and authigenic quartz crystals on points I to IV which correspond to the analysed AFM areas. EDX spectra of the entire image I and of the positions indicated by the rectangles in images II to IV are shown next to it.

RL I_4146

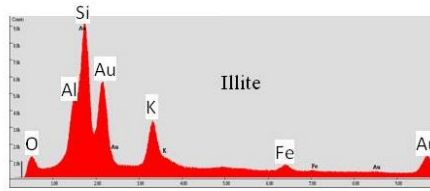
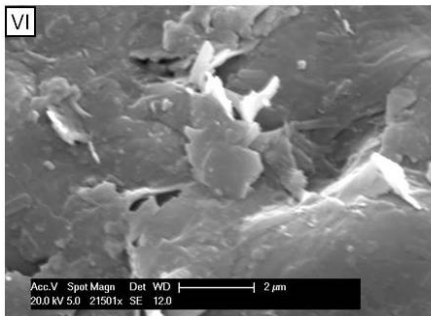
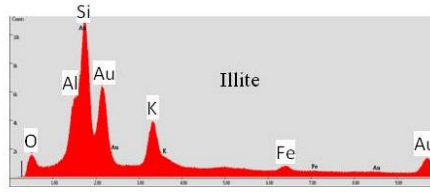
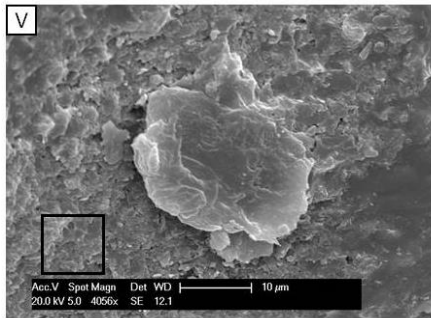
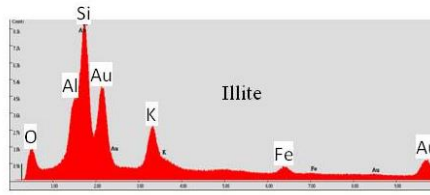
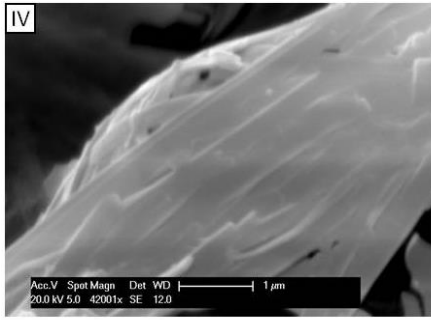
RL_4146_Qu_3



Appendix III.14: Sample RL_4146_Qu_3. CLSM image showing an overview picture of the grain RL_4146_Qu_3 at 20x magnification. The marked spots are the areas where AFM measurements were taken. The quartz surface roughness is shown in images Ia – VIa and in 3D images Ib – VIb.

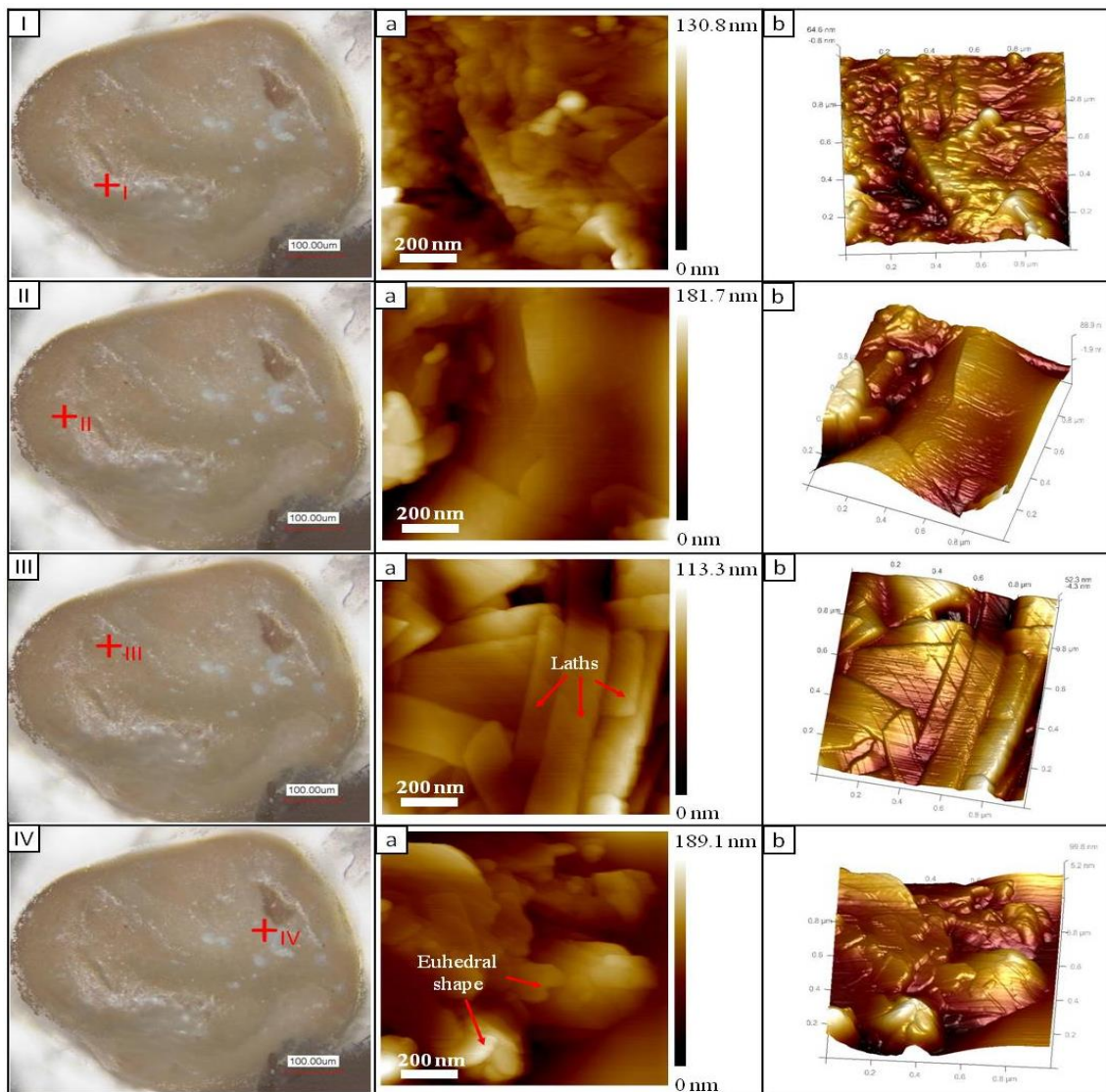


Appendix III.15: Sample RL_4146_Qu_3. SEM images display illite minerals which coat the quartz surface analysed by AFM. It is verified in the indicated area in image I and within the complete images II, III, by EDX analysis.

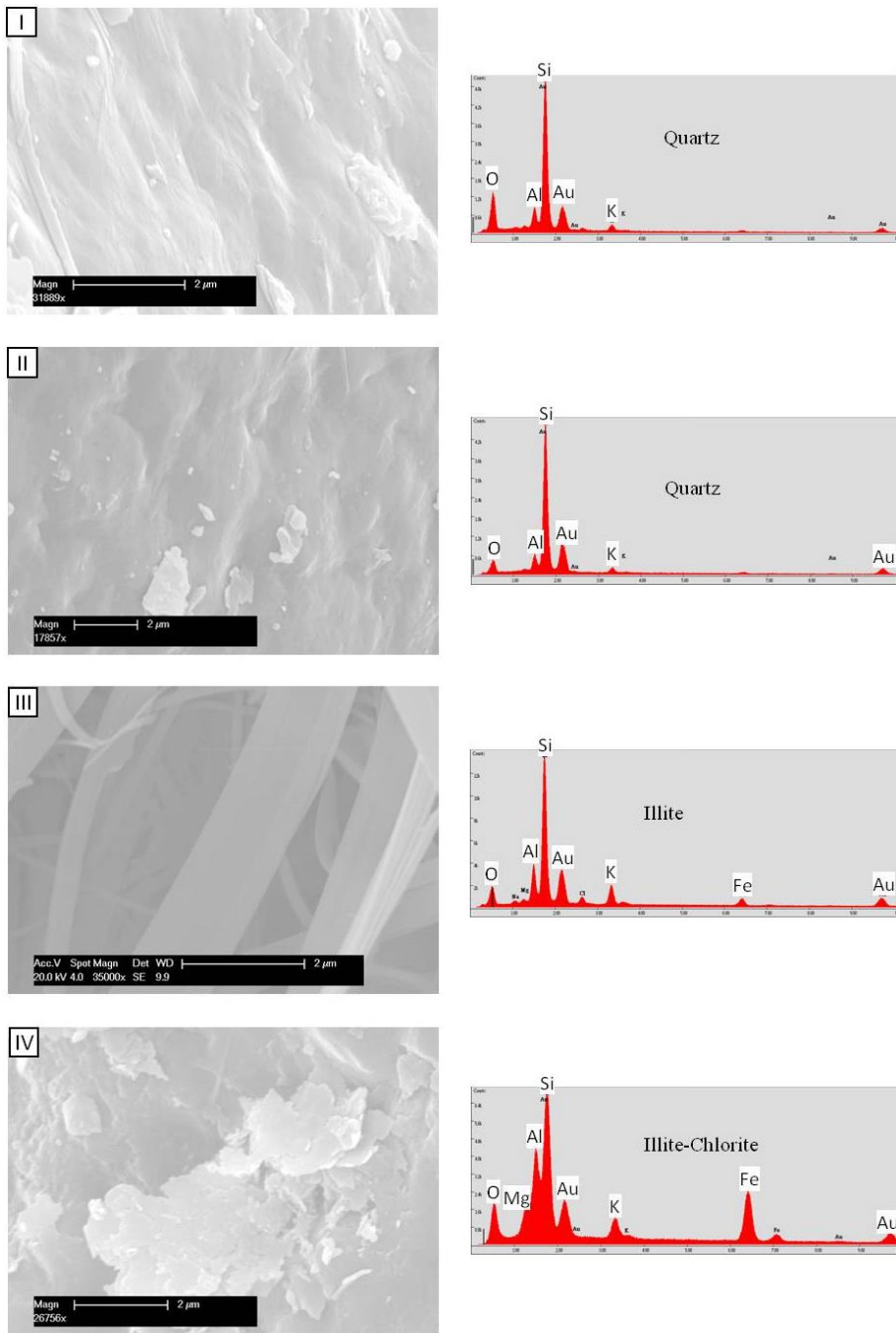


Appendix III.16: Sample RL_4146_Qu_3. SEM images display illite minerals which coat the quartz surface analysed by AFM. Illite is present in filaments, thin ribbons, and flakes. It is verified within the complete images IV, VI, and in the indicated area in image V, by EDX analysis.

RL I_4146_A

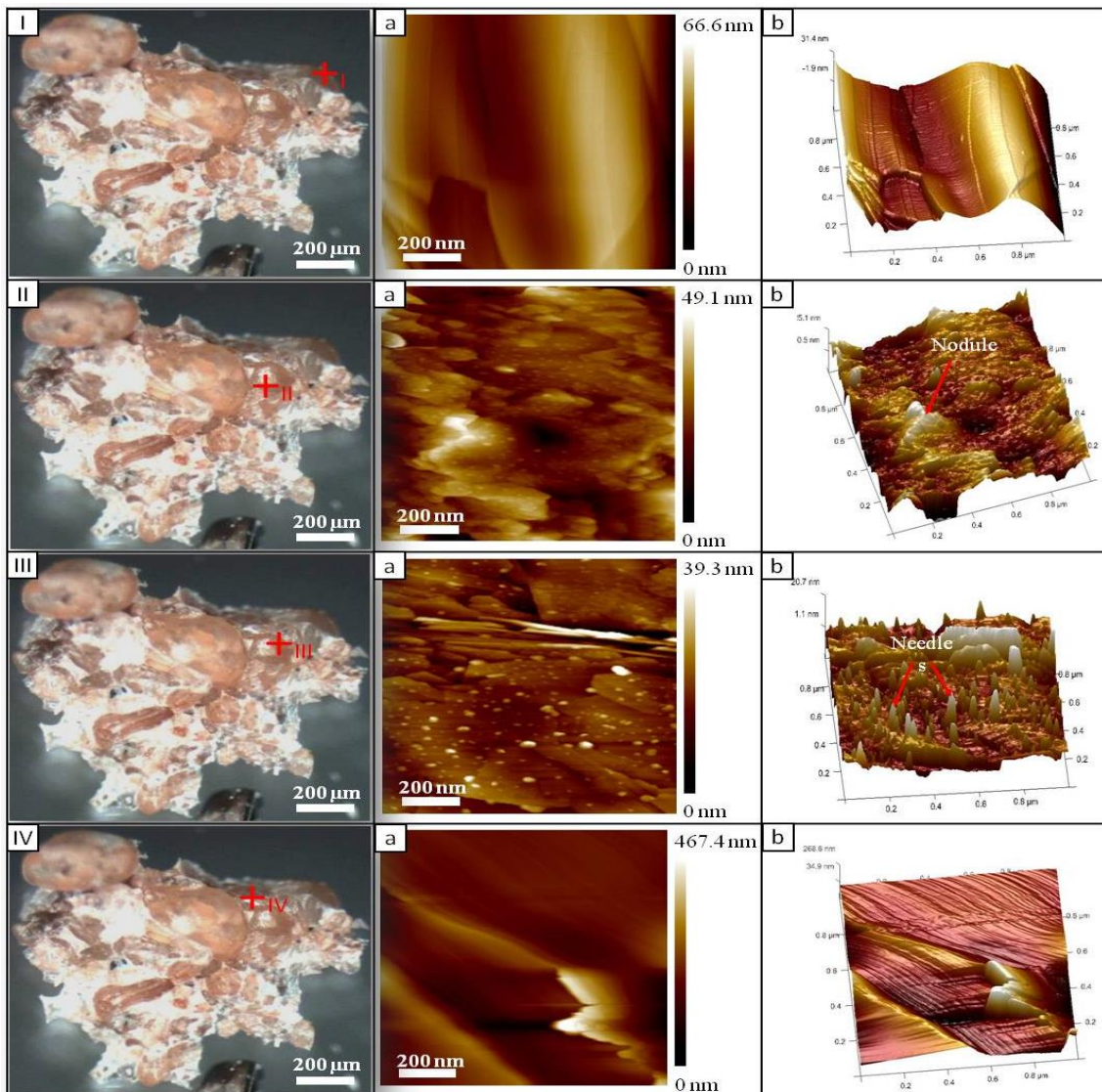


Appendix III.17: Sample RL I_4146_A. View of the quartz surface observed with CLSM at 20x magnification. The marks I to IV indicate the AFM analysed spots. The height images of the quartz surface are shown in Ia - IVa and as a 3D representation in Ib - IVb.

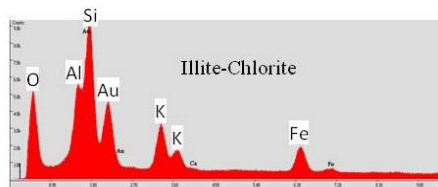
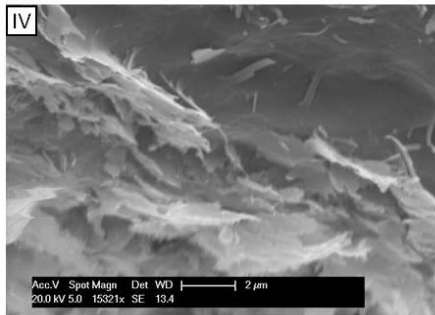
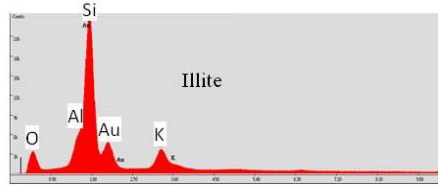
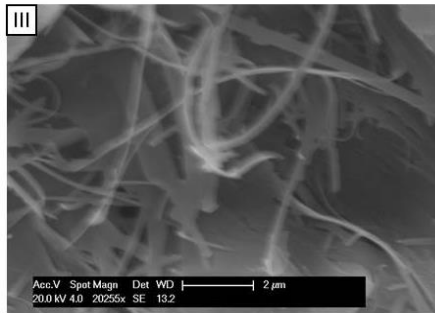
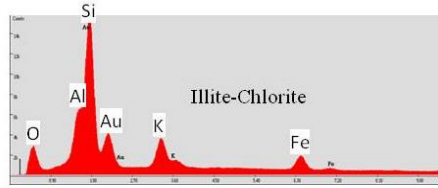
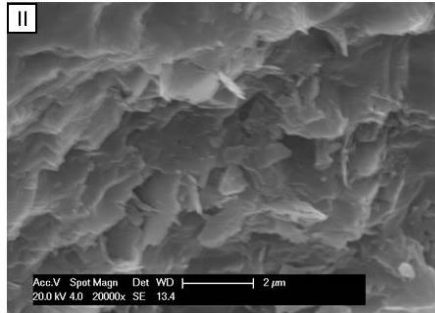
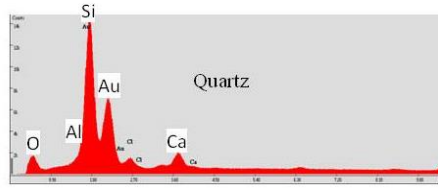
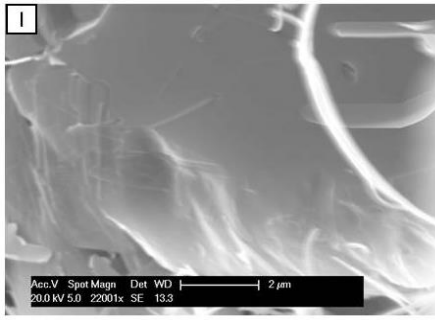


Appendix III.18: Sample RL I_4146_A. SEM and EDX spectra show the uncovered quartz surface at points I and II. Illite fibers and thin flakes of illite-chlorite overlay the quartz surface at points III and IV.

RL I_4146_B

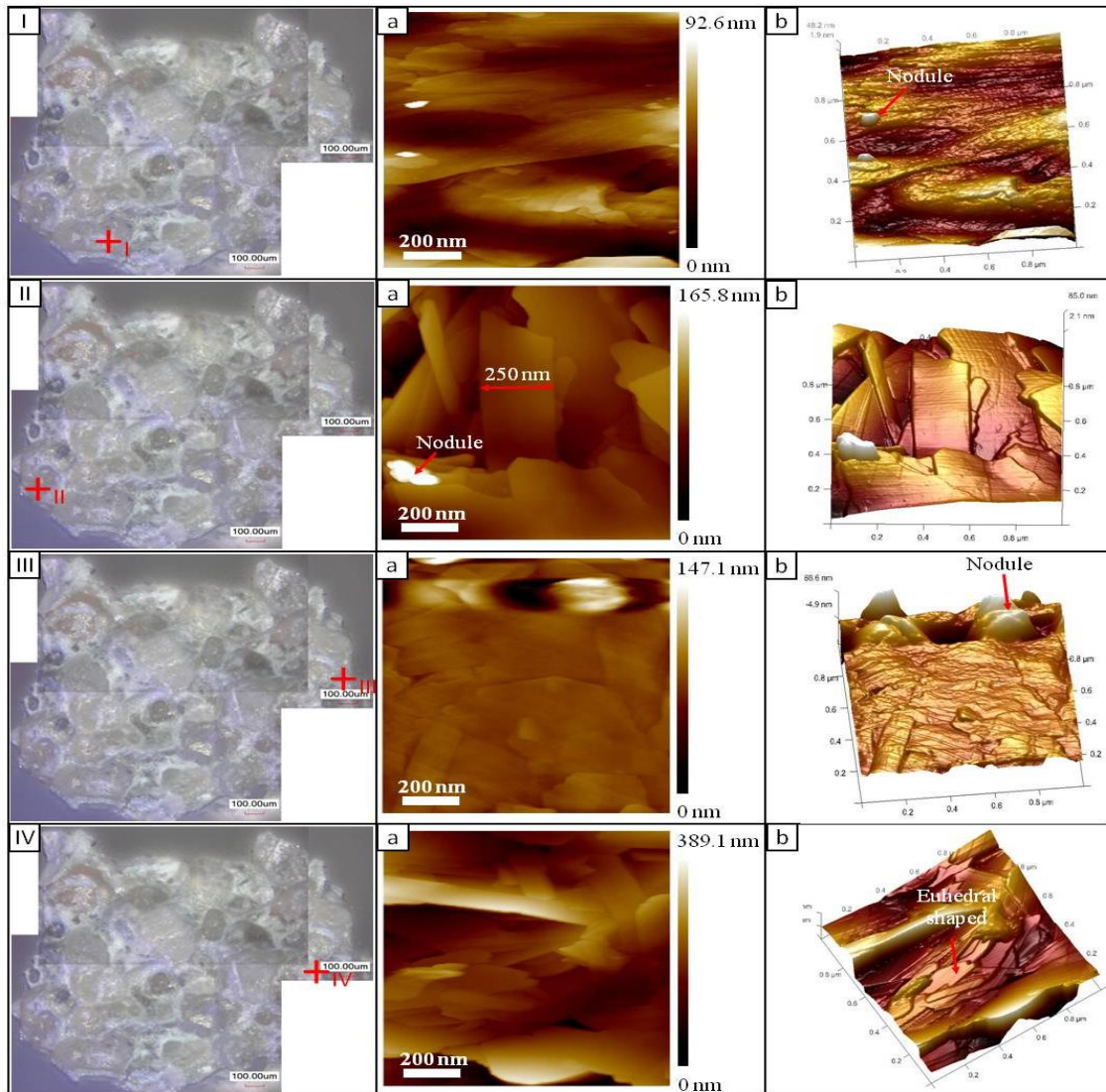


Appendix III.19: Sample RL I_4146_B. Overview image of sample Z5_4146_B taken with binoculars at 5x magnification (due to the size of the sample and the lowest CLSM magnification of 10x it is not possible to display the entire sample with one CLSM image. Therefore binoculars were used). The marks indicate the areas analysed by AFM. The AFM images Ia – IIIa display the grain topography and image IVa the surface of the cement region. Images Ib – IVb are the 3D illustrations.

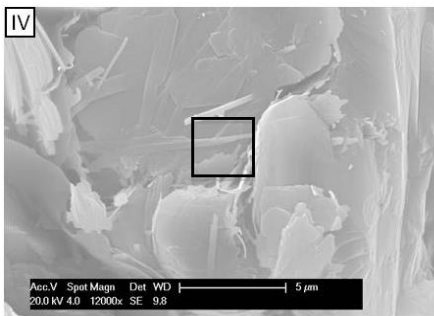
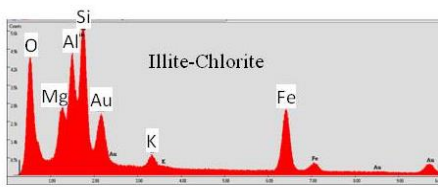
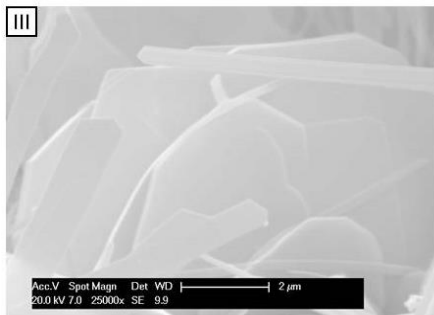
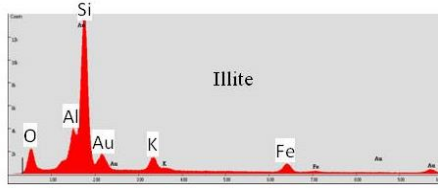
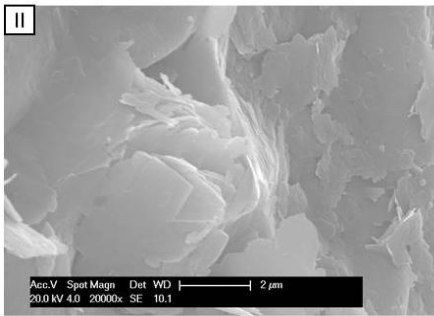
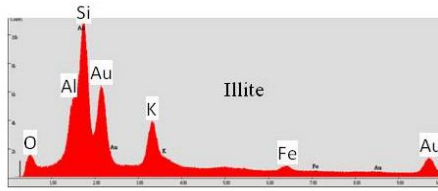
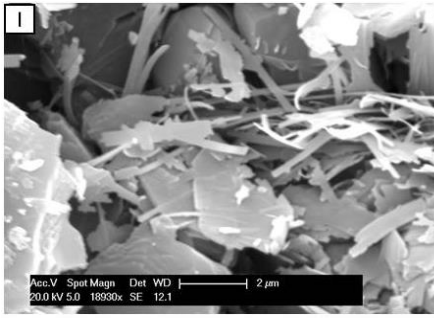


Appendix III.20: Sample RL I_4146_B. SEM images show illite, and illite-chlorite morphologies. Fibrous illite and flaky illite-chlorite grow over the grain at points II – III and form cement at point IV. The minerals are also verified by EDX.

RL I_4146_C

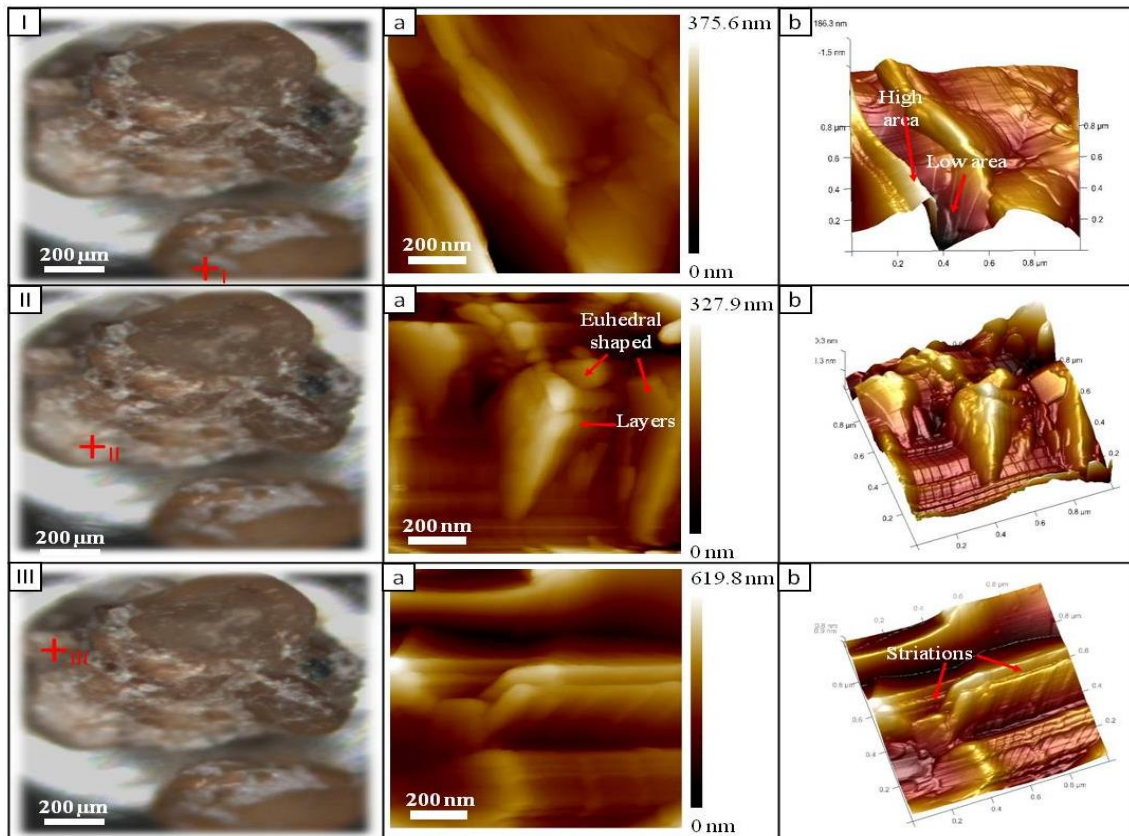


Appendix III.21: Sample RL I_4146_C. A CLSM overview of the sample at 10x magnification and areas I to IV analysed with AFM. The AFM images Ia – IIIa show the roughness of the grain surfaces and image IVa displays the roughness of the cement. Images Ib – IVb are the analogous 3D images.

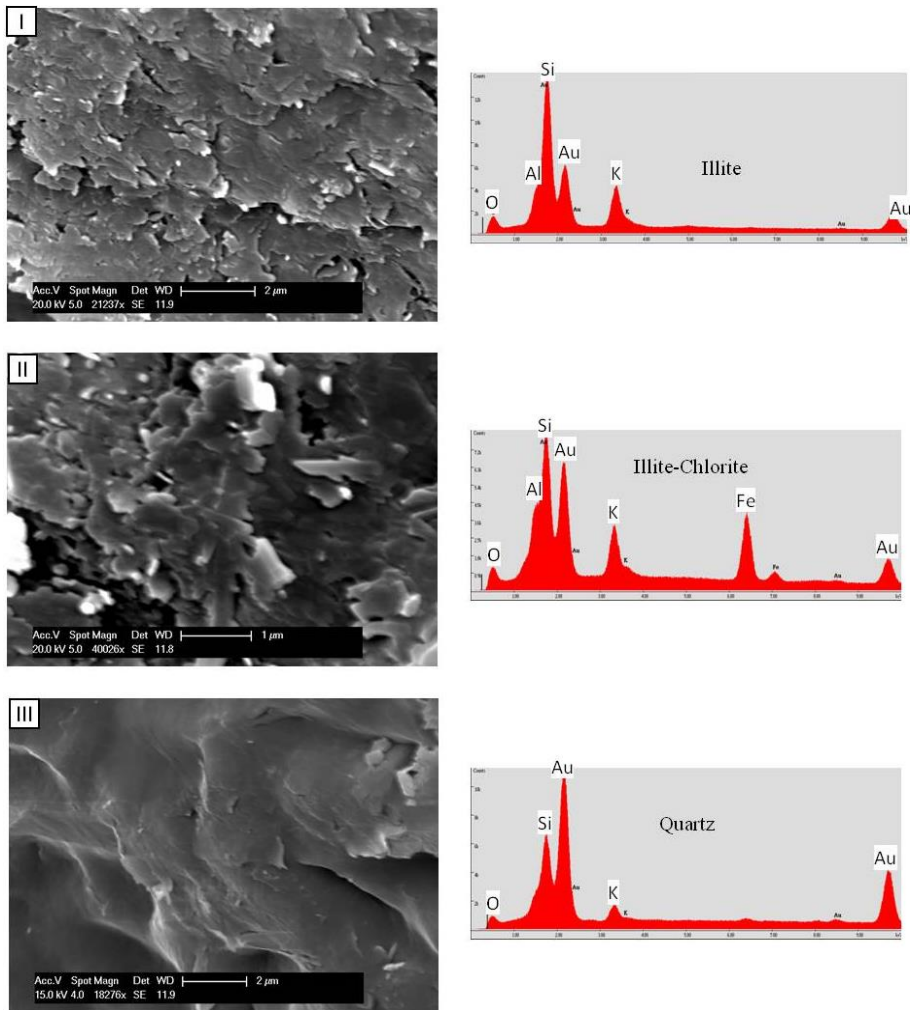


Appendix III.22: Sample RL I_4146_C. SEM images and EDX indicate that illite and illite-chlorite minerals overlay both the grain and the cement surfaces. The illite and chlorite are thin filaments, pseudo hexagonal crystals and platelets.

RL I_4146_D



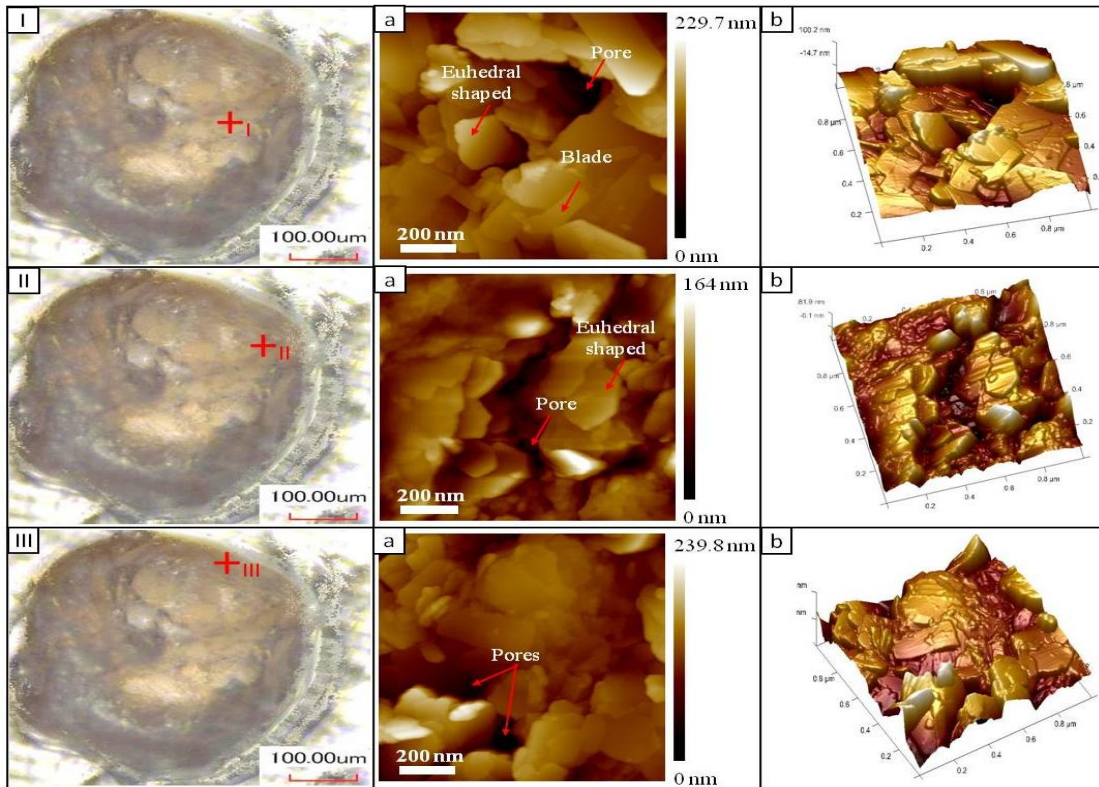
Appendix III.23: Sample RL I_4146_D. Overview image of the sample and the areas analysed with AFM and SEM from I - III. Images Ia - IIIa show the roughness of the grain surface and cement surfaces measured with the AFM. The surface roughness is displayed in 3D images Ib - IIIb.



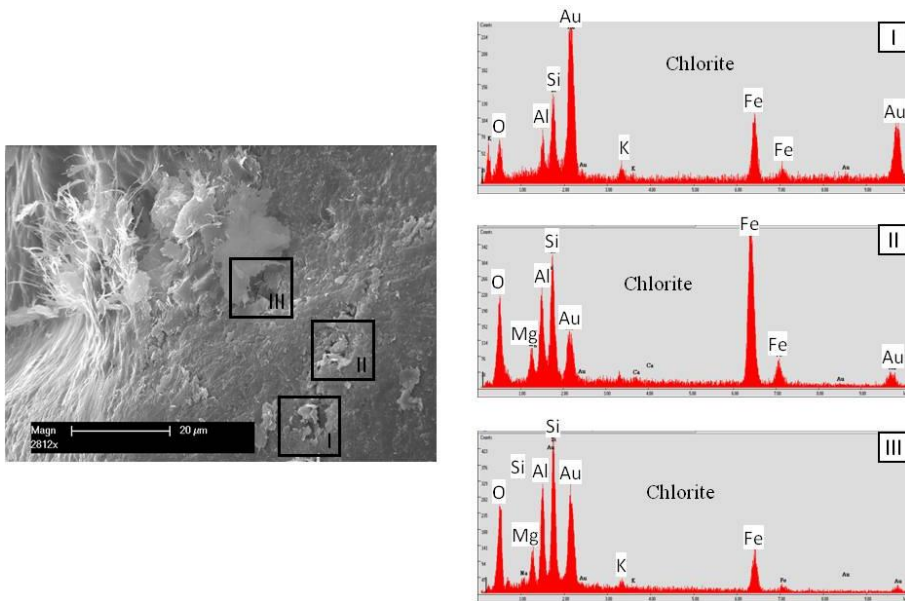
Appendix III.24: Sample RL I_4146_D. SEM images and EDX spectra show illite, illite-chlorite and quartz authigenic minerals, which overlay the grain (image I) and the cement surfaces (images II and III).

RL I_5041

RL I_5041_Qu_2

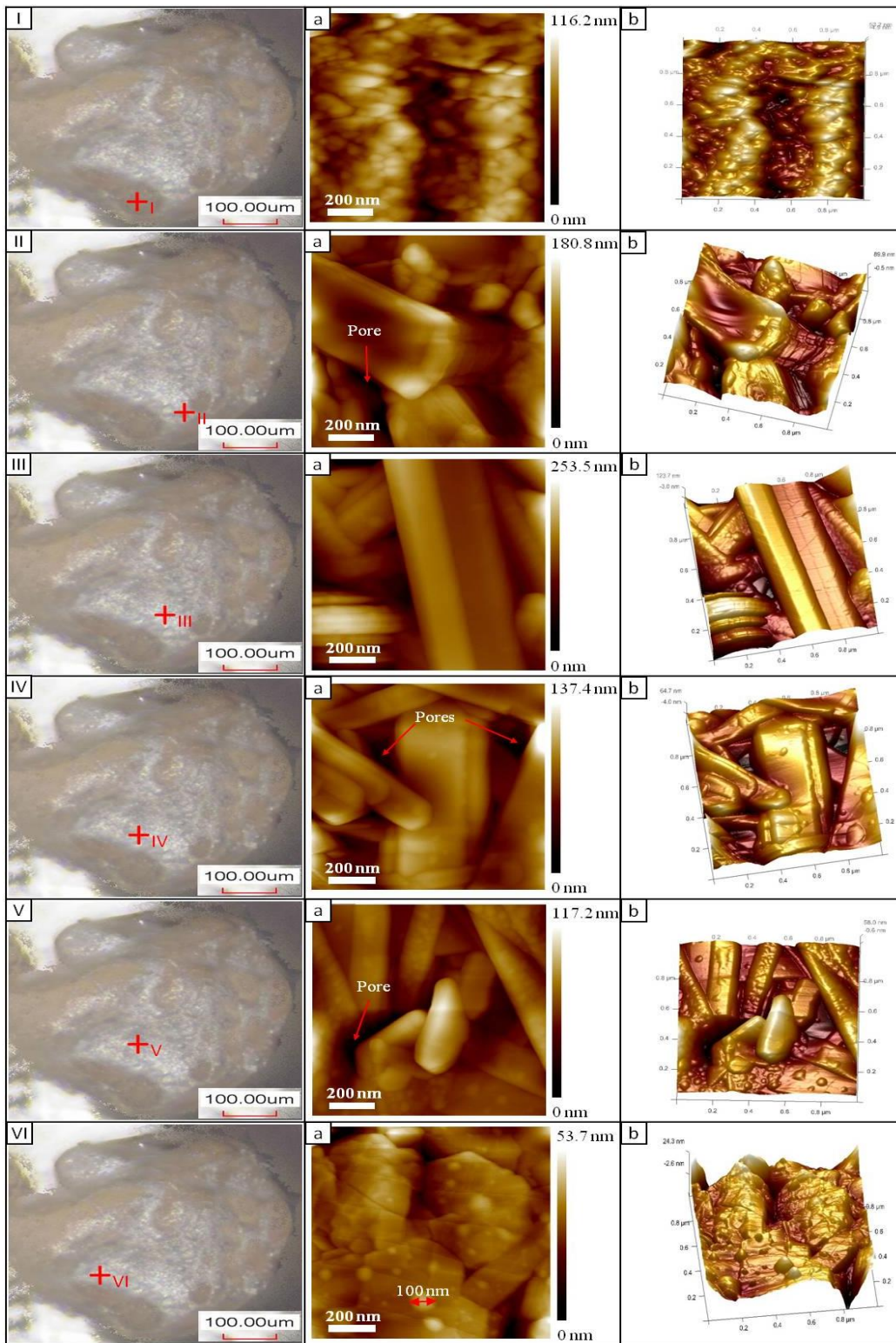


Appendix III.25: Sample RL I_5041_Qu_2. CLSM image shows an overview of the quartz surface at 10x magnification. Three spots were analysed with AFM, as numbered. The AFM images display the quartz surface in height images Ia – IIIa and in 3D displays Ib – IIIb.

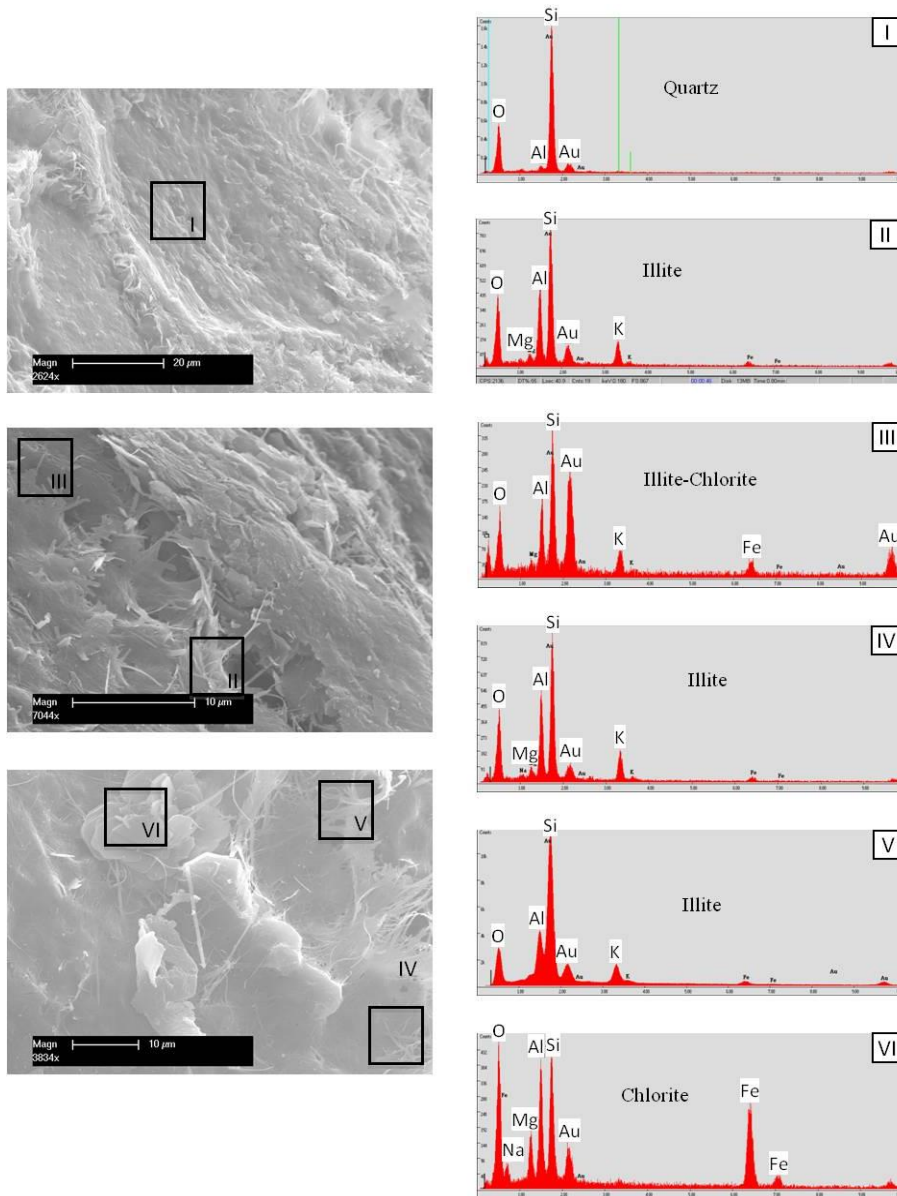


Appendix III.26: Sample RL I_5041_Qu_2. SEM images and element spectra show that all the quartz grain areas imaged by AFM are overlain by chlorite minerals.

RL I_5041_A

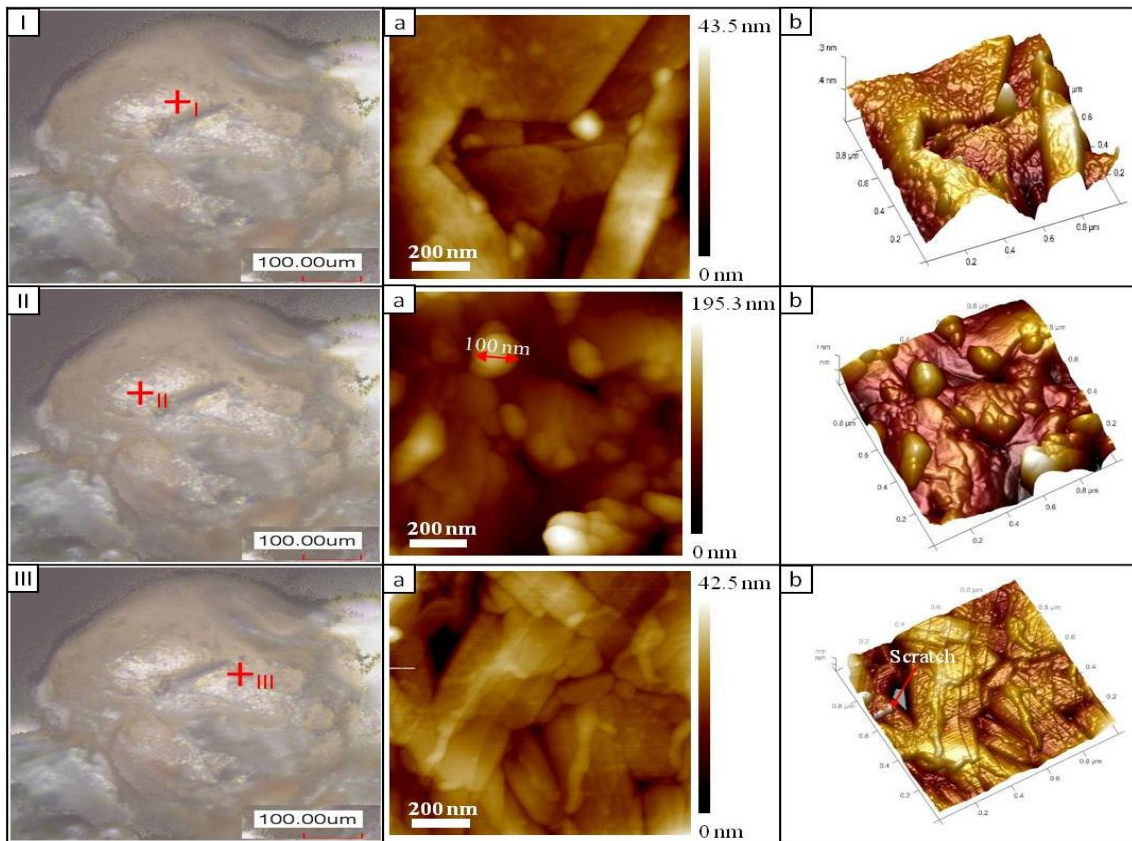


Appendix III.27: Sample RL I_5041_A. CLSM overview image of the quartz surface at 10x magnification. The quartz surface has various colours from white to brown. The red crosses indicate where AFM measurements were taken. AFM images Ia – IVa show the characteristic topography of the grain surface. Images Ib – VIb are the corresponding 3D displays.

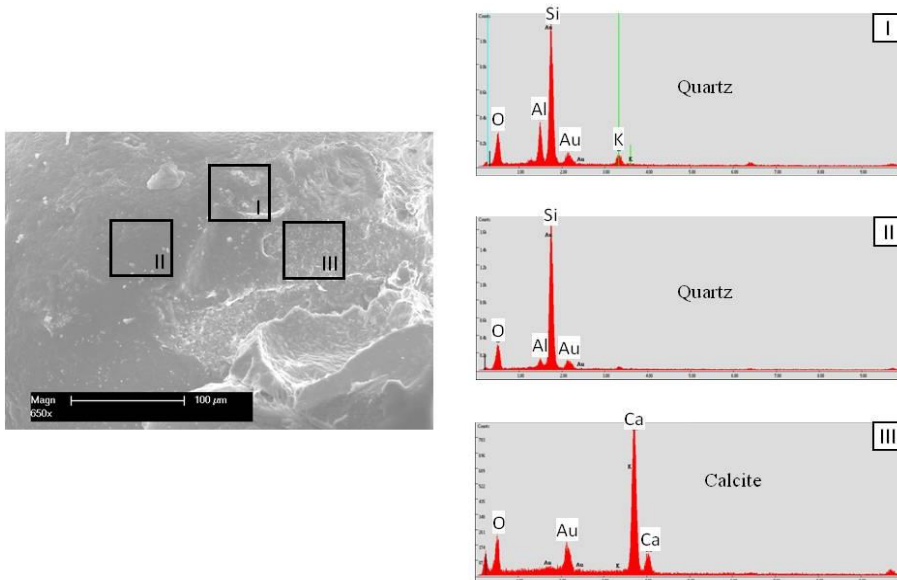


Appendix III.28: Sample RL I_5041_A. SEM images show that authigenic minerals overlay the grain surface. The areas are analogous to the imaged AFM areas indicated by rectangles I –VI. The EDX spectra show the corresponding element composition.

RL I_5041_B

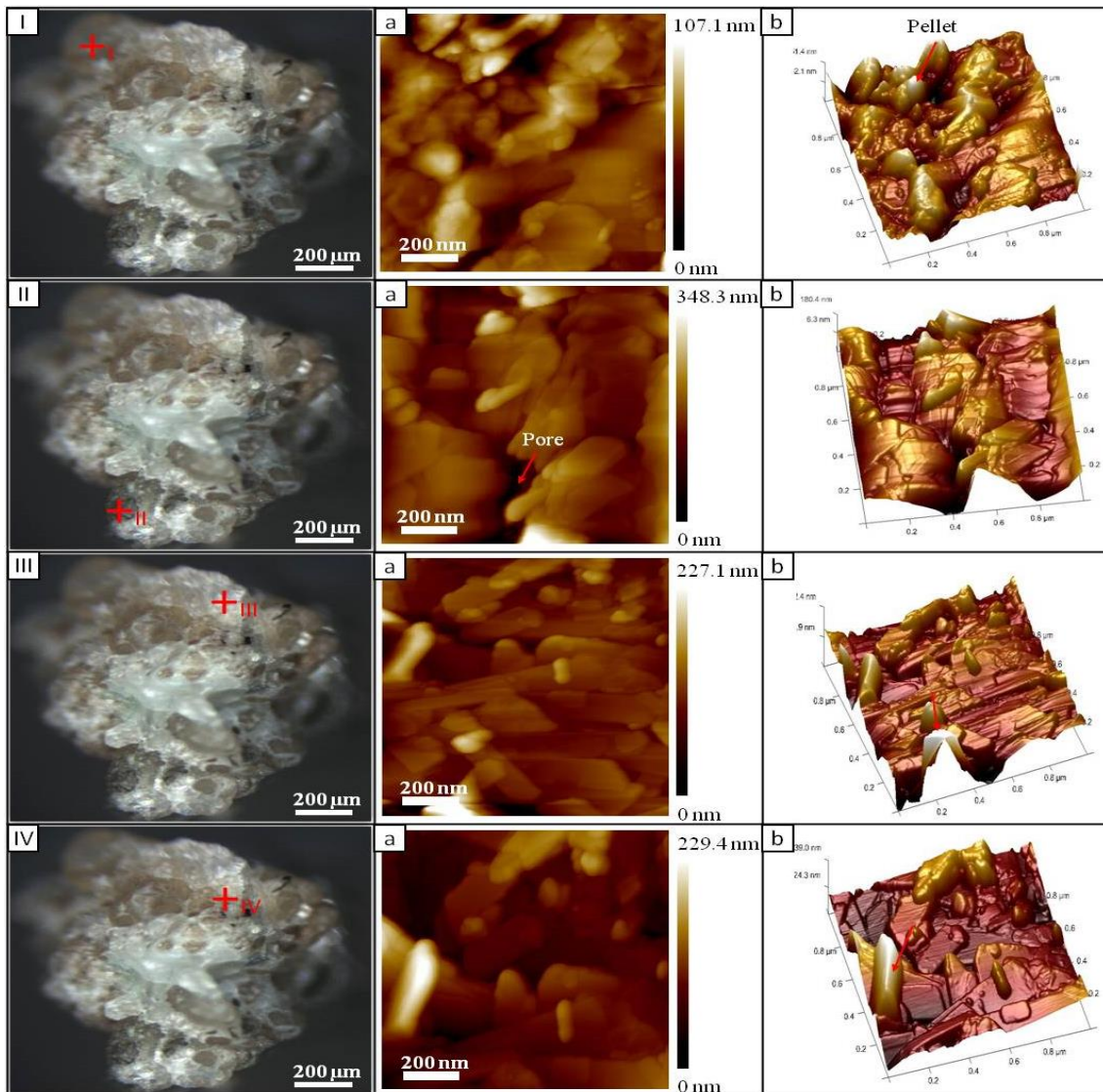


Appendix III.29: Sample RL I_5041_B. The CLSM image shows an overview scan of the quartz grain surface at 10x magnification. Crosshairs indicate the spots analysed with AFM. The AFM images show the topography of the quartz surface (images Ia – IIIa). The analogous 3D display is given in images Ib - IIIb.

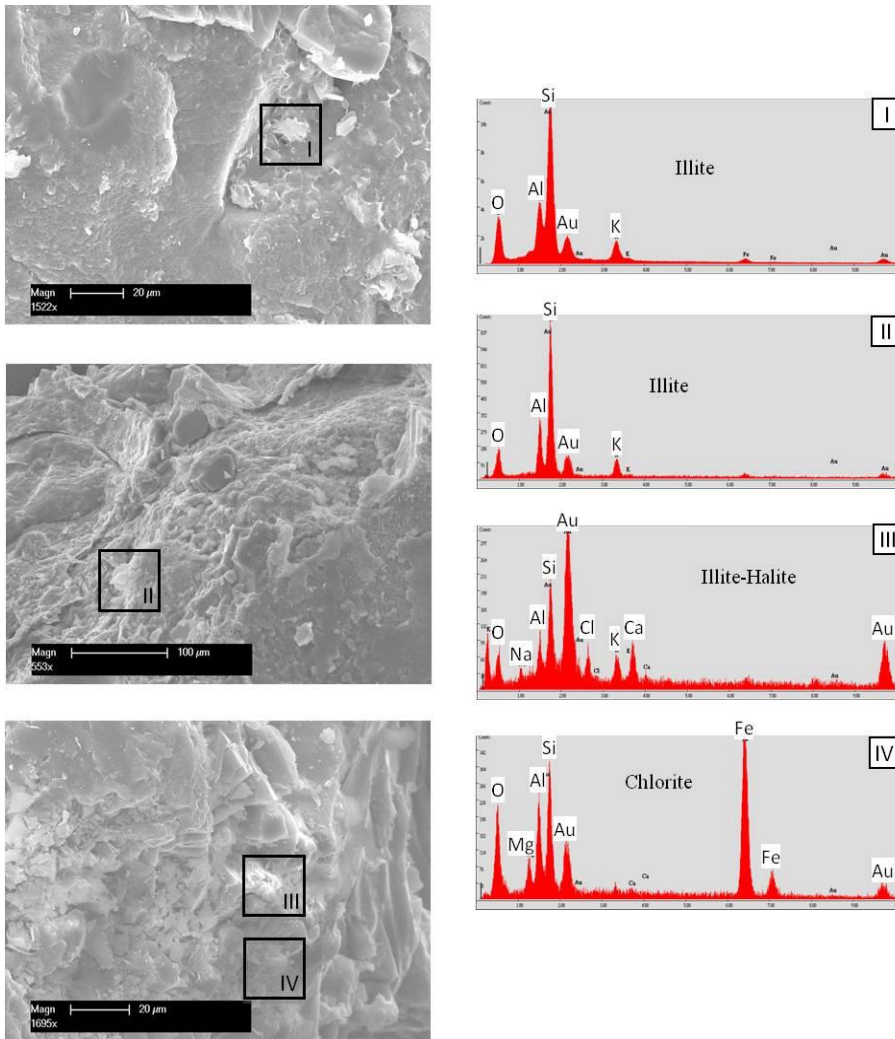


Appendix III.30: Sample RL I_5041_B. SEM image and element spectra (EDX) show that calcite overlays only the quartz surface at point III, while the other points show a blank, non-overgrown quartz surface.

RL I_5041_C

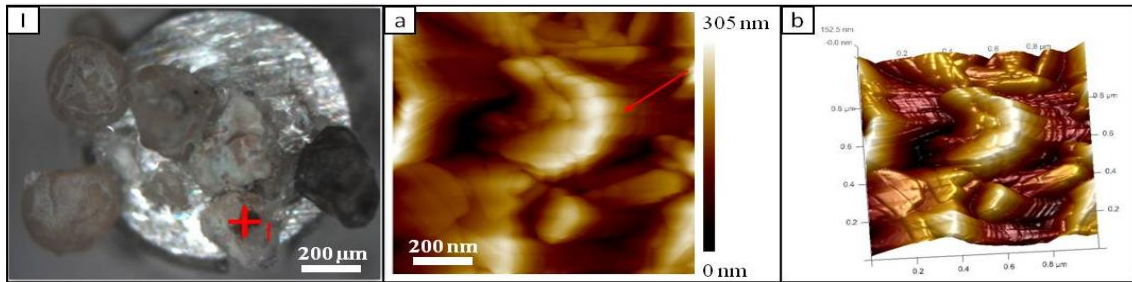


Appendix III.31: Sample RL I_5041_C. Overview image of sample RL I_5041_C taken with binoculars at 5x magnification and high resolution AFM images of the sample topography scanned at the points marked with the red crosses. The grain surfaces are displayed in the AFM images Ia – IIa and the cement surfaces in the AFM images IIIa – IVa. Images Ib – IVb are the analogous 3D representations.

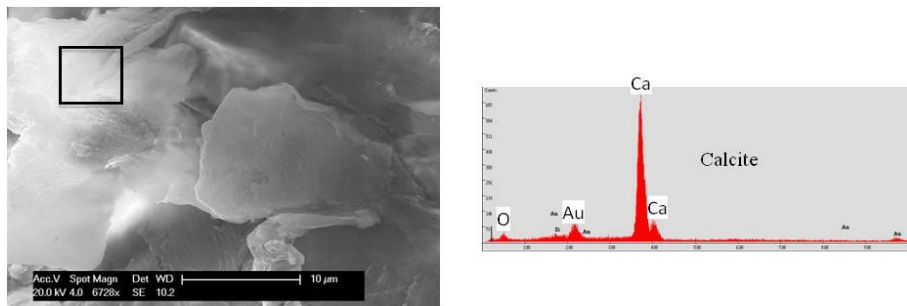


Appendix III.32: Sample RL I_5041_C. SEM images of the grain surface with 100 μm and 400 μm image size. The marked rectangles I – II show the grain surfaces which are overlain by illite and rectangles III – IV indicate the cement surfaces which are formed by illite and chlorite authigenic minerals. The element composition was determined by the corresponding EDX spectra (I - IV).

RL I_5041_E

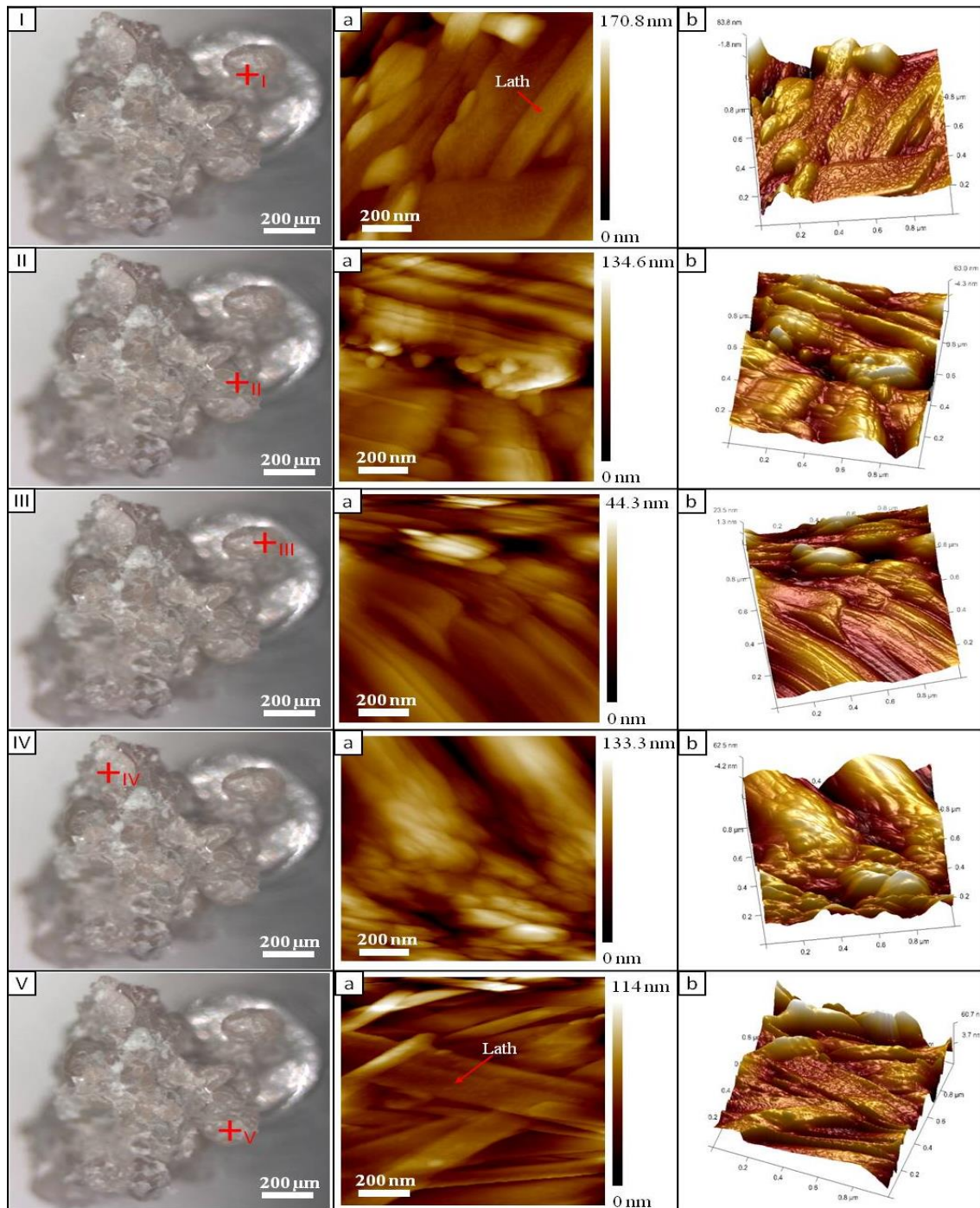


Appendix III.33: Sample RL I_5041_E. Overview image of the sample with binoculars at 5x magnification and label of the spot, which was scanned by AFM. The AFM images show the topography of the grain surface in image Ia and as a 3D image Ib.

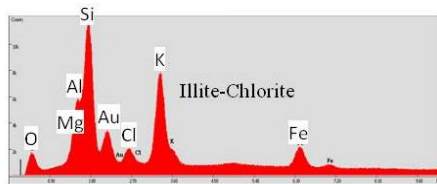
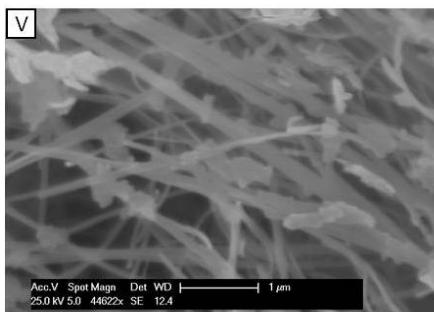
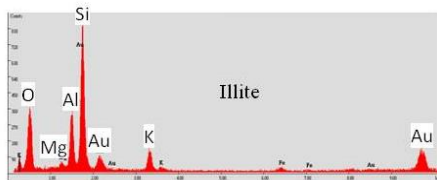
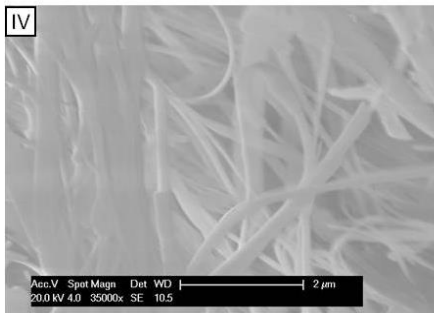
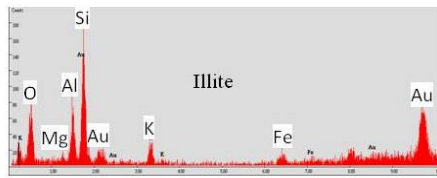
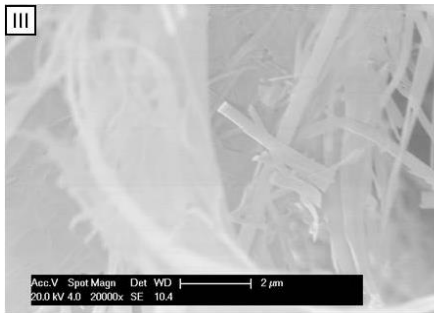
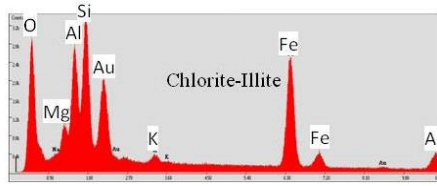
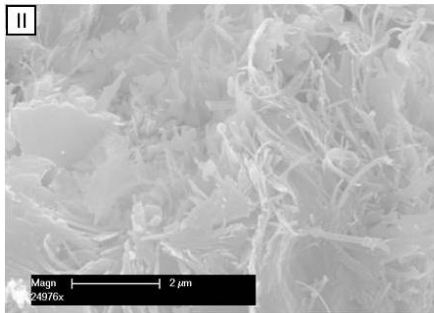
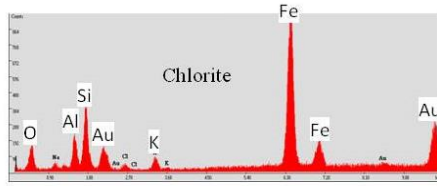
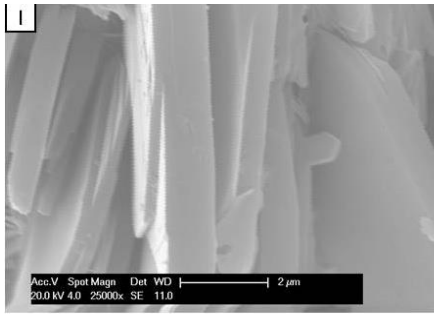


Appendix III.34: Sample RL I_5041_E. SEM image indicates that a calcite layer overlays the grain surface. The calcite is of sub euhedral shape. The spectrum corresponds to the rectangle in the SEM image.

RL I_5041_F



Appendix III.35: Sample RL I_5041_F. Overview image of sample RL I_5041_F taken at 5x magnification with binoculars (I - V) and marks of the spots that were measured with AFM (indicated by crosshairs). The roughness of the grain and cement surface is determined from the AFM height images Ia – Va and a 3D is given in images Ib – Vb.



Appendix III.36: Sample RL I_5041_F. SEM images of all analysed AFM areas. Both, the grain and the cement surfaces are overlain by illite and illite-chlorite minerals. Illite occurs in thin ribbons and chlorite is present as euhedral, pseudo hexagonal crystals, and individual platelets. The minerals were attested with EDX.

CURRICULUM VITAE

Personal

Name Lieu Kim Phuong
Born in Binh Duong, Viet Nam
Date of Brith 12.08.1973

Education

- Primary education:

09/1981 - 05/1985: Binh Nham Primary School

- Secondary education:

09/1985 - 05/1989: Binh Nham Primary –Secondary School

- High education:

09/1989 - 05/1991: Lai Thieu High school

09/1991 - 05/1992: Trinh Hoai Duc High school

- University:

09/1993 - 07/1997: University of Science–Vietnam National University-HoChiMinh City,

Major subject: Geology, Degree awarded: Bachelor of Science

11/2001 - 12/2004: University of Science–Vietnam National University-HoChiMinh City,

Major subject: Petrography, Mineralogy, Sedimentology, Degree awarded: Master of Science

2010 – 2013: PhD candidate, Ludwig-Maximilians-Universität, Munich, Germany

PUBLICATIONS

Altermann, W., Drobek, T., Frei, M., Heckl, W. M., Kantioler, M., Lieu, K. P., Stark, R. W. and Strobel, C. (2010). "Surface and Wetting Properties of Diagenetic Minerals and Sedimentary Grains in Reservoir Rocks (NanoPorO)." Geotechnologien Science Report **16**: 65-75.

Drobek, T., Kantioler, M., Lieu, K. P., Altermann, W., Frei, M., Strobel, J. and Stark, R. W. (2010). Pore surface topography in sandstone reservoirs. Schriftenreihe Deutsche Gesellschaft Geowissenschaften (SDGG). 145-146.

Drobek, T., Strobel, J., Park, S., Lieu, K. P., Altermann, W., Lemmel, H., Lindner, P. and Stark, R. W. (2011). Small Angle Neutron Scattering Analysis of Porous Reservoir Rocks. International Symposium of the Society of Core Analysts, Austin, Texas, USA.

Liêu, K. P., Altermann, W., Stark, R. W., Drobek, T. and Frei, M. (2012). "Characteristics of sandstone reservoir rocks from a well of the Northern German Basin." PetroVietnam **09**: 21-25.

Lieu, K. P., Drobek, T., Altermann, W. and Stark, R. W. (2010). Pore surface topography in sandstone reservoirs. Proceedings International Symposium Hanoi Geoenineering, Vietnam National University: 333-337.